Design, development, and characterization of a microwave electrodeless plasma thruster

by

Marco Riccardo Inchingolo

A dissertation submitted by in partial fulfillment of the requirements for the degree of Doctor of Philosophy in

Aerospace Engineering

Universidad Carlos III de Madrid

Advisor(s):

Jaume Navarro Cavallé
Mario Merino Martinez

Tutor:

Jaume Navarro Cavallé

2024

Dedicated to my family.

Illustration by Scherezade Barquero, background by Dall-E.

Acknowledgments

First and foremost, I would like to thank my thesis supervisors Jaume and Mario, this work would not have been the same without your mentoring. Thank you, Jaume for your dedication and for the countless invaluable hours spent discussing in your office, and Mario for your patience, you taught me to never settle and aim for perfection. I want to express my gratitude as well to Eduardo and Pablo, thank you both for leading the team and for having made this work possible.

I also would like to thank Stéphane, I still remember the first interview you had with me in far 2018. I wouldn't be working in this field if it wasn't for you, and also this time, thank you for having accepted my proposal and made the LIF experiments a reality. Thank you as well, Alfio, for the brilliant and efficient work performed together.

I am profoundly grateful to my Japanese mentors, professors Tsukizaki and Nishiyama, thank you for the priceless experience at JAXA. Thank you professor Tsukizaki, for teaching me LIF, and welcoming me to your team.

E ovviamente grazie ai miei genitori per avermi permesso di soddisfare la mia curiosità e insegnato i valori che mi hanno portato fin qui. Grazie anche ai miei fratelli per aver spianato la strada del dottorato (che inizialmente non avevo considerato). Grazie Mamma, Papà, Alessio, Marta, Yuhan e Erind, grazie a tutti voi per il continuo supporto. Al nuovo arrivato, Daniel, spero che sarai ispirato dai tuoi zii dottori e che anche tu seguirai il percorso che più ti appassiona (la biologia non è ammessa). Grazie anche ai miei cugini e zii, per il vostro affetto. Fabio, vedrai che la tua non è stata una pessima scelta.

Gracias Scherezade por representar mi familia en España, por enseñarme que ninguna dificultad es insuperable, por ser la persona que eres. Este viaje iba a ser muy diferente sin ti. Giuseppe thank you for your friendship, support, passions, and also obsessions, you are making me a stronger person in every way. Thank you Elena for your lifelong friendship and the endless calls during these years, Spain was not that far wasn't it? Thank you as well, Tatiana, for being my psychologist friend, I am sure our careers and life will continue to cross up to retirement.

Thanks to the Davides, Matteos, Albertos, Simone, Célian, and the whole EP2 team, you all are amazing friends and professionals, I feel lucky to spend all my days

and barritas with you. For the new entries, it is going to be a long journey, but I hope you are going to enjoy this trip at least as I did. Thank you as well, Mick, Xin, and Alvaro for your contribution and for being my inspiration in my early PhD years.

Gracias a todos los miembros de mi familia española, Nejla, Rubén, Andrea, Maca, Dani, y Hasib, gracias por haberme acompañado en este camino. E grazie anche agli amici di sempre, Stefano, Antonella, Giovanni, Domenico, Francesco, Nicola, Davide e a tutti gli altri, per sopportare la mia assenza e farmi sentire come se il tempo non fosse mai trascorso ogni volta che torno.

Last but not least, I would like to thank as well all my Japanese friends, Ani, Nono, Tsuji, Shogo, Koiso, Tabata, Shirasawa, Takagi, Abe, Miya, and Morishita you all made me feel at home on the other side of the world. I hope our lives will cross again. お疲れ様です!

Published and submitted content

The following list includes the works published in peer-reviewed journals or as conference proceedings. The contents of these works are fully or partially reproduced within this Thesis. Whenever material from these sources is included in this thesis, they are singled out with typographic means and an explicit reference.

Journal Publications

- Inchingolo M.R. (IMR), Merino M. (MM), Wijnen M. (WM), and Navarro-Cavallé J. (NCJ), "Thrust Measurements of a waveguide Electron Cyclotron Resonance Thruster", Submitted to Journal of Applied Physics (JAP), 2024. Chapter 6 wholly includes this entry and some additional content. The experiment design, data acquisition, and post-processing have been carried out by IMR. The paper has been written by IMR with feedback from MM and NCJ; WM has contributed to the design of the experimental assembly.

- Inchingolo M.R., Merino M., and Navarro-Cavallé J., "Plume characterization of a waveguide ECR thruster", Journal of Applied Physics (JAP), Volume 133, Issue 11, 2023. https://doi.org/10.1063/5.0138780. The article was awarded "Editor's Choice" by the JAP journal editorial office and had a dedicated "Scilight" dissemination online article available at https://aip.scitation.org/doi /10.1063/10.0017695. Chapter 5 wholly includes this entry and some additional content. The experiment design, data acquisition, and post-processing have been carried out by IMR. NCJ has contributed to the data acquisition. The paper has been written by IMR with feedback from MM and NCJ.

- Vinci A. E. (VAE), Inchingolo M.R., Mazouffre S. (MS) and Navarro-Cavallé J. (NCJ), "Ion dynamics in the magnetic nozzle of a waveguide ECR thruster via laser-induced fluorescence spectroscopy", J. Phys. D: Appl. Phys. 56, 2022. https://doi.org/10.1088/1361-6463/aca105. Chapter 7 wholly includes contributions from this entry. The experiment design, data acquisition, and post-processing have been carried out by IMR and VAE. The LIF lineshape acquisition and analysis have been carried out by VAE. The paper has been written by VAE and IMR with feedback from NCJ and MS. Extract from this work can also be found in the Ph.D. thesis of VAE.

Conference Proceedings

- Inchingolo M.R., Navarro-Cavallé J., "Faraday Cup Design for Electrodeless Plasma Thrusters", Aerospace Europe Conference (EUCASS). No. 488, Lausanne, Switzerland, 2023. Chapter B wholly includes this entry. The experiment design, data acquisition, and post-processing have been carried out by IMR. The paper has been written by IMR with feedback from NCJ.

- Inchingolo M.R., Navarro-Cavallé J., and Merino M., "Direct Thrust Measurements of a circular waveguide Electron Cyclotron Resonance Thruster", International Electric Propulsion Conference (IEPC), Boston MA, 2022. Chapter 6 partially includes contributions from this entry. The experiment design, data acquisition, and post-processing have been carried out by IMR. The paper has been written by IMR with feedback from MM and NCJ. The material from this source included in this thesis is not singled out with typographic means and references since the journal paper about thrust measurements above is referenced instead.

- Inchingolo M. R., Merino M., and Navarro-Cavallé J., "Hybrid PIC-Fluid Simulation of a Waveguide ECR Magnetic Nozzle Plasma Thruster," Space Propulsion Conference (SPC), No. 00192, Association Aéronautique et Astronautique de France, March 17-19, 2021. Chapter 4 wholly includes this entry. The simulations and post-processing have been carried out by IMR. The paper has been written by IMR with feedback from MM and NCJ.

Other research merits

- Shirasawa R., Inchingolo M. R., Morishita T., Tsukizaki R., and Nishiyama, K., "Backflow Xenon Ions Measurement by Laser-induced Fluorescence Spectroscopy in the Plume of a Microwave Discharge Ion Thruster", International Symposium On Space Technology and Science (ISTS), Kurume, 2023.

- Vinci A. E., Mazouffre S., Inchingolo M. R., Gomez V., Fajardo P., and Navarro-Cavallé J., "Probing xenon atoms and ions velocity in the magnetic nozzle of a helicon plasma thruster", 37th International Electric Propulsion Conference (IEPC), Massachusetts Institute of Technology, Cambridge, MA, USA, June 19,23, 2022.

- Mazouffre S., Vinci A. E., Inchingolo M. R., Navarro-Cavallé J., Fajardo P., "Ion transport in the magnetic nozzle of electrodeless plasma thrusters for spacecraft", 32nd International Symposium on Rarefied Gas Dynamics, Seoul, South Korea, June 4-8, 2022.

- Inchingolo M.R., Navarro-Cavallé J., and Merino M., "Design and Plume Characterization of a Low-Power Circular Waveguide Coupled ECR Thruster," 5th International Workshop on Micropropulsion and CubeSats (MPCS), Toulouse, 2021. Online oral presentation.

- Merino M., Sánchez A., Domínguez A., Bello E., Jiménez P., Inchingolo M., Navarro J., Cichocki F., Fajardo P., Ahedo E., Hidalgo C., Van Milligen B., Tabarés F., Calvo I., Velasco J., Cappa A., and de la Cal E., "Synergies between space plasma propulsion and magnetic confinement plasma fusion: PROMETEO project," XXXVII Reunión Bienal de la Real Sociedad Española de Física, RSEF, Zaragoza, 2019.

Abstract

This thesis delves into the design of a waveguide Electron Cyclotron Resonance Thruster prototype, the experimental characterization of its plasma discharge and plume, and the evaluation of its performance characteristics. The research aims to attain a purely electrodeless plasma thruster with comparable performance to conventional electric thrusters employing electrodes, addressing their inherent lifetime limitations.

Electric propulsion (EP) is an in-space propulsion technology that uses electric power to accelerate a propellant. This propellant is typically in the form of a plasma and accelerated using electric and magnetic fields, generating thrust. Typical established thruster technologies employ electrodes for plasma acceleration. However, these are subject to erosion or contamination, potentially leading to failure, and thus limiting the lifetime of a space mission. Electrodeless thrusters, on the other hand, use electromagnetic power to generate plasma and, typically, a magnetic nozzle to accelerate it, therefore they lack these lifetime-limiting components. Additionally, can operate on virtually any propellant gas (Xenon, Argon, Krypton, water, etc.). However, these technologies show limited performance and are still the subject of extensive research efforts.

The Electron Cyclotron Resonance (ECR) occurs when electromagnetic power (typically microwaves) is efficiently absorbed by a plasma immersed in a magnetic field. This phenomenon is extensively used in industrial plasma sources, and in the last decades, the applications in the electric propulsion field have become of interest to the EP community, thanks to the work of several research groups on Coaxial ECR thrusters. However, this technology is not purely electrodeless and necessitates the presence of a central conductor exposed to the plasma, subject to erosion. An alternative way of coupling power to the plasma using the ECR is employing a waveguide geometry which does not need the presence of the central conductor. On the other hand, this technology has shown limited performance in the past if compared to the coaxial one. This thesis contributes to a better understanding of this thruster with the development and experimental study of a waveguide Electron Cyclotron Resonance thruster (ECRT) prototype to identify the performance limitations and assess the viability of this technology. This objective is carried out firstly by designing an ECRT prototype, secondly, the discharge physics

is explored via simulation tools and the plume metrics characterized via electrostatic probe and LIF measurements. Finally, the thruster performance is directly assessed via thrust balance measurements.

The design of the waveguide thruster presented in this thesis is described in Chapter 3. The thruster is designed to work at a larger microwave frequency, 5.8 GHz, than the typically employed 2.45 GHz, allowing the reduction of the thruster dimensions and the down-scaling of the power requirement to a power lower than 400 W. A permanent magnet is used to generate the magnetic field necessary for the ECR and the creation of the magnetic nozzle for the plasma acceleration. An additional electromagnet is also included in the assembly to alter the resonance position and vary the shape of the magnetic nozzle. The design of the transmission line employed in the experiments is also presented.

To assess the thruster design, simulations of the discharge chamber and the near magnetic nozzle segment are performed using the HYPHEN code developed by the EP2 team. HYPHEN is a hybrid PIC-fluid code, that can be used to simulate, and has been validated on different types of electric thrusters. The geometry of the designed waveguide ECRT has been used as a baseline for defining the simulation domain. To simulate the electromagnetic power absorption at the ECR region, user-defined power deposition maps are provided for the electron fluid. Depending on it, different pressure, temperature, and current profiles are found, strongly affecting the discharge. Regions of magnetic drag may exist in the plume. A parametric analysis has been performed showing good scaling with the energy per particle. Performance metrics have been obtained, being in the 10% – 20% thrust efficiency range.

In Chapter 5 the first characterization of the plasma plume produced by the waveguide ECRT prototype is presented. The plume is probed with electrostatic probes, a Faraday cup, and a Langmuir probe, across a wide range of working points. Further information is gathered by analyzing the change in microwave reflection coefficient and thruster floating potential. The plume current analysis showed large divergence angles and poor plume utilization efficiency, below 70%. Relatively low electron temperatures have also been found, and electron cooling has been observed along the plume expansion. The effect of the magnetic field topology is analyzed by varying the electromagnet current. Using these data, a preliminary estimation of the thrust efficiency was performed, obtaining values below 2%.

Following the characterization of the plume, improvements in the thruster assembly are made by introducing a diffused radial propellant injector and a stub-tuner in the transmission line to reduce the level of power reflections. In Chapter 6, the performance of the thruster is further analyzed with the use of an amplified displacement hanging pendulum thrust balance, additionally, the plume characterization is completed by measurements of the ion energy by using an RPA. The thrust measurements led to an estimation of the thrust efficiency of up to 3.5 %. The per-

formed probe measurements allowed us to compute the partial efficiencies, showing that the energy efficiency, is the factor that limits the most the performance of the device, staying below 7%, the utilization was shown to be consistent with the previous measurements. For increased mass flow rates the plume has been found to become hollow, leading to a high divergence angle. Preliminary results regarding the existence of a population of energetic electrons have also been found.

Finally, in collaboration with the CNRS-ICARE laboratory, the LIF technique has been used to carry out additional measurements on the plume of this prototype. The plume has been analyzed for various conditions, and the related findings are discussed in Chapter 7. The magnetic nozzle length was not found to alter the terminal speed of the ions in the observed spatial range, however, it affects ion accelerations in the near-plume region. Large ion axial kinetic temperatures were found in the range of several thousands of Kelvins, a result that may hint at an extended ionization region. Further measurements were performed in the middle of the plasma discharge chamber, a region notoriously difficult to probe with intrusive probes. Findings show that the ions have a negative mean velocity (towards the backplate), therefore a big fraction of the ion production is thought to be lost at the thruster walls.

Two Appendices at the end of this work summarize parallel activities performed in the context of this thesis. Appendix A presents the work performed by the author at the Japanese Aerospace Exploration Agency (JAXA), where the LIF diagnostic has been used on the engineering model of the ECR gridded ion thruster used along the Hayabusa II mission, the technique has been used to assess back-sputtering phenomenon observed during in-flight operations. In Appendix B, Faraday Cups are tested on the plume of a Helicon thruster to evaluate the impact of design alternatives on the measured ion current density.

Resumen

Esta tesis se adentra en el examen experimental de la pluma de plasma y las características de rendimiento de un propulsor de resonancia electrón ciclotrón de guía de onda. La investigación tiene como objetivo lograr un propulsor de plasma puramente sin electrodos con un rendimiento comparable, abordando las limitaciones de vida inherentes de los propulsores eléctricos convencionales que emplean electrodos.

La propulsión eléctrica (EP) es una tecnología de propulsión espacial que utiliza energía eléctrica para acelerar un propelente. Este propelente generalmente se encuentra en forma de plasma y se acelera utilizando campos eléctricos y magnéticos, generando empuje. Las tecnologías de propulsores consolidadas, típicamente emplean electrodos para la aceleración del plasma. Sin embargo, estos son susceptibles a la erosión o contaminación, lo que podría provocar fallos y, por lo tanto, limitar la vida útil de una misión espacial. Los propulsores sin electrodos, por otro lado, utilizan energía electromagnética para generar el plasma, y una tobera magnética para acelerarlo, por lo que no tienen estos componentes que reducen la vida útil. Sin embargo, estas tecnologías muestran un rendimiento limitado y siguen siendo objeto de un extenso esfuerzo de investigación.

La resonancia de ciclotrón de electrones (ECR) ocurre cuando la potencia electromagnética (típicamente microondas) es absorbida de manera eficiente por un plasma sumergido en un campo magnético. Este fenómeno se utiliza ampliamente en fuentes de plasma industriales, y en las últimas décadas, las aplicaciones en el campo de la propulsión eléctrica han llamado la atención de la comunidad EP, gracias al trabajo de varios grupos de investigación en propulsores ECR coaxiales. Sin embargo, esta tecnología no es puramente sin electrodos y requiere la presencia de un conductor central expuesto al plasma, sujeto a erosión. Una forma alternativa de acoplar potencia al plasma utilizando la ECR es emplear una geometría de guía de onda que no necesita la presencia del conductor central. Por otro lado, esta tecnología ha mostrado un rendimiento limitado en el pasado en comparación con la coaxial. Esta tesis se inserta en este contexto con el desarrollo y el estudio experimental de un propulsor de resonancia de ciclotrón de electrones de guía de onda (ECRT) para identificar las limitaciones de rendimiento y evaluar la viabilidad de esta tecnología.

El diseño del propulsor de guía de onda presentado en esta tesis se describe en el Capítulo 3. El propulsor está diseñado para trabajar a una frecuencia de microondas

más alta, 5.8 GHz, de la comúnmente empleada de 2.45 GHz, lo que permite reducir las dimensiones del propulsor y reducir la potencia necesaria a una potencia inferior a 400 W. Un imán permanente se utiliza para generar el campo magnético necesario para la ECR y la creación de la tobera magnética para la aceleración del plasma. Un electroimán proporciona un grado de libertad adicional para modificar la posición de resonancia y variar la forma de la tobera magnética. También se presenta el diseño de la línea de transmisión empleada en los experimentos.

Para evaluar el diseño del propulsor, se realizan simulaciones de la cámara de descarga y del segmento cercano de la tobera magnética, utilizando el código HY-PHEN desarrollado por el equipo EP2. HYPHEN es un código híbrido PIC-fluido que se puede utilizar para simular, y ha sido validado sobre, diferentes tipos de propulsores eléctricos. La geometría del ECRT diseñado se ha utilizado como base para definir el dominio de la simulación. Para simular la absorción de potencia electromagnética en la región ECR se proporcionan mapas de deposición de potencia definidos por el usuario para el fluido electrónico. Dependiendo de esas se encuentran diferentes perfiles de presión, temperatura y corriente, que afectan significativamente la descarga. Es posible que existan regiones de resistencia magnética en la pluma. Se ha realizado un análisis paramétrico que muestra una buena escalabilidad con la energía por partícula. Se han obtenido métricas de rendimiento que se encuentran en el rango de eficiencia de empuje del 10% al 20%.

En el Capítulo 5 se presenta la primera caracterización de la pluma de plasma producida por el prototipo de propulsor ECRT de guía de onda. La pluma se explora con sondas electrostáticas, una copa Faraday y una sonda de Langmuir, en un amplio rango de puntos de trabajo. Se recopila información adicional analizando el cambio en el coeficiente de reflexión de microondas y el potencial flotante del propulsor. El análisis de la corriente en la pluma muestra ángulos de divergencia grandes y una baja eficiencia de utilización de la pluma, inferior al 70%. También se han encontrado temperaturas electrónicas relativamente bajas y se ha observado enfriamiento electrónico a lo largo de la expansión de la pluma. Se analiza el efecto de la topología del campo magnético variando la corriente del electroimán. Utilizando estos datos, se realiza una estimación preliminar de la eficiencia de empuje obteniendo valores por debajo del 2%.

Tras la caracterización de la pluma, se llevan a cabo mejoras en el montaje del propulsor mediante la introducción de un inyector de propelente radial difuso y un "stub-tuner" en la línea de transmisión para reducir el nivel de reflexiones de potencia. En el Capítulo 6 se analiza aún más el rendimiento del propulsor utilizando una balanza de empuje de péndulo colgante de desplazamiento amplificado, y además, la caracterización de la pluma se completa con mediciones de la energía iónica utilizando una RPA. Las mediciones de empuje llevan a una estimación de la eficiencia de empuje de 3,5%. Las mediciones de sonda realizadas nos permitieron calcular las eficiencias parciales, mostrando que la eficiencia energética es el factor que limita

más el rendimiento del dispositivo, manteniéndose por debajo del 7%. La utilización se mostró consistente con las mediciones anteriores. Para aumentos en los caudales de masa se ha encontrado que la pluma se vuelve hueca, lo que lleva a un ángulo de divergencia alto. También se han encontrado resultados preliminares sobre la existencia de una población de electrones energéticos.

Finalmente, en colaboración con el laboratorio CNRS-ICARE, se ha utilizado la técnica LIF para realizar mediciones adicionales en la pluma de este prototipo. La pluma se ha analizado en varias condiciones, cuyos resultados se discuten en el Capítulo 7. La longitud de la tobera magnética no altera la velocidad terminal de los iones en el rango espacial observado. Sin embargo, afecta las aceleraciones iónicas en la primera región de la pluma. Se encuentran altas temperaturas cinéticas axiales de iones en el rango de varios miles de Kelvin, un resultado que puede sugerir una región de ionización extendida. Se realizan también mediciones en el centro de la cámara de descarga de plasma, una región notoriamente difícil de explorar con sondas invasivas. Los hallazgos muestran que los iones tienen una velocidad media negativa (hacia la pared posterior), por lo que se cree que una gran fracción de la producción de iones se pierde en las paredes del propulsor.

Al final de este trabajo dos apéndices resumen las actividades paralelas realizadas en el contexto de esta tesis. El Apéndice A presenta el trabajo en la Agencia Japonesa de Exploración Aeroespacial (JAXA), el diagnóstico de LIF se ha utilizado en el modelo de ingeniería del propulsor de iones ECR utilizado en la misión Hayabusa II. La técnica se ha empleado para evaluar el fenómeno de sputtering observado durante las operaciones en vuelo. En el Apéndice B, se prueban Faraday cups en la pluma de un propulsor Helicón para evaluar el impacto de las alternativas de diseño en la densidad de corriente iónica medida.

Contents

A Assessment of Xenon Ions Backflow by LIF Spectroscopy in the Plume of a Microwave Gridded Ion Thruster   149

B Faraday Cup Design for Electrodeless Plasma Thrusters   165

Bibliography   182

List of Figures

List of Tables

Acronyms

AC Alternating Current.

AWG American Wire Gauge.

BC Boundary Condition.

CAD Computer Assisted Design.

CEX Charge Exchange Collisions.

CMA Clemmow-Mullaly-Allis.

CW Continuous Wave.

DC Direct Current.

DI Double Injector.

ECR Electron Cyclotron Resonance.

ECRIS ECR ion sources.

ECRT Electron Cyclotron Resonance Thruster.

EEDF Electron Energy Distribution Function.

EM Electromagnet.

EP Electric Propulsion.

EP2 Plasma and Space Propulsion Team.

EPT Electrodeless Plasma Thruster.

FC Faraday Cup.

FEM Finite Element.

FoV Field of View.

FP Faraday Probe.

GIT Gridded Ion Thruster.

HET Hall Effect Thruster.

HPT Helicon Plasma Thruster.

ICR Ion Cyclotron Resonance.

IEDF Ion Energy Distribution Function.

ITO Indium Tin Oxide.

IVDF Ion Velocity Distribution Function.

LCP Left-hand Circularly Polarized.

LEO Low Earth-Orbit.

LHR Lower Hybrid Resonance.

LIF Laser Induced Fluorescence.

LP Langmuir Probe.

MFAM Magnetic Field Aligned Mesh.

MN Magnetic Nozzle.

MW Microwave.

ND Neutral Density.

PC Plasma Discharge Chamber.

PIC Particle In Cell.

PM Permanent Magnet.

PMT Photomultiplier.

QCM Quartz Microbalance.

RCP Right-hand Circularly Polarized.

RF Radio-frequency.

RPA Retarding Potential Analyzer.

SEE Secondary Electron Emission.

SI Single Injector.

TB Thrust Balance.

TE Transverse Electric.

TEM Transverse Electromagnetic.

TL Transmission Line.

TM Transverse Magnetic.

TTPR Thrust To Power Ratio.

UC3M Universidad Carlos III de Madrid.

UHR Upper Hybrid Resonance.

VAPHER Variable Amplitude Hanging Pendulum.

VASIMR Variable Specific Impulse Magnetoplasma Rocket.

VDF Velocity Distribution Function.

VNA Vector Network Analyzer.

Chapter 1

Introduction

"The Earth is the cradle of humanity, but mankind cannot stay in the cradle forever."

- Konstantin Tsiolkovsky

It has been less than a century since the launch of Sputnik 1, the first artificial satellite, marked the dawn of the space age. Since then, we have witnessed a steady progression in our understanding of the Universe and our place within it. The early years were marked by significant milestones, including the Apollo program that landed humans on the Moon and interplanetary missions that expanded our understanding of the solar system. Not long after, the era of Space Shuttles and space stations saw the establishment of a continuous human presence in orbit.

In recent years, a paradigm shift has occurred with the commercialization of Space. Startups have emerged as key players, disrupting traditional state-driven models and driving innovation. The number of satellites in orbit is exponentially growing and companies are now developing their own rockets and spacecraft, offering a range of services from satellite launches to space tourism. One pivotal technological advancement that has significantly influenced the satellite market is onboard propulsion. With a particular emphasis on electric propulsion, spacecraft equipped with a propulsion system are able to perform maneuvers, carry a higher payload mass, extend their operational lifetime, enable responsive space operations, and satisfy the regulatory framework by performing de-orbiting maneuvers at the end of their lifetime.

As the space industry continues to evolve, electric propulsion is likely to play an even more central role in shaping the future of spacecraft technology. If this thesis contributes even in a small way to this endeavor, the effort will have been worthwhile.

1.1   Electric Propulsion

Rocket propulsion is a class of systems and methods to propel a body by accelerating and expelling part of its mass, the propellant. Generally speaking, this kind of propulsion method is essential in situations for which one cannot, or it is not convenient to, rely on a medium for propulsion, hence the need to carry and accelerate propellant to generate thrust through Newton's third law. Placing a satellite into orbit, propelling a missile, or performing orbital maneuvers are just a few examples of applications that require rocket propulsion.

For a pressure-matched rocket nozzle, the thrust force can be written as in equation 1.1.

$$F = \dot{m}_p v_e \tag{1.1}$$

where $\dot{m}_p$ is the propellant mass flow rate and v_e is the ejected propellant speed. v_e can also be expressed in terms of specific impulse $I_{sp} = v_e/g_0$ being $g_0 = 9.8$ m/s^2 the gravity constant. The larger the mass flow rate and the specific impulse, the larger the thrust. Typical chemical rocket engines expel large amounts of propellants in the order of hundreds or thousands of kg/s at moderately high $I_{sp} = 300 - 400$ s. This enables rockets like launch vehicles to generate substantial thrust levels, up to several thousands of kN, allowing them to lift off from the ground and deliver satellites into orbit. Due to the large $\dot{m}_p$ required they also need to bring large amounts of propellants with them, which is what reduces the payload fraction (payload mass/ take-off mass) to a few percent points.

In-space propulsion refers to the techniques employed to maneuver and accelerate spacecrafts once they have already reached space. In the majority of the cases, in-space propulsion is also rocket-propulsion. Its primary goal is to generate enough thrust to perform orbital maneuvers, set the spacecraft on interplanetary trajectories or simply station-keeping, among other purposes depending on mission definition.

The cost of maneuvers is typically expressed in terms of ΔV which is the variation in spacecraft speed needed to perform the maneuver itself, therefore this quantity depends on the initial and target trajectory. Delta V for typical maneuvers can range from hundreds of m/s to km/s depending on the mission. The famous rocket equation (also called the Tsiolkovsky equation)[1] links the ΔV to the spacecraft mass and propulsion system used:

$$\Delta V = I_{sp} g_0 \log \frac{m_0}{m_f}, \tag{1.2}$$

where m_0 and m_f are the initial and final mass of the rocket or spacecraft. This equation allows a straightforward estimate of the amount of propellant needed for a maneuver or mission given a propulsion system. To achieve a high Delta-V (e.g. long mission or expensive maneuver) it is necessary to lose a large amount of spacecraft

mass (propellant mass) and expel it at a large velocity.

For chemical rockets the I_{sp} value is limited by the available chemical energy stored in the propellant, thus very large masses are lost in a high ΔV maneuver involving chemical rocket engines, reducing the payload mass. The I_{sp} record was held by Rocketdyne in the 60s with a mixture of Lithium, Fluorine, and Hydrogen as propellant (the estimated I_{sp} was about 500 [2]).

Another approach is to not store the energy in the propellant, but to externally provide power for its acceleration. This form of propulsion is commonly referred to as electric propulsion (EP) [3], in which electric power is used to accelerate the propellant at very large velocities. With these technologies, much larger I_{sp} are achieved, theoretically only limited by the available power on board and the speed of light. Typical values are in the range of $600 - 4000$ s of I_{sp}.

However, the great increase in I_{sp} comes at the cost of thrust F. The typical expression for the thrust efficiency of electric thrusters is provided below [3]

$$\eta_F = \frac{F I_{sp} g_0}{2P}, \tag{1.3}$$

where P is the input electric power. Simplifying, at a given P, limited by the on-board power capabilities of the spacecraft, and η_F, increasing the I_{sp} results in a lower thrust and vice-versa.

Therefore, when operating electric propulsion systems, due to the onboard power limitations (typically limited by the size of the solar arrays), a very low mass flow rate is used (range of mg/s) and the thrust is in the order of mN. Power ranges can vary from W to kW depending on the mission. Hence, this kind of propulsion is not suitable for launching satellites but only as in-space propulsion. Consequently, to achieve the same ΔV longer firing times are required than chemical rockets. While for chemical rockets a maneuver can be considered impulsive, electric thrusters can fire continuously for thousands of hours at low thrust in a so-called low-thrust maneuver. Therefore, the ΔV to reach a target orbit may be different than the one for an equivalent impulsive maneuver and as well thruster dependent.

The maneuver and possibly the mission become longer, but the payload mass is increased due to the higher specific impulse. This is well shown by equation 1.2 where can be seen that EP enables lower propellant masses.

All of these factors must be taken into account when designing a space mission. As the technology matures, an increasing amount of satellites are equipped with electric thrusters. Considering the new mega-constellations of Starlink and One-web, electric propulsion is already the most used thruster technology nowadays [4]. Offering the advantage of increased mission lifetime, deorbiting capability, and reduced cost.

Main electric propulsion technologies

A variety of electric thrusters exist. They are grouped into three main categories based on their distinct thrust generation principles: electrothermal, electrostatic, and electromagnetic [5]. Electrothermal thrusters, such as resistojets and arcjets, use electrical energy to heat a propellant before expelling it to generate thrust relying on the pressure of the heated gas. Electrostatic thrusters, like ion thrusters and Hall-effect thrusters, operate by ionizing a propellant and using electric fields to accelerate and expel the ions to produce thrust. Lastly, electromagnetic thrusters, including magnetoplasmadynamic and pulsed inductive thrusters, rely on electromagnetic forces to accelerate and expel a propellant, offering unique advantages in terms of efficiency and specific impulse. Gridded Ion thrusters (GIT) and Hall effect thrusters (HET) are currently the most efficient and used technology of those [6]. Cross-section schemes of a HET and a GIT are shown in figures 1.1a and 1.1b.

(a) (b)
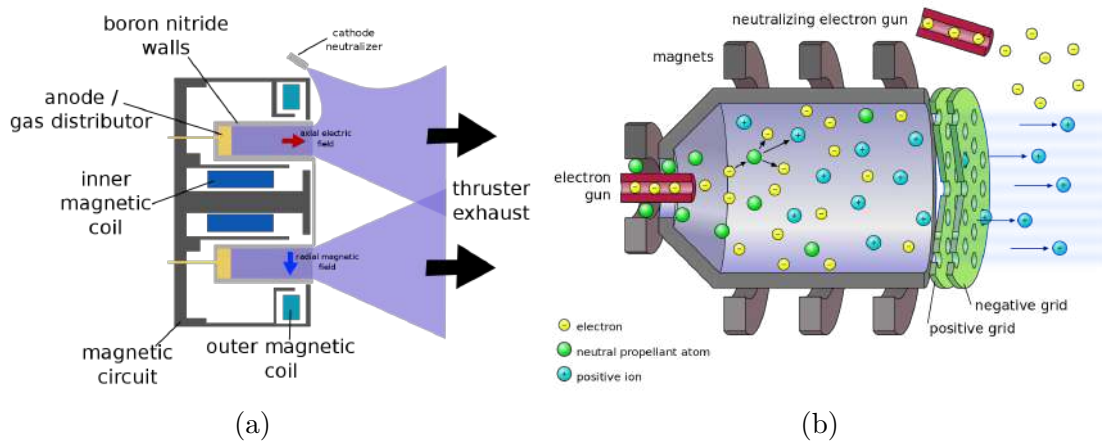
Figure 1.1: (a) Scheme of a Hall thruster [7] and (b) of a gridded ion thruster [8].

HETs typically consist of an annular discharge chamber including an anode upstream and a hollow cathode positioned on the exterior. In the simplest form, a radial magnetic field and an axial electric field constrict the electrons emitted by the hollow cathode in a gyrating motion about the axis, efficiently ionizing the neutral propellant. The resulting plasma is then accelerated by the electric field, producing thrust. A part of the cathode discharge current neutralizes the plasma beam. HETs offer relatively high efficiency, reaching up to $40 - 60\%$ [3, 9]. They are easily scalable to high powers (up to tens of kW) and can achieve I_{sp} levels in the range of 1500 s.

Ion thrusters, on the other hand, employ a grid system to accelerate propellant ions. The grid system consists of two or more electrodes with circular apertures, between the grids a bias in the range of kV is applied. Electrons emitted from an electron gun bombard the propellant, generating ions that are accelerated by the large electric field between the grids. This process results in a stream of accelerated ions, producing thrust. A hollow cathode emits the electrons to neutralize the plume.

Ion thrusters have the highest efficiency among electric propulsion systems, reaching up to 80% and I_{sp} in the order of 2000 – 5000 s, but also feature a high complexity at system level [3, 10].

Although being mature technologies both of these require the presence of electrodes exposed to the plasma. This fact can significantly limit their lifetime due to electrode erosion: Ion thrusters typically operate in the range of <30000 hours, while for Hall thrusters this is reduced to <10000 hours [11]. Additionally, the presence of hollow cathodes in the assembly limits their operability to a few propellants due to the required chemical stability: the electron emitter insert can easily be contaminated (e.g. by oxygen, sputtered materials, etc.) slowly leading to failure.

1.2 Electrodeless plasma thrusters

Electrodeless plasma thrusters (EPTs) emerge as a promising addition or alternative to both HETs and ion thrusters, addressing some of the limitations of thrusters with electrodes. EPTs use microwaves or radio-frequency waves to ionize and heat propellant, generating plasma without the need for electrodes. This eliminates the erosion and contamination issues associated with electrodes, potentially extending the thruster's lifetime. Electrodeless thrusters have also the potential for a higher thrust density with respect to the established technologies (particularly for the gridded ion thruster case) and they can be scaled to high powers up to the kW range. Finally, EPTs offer a wider range of propellant options, including noble gases, heavier elements, and even water vapor, opening the pathway for in-situ resource utilization like LEO air-breathing technologies or water exploitation on asteroid missions [12, 13]. As a downside, EPTs often exhibit lower thrust efficiency (<10%) and specific impulse. Additional drawbacks, such as in those devices exploiting a magnetic nozzle (MN, see below), typically include strong magnetic fields extending far from the thruster unit and larger plume divergence angles, aspects that may complicate the integration on a spacecraft. These performance limitations have primarily restricted EPTs to research laboratories, as they remain at relatively early stages of development.

A multitude of electrodeless plasma thrusters have been designed and tested [14, 15, 16, 17, 18]. In general, their working principle can be divided into two stages: plasma generation and acceleration. Plasma generation can happen with an alternating electromagnetic field stripping away electrons from the neutral propellant, these are heated by the propagating electromagnetic wave (as for the Helicon thruster) or by employing the electron cyclotron resonance (ECR) phenomenon, finally ionizing the remaining propellant through collisions. Plasma acceleration can also be obtained by a variety of different designs, these are well summarized in Bathgate *et al.* [17]. Most of these designs induce azimuthal plasma currents and exploit

the Lorentz force to accelerate the plasma along an axially diverging magnetic field. Magnetic nozzles emerged as one of the most promising candidates for efficient electrodeless thrusters. Typical rocket engines employ a form of de Laval Nozzle to convert the thermal energy of hot gas into kinetic energy. This mechanism cannot be employed to accelerate a hot plasma since it would lead to substantial plasma losses at the nozzle walls and overheating. Nevertheless, plasma does not necessitate physical walls to be bounded, and electric and magnetic fields can be used to direct it. A MN carries out this role by partially preventing plasma expansion in the radial direction and converting the internal energy in the electrons into well-directed ion kinetic energy. Among these devices employing MNs, helicon plasma thrusters, and ECR thrusters are particularly promising. These two are conceptually very similar: electromagnetic power is efficiently absorbed by the gas, creating a high-density plasma column which is then expelled and accelerated.

1.3 Historical background on ECR plasma devices

The ECR thruster technology is a convergence of expertise and knowledge from both the electric propulsion and plasma sources communities. This section delves into the historical development of ECR ion sources (ECRIS) and ECR thrusters (ECRT), tracing their evolution from early research concepts to present-day technologies.

As it is detailed in Chapter 2, devices that employ ECR heating, rely on the Electron Cyclotron Resonance phenomenon for power coupling. An ECR source is typically composed of a cylindrical plasma discharge chamber (PC) immersed in a magnetic field, $\boldsymbol{B}$. The magnetic field configuration for an ECRIS can vary, however an ECRT typically consists of a simply diverging MN. In both cases, the latter can be produced by electromagnets or permanent magnets. A neutral gas is injected into the PC and electromagnetic (EM) power at the frequency ω, is input in the discharge chamber through a window, transparent for the EM frequency used. The ECR happens locally in a region within PC where the condition $\omega = \Omega_{ce}$ is satisfied, with $\Omega_{ce} = eB/m_e$ the electron cyclotron frequency and where m_e is the electron mass, and e is the electric charge. The magnetic field satisfying this equality is here called B_{ECR}. Generally, ω falls within the microwave frequency range. At ignition, free electrons passing through this region are heated and undergo ionization collisions with neutrals, more electrons are produced which are in turn energized by the resonance in a chain reaction. The resulting plasma can be extracted and used for various applications in the case of ECRIS, or it can be directed through a magnetic nozzle to generate thrust in the case of ECRTs (refer to Section 2.2). A scheme of an ECR thruster is available in figure 1.2.
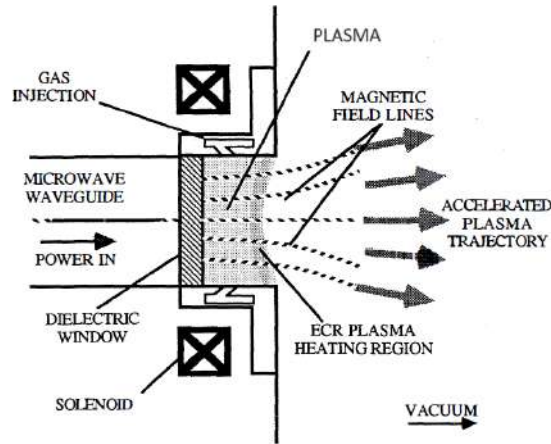
Figure 1.2: Scheme of a typical ECR thruster as illustrated by Sercel [19].

ECRIS development

ECRIS can serve a variety of purposes depending on their specific design. Commonly used sources are employed in the field of particle accelerators where it is of interest the production of large currents composed of highly charged heavy ions. Other applications include industrial surface processing such as surface etching/deposition and the production of high-density plasma from light ions, such as H or He, for nuclear fusion research.

The advantage of using ECRIS over other plasma source technologies is their capability to work without using electrodes for ionization purposes. Since, as mentioned, electrodes are typically subject to erosion from the plasma. The basic design of an ECRIS consists of a plasma chamber within which microwave power is injected. A magnetic field confines the plasma to reduce wall losses, the field must be large enough to obtain the ECR phenomenon. One or more resonance surfaces may exist in the volume. On one side of the plasma chamber, the magnetic field is lower, and an electrode is positioned (e.g. in the form of a grid), the latter extracts the ion current from the confining region so that this can be used on a target. ECRIS sources exist in two primary magnetic field configurations: the double mirror (magnetic bottle) and the min-B configuration. The min-B configuration can achieve higher densities, at the cost of higher complexity [20]. Figure 1.3 shows an example of the magnetic field for the Min-B configuration, for which nested resonance surfaces are obtained, enhancing microwave power coupling. The magnetic field required for ECRIS can be made in different ways, permanent magnets, coils, and more recently superconductors [21]. The use of superconductors is mainly driven by the desire to use higher magnetic fields, this is due to two main reasons: a higher magnetic field is required for the resonance as the electromagnetic frequency is increased, and a larger confining magnetic field reduces the losses to the discharge chamber walls. A higher microwave frequency allows obtaining a larger plasma density as the critical density for electromagnetic wave propagation scales as $n_{cr} \propto \omega^2$ [22] (refer to Section
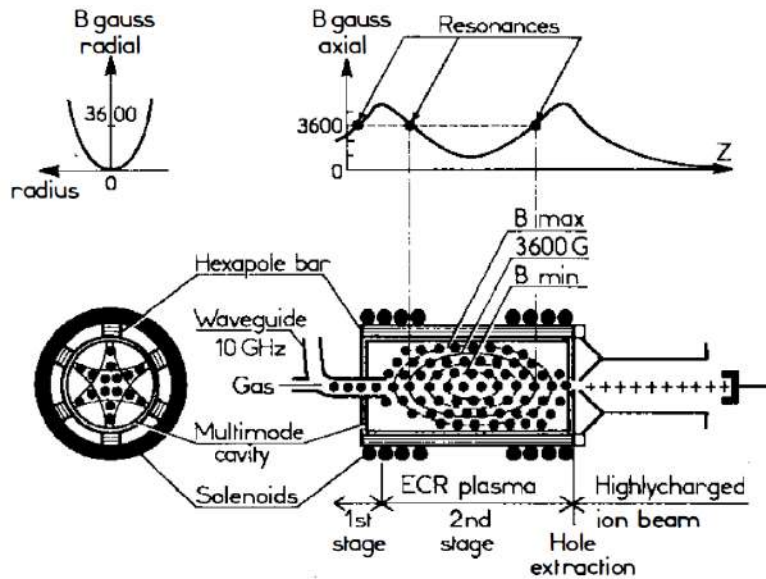
Figure 1.3: ECRIS with Min-B magnetic field configuration. For the shown design two nested resonance surfaces are obtained. [22]

2.1).

The foundations for the first generation of ECRIS devices were built in the 1960s (along with the first ECR experiments for plasma propulsion [23, 24]). The first ion source of this kind (called PLEIADE) was developed at the CEA laboratory in Grenoble by the team of Geller. These experiments were performed with microwaves at <10 GHz and working in the kW power range, simply-divergent magnetic field or double magnetic mirror configurations were used [25, 26, 23]. The first is useful for extracting large currents of single or low-charged ions, while the min-B configuration increases the plasma confinement time to obtain large currents of multiply-charged ions. The second generation of devices was led by the same lab in the 80's. The devices of this generation were equipped with a min-B configuration and were operated at a larger frequency (10-14 GHz), this allowed for achieving higher plasma density and the extraction of ions with a higher degree of ionization (up to Ar^{11+}) [20, 27, 28]. In the 2000s the third generation was born, and devices working at even higher microwave frequencies were created in Berkeley. The "Venus" reactor accounted for a microwave frequency of 28 GHz (in the kW power range) capable of extracting an ion current of up to 100 μA of Xe^{20+} [29, 30]. To achieve fields larger than $B_{ECR} = 1$ T, superconductive coils were used. Similar sources represent the current state of the art. Nowadays, ECR ion sources are used relatively commonly in the industry however they are still subject to research efforts to improve and expand their capabilities. The fourth generation of sources is expected to require the development of new high-power microwave generators at $50 - 100$ GHz together with innovative magnetic field topologies such as the ARC-ECRIS [31, 32].

8

ECR thrusters development
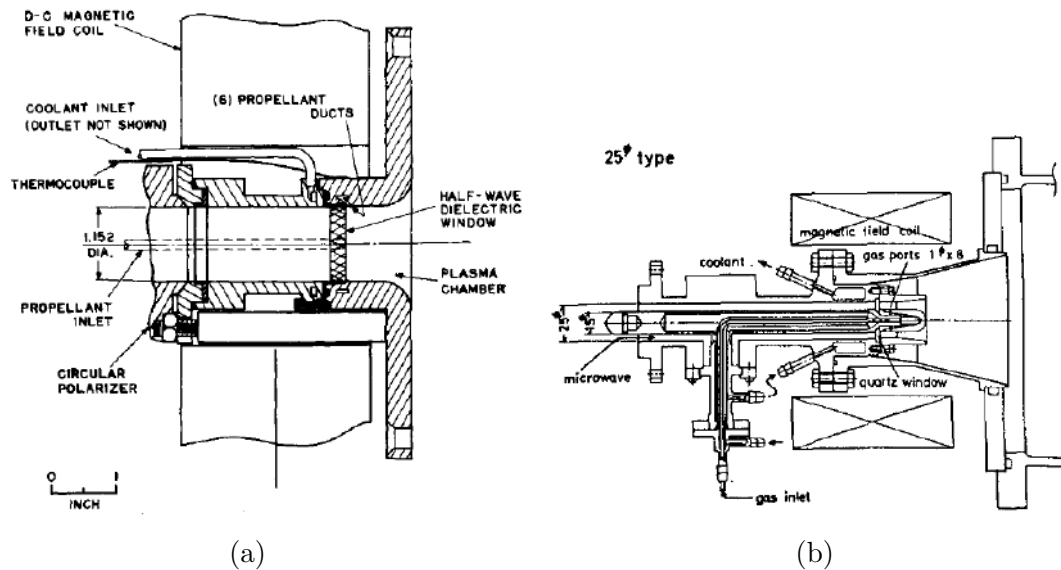
Figure 1.4: (a) Scheme of the Mark V-S engine prototype developed at the general electric laboratories (Cyclops Program) [33]. (b) Scheme of the coaxial ECRT prototype by the University of Tokyo [34].

Although both ECRIS and ECR thrusters originated from the same theoretical background, ECRIS design soon differentiated from the one of ECR thrusters because of the need to achieve large amounts of multiply charged ions at larger densities, aspect detrimental for plasma thrusters which instead prioritize singly charged ion acceleration. Thus, rather than using a magnetic bottle or min-B configurations which would result in a larger amount of multiply-charged ions, the majority of the designs presented in this section employ a simply divergent magnetic field necessary for the magnetic nozzle. Furthermore, as outlined in Section 2.1, the divergent field design facilitates a more effective microwave injection, eliminating the need for increased frequencies and magnetic fields to attain higher plasma density.

The development of ECR thrusters has not been continuous since their conception in the 1960s. Early attempts to achieve high thrust efficiencies proved challenging, leading to research activities being redirected towards more established technologies like ion thrusters and Hall thrusters.

The first concept prototype was built at the General Electric Laboratories with the work of Miller *et al.* [35] in a collaboration contract with NASA which lasted up to 1967 in the framework of the Cyclops program [35, 36, 33, 37]. These efforts were carried out almost in parallel with the development of the first generation of ECR ion sources [23, 22]. The first prototype developed was working at 2.45 GHz and 320 W, with a rectangular waveguide geometry (RG-48U), a good microwave power coupling was observed in the order of $80 - 90\%$ (a circular polarizer was not used), however quite poor utilization efficiency and energy efficiencies were found, being

both estimated to be lower than 20%. The plume appeared to be "hollow" and the dependence on the injection position and magnetic field shape and strength were analyzed. These first experiments proved that ion acceleration was possible and paved the groundwork for the next experimental iteration with a circular waveguide accelerator (Mark V-S engine) working at higher power and frequency (8.35 GHz, kW power range), a scheme of this prototype is available in figure 1.4a. The system employed a Right-hand polarizer which resulted in obtaining a power coupling close to 100%. For this second iteration [38, 33], a variety of propellants were tested (Ar, Kr, Xe, and Hg), and entrainment, out-gassing, and mass-flow measuring problems were encountered for noble gasses, for this reason, a large amount of experiments were performed with mercury. Thrust measurements in addition to on-axis Langmuir probe and calorimetric plume measurements were performed. A maximum efficiency of 10% was obtained with Hg, for specific impulses between 500 and 1500 s. The authors considered only magnetic thrust measurement for the efficiency calculation, however, additional thrust is expected to be provided by pressure forces on the PC. Considering pressure forces accounting for 20% of the total thrust [39, 40], the maximum efficiency would be increased by about 50%, bringing it not far from typical efficiencies for electrodeless thrusters. Although promising, the project did not have a follow-up since more efficient technologies were rising in that epoch, leaving multiple open questions regarding the origin of the losses limiting the performance.

In 1967, the first experiments with a coaxial geometry ECR thruster were performed by Nagatomo at the University of Tokyo [34]. The thruster was tested with Argon and a 2.45 GHz source working at 400 W of output power. Referring to the CMA diagram (refer to figure 2.2), in his work, Nagatomo highlights the importance of injecting microwaves from the regions above the ECR so that higher plasma densities can be achieved since the R wave can propagate without cut-offs, hence he suggests the use of a decreasing magnetic field in the plasma source. Magnetic thrust measurements were performed obtaining a thrust efficiency of 8% and up to 90% of utilization efficiency.

Further studies on ECR thrusters were only performed later in the 1990s with the work of Sercel at Caltech [41, 42, 19]. Sercel investigated the discharge of a circular waveguide ECR thruster working at a frequency of 2.12 GHz with a source capable of generating up to 20 kW of power, argon was used as a propellant. A 1-D model was developed to predict the expected plasma properties, however, a strong disagreement with the experiment was obtained, attributed to an unknown loss mechanism. Only 30% of MW power was estimated to be coupled to the plasma. Additionally, a rather low divergence efficiency of 24% has been reported as calculated from the proposed model. Direct thrust measurements were not performed, however, using the above estimations and on-axis measurements of the ion current and ion energies an efficiency of only 2% was obtained. Inaccurate microwave power measurements

and/or plasma turbulence were suggested to be a possible cause undermining the prototype performance. Further studies were performed in the same team, Kaufman and Goodwin [43] analyzed the effect that the vacuum tank pressure had on the plasma properties of the waveguide ECR thruster. The performance in terms of electron temperature, and consequently ion energy, was found to be strongly decreasing with the pressure a result that was verified later by other groups as discussed below. Also for this case, the work on waveguide ECR thrusters did not have a follow-up at Caltech.
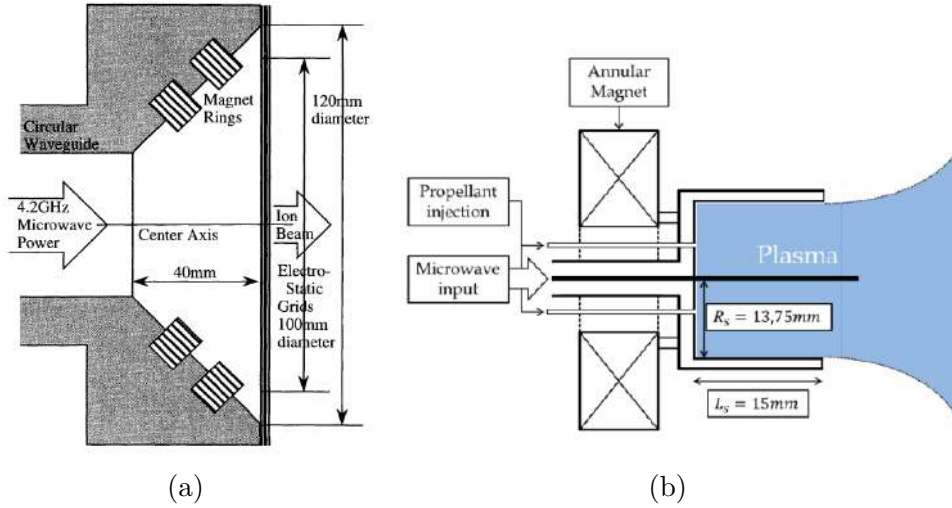
Figure 1.5: (a) Scheme of the $\mu 10$ thruster mounted on the Hayabusa spacecraft [44]. (b) Representation of the coaxial ECR thruster by ONERA [45].

In the early 2000s, through the work of Kuninaka *et al.* at the Japan Aerospace Exploration Agency (JAXA) [44, 46], a novel type of ECR thruster was designed to power the asteroid-visiting mission, Hayabusa (launched in 2003). This prototype, called $\mu 10$ was not electrodeless since it consisted of a gridded ion thruster with an ECR ion source stage for plasma generation and an ECR-powered cathode. This configuration ensured a longer lifetime and larger reliability with respect to hollow cathode technologies [47, 48]. This thruster was powered by a 4.2 GHz microwave generator ($B_{ECR} = 0.15$ T) injecting MWs through a waveguide into the discharge chamber, magnets are positioned in a rail-like configuration circling the inside of the chamber. This configuration ensures good screening of the inside walls of the thruster while guaranteeing a large resonance surface for plasma generation. After the success of the Hayabusa mission, an improved version of the thruster was launched in 2014 in the subsequent mission Hayabusa II [49]. To the best of the author's knowledge, these are the only ECR-powered devices that have been launched into Space to date. As part of this thesis, a collaboration with JAXA was established, during which the author has performed Laser Induced Fluorescence (LIF) measurements on the $\mu 10$ thruster. Further information can be found in the appendix A.

Research activities on the coaxial ECR thruster started at ONERA in the early 2010s [50], the first prototype was 13 mm diameter thruster powered with MW at 2.45 GHz and designed to operate in the kW range, with a magnetic bottle field configuration. Later studies moved to a much lower power in the order of tens of W, and a simply divergent magnetic field. Tests aimed to optimize the propellant injection strategy showed better performance with an axial injection. Ion energies up to 220 eV were found with Argon and up to 350 eV with Xenon. [51, 52]. In 2015, subsequent development with the work of Cannat *et al.* [53] further improved the thruster performance with a larger thruster diameter (27.5 mm) and a displacement of the resonance location closer to the injection holes. The larger diameter was helpful to reduce the losses to the walls. The thrust efficiency for this prototype was estimated to be about 16% with indirect measurements [53]. Subsequent direct thrust measurements led to an efficiency of about 11% [45].

In a later study (2021) [54], Petershmitt *et al.* examined the effects of the type of microwave coupling, coaxial vs waveguide, by comparing two thrusters with the same dimensions. As seen in Section 2.3, the size of a waveguide depends on the operating microwave frequency, for this case 2.45 GHz, however, the thruster diameter has been chosen to be the one of the coaxial thruster 27.5 mm diameter, for which the wave is evanescent at 2.45 GHz in a waveguide geometry (but not in a coaxial). To allow microwave propagation up to the discharge chamber, a dielectric filling was used. Thrust balance and probe testing resulted in a lower efficiency for the waveguide geometry (η_T =1% vs 5%, both at 25 W, 1 sccm of Xenon). This difference was attributed to the different electric field patterns of coaxial respect to a waveguide, and thus to a more localized electron heating in the proximity of the central conductor. In fact, high-energy electrons were observed in the plume, but only for the coaxial configuration of the device. The physical mechanism producing these electrons, and their influence on the plume expansion are not yet completely understood.

In 2023, outstanding results were reported by Desangles *et al.* [55] on thrust balance tests performed on a geometrically optimized version of the coaxial ECR thruster, these experiments were performed in the JUMBO facility at the Justus Liebieg University in Germany, where a pressure as low as 1e-7 mbar could be kept with a mass flow rate of xenon of 2 sccm (by comparison at ONERA the pressure was 4e-6 mbar). In these operating conditions, the thrust was found to be up 1.7 times the one obtained at ONERA, with ion energies up to 400 eV. The authors suggest that these differences are induced by the lower pressure (reducing electron collisions with background gas) and by facility effects related to the increased chamber dimensions. A total thrust efficiency of about 50% was reported for both a thruster working at about 30 W and one at 100 W. These results represent the first of this kind for a thruster relying on the magnetic nozzle expansion working in this power range. Further studies are expected to be performed in the future to

confirm these results at the ONERA facilities. However, problems related to central coaxial electrode erosion are also discussed, and it is estimated that the mass of this component would be reduced by 50% in 500 hours, posing serious lifetime problems.

Simulation efforts in collaboration with ONERA (during the MINOTOR project) were also carried out at the EP2 team in Madrid [56, 57]. The coaxial ECRT was simulated with the HYPHEN-SURFET platform. This hybrid fluid-PIC code (fluid electrons, ion particles) had already been used for simulating Helicon and Hall thruster [56, 58, 59], however, an additional wave module was developed to self-consistently simulate the electromagnetic wave power propagation and absorption. The simulation results [56, 57] suggest that the majority of the MW power is coupled in proximity to the inner electrode region due to the higher electric fields at that location (likewise in a simple coaxial), confirming the experimental results that suggested higher electron temperatures in proximity to the axis [54]. Additional improvements to this code were obtained through the work of Jimenez *et al.* [60] with the possibility to simulate higher-order propagating modes. This allowed for simulating the discharge physics in Helicon thrusters, where power was found to be also deposited in an ECR resonance in the plume downstream [60, 59].

ONERA's pioneering work has ignited global interest in coaxial ECRTs with other research groups investigating similar thruster designs. Research activities are being carried out at PEPL [61, 62, 63], the effect of background pressure was tested by Wachs *et al.* by injecting an additional flow of Xenon inside the vacuum chamber. Background pressure was raised from 1e-6 to 6e-5 mbar. Up to a 20% of difference was found in plasma potential measurements, suggesting that even lower pressures should be tested to find a lower acceptable limit [61]. Later, the same author investigated the two-MW frequency heating technique [62]. The results suggested that the presence of the second ECR does not have intrinsic benefits in power coupling if not thanks to the displacement of the resonance zone. It is found, as was observed by ONERA, that a resonance closer to the backplate is favorable. On the other hand, at Washington University potential use of water as a propellant is being investigated for the coaxial ECRT [13], a common trend also for other EP devices [64].

Finally, additional activities on waveguide ECRTs were carried out by Ganguli *et al.* [**gang19**] in 2019, where the potential uses for EP thruster application of an ECRIS (named CEPS) were analyzed. The magnetic field topology presented a separatrix on the axis. Ion energies up to 87 eV and electron temperature of 20 eV were found in the plume at 600 W with argon.

1.4   Motivation

Based on the presented studies, it is clear that the ECR thruster technology has good potential for in-space propulsion applications. ECR thrusters have shown the capability of working in a wide range of power ranges from tens of Watts to kW, and to be able to run with a variety of propellants. The work of the team at ONERA has shown the promising capabilities of coaxial ECR thrusters, which if confirmed, represent one of the most efficient thruster technologies in the low power and very low power range. However, unlike purely electrodeless designs, the central conductor experiences erosion, reducing the thruster's lifetime to some hundreds of hours.

The waveguide alternative, on the other hand, does not have any obvious lifetime limiting component, but it exhibited relatively lower performance during the past experiments. However, these results should not be interpreted as an intrinsic limit of this coupling geometry since the design optimization efforts have been rather limited in these time frames. In particular, the performance estimated by Crimi *et al.* is not far from those initially found by ONERA, therefore a large margin of improvement could be expected.

Investigating the primary loss mechanisms in waveguide ECRTs is fundamental to getting a deeper understanding of the involved MN physics and microwave-plasma coupling, a knowledge that could be used to devise effective performance enhancement strategies. Previous research activities on waveguide ECRTs such as the ones performed in the '60s and '90s, did not undergo a deep enough experimental characterization of the plume to fill this gap, being typically limited to on-axis plume measurements, thrust measurements for which only magnetic thrust was obtained, or particularly low measurement accuracy. With this incomplete information it is not possible to have a clear picture of the partial efficiencies, and thus limited information on the loss mechanisms could be extracted. In this regard, it is crucial to employ discharge modeling in the process since it can provide information otherwise inaccessible to experiments. Lastly, these works have primarily been focused on waveguide ECRTs in the kW power range, the hundreds of Watts power range (<400 W), expected to be crucial for the current spacecraft market, remains largely unexplored for these devices and was revealed to be a particularly interesting range for coaxial ECRTs. This potential highlights the need for further research into this power regime for waveguide thrusters as well, as it could significantly impact the design and performance of ECRTs.

1.5   Objective and Methodology

For the reasons above mentioned, the overarching objective of this thesis is to contribute to the understanding of the discharge physics in electrodeless MN thrusters,

specifically in understanding which are the main performance limiting mechanisms in waveguide ECR thrusters and to devise strategies to mitigate them, with the ultimate goal of understanding whether this thruster has a future for electric propulsion.

Following mainly an experimental approach, the above-defined primary objective can be broken down and further refined into the sub-objectives listed here below:

1. Design a waveguide ECR thruster and all the experimental setup and infrastructure necessary for its operation. This includes the design of the discharge chamber, the magnetic field generator, and the microwave transmission line, as well as the selection/design of all the necessary vacuum interfaces.

2. Explore the physics by performing simulations of the plasma discharge using the designed waveguide ECRT prototype as a reference model.

3. Achieve thruster ignition, steady-state operation, and assess working point parametric space of the ECRT.

4. Obtain a comprehensive set of plasma metrics at different positions in the plume, such as electron temperature, density, ion velocity, potential, etc. using electrostatic probe measurements or alternative diagnostics.

5. Perform direct thrust measurements to assess thruster performance such as thrust, thrust efficiency, and specific impulse.

6. Decompose thrust efficiency into its constituent components to identify and quantify dominant loss mechanisms.

7. Perform a critical comparison between indirect and direct thrust measurements to mutually validate the results.

8. Modify the thruster design as necessary.

9. Develop relevant diagnostics and related software tools for increasing the current capabilities of the EP2 experimental facility.

To achieve the objectives outlined above, the vacuum facility, diagnostic tools, and infrastructures of the EP2 laboratory and UC3M university will be used. The electrostatic probes that will be used in this study include a Langmuir Probe, a Faraday Cup, and a Retarding Potential analyzer. These will be mounted on a robotic probe positioning system able to move the probes in 2D to achieve a complete plume characterization. A pendulum thrust balance will be employed for direct thrust measurements. Additionally, the Laser Induced Fluorescence Spectroscopy technique is used in the context of a collaboration with the CNRS-ICARE laboratory. Regarding the plasma discharge simulations here presented, the 2D Hybrid PIC-Fluid code developed at EP2, named HYPHEN, is used.

1.6   Thesis Outline

The rest of this thesis is organized as follows:

- Chapter 2 provides the theoretical basis on the working principle of an ECR thruster. Examining the main aspects of the Electron Cyclotron Resonance, and magnetic nozzle.

- Chapter 3 presents the proposed design of the waveguide ECRT assembly. The presented prototype version is used throughout the thesis. The design of the subsystem is further detailed in related sections. Additional sections include the thermal and MW propagation simulation performed on the thruster head using commercial FEM software.

- Chapter 4 showcases the plasma discharge simulations performed with the HYPHEN code. These include the simulation of the discharge within ECRT plasma chamber and the initial segment of the magnetic nozzle. The dependence of the performance and the maps of the plasma variables on the imposed MW power absorption map is analyzed. This work has been presented at the Space Propulsion Conference 2021 with an oral presentation and related conference manuscript [65].

- Chapter 5 presents the results of the initial characterization of the waveguide ECRT object of this thesis. A Langmuir probe and a Faraday cup have been used to characterize the plume for different working points and injection types. Parts of the contents of this chapter are published in the peer-reviewed journal paper "Plume characterization of a waveguide ECR Thruster" [66].

- Chapter 6 includes the performed thrust balance measurement results. To evaluate partial efficiencies, supplementary electrostatic probe measurements are performed with Retarding Potential Analyzer, Faraday cup, and Langmuir probe. Parts of the contents of this chapter are under revision for publication in the peer-reviewed journal paper, "Thrust Measurements of a Waveguide Electron Cyclotron Resonance Thruster" [67].

- Chapter 7 includes results from the collaboration efforts between the CNRS-ICARE laboratory and EP2 to perform the LIF measurements on ECRT prototype. This chapter includes contributions from the peer-reviewed journal paper "Ion dynamics in the magnetic nozzle of a waveguide ECR thruster via laser-induced fluorescence spectroscopy" [68]. The ion velocity profiles are measured non-intrusively by using the LIF technique. This is done for various operation conditions and magnetic nozzle shapes.

- Chapter 8 summarizes the results and contributions brought by this thesis.

In the framework of this thesis, a research stay has been carried out at the Japanese Aerospace Exploration Agency (JAXA). This work is inserted in the scope of the Hayabusa II mission and aims to unravel the ion back-spattering phenomenon that was documented during the spacecraft's interplanetary journey. Related results are presented in Appendix A. This work was presented in an oral presentation at the ISTS conference 2023 [69] and subsequent developments are expected to be presented at the IEPC 2024 conference.

Appendix B, presents additional work related to the design and testing of electrostatic plasma probes, performed in the context of the ESA DTK (Diagnosis ToolKit) project. The latter had the objective of developing a flexible design of electrostatic probes for plasma propulsion diagnostics in a collaborative effort between the EP2 team and the CNRS-ICARE laboratory. Faraday Cups were tested on a Helicon thruster plume. Part of the work related to these activities has been presented at the EUCASS conference 2023 [70].

Chapter 2

ECR thruster working principle

"We are just an advanced breed of monkeys on a minor planet of a very average star. But we can understand the Universe. That makes us something very special."

\- Stephen Hawking

The objective of this chapter is to present some key concepts governing the operation of a waveguide Electron Cyclotron Resonance Thruster. This knowledge will serve as a valuable resource throughout the thesis and is at the basis of the prototype design choices taken in Chapter 3.

Section 2.1 provides an overview of electromagnetic wave propagation in a cold plasma immersed in a static magnetic field. Being the magnetic nozzle the primary ion acceleration mechanism in an ECR thruster, details on its working principle are provided in Section 2.2. Finally, Section 2.3 provides a brief introduction to wave propagation modes in circular waveguides.

2.1   Electromagnetic waves in cold plasma

To comprehend the underlying mechanisms of ECR, a thorough understanding of electromagnetic wave propagation in plasma is essential. Although employing a simplified cold plasma model may seem restrictive, it allows for the introduction of fundamental concepts and phenomena related to resonances and cutoffs.

A cold plasma is a plasma for which the temperature of particles can be considered negligible, hence particle velocities will be a Dirac-delta function centered on

the fluid velocities. This approximation gives a consistent result if the fluid velocity is small with respect to the phase velocity of the propagating wave. Only electron motion is taken into account, ions are considered stationary with zero fluid velocity, thus this analysis is valid only for frequencies much higher than the ion cyclotron frequency so that only electrons can follow the oscillations. Additionally, small amplitude waves are used so that first-order perturbations can be used for the variation of plasma properties. The plasma is immersed in a static magnetic field $\mathbf{B_0}$ and is homogeneous, infinite, and quasi-neutral. Finally, plane waves are considered.

To characterize electromagnetic wave propagation in plasma we consider the plasma as an anisotropic medium with a dielectric tensor and derive the wave equation for this medium from Maxwell equations.

The Maxwell equations are:

$$\nabla \cdot \mathbf{E} = \frac{\rho}{\epsilon_0}, \qquad\qquad \nabla \cdot \mathbf{B} = 0,$$
$$\nabla \times \mathbf{E} = -\frac{\partial \mathbf{B}}{\partial t}, \qquad\qquad \nabla \times \mathbf{B} = \mu_0 \left(\mathbf{J} + \epsilon_0 \frac{\partial \mathbf{E}}{\partial t} \right). \tag{2.1}$$

Being ϵ_0 and μ_0 the permittivity and permeability constants in vacuum and $\mathbf{J} = \overline{\overline{\sigma}} E$ the current density, with $\overline{\overline{\sigma}}$ the conductivity tensor. By combining Faraday's law and Ampere's law from Maxwell equations, the following wave equation can be obtained:

$$\nabla \times (\nabla \times \mathbf{E}) = -\frac{\partial}{\partial t} \left(\mu_0 \mathbf{J} + \frac{1}{c^2} \frac{\partial \mathbf{E}}{\partial t} \right) = -\mu_0 \left(\frac{\partial}{\partial t} \overline{\overline{\sigma}} + \epsilon_0 \frac{\partial^2}{\partial t^2} \overline{\overline{I}} \right) \mathbf{E}, \tag{2.2}$$

where $c = 1/\sqrt{\mu_0 \epsilon_0}$ is the speed of light. Equation 2.2 can be expressed in the frequency domain as shown in equation 2.3 where $\mathbf{k}$ is the wave propagation vector and ω the frequency of the wave propagating in the plasma medium.

$$\mathbf{k} \times (\mathbf{k} \times \mathbf{E}) + \frac{\omega^2}{c^2} \left(\overline{\overline{I}} + \frac{i\overline{\overline{\sigma}}}{\epsilon_0 \omega} \right) \mathbf{E} = 0 \tag{2.3}$$

The conductivity tensor can be found by expressing as well the electron momentum equation in the frequency domain and by employing the cold plasma approximation [71, 72]. For conciseness, the resulting tensor is reported in equation 2.4.

$$\overline{\overline{\sigma}} = \epsilon_0 \omega_{pe} \begin{pmatrix} \frac{i\omega}{\omega^2 - \Omega_{ce}^2} & \frac{\Omega_{ce}}{\omega^2 - \Omega_{ce}^2} & 0 \\ \frac{-\Omega_{ce}}{\omega^2 - \Omega_{ce}^2} & \frac{i\omega}{\omega^2 - \Omega_{ce}^2} & 0 \\ 0 & 0 & \frac{i}{\omega} \end{pmatrix} \qquad \overline{\overline{\epsilon}} = \epsilon_0 \overline{\overline{\epsilon_r}} = \left(\overline{\overline{I}} + \frac{i\overline{\overline{\sigma}}}{\epsilon_0 \omega} \right), \tag{2.4}$$

$\Omega_{ce} = eB/m$ is the electron cyclotron frequency, $\omega_{pe} = \sqrt{n_e e^2/\epsilon_0 m_e}$ the plasma frequency, and $\mathbf{B_0}$ is aligned with the z axis. In equation 2.4 collisions have been

neglected. Therefore the wave equation can be written as:

$$\mathbf{k} \times (\mathbf{k} \times \mathbf{E}) + \frac{\omega^2}{c^2} \epsilon_0 \overline{\overline{\epsilon_r}} \mathbf{E} = 0 \qquad (2.5)$$

By introducing the refractive index $\eta = c/v_{ph} = kc/\omega$ with v_{ph} the phase velocity, and θ the angle between $\mathbf{B_0}$ and $\mathbf{k}$, the homogeneous system in equation 2.6 is obtained from equation 2.5.

$$\begin{pmatrix} \left(S - \eta^2 \cos^2 \theta\right) & -iD & \eta^2 \sin\theta \cos\theta \\ iD & \left(S - \eta^2\right) & 0 \\ \eta^2 \sin\theta \cos\theta & 0 & \left(P - \eta^2 \sin^2 \theta\right) \end{pmatrix} \begin{pmatrix} E_x \\ E_y \\ E_z \end{pmatrix} = 0 \qquad (2.6)$$

The rest of the variables in equation 2.6 are defined below:

$$S = 1 + \frac{X}{Y^2} \qquad\qquad D = \frac{X}{Y} \qquad\qquad P = 1 - X$$

$$Y = \frac{\Omega_{ce}}{\omega} \qquad\qquad X = \frac{\omega_{pe}^2}{\omega^2}$$

To have a non-trivial solution for the electric field, the determinant of this system must be zero. Thus the general form of the dispersion relation is written as in equation 2.7.

$$(S \sin^2 \theta + P \cos^2 \theta)\eta^4 - [RL \sin^2 \theta + S P (1 + \cos^2 \theta)]\eta^2 + PRL = 0, \qquad (2.7)$$

in which the notation

$$R = S + D, \qquad\qquad L = S - D,$$

$$S = \frac{1}{2}(R + L), \qquad\qquad D = \frac{1}{2}(R - L),$$

is used, where R, L, S, D stand respectively for Right, Left, Sum, and Difference. A quadratic equation in η^2 has been obtained indicating that, for each frequency ω, two possible solutions (modes) can exist, each with two opposite directions of propagation. This complex equation can be simplified by taking characteristic propagation directions as parallel and perpendicular to the magnetic field. To focus on the core concepts, only the analysis for these two directions will be presented here being more relevant for ECR thrusters. More information can be found on [72, 71].

Direction Parallel to B₀

For the case of $\mathbf{k} \parallel \mathbf{B_0}$, equation 2.7 is simplified to the form:

$$P(\eta^4 - 2S\eta^2 + S^2 - D^2) = 0 \tag{2.8}$$

The solution $P = 0$ leads to $\omega = \omega_{pe}$, coinciding with oscillations at the plasma frequency which is not considered a propagating mode. Hence, two propagating modes are obtained $\eta_R^2 = S + D = R$ and $\eta_L^2 = S - D = L$. The first solution represents the Right-hand circularly polarized wave (RCP) and the second is the Left-hand circularly polarized wave (LCP). Their name refers to the direction of rotation of the electric field with respect to $\mathbf{k}$. The RCP follows the right-hand rule, while the LCP rotates in the opposite direction. To see this it is sufficient to calculate E_x/E_y giving $-i$ and i for the RCP and LCP respectively. By substituting the definitions of R and L, the following is obtained:

$$\eta_R^2 = R = 1 - \frac{\omega_{pe}^2}{\omega(\omega - \Omega_{ce})}, \qquad \eta_L^2 = L = 1 - \frac{\omega_{pe}^2}{\omega(\omega + \Omega_{ce})}, \tag{2.9}$$

Note how for $\omega = \omega_{ce}$, the refractive index for the RCP, η_R, tends to infinity meaning that the $v_{ph} \to 0$. This corresponds to the Electron Cyclotron Resonance. The magnetic field satisfying this condition is here called B_{ECR}. From the physical point of view, the ECR happens when the electrons rotate about the magnetic field lines with the same direction, phase, and angular velocity as the propagating electromagnetic wave (RCP). In the reference frame of an electron, a constant electric field exists which results in a continuous electron acceleration in the direction perpendicular to the magnetic field. This efficient transfer of energy from the electromagnetic wave to the electrons results in a significant increase in their energy perpendicular to the magnetic field and consequently in the enlarging of the electron Larmor radius.

Similarly, in the case of low-frequency electromagnetic waves, the ion motion should be included in the analysis and η_L would tend to infinity for the case of $\omega = \Omega_{ci}$ the ion cyclotron frequency, corresponding to the Ion Cyclotron Resonance (ICR). This resonance is used for the second heating stage in the VASIMR thruster concept [73, 74].

Direction Perpendicular to B₀

For the case of $\mathbf{k} \perp \mathbf{B_0}$, equation 2.7 becomes:

$$\left(\eta^2 - P\right)\left(\eta^2 - S + \frac{D^2}{S}\right) = 0 \tag{2.10}$$

Two solutions exists for η^2 corresponding to the so-called ordinary η_O, and extraordinary mode η_X:

$$\eta_O^2 = P = 1 - \frac{\omega_{pe}^2}{\omega^2} \qquad\qquad \eta_X^2 = \frac{RL}{S} = \frac{(\omega^2 - \omega_{01}^2)(\omega^2 - \omega_{02}^2)}{\omega^2(\omega^2 - \omega_{uh}^2)} \qquad (2.11)$$

with

$$\omega_{uh} = \sqrt{\omega_{pe}^2 + \Omega_{ce}^2}, \qquad \omega_{01} = \frac{1}{2}\left(-\Omega_{ce} + \sqrt{\Omega_{ce}^2 + 4\omega_{pe}^2}\right), \qquad \omega_{02} = \frac{1}{2}\left(\Omega_{ce} + \sqrt{\Omega_{ce}^2 + 4\omega_{pe}^2}\right).$$

The ordinary mode corresponds to a mode with electric field parallel to the direction of B_0, thus the electrons are accelerated only in that direction and are not subject to the Lorentz force since $u \times B_0 = 0$. This mode is also called TEM since the electric and magnetic fields of the wave are perpendicular to the direction of propagation **k**. This mode has no resonances.

The extraordinary mode is instead a TM mode (Transverse Magnetic) since the magnetic field is perpendicular to the direction of propagation but the electric field, in general, it is not. Unlike the ordinary mode, the extraordinary mode has a resonance for the upper hybrid frequency ω_{uh}, which is called Upper Hybrid Resonance (UHR). Similarly, for the analysis including the ion response the Lower Hybrid Resonance (LHR) can occur.

CMA diagram

The refractive index (or the phase velocity) for the different solutions found in the previous paragraph can be visualized in what is called a wave normal surface. An example of this is shown in figure 2.1. This diagram shows the normalized phase velocity $v_{ph}/c = \eta^{-1}$ in a polar plot against the angle θ between **k** and B_0. In general, the solutions present fast waves and slow waves, depending on v_{ph} being greater or lower than c. The speed of light is also indicated with a dashed circle and a letter indicates the name of the modes previously found.

All the solutions for the dispersion relation in a cold plasma can be summarized in a single diagram called Clemmow-Mullaly-Allis (CMA). The axis of the diagram are X and Y^2, hence, at a fixed frequency ω the density increases towards the right and the magnetic field towards the top of the diagram. An alternative diagram version uses X and Y for the axis. The CMA diagram for the electrons is shown in figure 2.2, it is divided into 8 regions indicated with Roman numbers, these regions are delimited by resonances ($\eta \to \infty$) or cut-offs ($\eta \to 0$). In each of these regions, different combinations of the modes discussed above can propagate as indicated by the displayed wave-normal surfaces. Note that the wave-normal surface magnitudes change for each point in the diagram, however, their generic shape does not change within a region.
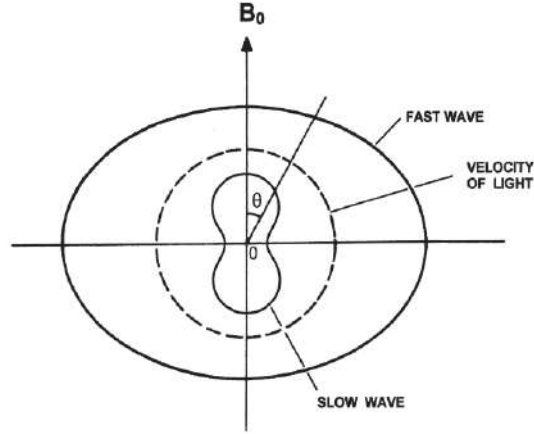
Figure 2.1: Example of wave normal surface [72].

Multiple of these regions can exist in a plasma volume depending on ω, density, propagation direction, and the magnetic field. Therefore in the complex environment of the discharge chamber of an ECR thruster, several of those can be crossed by a propagating electromagnetic wave [56, 59]. As seen in this chapter, it was possible to obtain analytical expressions of the dispersion relation in a uniform infinite cold plasma. However, in a real scenario, none of these ideal conditions are met and a numerical approach should be used to simulate the wave propagation and absorption in the discharge chamber of waveguide ECRT. In the absence of a full-wave code able to perform this type of analysis, for the simulations described in Chapter 4 a different approach is used. The plasma discharge is simulated with a Hybrid PIC-fluid code (PIC for heavy species and fluid for the electrons) and power absorption is imposed at the ECR region on the electron fluid using a 2D power deposition map. Future studies are expected to target this problem with a self-consistent full-wave solution.

Nevertheless, the cold plasma model can be used to extract useful considerations to use as a guideline for ECR thruster design. The R wave, responsible for the ECR, propagates in region I in all directions as a fast wave and is cut off by $R = 0$ at the boundary with region II. For magnetic fields higher than $B_{ECR} = \omega m_e/e$ (regions VI, VII, and VIII) the R wave can propagate without reflections across under-dense and over-dense plasmas if the propagation direction is parallel to the magnetic field lines. For regions VII and VIII, in the case of propagation in other directions different than the parallel one, the propagation is bound within a "resonance cone" since v_{ph} approaches zero for certain θ, as shown by the wave normal surfaces. Region V, instead, does not allow any wave to propagate and all the incoming waves will be reflected. This property of over-dense plasmas ($\omega_{pe} > \omega$) was used in the past to propagate radio waves across the oceans by exploiting the wave reflection from the ionosphere. The existence of this region also justifies the trend of increasing ω in the development of ECRIS sources (refer to Section 1.3) to attain higher plasma

densities.

From these observations, it seems convenient to design an ECR thruster so that within the plasma chamber (PC): i) k is directed downstream and parallel to the applied magnetic field, B_0; ii) B_0 simply decreases along the length of the discharge chamber with a maximum value above B_{ECR}; iii) the ECR condition is met within the PC. These conditions ensure that the R mode propagates in regions VI, VII, or VIII (depending on the density) and does not cross any non-propagation region before the absorption at the ECR. The magnetic field and power injection strategy of the prototype described in Chapter 3 follow these simple design rules. With such a thruster configuration, it may be possible that the conditions for $\omega = \omega_{uh}$ may be met downstream of the ECR surface (lower density and lower magnetic field). However, the electromagnetic power propagating in this region is expected to have been strongly damped by the absorption at the ECR, additionally, due to how the wave is typically launched in these devices, k is expected to be mostly parallel to B_0. For these reasons, the UHR is expected to play a minor role in ECRT [56].

In a waveguide ECR thruster, the plasma is not cold neither infinite nor uniform, or collisionless, with plasma properties and magnetic field varying across the few centimeters of the metallic plasma discharge chamber typically bounding the plasma. As a result, the electromagnetic fields will strongly vary depending on the specific plasma conditions. However, we have seen that some general thruster design principles can still be extracted and will be used in the next chapter.
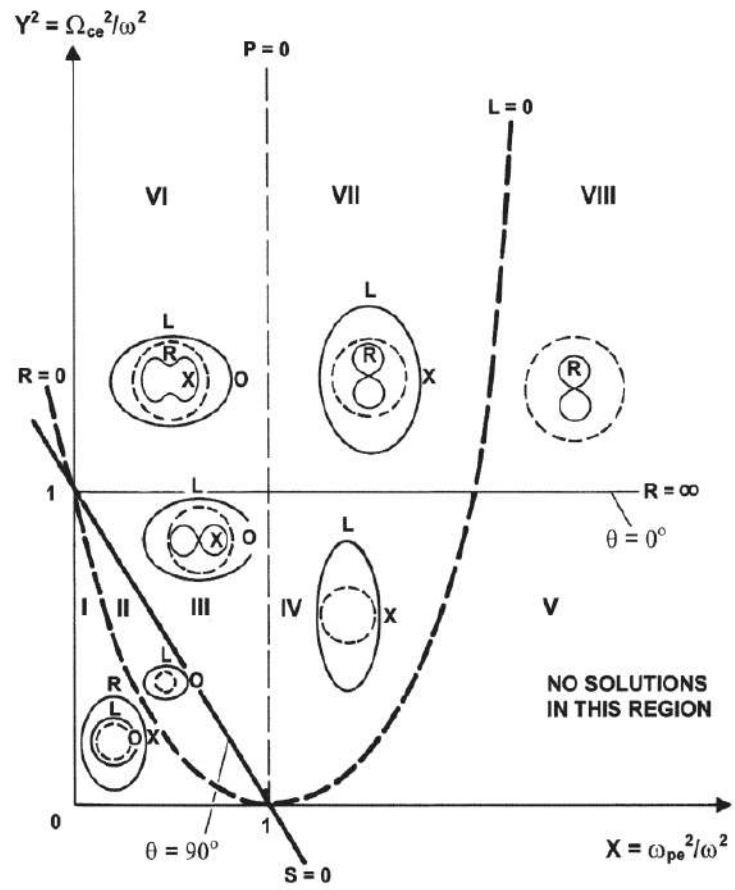
Figure 2.2: CMA diagram for the cold plasma model [72].

2.2 The magnetic nozzle

In analogy to a de Laval Nozzle, a magnetic nozzle simply consists of a magnetic field externally applied to a plasma, capable of supersonically guiding its expansion into a vacuum. A schematic view of a magnetic nozzle is shown in figure 2.3a. Magnetic nozzles represent the acceleration stage for several different plasma thrusters, namely RF thrusters, the VASIMR thruster, and of course ECRTs [18, 74, 55]. Compared to other plasma acceleration mechanisms, a magnetic nozzle offers several advantages. First of all, it does not necessitate electrodes for the ion acceleration, but only a magnetic field source (permanent magnet or a coil), it is thought that this will lead to a lifetime increase, since electrodes, typically hollow cathodes, are one of the main lifetime-limiting components being subject to sputtering or contamination. Additionally, the output plasma is current-free, hence it does not require a neutralizer. In the case of using coils for the magnetic field generation, thrust vectoring could be achieved without moving components. Other advantages include large scalability to different power ranges and propellants, and the large thrust density typical of these devices.

(a) (b)
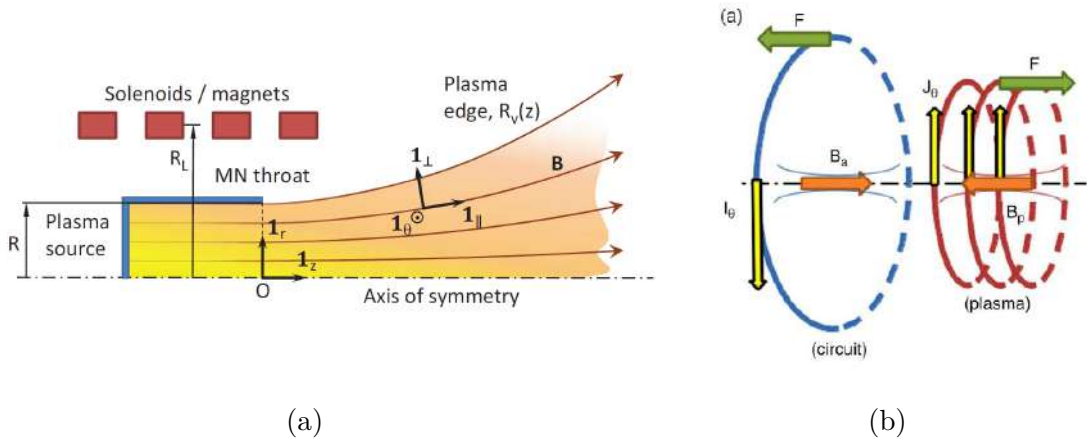
Figure 2.3: (a) Schematic representation of a magnetic nozzle. (b) Scheme of the magnetic forces exchanged between the induced magnetic field $\mathbf{B_p}$ created by the plasma current $\mathbf{j}_\theta$ and an electromagnet with current I_θ creating an applied magnetic field $\mathbf{B_a}$ on the plasma. Figures from Ref. [75], adapted with permission.

Several works have contributed to the study of magnetic nozzle expansion through numerical [42, 75, 76, 77] and experimental activities [18, 78, 79, 80]. The basic working principle of the MN relies on the large mass difference between the ions and the electrons. In a strong enough magnetic field, the electrons are considered to be well-magnetized, orbiting about the magnetic field lines, while the ions are partially magnetized or unmagnetized. The electrons are hot with a temperature T_e while the ions are typically considered to be cold. Due to their larger mobility, the electrons diffuse fast along the MN, leaving the ions behind, therefore an ambipolar electric field develops accelerating the ions downstream and the electrons upstream.

Only these electrons with a large enough velocity to overcome this potential well (free electrons) can escape and neutralize the ion beam obtaining a current-free plume. Thanks to the radial confining effect of MN, the radial diffusion of electrons is reduced, enabling the conversion of the internal energy of the plasma into a well-directed energetic ion beam.

While for gridded ion thrusters the force is transmitted to the thruster body through electric forces between the ions and the grids, for a MN thruster the mechanism of force transmission relies on two effects: pressure thrust, F_p, and magnetic thrust, F_m. Thus we can write the total thrust F acting on a MN thruster as in equation 2.12.

$$F = F_p + F_m. \tag{2.12}$$

The first term is the thrust which results from the ion and electron pressure acting on the internal walls of the thruster, thus it is not intrinsic to the presence of the magnetic nozzle. The second effect is brought by the diamagnetic nature of the plasma. The plasma currents that develop in a MN give rise to a plasma-induced magnetic field opposing the magnetic nozzle's static magnetic field. Hence, the magnetic thrust is transmitted through the Lorentz force acting on the magnetic field generator (a coil or a permanent magnet). A scheme of the forces acting on the device is available in figure 2.3b.

In the past, multiple experiments have been conducted to evaluate the different contributions of magnetic and pressure thrust. In general, those are performed by employing a thrust balance and measuring separately the thrust on the magnetic field generator and the one on the plasma discharge chamber. Examples of these experiments can be found in [39, 40], F_m typically accounting for $50 - 80\%$ of the total thrust.

Upon closer inspection, the magnetic thrust force is the volumetric integral in the z direction of the contribution of the magnetic forces due to the local currents in the plume volume V:

$$F_m = \int_V (-\mathbf{j} \times \mathbf{B}) \cdot \mathbf{1_z} dV = \int_V -j_\theta B_r dV, \tag{2.13}$$

where j_θ is the current density in the θ direction, sum of the contribution from the electrons and ions, $j_\theta = j_{e\theta} + j_{i\theta}$, $\mathbf{B}$ is the magnetic field and B_r its radial component. Singly-charged ions are assumed. Two-fluid models [75, 81] can provide a satisfactory description of the phenomena happening in a magnetic nozzle. Without substantial loss in generality, a quasi-neutral plasma of density n, composed of fluid electrons and ions immersed in a magnetic field can be considered. The plasma is assumed collisionless, the electrons have an isotropic temperature T_e, pressure $P_e = nT_e$, and a negligible mass, while the ions are cold with $T_i \ll T_e$. By employing the continuity and momentum equations, it can be found that the electron azimuthal current is

given by:

$$j_{e\theta} = \frac{1}{B}\left(\frac{\partial P_e}{\partial \mathbf{1}_\perp} - en\frac{\partial \phi}{\partial \mathbf{1}_\perp}\right),$$
(2.14)

where ϕ is the plasma potential. We can conclude that $j_{e\theta}$ is driven by both the ExB drift and the diamagnetic drift. While the diamagnetic drift typically prevails and contributes to magnetic thrust, the ExB drift induces magnetic drag. Concerning the ions, azimuthal currents may develop downstream as they separate from the magnetic field lines, contributing to drag creation. However, the latter contribution is generally small with respect to the electron one for large enough electron temperatures. Similar results are also obtained in the simulations discussed in Chapter 4 where a more complex hybrid PIC-fluid approach (HYPHEN code) is used to simulate the plasma discharge and MN expansion. It is worth noting that being the plasma-induced magnetic field $\mathbf{B_p}$ created by the j_θ currents opposing the applied MN magnetic field, the total resulting field $\mathbf{B} = \mathbf{B_a} + \mathbf{B_p}$ will be lower and more divergent than the applied one $\mathbf{B_a}$. The divergence angle of a plasma beam ejected through a magnetic nozzle can be large, it can be found [75], that it is strictly correlated with the shape of the magnetic field, longer nozzles achieve a lower divergence angle. Therefore it is necessary to correctly design the magnetic field so that a low divergence angle is obtained. This has been taken into account during the design process in Chapter 3 and an experimental proof of this correlation is presented in Chapter 5.

While the thrust force is transmitted to the thruster body through magnetic and pressure forces according to equation 2.12, the ions are accelerated by the ambipolar electric field. By assuming a polytropic law for the electron expansion of the form $T_e/n^{\gamma-1} = C$ with C a constant, the electron momentum equation can be used to obtain an estimation of the total potential drop in the plume of a magnetic nozzle thruster as provided by equation 2.15:

$$|\Delta\phi| = \frac{\gamma}{\gamma - 1}T_{e0},$$
(2.15)

where T_{e0} is the electron temperature at the magnetic nozzle throat. Numerous experimental investigations have been conducted to determine the value of γ in a magnetic nozzle by examining electron cooling in the plume [82, 79, 83, 84, 85]. In most cases, a range between 1 and 5/3 is found, corresponding respectively to an isothermal and adiabatic expansion. Similar results have also been found in the framework of this thesis and are discussed in Chapter 5.

However, due to the complex nature of the near-collisionless electron cooling along the plume (involving multiple electron sub-populations), a model employing a polytropic law is rather simplistic and a kinetic approach should be used instead [86, 87]. The latter involves considering the conservation of the magnetic moment, and

total energy on magnetic field lines, and observing the evolution of the electron energy distribution function along the plume at equilibrium. Depending on the initial electron velocities, three distinct main populations of electrons can be identified: reflected, trapped, and free electrons. The reflected electrons are emitted by the source and return to it, the trapped electrons are constrained by the electric field which pushes them upstream, and by the conservation of their magnetic moment pushing them downstream (magnetic mirror). The free electrons are those that have enough energy to escape the potential well and are responsible for neutralizing the plume. Thus the near-collisionless electron cooling along the expansion depends on the average energy and fraction of all these populations.

Finally, it is worth discussing the mechanism for plasma separation from the magnetic streamlines. Typically, models assume the electrons to be tightly attached to the magnetic field lines. Since the magnetic field has to have zero divergence all the magnetic field lines turn back to the thruster. Therefore, to obtain a net thrust, the plasma has to detach from the magnetic field lines, failing to do so, would result in a zero net thrust and the damage of spacecraft surfaces by energetic particle impact. Various studies have tried to provide an answer to the detaching mechanism, both numerically and experimentally [88, 89, 90], some of the main proposed hypotheses include: detachment by electron inertia, by the self-induced magnetic field (which creates a separatrix within the plume), and ions demagnetization. The studies performed by Merino *et al.* in [91, 75] have shown that ion demagnetization through ion inertia is to be considered the prominent explanation for the phenomena. Downstream, the ambipolar electric field which was keeping the ion velocity streamlines attached to the magnetic field lines, is not sufficient and the streamlines separate inwardly. Farther downstream, the plume is neutralized through electron demagnetization.

2.3   Propagating modes in a circular waveguide

This section presents some features of the propagation of microwaves in a circular waveguide transmission line. This knowledge will come in useful for the design choices taken in Chapter 3.

The simple geometry of a circular waveguide is displayed in figure 2.4, the cylindrical conductor has a radius *a* and the electromagnetic wave propagation direction is along *z*. In contrast with coaxial TLs or Micro-strip TL which rely on multiple conductors, a waveguide is a type of transmission line (TL) made of a single conductive element in the form of a hollow tube, this fact determines the modes that can propagate within it. In an equivalent nomenclature used for wave propagation in plasma, we can define TEM (Transverse Electromagnetic) for which the electric and magnetic field are both on a plane perpendicular to *z*, and TE (Transverse Electric) and TM (Transverse Magnetic) modes for which the Electric field and Magnetic field are zero respectively in the propagation direction (in this case *z*). While multi-conductor TLs can support the propagation of TEM (Transverse Electromagnetic) modes, waveguides can only support TE and TM modes. The same applies to the case of a circular waveguide.
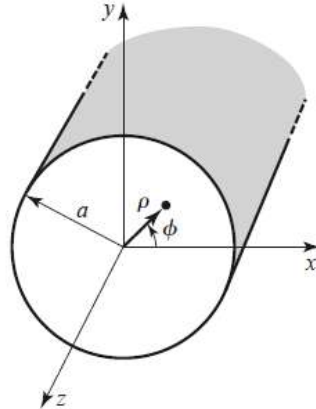
Figure 2.4: Section view of a circular waveguide [92].

In a circular waveguide of radius *a*, an infinite amount of TE_{nm} and TM_{nm} modes can propagate, where *n* and *m* indicate the number of radial and circumferential variations respectively. However, for a given excitation frequency ω, not all of these modes can exist at the same time.

Electric and magnetic field propagation along the *z* direction can be modeled through the complex propagation constant $\gamma = \alpha + i\beta$, where α is the attenuation and β the propagation constant. Hence a field $\mathbf{\Psi}$ (electric or magnetic) can be written as $\mathbf{\Psi}(\rho,\phi,z) = \mathbf{\Psi}(\rho,\phi)e^{\gamma z}$.

The propagation constant β, can be found as $\beta = \sqrt{k_c^2 - k^2}$, where $k = \omega \sqrt{\mu\epsilon}$ is the

$$TE_{11} \qquad\qquad TM_{01}$$

(a)   (b)
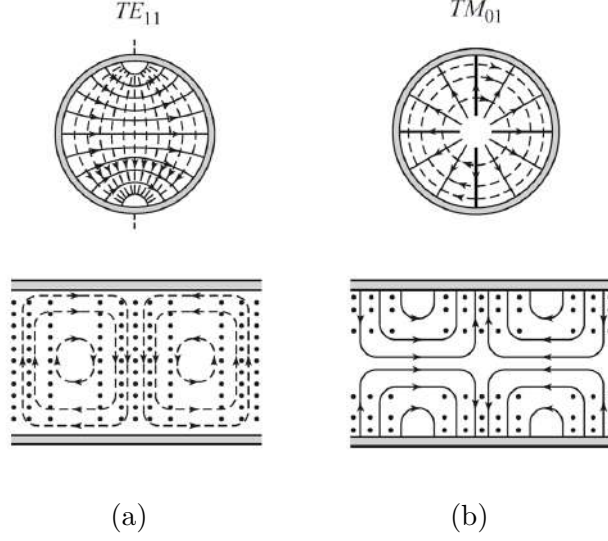
Figure 2.5: TE11 (a) and TM01 (b) modes of a circular waveguide. Solid lines and dashed lines indicate electric and magnetic fields respectively [92].

wave number and k_c is the cutoff wave number. By solving the Maxwell equations in a cylindrical geometry, and by applying the tangential electric field at the waveguide surface to be zero as a boundary condition, it can be found that k_c depends only on the excited mode, and the waveguide geometry:

$$k_c = \frac{p'_{nm}}{a} \qquad \text{TE mode} \qquad\qquad (2.16)$$

$$k_c = \frac{p_{nm}}{a} \qquad \text{TM mode,} \qquad\qquad (2.17)$$

p_{nm} and p'_{nm} are the mth roots of the Bessel function of the first kind J_n, and of its derivative J'_n [92]. For an excitation frequency ω_{c-nm} such that $k \to k_c$, the propagation constant $\beta \to 0$. The electromagnetic wave cannot propagate and becomes evanescent as it is exponentially damped along z. ω_{c-nm} is called cutoff frequency and can be defined for the TE_{nm} and TM_{nm} mode.

Additionally, it can be shown that $\alpha \to \infty$ if $\beta \to 0$ [92], thus for a frequency close to the cut-off frequency the losses are strongly increased. Figure 2.6 shows the attenuation of various propagating modes in a circular waveguide. At a given radius, the mode with the lowest cut-off frequency is called "dominant mode", which for the circular waveguide is the TE_{11} mode. Thus, waveguide dimensions are chosen to accept only the propagation of the dominant mode for a given frequency range. Doing otherwise would result in the possible excitation of higher-order modes traveling at different propagation speeds (e.g. important for communication applications), with different impedances and power ratios, greatly increasing the complexity of the transmission line analysis. As we will see in Section 3, the same design principle has been used for other waveguide ECRTs, and is used as well to determine the operating frequency and size of the ECRT prototype and the waveguide transmis-

sion line used. Note that these considerations are only valid for a uniform, isotropic medium filling the waveguide. As seen in Section 2.1, due to the presence of plasma within the waveguide, a description of the modes propagating in a waveguide ECRT is considerably more complex and requires intensive simulation efforts.
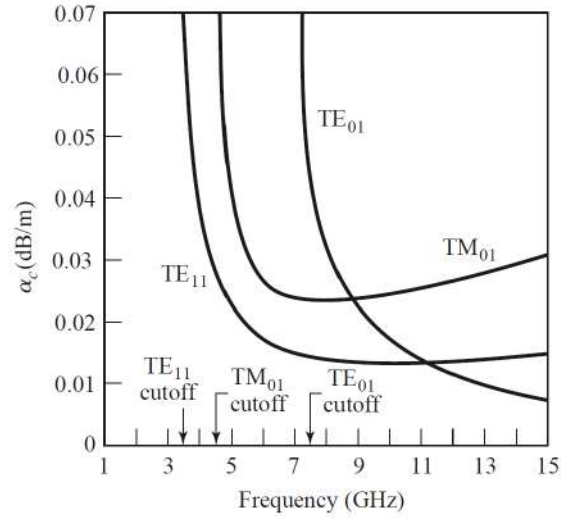
Figure 2.6: Conductor attenuation of various modes in a circular waveguide [92].

Chapter 3

ECR Thruster Prototype

"Manufacturing is more than just putting parts together. It's coming up with ideas, testing principles and perfecting the engineering, as well as final assembly."

- James Dyson

In this chapter, the waveguide ECRT prototype object of this thesis is presented. Starting from the design requirements, the plasma discharge chamber (PC) size, microwave frequency, and working point range are determined in Section 3.1. The PC design and magnetic field generator are discussed in Section 3.2 and 3.3 respectively. The thruster head assembly is presented in Section 3.4. The thermal analysis in Section 3.5 is used to iterate on the preliminary design. The transmission line components necessary for delivering power to the thruster are presented in Section 3.6. Finally, electromagnetic wave propagation simulations are performed in Section 3.7 to further characterize the prototype's expected behavior. Section 3.8 summarizes the work done.

3.1 ECRT sizing

3.1.1 Definition of operational and design requirements

In alignment with the goals outlined in Section 1.4, this prototype aims to provide a breadboard model for investigating the physics of waveguide ECR thrusters. As we will see below in Section 3.1.2, due to the large variability in design, performance, and testing conditions between the waveguide ECRTs taken as a reference, the ob-

jective is to obtain a first prototype able to function in a wide range of operational points (power and mass flow rate) and identify via experimental characterization the optimal operating conditions. It has been shown that this thruster type can operate across a broad spectrum of power levels, however, our focus lies in the previously unexplored hundreds of watts power range (<500 W), of interest for the mini/small-satellite category [93, 94]. Thus, a reference power range of $100 - 400$ W is chosen for this first prototype which fits well within the EP2 testing facilities.

The scarcity of xenon has emerged as a significant challenge for the electric propulsion industry in recent years. Despite this concern, xenon propellant is selected for this prototype. This decision is primarily driven by the extensive availability of relevant data in the literature, especially those on coaxial ECRTs, which is crucial for conducting performance comparisons. In this regard, in Chapter 1 we have seen how the background pressure has a large impact on the MN performance. Thus, as an additional requirement, we shall limit the propellant mass flow rate to keep the chamber pressure as low as possible and avoid undesired effects on the MN plasma expansion. In the EP2 facility, the pressure typically ranges from 2e-6 to about 5e-5 mbar, scaling almost linearly between 1 to 50 sccm of Xenon ($0.1 - 5$ mg/s).

In Section 1.3, we have seen that waveguide ECR thrusters achieved thrust efficiencies (η_T) and specific impulses (I_{sp}) in the ranges of $1 - 10\%$ and $100 - 2000$ s respectively [33, 19, 55]. Thus, considering average levels of η_T and I_{sp} and power in the range of $100 - 400$ W, we can expect a thrust level of about $1 - 4$ mN ($\eta_T \approx 5$ %, $I_{sp} \approx 1000$ s).

Concerning mass and dimensional requirements, in order to be of future interest in this satellite category its mass shall be reduced as much as possible to be competitive (<2kg) [95, 96]. However, given the prototype's purpose for scientific research, testing facility constraints primarily dictate dimensional and mass limitations. In particular, the prototype shall permit easy experiment mounting/dismounting operations to be carried out by a single person. For the same reason, thermal requirements do not represent a critical constraint for this prototype, however, the possibility of reaching thermal equilibrium while testing or, a long enough firing time span, is desirable to achieve plasma steady state conditions and perform typical plasma diagnostics experiments.

Finally, these high-level design requirements are summarized in table 3.1.

3.1.2 Scaling laws

Starting from the requirements discussed above, this section aims to provide a first estimate for the plasma discharge chamber size (diameter D_T and length L_T), MW frequency, and mass flow rate working range. To do this, some scaling factors are

Parameter	Value
Mass/Size	<10 kg, compact
Power	$100 - 400$ W
Thrust	$1 - 4$ mN
Propellant consumption	<50 sccm of Xenon
Continuous testing capability	> 10 min testing

Table 3.1: Design requirements for the ECRT prototype.

	Propellant	f [GHz]	D_T [mm]	L_T[mm]	P_T [W]	$\dot{m}_p$ [mg/s]	$P/\dot{m}_p$ [eV/part]	n_n [part/m^3]
Crimi [33]	Mercury	8.35	29.2	25.4	820–2460	0.33 – 2.4	1100 – 10000	1e19 – 7.5e19
Sercel [19]	Argon	2.115	128	64	100–3000	0.15 – 0.6	100 – 6300	5.4e17 – 2.1e18
ONERA [45]	Xenon	2.45	27	15	20 – 50	0.06–0.4	135 – 1130	2.7e18 – 1.8e19

Table 3.2: Summary of the design parameters for the ECRT by Crimi, Sercel, and Onera. Ranges of the energy per particle, $P/\dot{m}_p$, and neutral densities n_n are also shown.

considered, such as the power-to-mass flow rate ratio $P/\dot{m}_p$, the neutral density n_n (in plasma-off conditions), and the circular waveguide diameter/ MW frequency relation.

Table 3.2 shows the operating points of the ECR thrusters by Crimi, Sercel, and Onera. Different frequencies, power levels, propellants, and mass flow rates have been tested for each of these designs. While Argon, Krypton, and Xenon were also tested by Crimi *et al.*, as discussed in Section 1.3 the mass flow measurements for these gases were not considered to be reliable. Thus, in this section, only Mercury-related data will be discussed. Concerning the data shown by Onera, in this section we will only refer to those related to the thruster prototype having coaxial coupling and not the ones for the waveguide one (refer to 1.3). This choice is justified by the more extensive thruster characterization and optimization performed on this thruster. Additionally, the two coupling designs share the same physical dimensions, MW operation frequency, and operating point, but with very different performances [54], thus some of the conclusions discussed here would be equivalent. With the exception of Onera targeting low powers, the previous works were focused on the high-power range (>500 W).

As discussed in Chapter 2, in a magnetic nozzle thruster, the potential drop in the plume and the ion energy are proportional to the electron temperature T_e. In principle, one can assume that to obtain a similar order of magnitude for T_e as the one in previous works, a comparable amount of energy should be provided to each injected atom, this is expected to be proportional to the power-to-propellant flow rate ratio $P/\dot{m}_p$. The latter is expressed in eV/particle so that this quantity does not depend on the atom mass of the propellant taken into account. A too-large value of $P/\dot{m}_p$ may result in multiple ionization due to the large electron temperature, possibly degrading performance. On the other hand, it is probable [97] that ignition will not be possible or performance strongly degraded at very low $P/\dot{m}_p$ levels (low

electron temperature). Having a design target for the power, $P/\dot{m}_p$ is a good scaling parameter to identify minimum and maximum propellant flow rate requirements. Table 3.2 shows that the values previously tested for $P/\dot{m}_p$ can vary across orders of magnitudes. Onera [53, 45, 54, 55] explored a subset of the range by Sercel, finding the highest thruster efficiency η_T for 400 eV/particle (at 30 W and 0.1 mg/s of Xenon). Concerning Crimi *et al.* a peak of η_T was found for about 5000 eV/particle (at 820 W and 0.35 mg/s of Mercury). On the other hand, the experiment performed by Sercel found the highest ion energy at 2000 eV/particle (750 W and 0.15 mg/s of Argon). The differences in the explored ranges and optima are probably linked to the different thruster designs, MW generators power output, frequency ranges, and propellants used (different ionization energies: E_{i1-Hg} = 10.4 eV, E_{i1-Xe} = 12.1 eV, E_{i1-Ar} = 15.8 eV).

Since no clear agreement is found in those works, it is convenient to be able to investigate a range covering at least the best performance found ($P/\dot{m}_p$ between 400 – 5000 eV/particle). With this range of $P/\dot{m}_p$ and power P_T between 100 – 400 W (as discussed above), a minimum requirement of $\dot{m}_p$ between 0.1 and 0.34 mg/s is obtained, in which we expect to find optimal performance. A larger or lower mass flow rate would extend the range of $P/\dot{m}_p$ explored for this prototype.

The plasma discharge chamber (PC) diameter D_T and length L_T are still free parameters. A larger D_T can be beneficial since the surface-to-volume ratio is reduced and so are expected to be the plasma losses to the walls with respect to the extracted current [98]. However, a too-large D_T may increase the loss of neutrals and reduce the utilization efficiency. Thus an optimal condition should exist. With the objective of identifying a basic scaling law for the PC diameter, we will now compare the neutral density ranges explored by the above-mentioned studies. The neutral density can be found as in equation 3.1.

$$n_n = \frac{\dot{m}_p}{M c_s A_T} \tag{3.1}$$

Where A_T is the discharge chamber cross-section $A_T = \pi D_T^2/4$, $c_s = \sqrt{\gamma k_b T/M}$ is the neutral sound speed, with γ the adiabatic index, k_b the Boltzmann constant and M the propellant species atom mass. Thus, n_n scales with the inverse of the thruster cross-section. The ranges investigated by previous studies are available in table 3.2. As done before, we want to obtain a similar n_n range as those of previous works, the mass flow rate which provides this density for a given D_T, is given by:

$$\dot{m}_p = \dot{m}_{p,R} \sqrt{\frac{M}{M_R}} \frac{D_T^2}{D_{T,R}^2}, \tag{3.2}$$

where the subscript R indicates reference values. Figure 3.1 shows the thruster diameter as a function of the so-calculated mass flow rate. Since different propellants
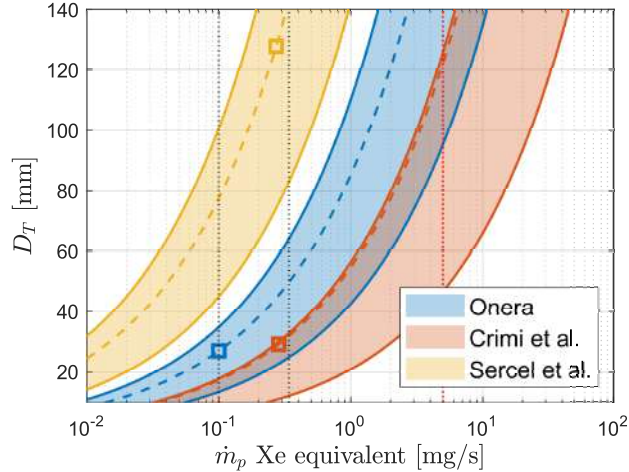
Figure 3.1: Equivalent Xe mass flow rate as defined in equation 3.2. The areas in blue, red, and yellow, cover the n_n ranges tested by Onera, Crimi, and Sercel respectively for a given thruster discharge chamber diameter D_T. The $\dot{m}_p$ leading to the best performance is shown by a dashed line, and a marker is positioned at the corresponding diameter. The black dotted lines identify the range where best performance is expected (0.1 mg/s – 0.34 mg/s). The red dotted line is positioned at 50 sccm as the limit from the testing facility.

were employed, the mass flow rates have been expressed in terms of Xenon equivalent. The curves delimiting the colored regions represent constant n_n for different diameters, and the density increases moving toward the right bottom corner. The n_n values leading to the best-measured performance for these thrusters can be found for $\dot{m}_p$ on the dashed lines. Again, little to no overlapping occurs and no optimal range emerges. Crimi *et al.* used up to 2 mg/s (20 sccm) of $\dot{m}_p$ Xenon equivalent, resulting in prohibitively high $\dot{m}_p$ at $D_T > 50$ mm to be necessary to obtain similar neutral densities as the maximum tested. However, the best performance was found for much lower values (≈ 0.3 mg/s). On the other hand, due to the large thruster diameter, Sercel tested with one order of magnitude lower densities. The indicated $\dot{m}_p$ ranges cannot be satisfied all at the same time for a given D_T. As mentioned, we expect to find the best performance in this power range at low mass flow rate levels 0.1 – 0.34 mg/s. Additionally, lower mass flow rates are convenient since as discussed in the previous section, they lead to a lower vacuum chamber pressure. Thus, since a better performance was experienced by Crimi and Onera, it is convenient to approach those with a $D_T \lesssim 50$.

An additional constraint on thruster diameter is provided by the need to propagate microwaves through a waveguide to deliver power to the plasma. With the exception of the Onera waveguide ECRT [54], a general design principle to reduce MW power reflections has been to keep the same diameter between the waveguide and the PC as discussed in Chapter 1. In Chapter 2, it was shown that in a waveguide of a given size, different modes can coexist depending on the microwave frequency.
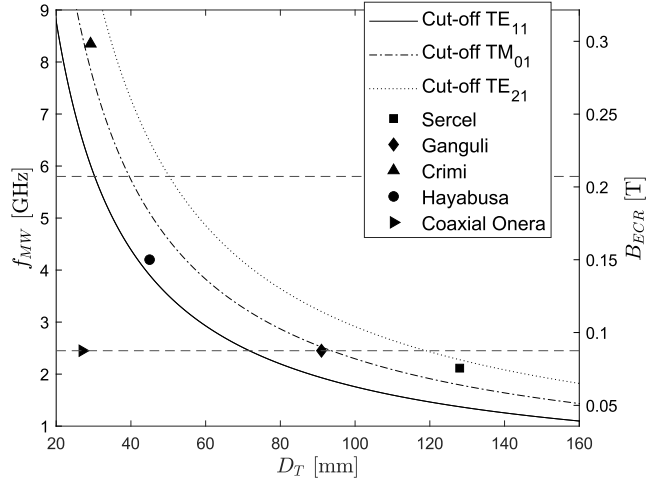
Figure 3.2: Left axis: Discharge chamber diameter/circular waveguide mode cut-off diameter as a function of the input microwave frequency. The dashed and the dashed-dotted lines indicate the cut-off for the dominant TE_{11} mode, and the TM_{01}. The dotted line shows the cut-off diameter for the TE_{21} mode. The markers indicate the thruster diameters of other waveguide ECRTs (refer to Chapter 1) and of the coaxial ECRT of ONERA. In the case of the Hayabusa thruster, the waveguide segment is considered and not the discharge chamber diameter. Right axis: Magnetic field required for the ECR at a given microwave frequency.

Figure 3.2 shows a plot of the cut-off dimensions for different electromagnetic modes and frequencies. The data points for some of the PC diameters of the ECRTs discussed in Chapter 1 are also shown. Note how for Sercel's [19] and Crimi's [33] cases the waveguide dimensions allowed the propagation of the TM_{01} mode, while the coaxial ECR of ONERA can lay below the curves because of the coaxial design and thus the propagation of the TEM mode.

Hence the choice of the PC diameter is closely related to the operating microwave frequency: $D_T \propto 1/f_{MW}$. In turn, f_{MW} influences other factors such as the magnetic field strength. Increasing the operating microwave frequency corresponds to a linear increase in the magnetic field required for the ECR, $B_{ECR} = \omega_{ECR}m_e/e$. In the typical, simply divergent magnetic field configuration, this corresponds to an overall increase in the magnetic field strength. An ECRT can benefit from a stronger field in different ways, by both improving the electron confinement in the discharge chamber and plume regions. Helping reduce the plasma losses to the lateral walls and the divergence of the beam [99]. On the other hand, a too-large magnetic field may magnetize the ions and lead to the opposite effect and increase plume divergence [75]. Nevertheless, in the range MN thrusters typically operate, ions are rapidly unmagnetized at a small distance from the thruster exit plane as they accelerate and the magnetic field decays. A stronger magnetic field possibly increases as well the overall size of the magnetic field generator which is an additional factor to take into account for the choice of the frequency and thruster radius.

Nevertheless, the microwave power supply availability in frequency and power ranges greatly reduces the choices available. Commercially available microwave generators fulfill the entire bandwidth in figure 3.2. However, excessively high costs of MW generators granting relatively high power (and power variability), in addition to the availability and cost of transmission line components, limited the choice to three of the typically commercially available frequencies: 915 MHz, 2.45 GHz, and 5.8 GHz. These are commonly used in relatively large power industrial applications, such as microwave heating and plasma generation [100, 101].

As a result of what was previously discussed regarding the neutral densities, together with the objective of obtaining a more compact design, led to the choice of a MW generator at 5.8 GHz which could be regulated in power between 80-800 W. This component is further discussed in Section 3.6. However, in the framework of this thesis, the MW power output is limited to 400 W to prevent damage to the waveguide vacuum chamber feed-through (refer to 3.6). The choice of this frequency also allows for addressing a frequency range that has never been previously tackled for a waveguide ECRT.

Once the frequency has been chosen, the resonance magnetic field and the minimum and maximum thruster diameter are defined respectively as $B_{ECR} = 0.207$ T and $30 < D_T < 40$ mm (obtained in accordance to figure 3.2). Commercially available circular waveguide components (see Section 3.6 for further information) restricted the choice of discharge chamber diameter to $D_T = 36$ mm. With the expected mass flow rate range discussed above, this diameter allows testing in the same neutral density regimes as Onera, and Crimi for $\dot{m}_p > 0.34$ mg/s but not in the one of Sercel, which was particularly low being $D_T = 128$ mm.

Finally, the estimation of the length of the PC, L_T, is not straightforward to perform. A possible procedure would be to size L_T based on the expected mean free path of neutrals to ensure a complete ionization. However, this requires the knowledge of quantities that are not known a priori (such as the electron density and temperature in the PC), other factors may also play an important role in the optimization of this quantity such as the plasma losses to the walls or the magnetic field divergence angle. Thus, an experimental parametric analysis would be necessary to identify the optimal length range since a too-long PC may increase the wall losses. For the first prototype, a thruster length of $L_T = 20$ mm is chosen which brings the design close to the D_T/L_T employed by both Onera and Sercel (refer to table 3.2).

Considering the mass flow rate ranges discussed above, the resulting operating range for $P/\dot{m}_p$ lies between 320 eV/particle (80 W at 0.34 mg/s) and 5400 eV/particle (400 W at 0.1 mg/s). Finally, table 3.3 summarizes the expected operational range and thruster dimensions of the waveguide ECRT prototype.

Parameter	Value
D_T, L_T	36 mm, 20 mm
P_T	$80 - 400$ W
$\dot{m}_p$ (Xe)	$1 - 3.5$ sccm
f_{MW}	5.8 GHz
B_{ECR}	0.207 T

Table 3.3: ECRT design point and expected operating range.

3.2   Discharge chamber Design

The thruster design must be compliant with the sizing and scaling laws discussed in Section 3.1. A close-up CAD representation of the plasma discharge chamber and related components is displayed in figures 3.3a and 3.3b, while a photo of the fully assembled plasma discharge chamber is available in figure 3.4.

(a)   (b)
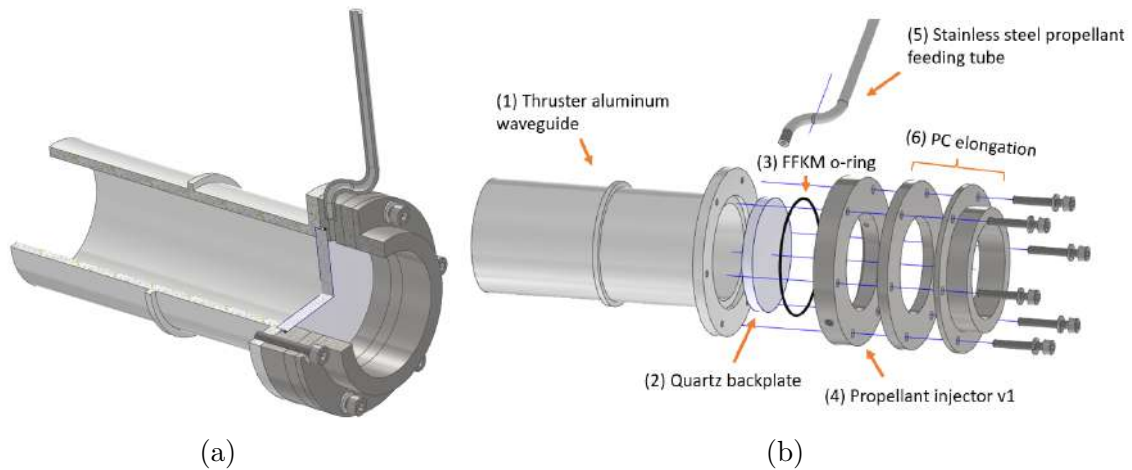
Figure 3.3: (a) Close-up view of the discharge chamber. (b) Exploded view of the discharge chamber mounting.

Figure 3.4: Photo of the assembly of the thruster aluminum waveguide and plasma chamber.

Referring to figure 3.3b, an aluminum waveguide (1) is positioned at the back

of the discharge chamber. The aluminum waveguide is not exposed to the plasma, however, it serves several purposes:

- It is required to deliver MW power to the PC: it has the same internal diameter (*ID* = 36 mm) as the discharge chamber and the DC-block (see Section 3.6).
- Provides a reference position for the magnetic field generator, this is done by the use of the external 2 mm annular step visible in the middle of the waveguide.
- To assemble the plasma chamber: the connection to the PC is realized through threaded connections, the groove on the right side provides the housing for the backplate.

Downstream the aluminum waveguide, a quartz backplate (2) prevents the gas from diffusing upstream into the waveguide. Quartz (SiO_2) is the material of choice thanks to its low loss-tangent ($\approx$ 1e-4) in the MW range and good thermal stability and cost. To prevent the loss of neutrals upstream, the quartz is equipped with a high-temperature perfluoroelastomer (FFKM) o-ring (3). The backplate is positioned between the waveguide and the propellant injector.

The propellant injector (4) is the component through which the neutral gas is injected into the PC. Two interchangeable designs have been proposed and tested: injector v1 and v2, both are of the radial injection type, however, they differ in the number of holes used to inject the propellant. Injector v1 presents two symmetrical holes (refer to figure 3.5a), these have a diameter of Φ_{inj} = 2 mm and are positioned 2 mm downstream of the backplate. Both holes are respectively connected to a stainless steel propellant tube (5). The shape of the injection tube (figure 3.3b) is such to not interfere with the magnetic field generator (refer to Section 3.4). This injector has been used to characterize the thruster as in Chapter 5.
Injector v2 aims to make the neutral density azimuthally uniform using twelve injection holes. This is achieved with a single propellant tube connected to a series of two internal annular chambers used to homogenize the flow of neutrals. A section view of the injector v2 is available in figure 3.5b where the two channels are visible. A fitting lid closes the injector v2 assembly. This type of injector has been used when characterizing the thruster with the thrust balance as in Chapter 6 and Chapter 7.

The rest of the downstream stainless steel cylindrical components (6) serve no other purpose than to elongate the discharge chamber and potentially promote ionization.

3.3   Magnetic field generator

The magnetic field has a strong influence on the performance of an ECR thruster. As seen in Chapter 1, it is at the basis of the electron cyclotron resonance phenomenon,
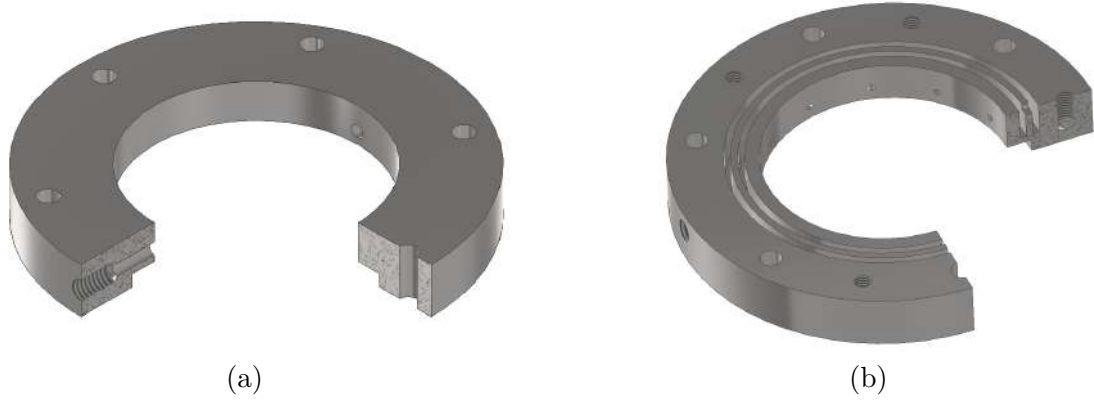
Figure 3.5: (a) CAD section view of the propellant injector v1. (b) CAD section view of the propellant injector v2, a fitting lid (not visible in the figure) positioned at the top of the injector encloses the channels preventing leaks.

it is essential for the ion acceleration in the magnetic nozzle and increases the plasma confinement in the PC, reducing the losses at the internal walls.

In order to accomplish these roles, multiple requirements can be defined:

- A purely diverging magnetic field within the thruster and plume is advantageous for two primary reasons. Firstly, it facilitates approaching the resonance from region VIII of the CMA diagram (refer to Chapter 1), promoting MW coupling and enabling the formation of an over-dense plasma. Secondly, it enables the creation of a magnetic nozzle, which efficiently guides and accelerates the plasma.
- The magnetic field strength must be equal to $B_{ECR} = 0.207$ T (@5.8GHz) at some location within the PC.
- The magnetic field gradient in the plume shall be as low as possible (low plume divergence angle).
- The magnetic field generator shall be able to sustain high temperatures ($T_{max} \approx 200°C$).
- The magnetic field shall be tunable.
- Low cost, limited mass, and safe when manipulated.

The requirements described above can be accomplished with multiple configurations: axially magnetized magnets, electromagnets (water-cooled or not), or radially magnetized magnets. Each of these possibilities has been analyzed with magnetic field simulation tools. However, for the sake of conciseness, only the final configuration will be treated here: consisting of a combination of a permanent magnet and an electromagnet.

The permanent magnet is responsible for the creation of the magnetic field for the ECR and the magnetic nozzle. Thus, the thruster can be operated without using the electromagnet, saving the waiting time required between successive operations

due to coil heating up. In the case of waveguide ECRTs, permanent magnets can reach a considerable mass. This is mainly due to the geometrical requirements necessary to not interfere with the presence of the thruster waveguide. This problem is greatly reduced in the case of coaxial ECRT thrusters, which have the possibility to have lower magnet inner diameters. On the other hand, the only purpose of the electromagnet here presented is to allow tunability of the magnetic nozzle divergence. Note that using the electromagnet also the resonance surface is displaced. A cross-section of the assembly permanent magnet + electromagnet is shown in figure 3.15a.

3.3.1 Permanent magnet

The permanent magnet used for this prototype is a radially magnetized ring magnet. This configuration offers a reduced mass with respect to an axially-magnetized ring magnet. Referring to figures 3.6(b-c), moving along the axis of an axially magnetized ring magnet, we can find a magnetic field $|B|$ peak in its center, a separatrix, and a lower secondary peak; whereas for a radially magnetized ring magnet, a separatrix is produced in its center and only one peak can be found downstream. For both cases, the proposed useful region for the discharge chamber of an ECR thruster is the region downstream of the last magnetic field peak (to create the magnetic nozzle and promote MW coupling). This region should contain a magnetic field large enough to reach B_{ECR}. Thus, being the second peak of an axially magnetized ring magnet much smaller than the one of a radially magnetized magnet, a larger magnet would be needed to reach B_{ECR}.

<div align="center">(a)   (b)   (c)</div>
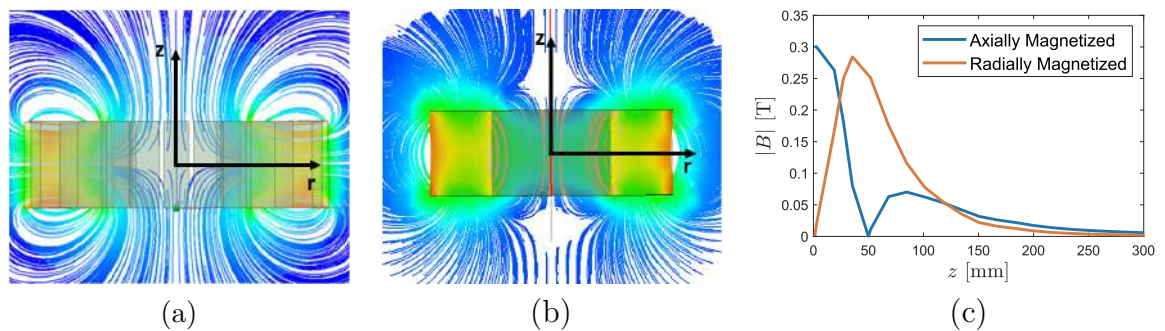
Figure 3.6: (a) Simulation of the magnetic field streamlines produced by a series of magnets positioned in a circular pattern with magnetization along the radial direction, forming a radially magnetized ring magnet. (b) Simulation of the magnetic field streamlines of an axially magnetized ring magnet. (c) Example of the trend of $|B|$ along the axis of a ring magnet for two different magnetization types. Dimensions $R_{in} = 40$ mm, $R_{out} = 80$ mm, $H = 55$ mm, material Neodymium grade N42. Figures produced with Ansys Maxwell and FEMM.

Although convenient, a radially magnetized ring magnet requires special procedures for manufacturing, raising the cost. A solution to this problem is to divide the

ring magnet into small sectors that can be easily radially magnetized, however, the repulsive force between the magnets can reach several kilograms. Thus, a special enclosure has to be designed, and the magnets need to be glued together.

The design of the magnet has been started with a 2D axisymmetric analysis carried out with the software Ansys which allows executing parametric analysis to estimate the dimensions of the magnet. In these simulations, the magnet is a perfect radially magnetized ring magnet. Subsequently, a 3D simulation is performed for the final design.

Figure 3.7 shows the basic parameters used in the setting up of the simulation domain.
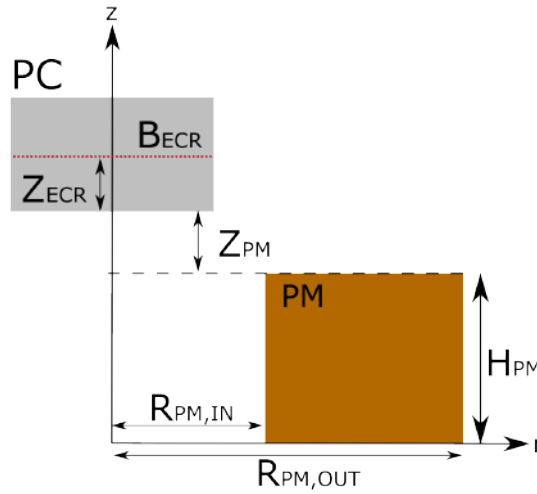
Figure 3.7: Ansys 2D simulation parameters used for the permanent magnet (PM) optimization. The plasma discharge chamber (PC) is also shown. The dotted line indicates the position of the resonance field B_{ECR}. The dashed line is the top face of the permanent magnet.

The parameters varied for the parametric analysis are inner and outer radii $R_{PM,in}$ and $R_{PM,out}$, and the magnet height H_{PM}.

Two magnet materials have been analyzed: NdFeB grade N42EH and SmCo YXG-32. Both allow reaching high working temperatures and present high remanence (refer to table 3.4).

	NdFeB N42EH	Sm2Co17 YXG-32
Remanence B_r [T]	1.305	1.124
Permeability μ_r	1.1443	1.0654
Maximum Temperature [°C]	200	300
Temp. coefficient of remanence [%K]	−0.12	−0.05
Density [Kg/m^3]	7700	8500

Table 3.4: Neodymium and Samarium Cobalt magnet characteristics.

The configurations are compared based on two objectives: mass and on-axis magnetic field gradient $\partial B/\partial z$ downstream of the resonance. Both of them should be minimized for a more compact design and a lower divergence angle of the MN. Additionally, the configurations are subject to an inequality constraint of $Z_{PM} + Z_{ECR} > 21$ mm, to be able to position B_{ECR} approximately at the PC center (refer to figure 3.7). The choice is performed with a Pareto-front approach prioritizing the reduction of the magnet mass. The identified optimal configurations for the two magnet materials are shown in table 3.5.

	NdFeB N42EH	Sm2Co17 YXG-32
H_{PM} [mm]	30	30
$R_{PM,in}$ [mm]	27	27
$R_{PM,out}$ [mm]	62	72
Z_{ECR} [mm]	12.7	14.2
Mass [Kg]	2.26	3.57

Table 3.5: Optimal configurations identified for NdFeB N42EH and Sm2Co17 YXG-32 radial magnetized ring magnet. For both configurations $z_{PM} = 11$ mm.

The material Sm2Co17 YXG-32 was chosen for the final configuration being it more cost-effective with respect to the NdFeB N42EH and with better thermal properties, trading off the magnet mass saving. As mentioned, these results are relative to a perfect ring magnet radially magnetized. Additional simulations showed that 12 sectors were enough to guarantee magnetic field uniformity (see figure 3.8a and 3.8b).

Figures 3.9a and 3.9b show the magnetic field simulations produced by the final configuration of the permanent magnet. Note that the magnetic field peak is behind the backplate in accordance with what is mentioned in the magnetic field generator requirements to obtain a purely diverging magnetic field (refer to Section 3.3 and Chapter 1). Once the magnet has been manufactured, the magnetic field has been measured with a 3-axis magnetic field probe (Lakeshore MMZ-2508-UH). Referring to figure 3.9b the field is in good agreement with the one predicted by simulations. The measured magnetic field peak results about 70 Gauss below the expected value, such a small difference could be caused by misalignment errors or differences in the magnet material properties with respect to table 3.4.

Finally figures 3.10a and 3.10b show the complete magnet assembly composed of 12 sectors enclosed in an aluminum casing.

(a)

(b)
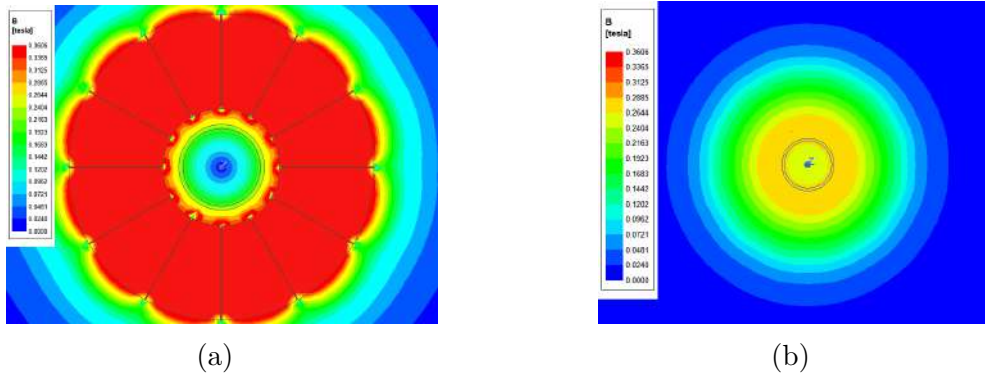
Figure 3.8: Top view of the magnetic field in a section plane 30 mm (a) and 60 mm (b) from the surface of the permanent magnet. The asymmetries introduced by the 12-sector division of the magnet are no longer noticeable at 60 mm. Figures obtained using Ansys Maxwell.

(a)

(b)
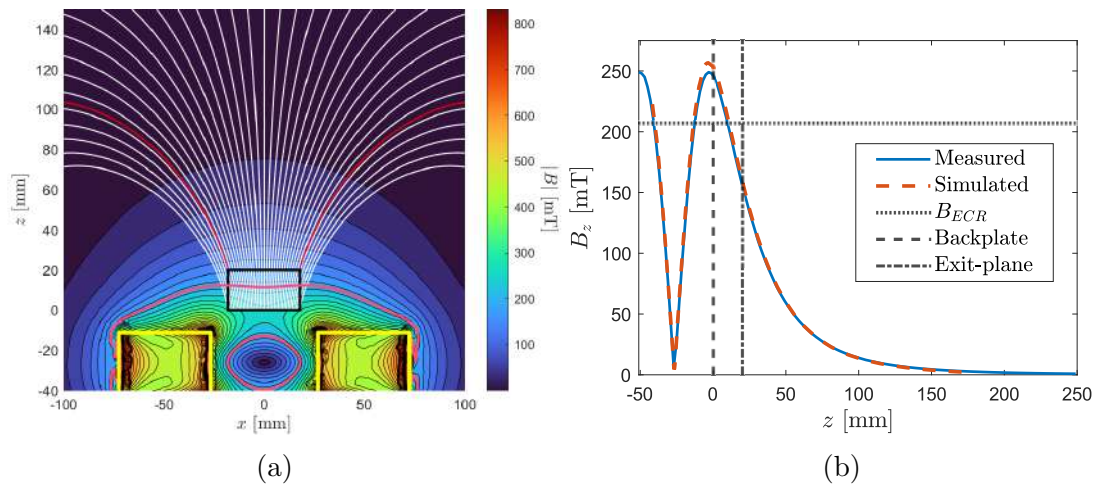
Figure 3.9: Figures derived by Ansys Maxwell simulations. (a) 2D view of the magnetic field produced by the permanent magnet, the magnetic field streamlines are also shown. In white are represented the magnetic field streamlines. Red streamlines indicate those that depart from the lips of the PC exit-plane. The resonance surface is indicated in magenta. The orange and yellow boxes represent respectively the cross-section of the electromagnet and permanent magnet. (b) Comparison of the simulated and measured magnetic field produced by the permanent magnet along the axis of the ECRT prototype.

<div style="text-align:center">(a)   (b)</div>
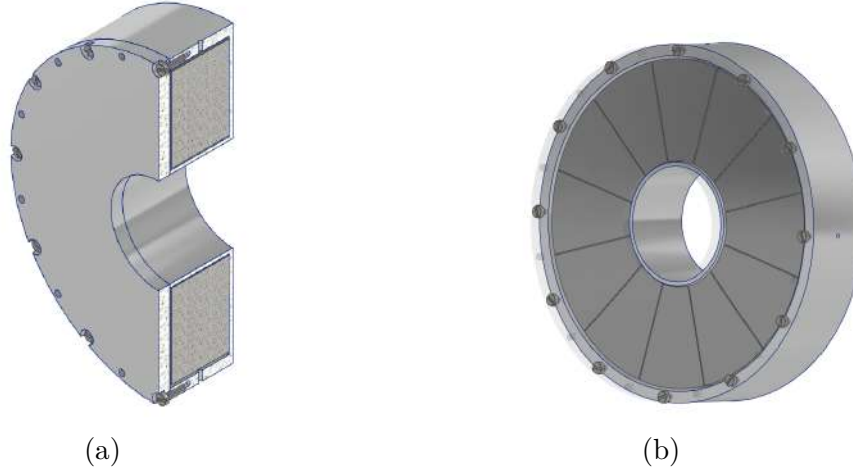
Figure 3.10: (a) Cross-section view of the magnet assembly within the casing. (b) Permanent magnet with the top part of the casing removed.

3.3.2 Electromagnet Design

In Section 3.3, we mentioned that the permanent magnet alone can create a magnetic nozzle and guarantee the presence of the ECR within the discharge chamber. Hence, the sole purpose of the electromagnet is to be able to tune the magnetic nozzle divergence and the resonance position. The objective is to provide enough freedom to study the role of these two factors during the experimental testing. This is done by superposing the electromagnet magnetic field to the one of the permanent magnet.

To affect the MN divergence and field while consuming low amounts of power (slower coil temperature increase) it is necessary to position the electromagnet as close as possible to this region. Thus, being the permanent magnet upstream of the PC, the electromagnet has been designed to exploit the space left available around the plasma discharge chamber. Consequently, the dimensions of the coil were imposed by geometrical factors, such as the external diameter of the discharge chamber, the gap necessary for the injector tubes, and the spacing with the permanent magnet. A CAD view of the coil assembly and positioning is shown in figures 3.11a - 3.11c.

The copper wire chosen is an AWG 9 with Kapton Enamel insulation, able to reach temperatures up to 200°C. Enabling several minutes of testing in vacuum condition. For a better filling factor, an orthocyclic winding with an equal number of turns per layer has been chosen. Figure 3.12 shows the topology of the field generated by this electromagnet.

<div style="text-align:center">(a)   (b)   (c)</div>
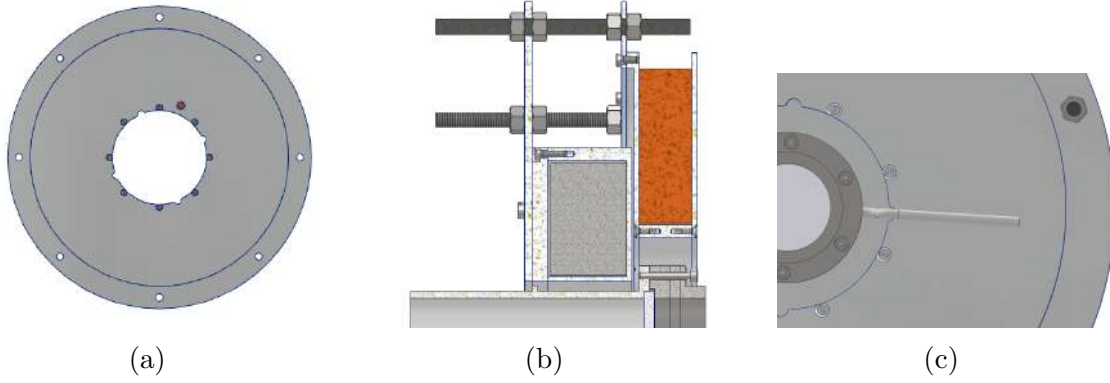
Figure 3.11: (a) Frontal view of the coil spool. (b) Cross-section view of the coil in its position in the assembly (red surface). The permanent magnet (dark gray surface) and the plasma discharge chamber are also shown. (c) Detail of the injector tubes positioned in correspondence of a notch in the coil spool in order to reduce to the minimum R_{c-in} and save power.
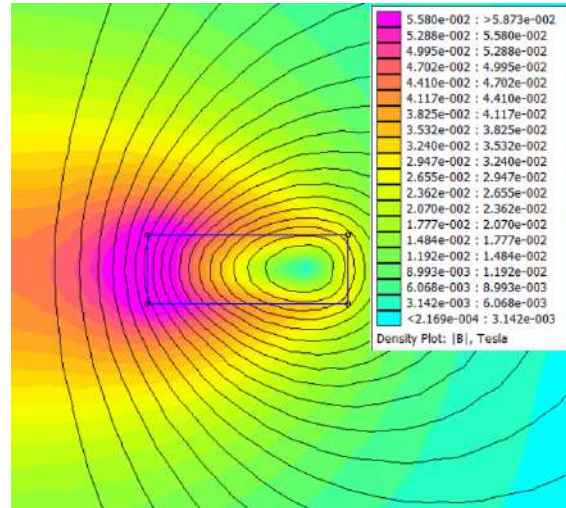
Figure 3.12: Topology of the magnetic field generated by the electromagnet. The rectangle indicates a region filled with 132 turns of wire ($N_{tl} = 6$, $N_l = 22$) carrying a current of $I_c = 40$ A. Axisymmetric simulation performed with the FEMM software.

Parameter	Value
N_{tl}, N_l	6 , 22
Wire Type	AWG 9 Kapton Enamel ($T_{c-max} = 200$ °C)
R_{c-in} [mm]	47.15
R_{c-out} [mm]	107.45
H_c [mm]	20.8
Coil Resistance [Ω]	0.179
I_c [A]	0–40

Table 3.6: Electromagnet design parameters and dimensions. N_{tl} is the number of wire turns per layer, N_l is the number of layers. R_{c-in}, R_{c-out}, and H_C are the inner radius, outer radius, and height of the coil.

(a)

(c)

(b)

(d)
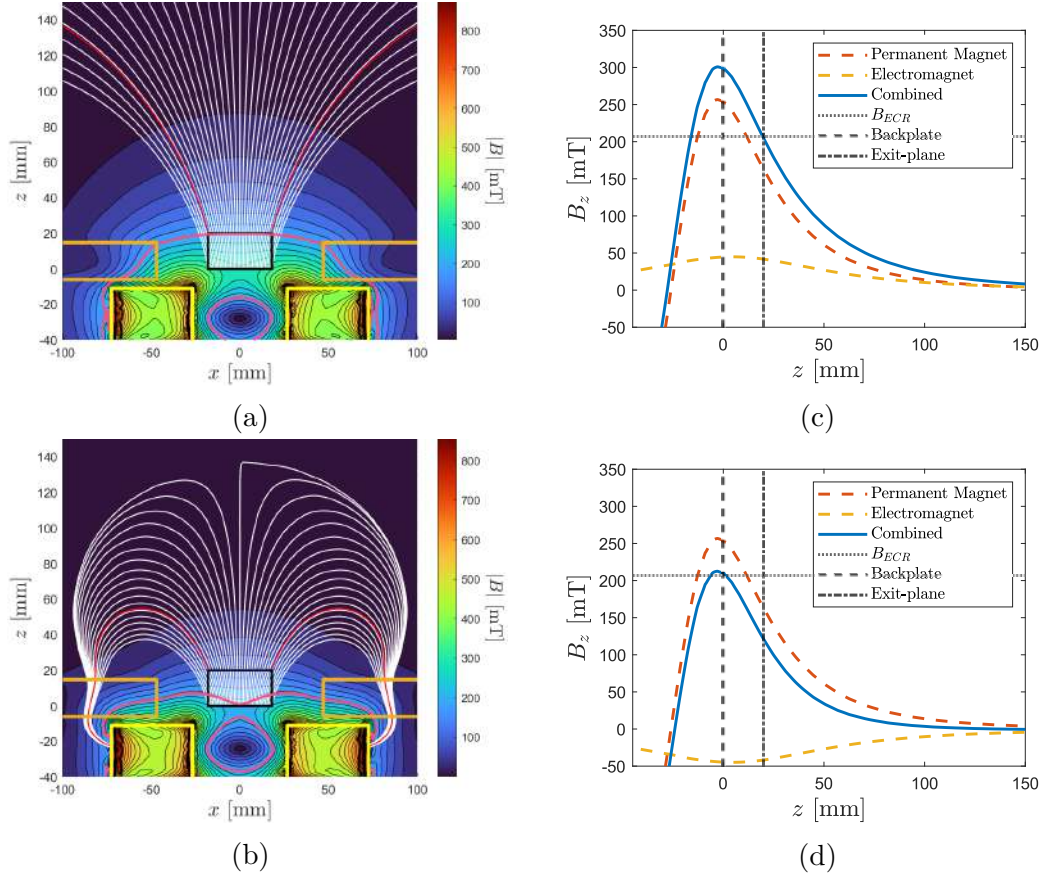
Figure 3.13: Figures derived by Ansys Maxwell simulations. (a-b) Sum of the PM magnet field + electromagnet @ $I = 40$ A and $I_c = -40$ A. In white are represented the magnetic field streamlines. Red streamlines indicate those that depart from the lips of the PC exit-plane. The resonance surface is indicated in magenta. The orange and yellow boxes represent respectively the cross-section of the electromagnet and permanent magnet. (c-d) Magnetic field along the thruster axis resulting from the superposition of the field produced by the electromagnet and permanent magnet, for $I_c = 40$ A (c) and $I_c = -40$ A (d).

3.3.3 Superposition of the magnetic fields

The magnetic fields from the permanent magnet and the electromagnet combined are shown in figures 3.13a - 3.13d. The electromagnet allows displacing the resonance position up to the thruster exit plane by applying a current $I_c = 40$ A (refer to figure 3.13a and 3.13c). On the other hand, the resonance is displaced to the backplate for $I_c = -40$ A. Notice how for the negative current the shape of the resonance region is also affected while for positive currents it stays mainly flat.

When the electromagnet is used, the magnetic nozzle divergence is also affected as visible in figure 3.13a and 3.13b. Positive currents, reduce the divergence angle, while negative currents enlarge it. Due to the different magnetic field gradients produced by the coil and permanent magnet, a separatrix is created in the middle of the plume for $I_c < 0$ A. The separatrix moves towards the thruster as I_c becomes

(a)   (b)
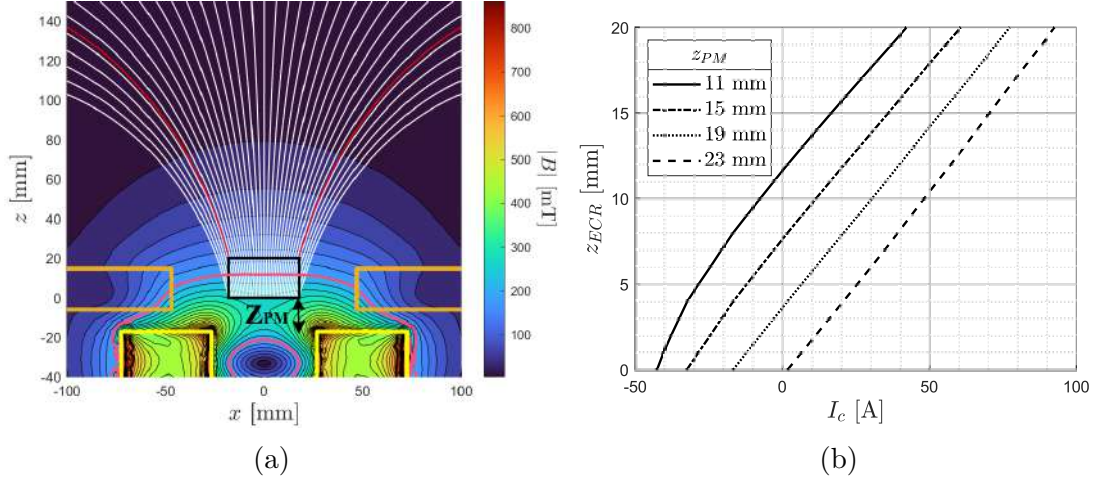
Figure 3.14: Figures derived by Ansys Maxwell simulations. (a) 2D plot of the magnetic field shape obtained for $z_{PM} = 17$ mm and $I_c = 30$ A. In white are represented the magnetic field streamlines. Red streamlines indicate those that depart from the lips of the PC exit-plane. resonance surface is indicated in magenta. z_{ECR} is kept constant at 11.5 mm ($z = 0$ coincides with the backplate). The orange and yellow boxes represent respectively the cross-section of the electromagnet and permanent magnet. (b) Relationship between coil current I_c, resonance position z_{ECR}, and magnet position z_{PM}.

more negative. Due to the azimuthal currents in the plume, a separatrix is expected to be naturally present in the plume of a magnetic nozzle thruster, however, having one in proximity to the PC strongly distorts the magnetic nozzle shape with the possible results of large currents flowing back to the thruster, and in reduced or no-net thrust. For this reason, in Chapter 5, the effect of the electromagnet current on the plume properties is discussed for positive values of I_c only.

Nevertheless, by varying the relative distance between the permanent magnet and the backplate (Z_{PM}) while keeping the electromagnet in the original position, it is possible to modify the magnetic nozzle divergence without displacing the ECR. Figure 3.14a shows one of these cases. For a given z_{ECR} the nozzle divergence angle can be reduced by increasing I_c and z_{PM} according to figure 3.14b. This possibility increases the flexibility of this prototype design, however, the latter has not been tested in the framework of this thesis, where the nominal spacing $Z_{PM} = 11$ mm was used.

3.4 Thruster head assembly

The complete assembly is here presented. The two main sub-assemblies (the discharge chamber and the magnetic field generator) are mounted on an aluminum panel as displayed in figure 3.15a. In turn, the latter is mounted on a series of aluminum profiles. The mechanical joint between the PC and the Magnetic field generator is achieved through the waveguide adapter and 8 mounting rods. The waveguide adapter is made of anodized aluminum (yellow) and Teflon (orange). As will be discussed in Section 3.5, this solution improves thermal management while keeping the PC floating. The Teflon ring is in contact with the thruster-waveguide reference annular step and with the permanent magnet (refer to Section 3.2) ensuring the alignment with the magnetic field generator. The thruster-waveguide position is secured with a set screw at the back of the panel.

Figure 3.15b shows the prototype fully assembled and positioned on a structure made from aluminum profiles. In Chapter 6, direct thrust measurements with a thrust balance are taken. The flexible design here described allows interfacing with the thrust balance through a simple adapter mounted on a lighter version of the aluminum panel as shown in figure 3.16.

(a)   (b)
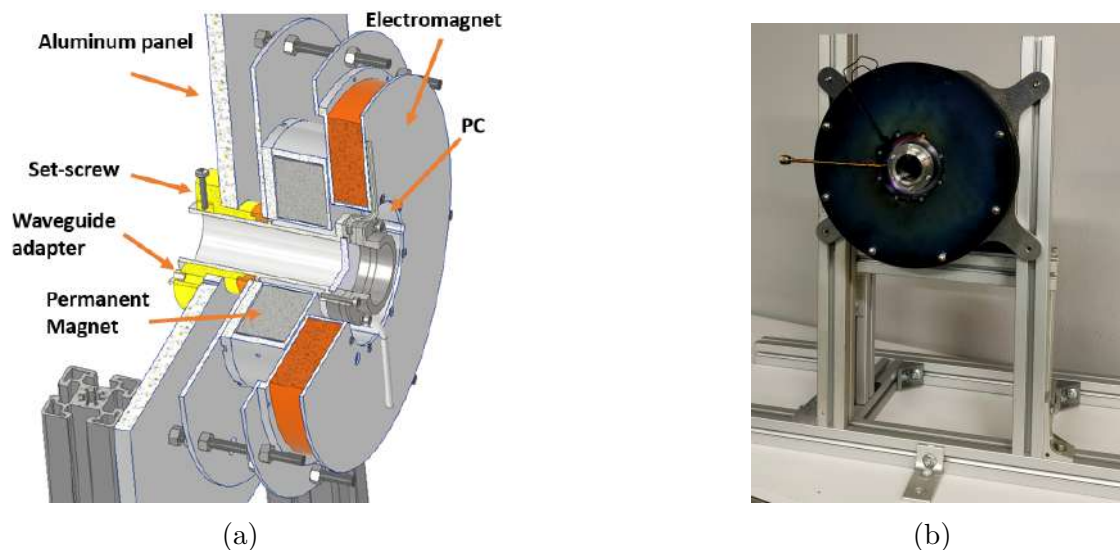
Figure 3.15: (a) 3/4 section CAD view of the assembled ECRT prototype. (b) Photo of the assembled ECRT prototype.
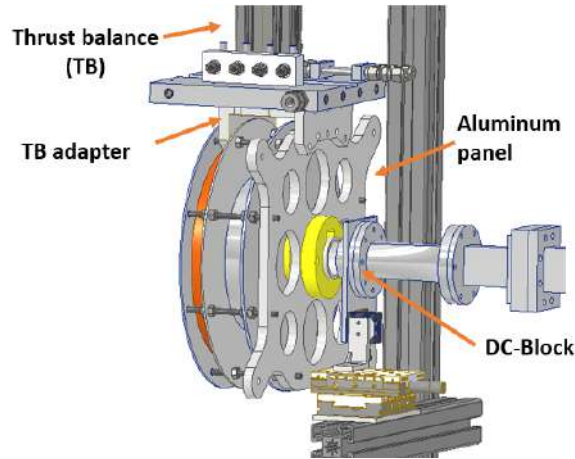
Figure 3.16: Back-view of the thruster mounted on the thrust balance.

3.5 Design improvements derived from thermal analysis

As outlined in the design requirements (Section 3.1.1), to ensure long-duration thruster firings and reduced cool-down times, a robust thermal design is crucial. To achieve this objective, thermal analysis simulations were conducted using Ansys Workbench software. The software uses FEM analysis to obtain a steady-state solution of the heat equation. The software allows importing a CAD geometry, to define the materials, and boundary conditions (BC) at the interfaces and domain boundaries. Different thermal simulations were conducted in order to identify whether limit temperatures are reached when both the thruster and the coil are active. As will be shown in this section, those allowed us to identify thermal problems, and to address them by different design choices. In particular, three components were targeted: the thruster waveguide, the waveguide adapter, and the backplate thickness. Additionally, simulations were helpful in identifying components prone to reaching limit temperatures during testing.

The following boundary conditions are used:

- Heat flow applied on the internal surfaces of the thruster (steel components and quartz plate) for a total deposited power of P_T, equal to the input power (i.e., assuming zero thrust efficiency).
- Volumetric heating on the electromagnet P_{coil} due to Joule heating.
- Vacuum between the components.
- Surface-to-surface radiation BC between the waveguide and the internal surface of the magnet and between magnet and coil mounting plates (Emissivity $\epsilon = 0.3$).
- Surface to ambient radiation BC for the coil front-plate, the coil mounting-

	A	B	C	D
P_T	400 W	400 W	400 W	400 W
P_{coil}	0 W	0 W	0 W	500 W
t_{WG}	2 mm	2 mm	3 mm	3 mm
t_{back}	2 mm	2 mm	4 mm	4 mm
Waveguide adapter material	Teflon	Al	Al + Teflon	Al + Teflon

Table 3.7: Thermal simulation settings for the cases A, B, C, D. t_{WG} is the thickness of the thruster aluminum waveguide, while t_{back} is the thickness of the discharge chamber quartz backplate. Case C and D, are simulations performed with the final dimensions and materials of the waveguide adapter.

plate, and the thruster backplate ($\epsilon = 0.3$).

- Fixed temperature BC on the surfaces in the proximity of the screws of the aluminum plate ($T = 22°C$).
- The permanent magnet and casing are considered as a single object.

Figure 3.17 shows an example of the thruster head meshed geometry.
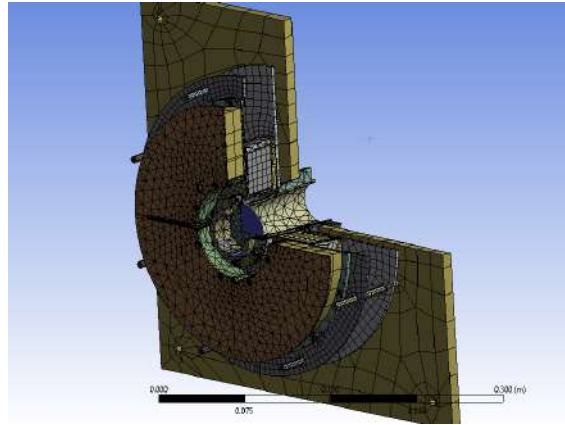
Figure 3.17: Example of the mesh used when performing the thermal analysis simulations with the software Ansys Workbench, the geometry displays the thruster head prototype.

Figures 3.18-a,d show the results of the performed thermal simulation. The parameters used for each simulation in figure 3.18 are summarised in table 3.7. In an iterative approach between design and thermal modeling, this set of simulations led to the prototype design discussed in Section 3.4 which was subsequently manufactured.
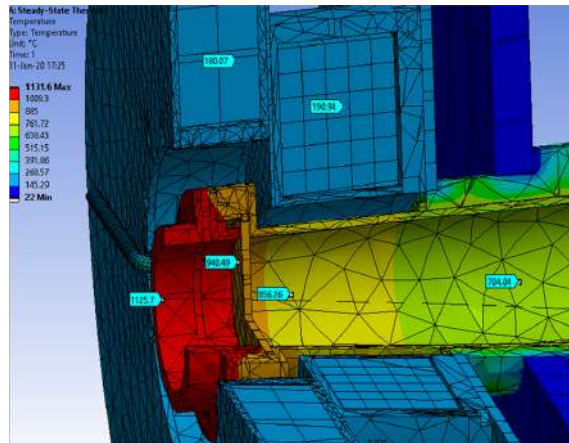
(a) Case A
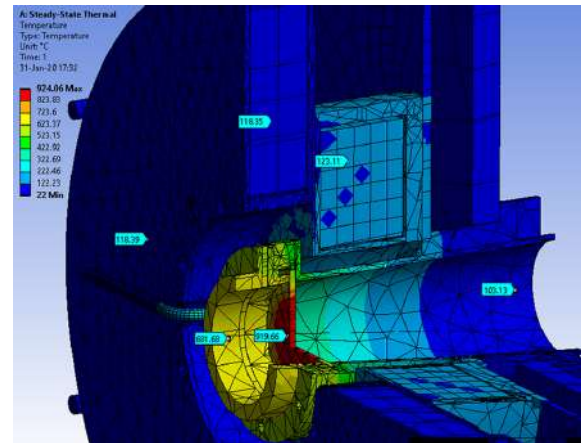
(b) Case B
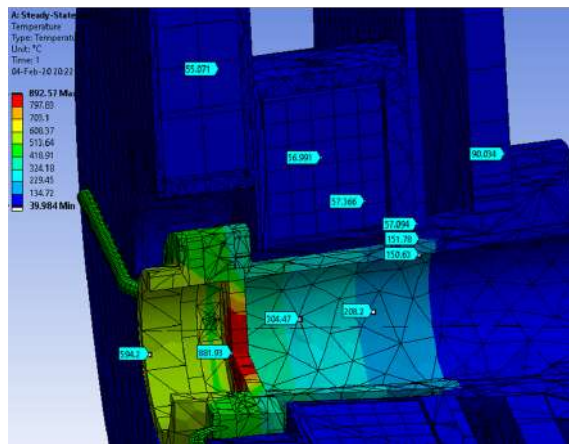
(c) Case C
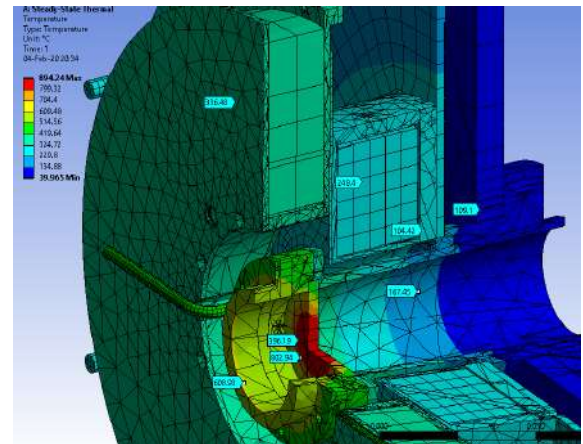
(d) Case D

Figure 3.18: (a) Case A: waveguide adapter entirely in Teflon, Quartz backplate of 2 mm thickness. (b) Case B: waveguide adapter in aluminum, Quartz backplate of 2 mm thickness. (c) Case C: waveguide adapter in aluminum, Quartz backplate of 4 mm thickness, waveguide of 3 mm thickness. (d) Case D: geometry equivalent to C, P_{coil} = 500 W. Case C and D, are simulations performed with the final dimensions and materials of the waveguide adapter.

The first prototype design accounted for both a thruster waveguide and backplate 2 mm thick and a waveguide adapter made of Teflon. In all the shown cases, a Teflon separator sheath 1 mm thick is positioned between the permanent magnet and the electromagnet. Initially, a Teflon waveguide adapter is considered for Case A, this provides electrical insulation to the thruster so that no current is extracted from the PC source while the thruster is firing. However this component also considerably increases the thermal resistance, making both the stainless steel and aluminum components approach prohibited temperatures in steady-state with temperatures of more than 1000°C (refer to figure 3.18-a). For this reason for the configuration (b) (refer to figure 3.18-b) a waveguide adapter made of anodized aluminum was chosen. The temperatures greatly reduced at the PC, however, the magnet and the coil also resulted in being affected reaching more than 100 °C (figure 3.18-b). To avoid this problem, an annular teflon component is positioned in front of the
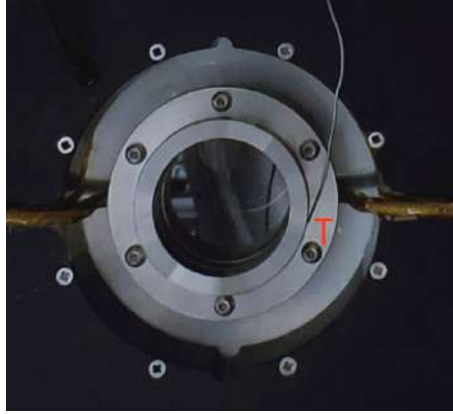
Figure 3.19: Front view of the assembled PC. "T" indicates the position of the discharge chamber wall thermocouple.

waveguide adapter to better isolate the thermal path between the magnet and the discharge chamber. The results are visible in figure 3.18-c. Additionally, for this configuration, the thickness of the thruster waveguide and the quartz disk have been increased respectively to 3 and 4 mm. The quartz disk thickness has been increased to be able to better resist thermal stresses. Concerning T_{WG}, its increase makes the waveguide stiffer and slightly increases the surface contact (the internal diameter stayed the same). In the last simulation 3.18-d a volumetric power source is provided to the coil (500 W), showing that the coil is not able to work in steady-state since the limit temperature is $T_{c-max} = 200\,°C$. Additionally, the permanent magnet is also heated. For this reason, the final version of the prototype employs a vacuum gap between the magnet and coil instead of the 1 mm thick Teflon sheath, this solution was initially avoided to simplify the assembling.

The aluminum, stainless steel, and quartz components, can tolerate the temperatures shown in figure 3.18-(c,d). However, this is not the case for the FFKM o-ring surrounding the quartz backplate, since the thermal analysis predicts temperatures between 400–500°C (the maximum allowed temperature for this material is between 270–300°C). Hence, this component represents the most critical aspect from the thermal point of view. To account for this problem during thruster firings, the temperature is monitored through a thermocouple placed on the outer walls of the PC, and the testings are stopped when the temperature approaches 250°C. At that point, the thruster is left to cool down. Figure 3.19 shows the thermocouple position during operation. With this approach, steady-state temperatures are not always reached and typical thruster firings can last about 10 minutes (depending on the thruster working point). In contrast, the time span for cooling down is in the order of 30-50 minutes.

3.6   Transmission line

In this section, each of the transmission line (TL) components necessary to deliver MW power to the ECRT prototype is presented. This setup will be used in chapters 5 and 6 with a few variations.

The role of the transmission line is to deliver the microwave power produced by the generator to the thruster. Additionally, certain elements in the TL allow us to measure and tune the MW power. Due to the complexity of the setup, multiple components are used. A scheme is available in figures 3.20 and a CAD view of the assembly outside and within the vacuum chamber is available in figure 3.21. Each of these components is described in Section 3.6.2, and some standard definitions of TL fundamentals are introduced in Section 3.6.1. These will come in useful throughout the thesis.
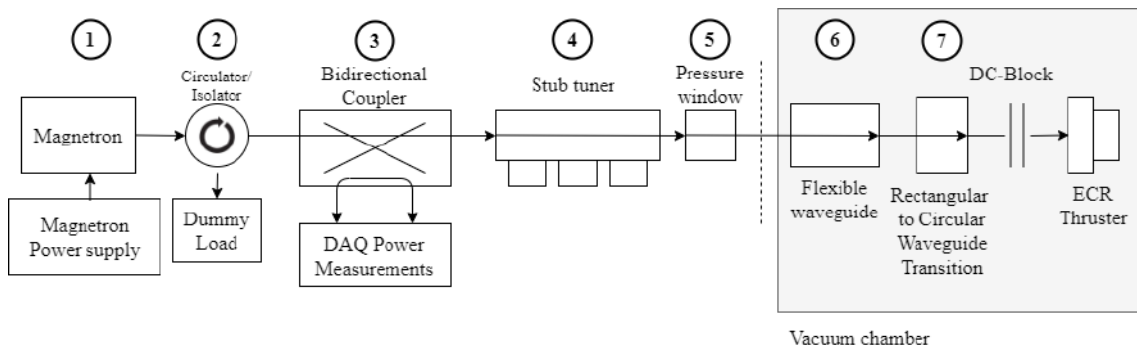
Figure 3.20: Scheme of the transmission line used to provide the microwave power to the ECR thruster prototype.
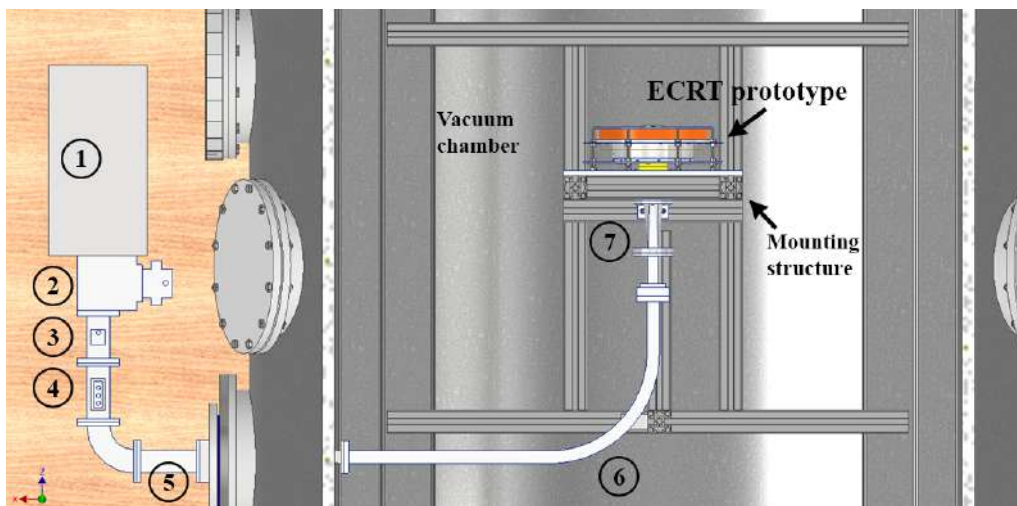
Figure 3.21: CAD top view of the transmission line used during the ECRT testing. The setup is installed into the EP2 large vacuum chamber facility. (1) Magnetron microwave generator, (2) Circulator, (3) Bidirectional coupler, (4) Stub tuner, (5) Pressure window, (6) Flexible rectangular waveguide segment, (7) Rectangular to circular waveguide transition.

3.6.1 TL fundamental definitions

Each component in a transmission line (TL) can be characterized by its capability of reflecting or transmitting electromagnetic waves at its ports. In the classical definition, these electromagnetic waves are in the form of voltage waves, however for the case of waveguide transmission lines, since a single conducting element is employed, voltage is not defined. Therefore, equivalently, the so-called power waves *a* and *b* are used, where *a* identifies the power wave incoming into the port and *b* the out-coming. These are complex numbers such that $|a|^2$ and $|b|^2$ give a real power (incoming and outgoing power) [92, 102, 103].

The property to transmit or reflect power waves can be expressed in the form of a square matrix, called scattering matrix, S. The size of the matrix depends on the number of ports of the TL element, this can be arbitrary, a visualization is available in figure 3.22. As an example, an element with one port typically represents a load, a simple TL segment is a 2-port network and a Directional coupler is a 4-port network. The S matrix relates an input wave at each port with a reflected wave at each port as in equation 3.3. The scattering matrix of a TL component is symmetric if the TL doesn't contain any non-reciprocal materials (ferrite, plasma, etc.) [92].

$$\begin{bmatrix} b_1 \\ b_2 \\ \vdots \\ b_N \end{bmatrix} = \begin{bmatrix} S_{11} & S_{12} & \dots & S_{1N} \\ S_{21} & S_{22} & \dots & S_{2N} \\ \vdots & \vdots & \ddots & \vdots \\ S_{N1} & S_{N2} & \dots & S_{NN} \end{bmatrix} \begin{bmatrix} a_1 \\ a_2 \\ \vdots \\ a_N \end{bmatrix} \tag{3.3}$$
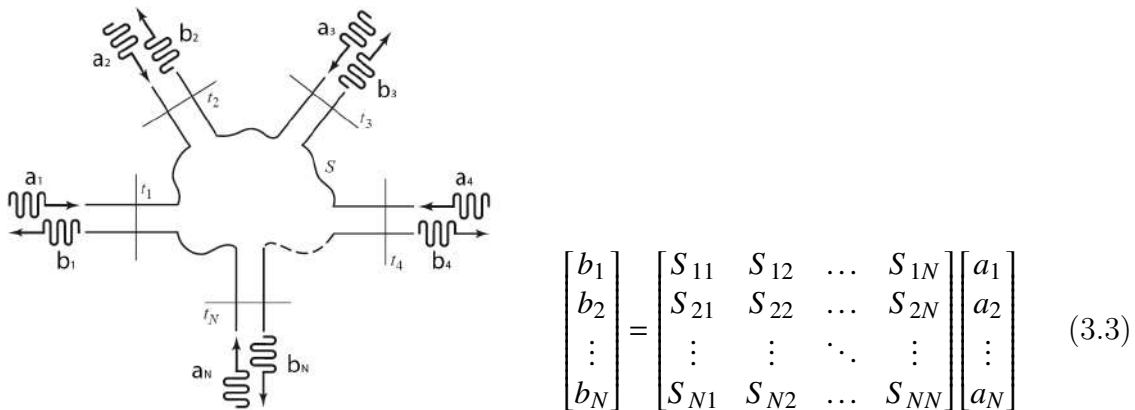
Figure 3.22: Scheme of a generic transmission-line component with N ports, t_i identifies the ports, *a* and *b* are incoming and outgoing power-wave respectively [92].

The characteristics of transmission-line components are not typically expressed in terms of matrix S, but it is more convenient to talk about Transmission, Isolation, Insertion loss, Return loss, etc. All of these are typically expressed in dB, therefore for clarity, their logarithmic and linear definitions will be presented below. These parameters are determined with a VNA (Vector Network Analyzer).

Reflection coefficient and Return Loss: The reflection coefficient of a port *i* is the diagonal element $\Gamma_i = S_{ii}$. Representing the ratio between the power wave

that is reflected from the port i while providing power to the same port i. All the other ports are matched. So that $|\Gamma_i|^2$ gives the fraction of reflected power. When expressed in dB, it is called Return Loss:

$$R_{Li} = -20\log_{10}|\Gamma_i|, \tag{3.4}$$

Transmission coefficient: This quantity is an off-diagonal element of the scattering matrix, S_{ij}, quantifies how much of the input power in port j is transmitted to port i, when all the other ports are matched. The transmission coefficient $|S_{ij}|^2$ is the fraction of transmitted power. Expressed in dB takes the name of Insertion loss:

$$I_{Lij} = -20\log_{10}|S_{ij}|, \tag{3.5}$$

For the case of the isolator (2) and directional coupler (3) (refer to 3.20), a distinction must be made. These devices are respectively 3 and 4-port networks. The large majority of the power is transmitted from ports 1 to 2 on the waveguide transmission line, while a small fraction is withdrawn for power measurement purposes by the remaining ports. Thus, the "Coupling" coefficient, C, is equivalent to the transmission and quantifies how much power is withdrawn. In dB terms, C is typically large, since the power measuring devices typically work in the range of mW.

Isolation: It characterizes how well a network can prevent signals from one port from leaking or coupling into another port. It is an important parameter for the case of an isolator. In its most simple form, an isolator is a 2-port network and power can flow in one direction only, from port 1 to 2, for this reason, S for an isolator is non-symmetric (it contains ferrite). The isolation quantifies this capability by providing the ratio between the output power at port 1 and the power input at port 2. In the case of an Isolator, the isolation is:

$$I = -20\log_{10}|S_{12}| \tag{3.6}$$

Directivity: Directivity is a fundamental parameter characterizing directional couplers. These are 4-port devices that can withdraw a small amount of power flowing within a TL segment in the forward or backward direction. Directivity quantifies how well they can discern between forward and backward power.

$$D = 20\log_{10}|S_{31}| - 20\log_{10}|S_{41}| \tag{3.7}$$

3.6.2 Transmission line components

On the choice of coaxial vs. Waveguide transmission line As mentioned in the 3.1 and 3.2, the PC has a circular waveguide geometry, however, the choice between the use of coaxial lines or waveguides to deliver the MW power to the PC is open. The benefits brought by a coaxial are multiple: flexible line, small footprint, and lower price. However, the performance of such cables lowers with the frequency, in particular at 5.8 GHz, the attenuation typically reaches values of 0.2 dB/m or higher. This means that cable overheating represents a major issue during experimental testing in a vacuum. Additionally, the isolator, directional coupler, stub-tuner, and MW vacuum chamber feed-through, below discussed, are not commercially available in coaxial format at this frequency and power range. This led to the choice to use waveguides to transmit power. The waveguide flange used is the European standard rectangular flange for this frequency, the WR159/UDR58, this standard is used for the entire transmission line up to the rectangular to circular waveguide adapter.

(1) Microwave generator The microwave generator chosen is an IBF PGEN5800/0.8 Magnetron generator, it can supply microwave power in the range P_{set} = 80 − 800W at frequency f = 5.8 GHz, where P_{set} is the power set on the control panel of the device. The actual power delivered to the thruster, P_T, depends on the level of reflections and absorption happening in the transmission line.

The frequency spectrum of the generator has been characterized with a spectrum analyzer. The results are shown in figures 3.23(a-b).

<div align="center">(a)   (b)</div>
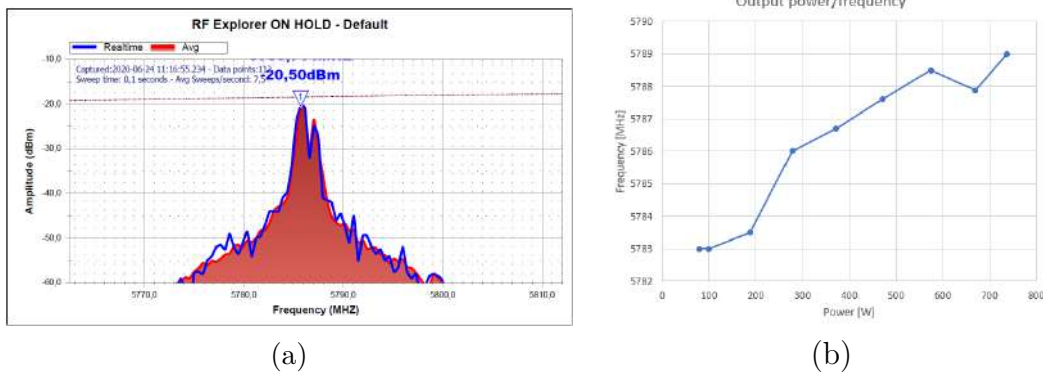
Figure 3.23: (a) Microwave frequency spectrum at P_{out} = 300W. (b) Magnetron output microwave frequency depending on the output power.

A dependence with power has been observed accounting for only a few MHz as shown in table 3.8. The mean output frequency is $\bar{f}$ = 5.786 GHz, thus the resonance is expected to be displaced 0.1 mm from the values presented in 3.3.3. These differences will be considered to be negligible throughout the rest of the thesis.

Parameter	Value
Δf	6 MHz
$\bar{f}$	5.786 GHz
ΔB_{ECR}	2 G
ΔX_{ECR}	0.04 mm

Table 3.8: Magnetron frequency spectrum information and expected effects on the resonance position. Δf corresponds to the frequency variation with respect to mean value $\bar{f}$ due to the variation in output power, equivalently ΔB_{ECR} is the displacement of the resonance magnetic field with respect to B_{ECR}. ΔX_{ECR} is the displacement of the resonance field due to the frequency variation Δf.

(2) Circulator/Isolator The circulator is a 3-port network component able to redirect power flowing from port 1 to port 2 and power flowing from port 2 to port 3. This characteristic allows redirecting the reflected power to another port. In this configuration it is positioned downstream of the output port of the magnetron, in this way, the reflected power from the thruster is redirected to another load so that the magnetron is not affected (response governed by the Rieke diagram [104]). This configuration, including the dissipation load, is also called "Isolator". The isolator used is the IBF-WR159ISOLATOR01SA, its main characteristics are described in table 3.9. This isolator includes also a reflected SMA coaxial output on the included water-cooled load in order to track the reflected power.

Parameter	Value
Isolation	≥ 20 dB
Insertion Loss	≤ 0.25 dB
Return Loss	≥ 20 dB
Reflected power Coupling	50 dB ±1 dB

Table 3.9: Characteristics of isolator IBF-WR159ISOLATOR01SA.

(3) Dual Directional coupler The Bi-Directional coupler is a passive 4-ports network. It is capable of coupling small amounts of power (determined by the coupling factor) to the two coupling ports distinguishing between forward and backward (reflected) power, in the context of this thesis, these quantities are indicated with P_F and P_R respectively. This device is mainly used when forward and reflected power measurements are necessary, which can be done by positioning power sensors downstream of the coupling ports. In order to have a correct reading of the forward and reflected powers it is necessary to position the directional coupler upstream of the stub tuner (see the Section 3.6.2 for more information). The Directional coupler used is the IBF-WR159DDC60NA/SA, which is a dual-directional coupler, and allows for more precise and simultaneous measurements of forward and reflected power. Its characteristics are available in table 3.10.

Parameter	Value
Fwd. and Refl. Coupling factor	61.92 dB, 61.79 dB
Directivity	≥ 25 dB
Return Loss	≥ 12.7 dB

Table 3.10: Characteristics of Directional coupler IBF-WR159DDC60NA/SA. The coupling factors have been calibrated with a VNA.

(4) Stub tuner The stub tuner is a 2-ports matching network. It is composed of a simple waveguide straight in which 3 screws (stubs) are inserted on its centerline (refer to figure 3.24). By rotating the stubs their insertion length into the waveguide varies, this alters the scattering matrix of the component. By choosing the appropriate stub length, a mismatched load can be matched.

The stub tuner is a MUEGGE-GA1021. A picture of the component is available in figure 3.24.
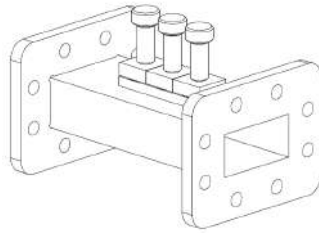
Figure 3.24: CAD representation of the stub tuner MUEGGE-GA1021.

(5) Pressure Window The pressure window realizes the interface between the ambient pressure and the vacuum inside the vacuum chamber. It is a component commonly used in waveguide assemblies in order to keep segments of the transmission lines under vacuum and reduce the possibilities of water-drop formation. For this application, it is connected to the atmosphere side of a custom-made vacuum stainless steel flange as visible in figure 3.25(a-b). The pressure window chosen is a MUEGGE-GA2604. A CAD view is shown in figure 3.25-c and its main characteristics are listed in table 3.11. It is a piece of waveguide presenting a quartz window pressed between two o-rings, allowing microwave power to flow, but keeping air tightness. An additional o-ring on the mating waveguide surfaces ensures that the waveguide connection is also vacuum-proof. Due to the maximum input power limit of this component, the microwave power supply described in this section is used below 400 W. This prevents potential damage to the feed-through in the case of total power reflection.
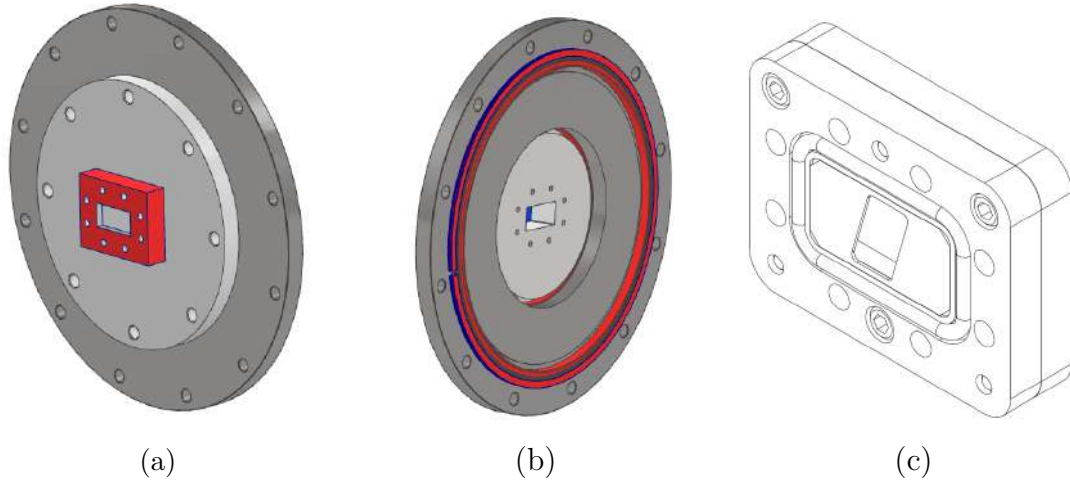
Figure 3.25: (a) Air side of the custom vacuum flange, in red the pressure window. (b) Vacuum side of the custom vacuum flange. (c) Pressure window (Image from datasheet).

Parameter	Value
Freq	5.8 GHz ± 75 MHz
Max CW Input Power	700W to matched load
Input VSWR	1.2 max
Insertion Loss	0.16 dBm Max
ΔP_{max}	2 bar
Leak rate	10^{-7} Torr-lit/sec max. with SF_6
Oper. Temp.	-54°C to +232 °C

Table 3.11: Pressure window MUEGGE-GA2604 characteristics.

(6) Flexible waveguide   A flexible waveguide is a piece of waveguide that can be flexed. There are multiple kinds and implementations of flexible waveguides, the ones that can twist or bend only, and those able to do both. The ones used in this context are of the bend-twistable type.

Two segments of flexible waveguides are present in the assembly. A short segment (120mm) is positioned just before the pressure window, it serves the scope of avoiding applying a direct torque on the pressure window absorbing possible mechanical shocks. A longer segment (800mm) is positioned on the vacuum side and it is the link between the pressure window and the thruster, achieving with its curvature an angle of 90°. This segment has been chosen to be flexible in order to have easier assembling and thruster-aligning operations. Some of the specs for the two waveguides are resumed in table 3.12.

Parameter	Value	
Length	120 mm	800 mm
Insertion loss	0.015 dB	0.1 dB
Return Loss	35 dB	35 dB< RL <50 dB
Maximum CW average power	2.5 KW	2.5 KW
Min E-Plane Bend Radius (Repeated)	464 mm	464 mm
Min H-Plane Bend Radius (Repeated)	928 mm	928 mm
Maximum Twist (Repeated)	45 °/m	45 °/m
Oper. Temp.	-70°C to +150 °C	-70°C to +150 °C

Table 3.12: Flexible waveguide datasheet information.

(7) Rectangular to Circular waveguide transition The rectangular to circular waveguide transition is a tapered and stepped connection that allows the transformation from the TE_{01} fundamental mode of the rectangular waveguide to the TE_{11} mode of the circular waveguide. The exit diameter of the circular waveguide transition corresponds to the one of the DC-block and the ECRT aluminum waveguide. The transition chosen is the FLANN Microwave 14643, compatible with frequencies between 5.38 – 8.18 GHz.

DC-block The DC-block is a component necessary to keep the thruster electrically floating during the operations. This component consists essentially of a vacuum gap between the TL and the aluminum waveguide positioned at the back of the thruster. The gap is small enough to allow negligible MW radiation from the gap itself, to study the behavior at different gap sizes ANSYS simulations were performed as discussed in Section 3.7.3. In the experiments performed in the following chapters, the DC-block distance is kept in the range of 2 – 3 mm. For optimal performance, the two waveguide segments need to be closely aligned, for this reason, the upstream DC-block segment is mounted on a 3-axis manual linear stage as shown in figure 3.26.
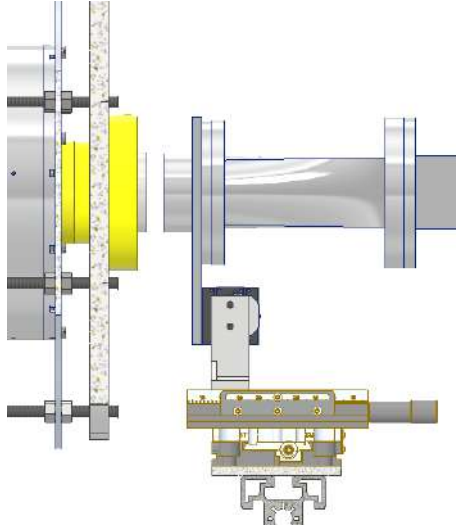
Figure 3.26: CAD view of the 3-axis linear stage system used to align the DC-block inside the vacuum chamber.

3.7 Electromagnetic simulations

This section presents simulations of the propagation of microwaves in the final prototype design. Those are used to quantify the MW power radiated, P_{rad}, from the thruster and identify potential issues with the DC-block (refer to Section 3.6) or excessive power absorption at the quartz backplate. The commercial software Ansys HFSS is used for this purpose. HFSS employs FEM analysis to determine the distribution of electromagnetic fields within a user-defined region by solving Maxwell's equations in the frequency domain.

3.7.1 Model and Boundary conditions

Two different 3D models were used to test respectively the microwave radiation from the PC and the DC-block. In this context, we will refer to them as configurations A and B. The models are available in figures 3.27a and 3.27b.

Case A (figure 3.27a), consists of the thruster discharge chamber + waveguide CAD model, where all the components have been assigned with the corresponding material properties from the material library of HFSS. The second one (figure 3.27b), case B, consists of two aligned circular waveguides, the two can be displaced arbitrarily creating the vacuum gap of the DC-block. Both cases employ vacuum conditions within the waveguides.

Concerning wave excitation, wave ports are used in both cases, enabling microwave energy (at 5.8 GHz) to flow into and out of the simulation. The excitation field pattern is determined based on the shape of the surface where the wave port
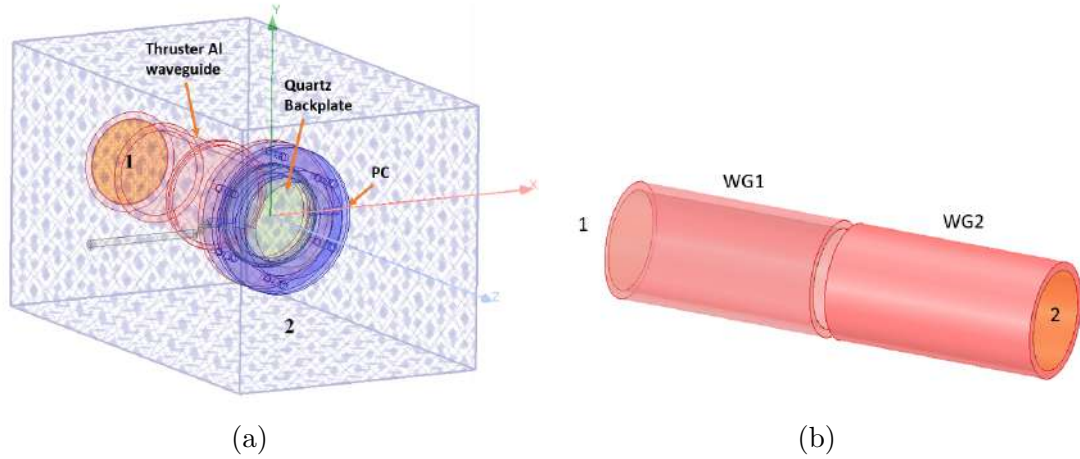
Figure 3.27: (a) Case A: Modeled geometry and BC definition (1:wave-port, 2:radiation boundary) (b) Case B: Two circular waveguides (WG1 – WG2) separated by the distance δ_{DC}, the excitation is set at wave-ports 1 and 2. Electromagnetic simulations performed with Ansys HFSS.

is defined. Infinite modes can exist on each wave port but only some of them can propagate. The software allows defining the number of modes that the port will accept. The electric field solution at the port will be forced to be a linear combination of these modes. Hence, defining only one mode can lead to erroneous results. In the following simulations, four modes will be simulated per port since adding more modes has been seen to not affect the results. As visible in figure 3.28, the four resulting modes correspond to: mode 1-2 TE_{11} mode, mode 3:TM_{01}, mode 4: TE_{21}.
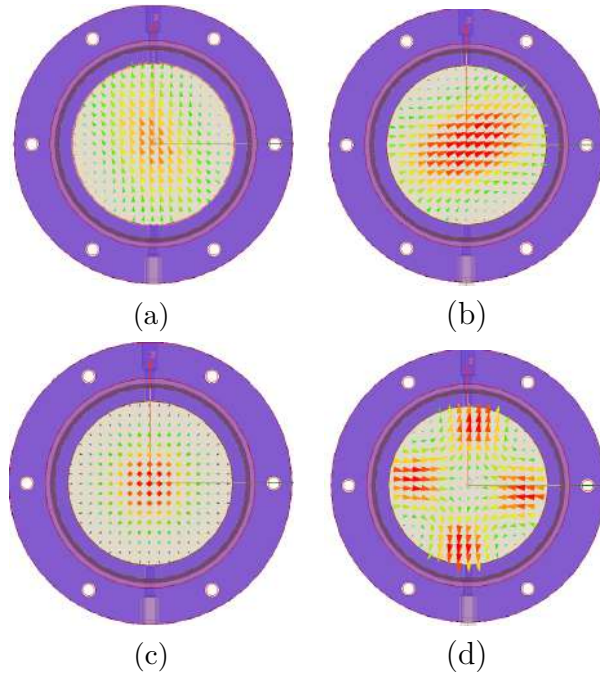
Figure 3.28: Front view of the discharge chamber exit plane showing the Electric field pattern at the wave-port for modes 1-4 corresponding respectively to (a-b) TE_{11} mode, (c) TM_{01}, (d) TE_{21}. Simulation performed with Ansys HFSS.

For case A, only one wave port is active. In this simulation, for the far-field, an additional "radiation boundary" is used on the domain surfaces. To ensure minimal MW reflection at these boundaries and prevent spurious results, the simulation domain has been extended up to a minimum distance of $\lambda/4$ from the source (where λ is the wavelength in vacuum at 5.8 GHz). Note that the results presented here will only provide a representation close to reality if plasma is not present within the discharge chamber. In fact, the presence of plasma will completely alter the impedance of the PC.

For case B, since the discharge chamber + plasma impedance is not known a priori, to keep the simulation as generic as possible, the PC has not been included in the simulation. Thus, the S parameter of the system is characterized as a two-port network, (visible in pink in figure 3.27b), each one at the one extremity of the circular waveguides. This situation corresponds to the case of a perfectly matched PC attached to one of the two wave ports (all the incoming MW power is absorbed by the plasma). The waveguide diameter used is D_{WG} = 36 mm as discussed in Section 3.2.

Being the problem linear with power, 1 W is chosen as the input reference power at the excitation wave-port for both cases A and B.

3.7.2 Case A: Discharge chamber radiated power

The simulations for case A aim to identify how much power is radiated from the discharge chamber when no plasma is present within the PC. In fact, in this condition, the amount of MW power radiated depends only on the geometry and materials of the PC. This situation can occur before ignition and may represent a safety concern.

As discussed in Section 3.7.1 a radiation BC and a single excitation wave-port are used. An example of the electric field produced in this situation is given in figure 3.29
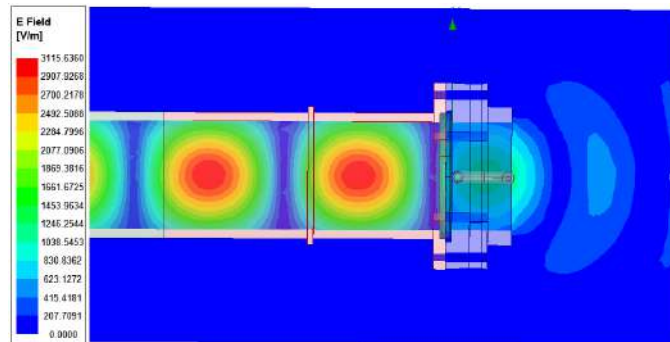
Figure 3.29: Plot of the electric field @ 5.8 GHz propagating in the PC. Microwaves can be observed radiating from the exit plane.

At 5.8 GHz, the obtained reflection coefficient for the main mode is $\Gamma = 0.77$ meaning that the reflected power at the wave port is $\Gamma^2 = 0.59$. Thus, 59 % of the power is reflected, and 41% of microwave power is radiated or absorbed by the quartz backplate. The latter represents a very small amount ($< 0.1\%$).

This suggests that the vacuum chamber observation flanges must be protected with metallic grids to prevent microwave radiation outside of the vacuum chamber. This is especially true during thruster ignition since there is no plasma to absorb the radiated power.

3.7.3 Case B: DC-block radiated power

The DC-block is a waveguide component necessary to permit the microwaves to propagate from the transmission line to the discharge chamber, without a direct electrical connection. This ensures that the PC can stay electrically floating during thruster operation, that the plume is quasi-neutral, and no net current leaving the thruster. In this context, the DC-block is simply made out of two aligned circular waveguide segments, with a vacuum gap in between ensuring the electrical insulation. If the gap is sufficiently small, the microwave-radiated power from the gap can be considered negligible. This solution has been implemented successfully in [54]. The design of the DC-block is further discussed in Section 3.6

The radiated power can be directly computed from HFSS as an output parameter. The distance between the two waveguides δ_{DC} has been swept between 0 mm and 10 mm. As can be seen in figure 3.30a the P_{rad} is very low, corresponding to less than 2% if $\delta_{DC} < 3$mm, confirming that no significant power is lost in this kind of waveguide DC gap configuration. In figure 3.30b a plot of the electric field is available. A reacting electric field is being created at the boundaries of the waveguides, thus not being radiated.

(a)   (b)
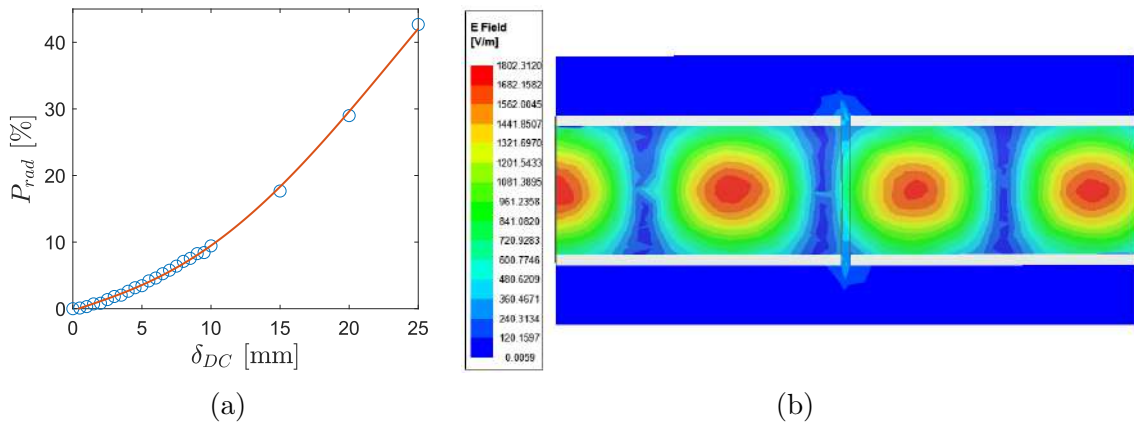
Figure 3.30: (a) Percentage of radiated power to input power from the gap between the two waveguides as a function of the distance between the waveguides. (b) Electric field pattern for mode 1 excitation in the DC-block.

3.8 Summary

In this chapter, the design of the breadboard thruster model used for the successive experimental campaigns is presented. This prototype is designed to be a versatile experimental platform for exploring the mechanisms that cause losses in waveguide ECRTs, ultimately aiding in the optimization of their operation. Firstly, the sizing of the prototype has been discussed, the higher chosen frequency (5.8 GHz) range allowed us to achieve a compact design appropriate for the low target power. This also raises the field requirements for the ECR to 0.2 T if compared to the classical 2.45 GHz (0.0875 T). The resulting thruster dimensions are D_T = 36 mm, L_T = 20 mm. The thruster is expected to be operated at a mass flow rate lower than 0.4 mg/s and power between 80 – 400 W. The total weight of the thruster head, including the permanent magnet and electromagnet, is about 9.6 kg.

The thruster head design clearly separates the magnetic field generator assembly from the discharge chamber. This design facilitates assembling and component substitution. The PC can be equipped with different propellant injectors (two and 12 radial injector holes) and different lengths of the discharge chamber walls. On the other hand, the magnetic field generator is divided into a permanent magnet and an electromagnet to be able to fine-tune the magnetic nozzle divergence and resonance position. The transmission line components have also been presented highlighting their specifications and role in the assembly.

Finally, thermal analysis and electromagnetic wave propagation simulations were conducted to refine the design and verify its functionality prior to the experimental phase.

Chapter 4

ECRT Discharge simulations [1]

> *"Space is to place as eternity is to time."*
>
> - Joseph Joubert

In this chapter, the discharge produced by an ECR thruster with dimensions as described in Chapter 3 is simulated using a quasi-neutral 2D axisymmetric hybrid PIC-fluid code. The simulated region includes the plasma discharge chamber and the near-plume region. The ECR region is modeled as a heating term in the energy equation for the electron fluid using two different power absorption maps. The main trends in the plasma discharge are evaluated, and the results presented in terms of 2D maps of the relevant quantities in the discharge. A parametric study on the propellant mass flow rate and deposited power is performed for one of the two power absorption maps.

The structure of this Chapter is as follows. Section 4.1 provides an introduction to the topic. Section 4.2 details the numerical model and defines the employed power absorption profiles. Section 4.3 presents the findings of the study. Finally, Section 4.4 summarizes the work done and offers concluding remarks.

4.1 Introduction

During the design process of an electric thruster, plasma discharge simulations can come in useful to enhance our comprehension of loss mechanisms and possibly suggest design improvements: simulations offer the potential to access information on

---

[1]This chapter reproduces with adaptations the conference paper: M. R. Inchingolo, J. Navarro-Cavallé, and M. Merino "Hybrid PIC-Fluid Simulation of a Waveguide ECR Magnetic Nozzle Plasma Thruster", Space Propulsion Conference (SPC), 2021 [65].

plasma quantities that are experimentally challenging to obtain or inaccessible, conversely, experiments provide the data required to corroborate and validate these simulations. Different quasi-1D models were proposed in the past [19, 105, 106] obtaining in some cases good estimations of the thruster performance [106]. At EP2-UC3M, an axisymmetric full-wave 2D code (HYPHEN-ECRT/SURFET) [107, 56] has been used in the frame of the MINOTOR project [108], to simulate the discharge of the ECRT developed at ONERA and improve its current physical understanding.

Nevertheless, the circular waveguide thruster concept has not yet been explored by a 2D model. This chapter aims to address this aspect by simulating the EP2 ECRT prototype using the HYPHEN simulation platform. The lack of implementation of the $m = \pm 1$ wave propagation mode in a circular waveguide, for the current HYPHEN version, has been mitigated by prescribing the power deposition profile near the ECR region. This approach, while not self-consistent, provides a preliminary understanding of the discharge physics of the new ECRT prototype. In particular, this study tries to assess to what extent the power deposition profile, and the operating point affect the thrust and plasma transport variables in the magnetic nozzle and what are the thruster performances to be expected in the upcoming experiments.

4.2   ECRT model and simulation setup

The model used to assess the expected key aspects of the plasma transport as well as the propulsive performances of this ECRT prototype, is a two-dimensional axisymmetric hybrid PIC-fluid code [109, 110, 111] based on previous plasma simulating platforms being developed within the EP2 team [112, 113]. In this code, heavy particles (neutrals and ions) are modeled with a particle-in-cell kinetic model, whereas the electrons are treated as an anisotropic fluid. Because of the different models used for the two species, it is numerically convenient to operate on different types of spatial meshes [110, 114] and interpolate between them when required. A structured mesh is used for heavy species (PIC-mesh) and a non-structured magnetic field aligned mesh for the electrons (MFAM-mesh). Further details can be found in [109, 110, 115].

The basic simulation loop proceeds as follows. The PIC module takes as inputs the electric potential ϕ, the electron temperature T_e, and the electron current density $\mathbf{j_e}$, following a PIC scheme, these are used to propagate in time the trajectory of the heavy species and obtain the particle densities and fluxes, which in turn are the input for the electron fluid module. Here, imposing plasma quasi-neutrality, the continuity, momentum, and energy equations are solved for the electron-fluid, obtaining $\mathbf{j_e}$, ϕ and T_e for the new time-step, thus closing the loop. Furthermore, in

the electron-fluid loop, the conditions at the plasma sheath (boundaries of the quasi-neutral domain) are calculated with a dedicated sheath sub-module [116, 110]. The sheath module includes a specific set of modeling parameters for SEE and electron fluxes, in this work those of BN will be used. Further information about the sheath module and how SEE is modeled can be found in reference [116, 110].

Anomalous cross-field turbulent transport is instead modeled as a set of three empirical parameters in the momentum α_{tm}, energy α_{te} and heat flux α_{tq} equations of the fluid model. The settings here used, consider all the three parameters as equal to $\alpha_{tm} = \alpha_{te} = \alpha_{tq} = 0.02$. More information on this empirical model can be found in [109, 117].

The code allows the selection of boundary conditions, domain geometries, collision types (excitation, primary and secondary ionization, recombination, etc.), material surfaces, and injection characteristics. The flexibility of this code makes it possible to simulate several different thrusters, such as Hall Effect Thrusters (HET) [109], Helicon Plasma thrusters (HPT) [118], coaxial ECRT thruster [56] or the waveguide ECRT object of this thesis.

The working principle of an ECRT is based on the efficient microwave power absorption at the electron cyclotron resonance location. In this context, power absorption is modeled in the HYPHEN electron fluid module as an additional term Q_a in the electron internal energy equation (eq. 4.1).

$$
\begin{aligned}
\frac{\partial}{\partial t}\left(\frac{3}{2}n_e T_e\right) + \nabla \cdot \left(\frac{5}{2}n_e T_e \mathbf{u_e} + \mathbf{q_e}\right) = \mathbf{u_e} \cdot \nabla p_e + \\
+ \sigma_e^{-1}\mathbf{j_e} \cdot (\mathbf{j_e} + \mathbf{j_c}) + Q_e + Q_a
\end{aligned}
\tag{4.1}
$$

Where n_e, T_e, $\mathbf{u_e}$, p_e, $\mathbf{j_e}$ are respectively the electron density, the isotropic electron temperature, the electron fluid velocity, the electron pressure and the electron current density, while $\mathbf{q_e}$ is the electron heat flux [109]. The electron parallel conductivity is defined as $\sigma_e = n_e e^2/(m_e \nu_e)$ with m_e and ν_e the electron mass and electron collision frequency respectively, $\mathbf{j_c}$ is a source term computed in the PIC module that takes into account the effect of electron collisions with the heavy species [109]. Concerning the terms Q_e and Q_a, the first represents the energy sink due to the ionization and excitation collisions, the latter, as mentioned, models the plasma-microwave absorption.

To determine the Q_a profile a wave module should be used, which would model the microwave propagation into the plasma by solving the Maxwell equations. This capability for a mode different than TEM ($m = 0$) [107, 56], such as the one propagating in a circular waveguide ($m = \pm 1$), is not yet implemented in this code and will be subject of future work. For this reason, the Q_a spatial profile will be here assumed as described in Section 4.2.1.

Figure 4.1a describes the axisymmetric plasma domain used for all the simulations analyzed in this study. The domain is divided into two regions, the plasma source and the plasma plume region. The plasma source region has dimensions of $R_T = 18$ mm and $L_T = 20$ mm, whereas the plasma plume domain extends from $z = L_T$ to $z = L_D = 108$ mm and has an outer radius of $R_D = 54$ mm. The injection is represented by a ring of injection surfaces positioned at $r = 18$ mm, $z = 2$ mm, with 2 mm width, and the reference for the potential ϕ is positioned in a region with low numerical noise inside the plasma source.

The boundary surfaces of the simulations shown here are of three types: Axisymmetric (B1), Dielectric (B2), and Free Loss (B3). The B1 boundary consists of axisymmetric boundary conditions. B2 corresponds to the local zero-current condition $\mathbf{j_e} \cdot \mathbf{1_n} = -\mathbf{j_i} \cdot \mathbf{1_n}$, ion recombination, neutrals diffused reflection and $\mathbf{q_e} \cdot \mathbf{1_n}$ provided by the sheath module. On the free loss (B3) surfaces $\mathbf{j_e} \cdot \mathbf{1_n} = -\mathbf{j_i} \cdot \mathbf{1_n}$ and $\mathbf{q_e} \cdot \mathbf{1_n} = 2 T_e n_e \mathbf{u_e} \cdot \mathbf{1_n}$, furthermore, the PIC macro-particles are removed from the simulation. These boundary conditions, make the external boundary locally current-free. On a side note, even though the prototype described in Chapter 3 is equipped with metallic lateral walls, the lack of implementation of metallic boundary conditions at the time of this study, dictated the use of a dielectric boundary condition. Specifically, the properties of Boron-Nitride were used for the B2 surfaces.

The results shown here are obtained simulating neutral xenon atoms, singly- and doubly-ionized ions, thus they also include the effect of inelastic collisions such as single ionization, double ionization, and excitation [109].

Figure 4.1 shows the MFAM and PIC meshes used in the following sections. The MFAM mesh has been constructed with the iso-potential lines and streamlines of the magnetic field and counts of about 1900 cells compared to the 2300 of the structured PIC mesh. The typical cell size for both meshes is between 0.3 mm^2 and 10 mm^2. A simulation of $t_{sim} = 5 \cdot 10^{-4}$ s of an ECR thruster with the above-described settings, using a simulation time-step $dt = 2 \cdot 10^{-8}$ s, takes about 9 hours to run on a workstation with ten cores of an Intel Xeon 6230 processor.

The range of applied power and mass flow rate explored in these simulations spans $P_a = 100 - 300$ W and $\dot{m}_p = 1 - 3$ mg/s. As seen in Chapter 3, this mass flow rate range is about ten times larger than the design point. This choice was constrained by the code's inability to generate stable solutions for lower values of $\dot{m}_p$, future implementations will address this limitation. Nevertheless, as we will see in Chapter 5, this range of operational parameters has also been explored experimentally.

4.2.1 Power absorption profiles

Figures 4.2a and 4.2b show the two power deposition profiles used in this work which will be here called "Profile A" and "Profile B" respectively. Both profiles
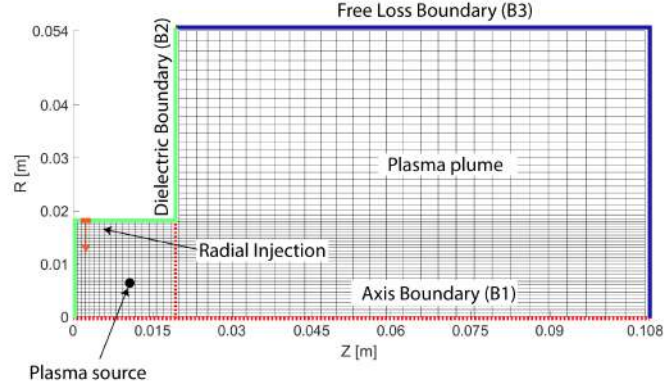
(a)
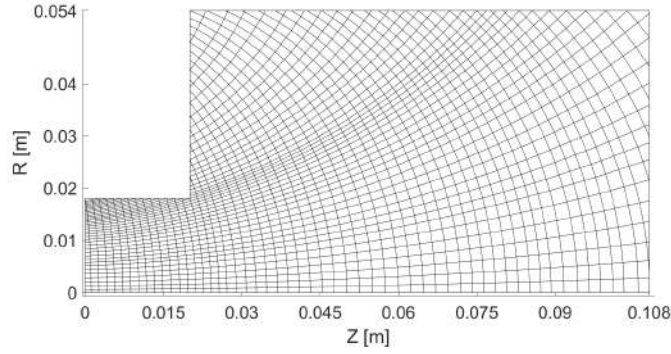
(b)

Figure 4.1: (a) PIC mesh and domain boundaries representation, (b) Magnetic field aligned mesh (MFAM).

are centered along the constant magnetic field surface at $B_{ECR} = 0.2$ T and have a thickness of $\Delta B = \pm 0.01$ T.

The power absorbed by the plasma is expected to be proportional to the square of the electric field magnitude in the wave [71, 56]. However, modeling the microwave propagation in the plasma would require a wave module, thus to simplify the problem, the electric field distribution in a circular waveguide in a vacuum was used to scale the power deposition profile A.

In this geometry, the dominant mode is the transverse electric mode TE_{11}, which produces a non-axisymmetric electric field. In order to use it as a scale rule, it has been averaged azimuthally, and normalized. Following this procedure figure 4.2a was obtained. The region here shown is the full volume of the plasma source, whereas, in the rest of the domain, no power is deposited. Profile A is used in this study for the nominal simulation scenario.

To compare and study the sensitivity to the absorption profile, a second power deposition profile (profile B) was assumed. Figure 4.2b shows a constant volumetric power absorption along the magnetic field surface centered in B_{ECR}, with a thickness of $\delta_{ECR} \approx 5$ mm.
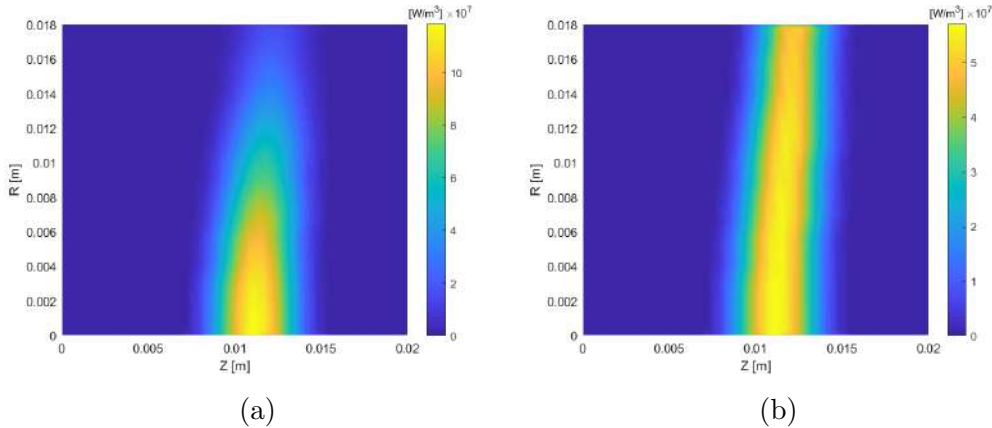
Figure 4.2: Thruster chamber region with Gaussian smoothed power deposition profiles Q_a for a total deposited power of $P_a = 200$ W. (a) Power deposition profile A. (b) Power deposition profile B .

While the self-consistent Q_a profile requires solving the EM field, previous simulations of ECRT thruster suggest that a profile like A or B represents approximately the main characteristics of the absorption profile in the whole simulation domain [56]. Thus by studying these, we expect to understand the main aspects of the plasma transport and to be able to assess the influence of the Q_a profile as it will be shown in Section 4.3.2. As stated above, future work will revisit this assumption and compute the absorption profile with a full wave, non-axisymmetric code.

4.3   Results and Discussion

In Section 4.3.1 the main plasma transport features are first analyzed for the nominal power deposition profile (Profile A) described in Section 4.2.1, whereas the effects and the main differences induced by using profile B are discussed in Section 4.3.2. For both cases, the working point $P = 200$ W and $\dot{m}_p = 2.5$ mg/s, and the same magnetic topology is chosen. Then a parametric analysis of power and mass flow rates is carried out only for the nominal profile A in Section 4.3.3 where power and mass flow rates are varied in a set of 10 simulations.

All the plasma transport 2D maps here discussed are those obtained at steady state conditions, which is reached after $t_{ss} = 0.4$ ms (being $t = 0$ ms the time at which the fluid-pic models start to being solved together). The depicted plots correspond to averaged quantities for a time period of 0.125 ms. Furthermore, to alleviate boundary effects, the simulation domain has been cropped and only the region up to $z = 0.08$ m and $r = 0.035$ m is kept in this work.

4.3.1 Discharge physics

Referring to figure 4.2a, the main effect of concentrating the electron heating region towards the axis is an increased electron temperature in that region, which then tends to spread along the affected magnetic field lines. This spread happens because of the very high electron mobility in the parallel direction and is well visible in figure 4.3a. Going towards higher radii, T_e decreases because of the reduced power deposited, limited electron mobility in the perpendicular direction, and higher collision rates due to the higher density of heavy particles (figure 4.3b and 4.3c).

The plasma density profile (see figure 4.3c) is influenced by the electron temperature T_e, the plasma potential ϕ (figure 4.3d) and the neutral density. Starting from the axis, the density increases radially up to a maximum of 10^{19} m^{-3} because of the increased neutral density (being the injection closer) and moderately high T_e, then decreases again in the proximity of the wall due to recombination, as shown in figure 4.3b.

As a consequence of the electron temperature and density behavior, the electron pressure $P_e = n_e T_e$, shows a peak at an intermediate radius of the plasma source region which then elongates towards the plume.

Electron pressure on the backplate as well as the ion momentum flux on the thruster walls along the z direction are responsible for the pressure thrust at the thruster walls, here defined as in equation 4.2.

$$F_p = \sum_s \int_{\partial\Omega_w} (n_s T_s \mathbf{1}_z \cdot \mathbf{1}_n + m_s n_s u_{zs} \mathbf{u}_s \cdot \mathbf{1}_n)\, \mathrm{d}S \qquad (4.2)$$

Where the subscripts "s" refer to the heavy species. $\partial\Omega_w$ is the thruster wall surface and m_s is the heavy species particle mass.

In figure 4.3g the plasma pressure can be visualized as well as its gradient, where the latter presents a dominant radial component in the overall domain. This component plays a fundamental role in the electron perpendicular momentum balance, which in turn, defines the electron azimuthal current density $j_{\theta e}$, which can be approximated as in equation 4.3:

$$j_{\theta e} \approx \frac{\chi}{1+\chi^2}\mu_e\left(\frac{\partial p_e}{\partial 1_\top} - en_e\frac{\partial\phi}{\partial 1_\top}\right) \qquad (4.3)$$

where $\mu_e = e/(m_e\nu_e) = \sigma_e/(n_e e)$ is the electron parallel mobility, $\chi = \omega_{ce}/\nu_e = \mu_e B$ is the Hall parameter, and where the collisions term $j_{\theta c}$ and $j_{\theta i}$ have been neglected being their contribution small.

Referring to equation 4.3, being the perpendicular electric field small, $j_{\theta e}$ will be mainly dictated by the perpendicular pressure gradient. This is well visible in figure 4.3f which represents the $j_{\theta e}$ contributions to the magnetic force per electron.

Here two regions can be distinguished, identified by the change in sign of $j_{\theta e}$ and consequently in the direction of the magnetic force. One produces a positive magnetic force along z (thrust), and the other produces a negative one (drag). The latter being at smaller radii also represents a smaller volume and, thus has a less important role. The integral in the full domain of the magnetic force will give the magnetic thrust as in equation 4.4.

$$F_m \approx \int_V -j_{\theta e} B_r dV \tag{4.4}$$

Where $j_\theta \approx j_{\theta e}$ since the ion azimuthal current density $j_{\theta i}$ contribution results to be negligible. Thus, the total Force F exerted on the thruster will be given by the sum of the pressure and magnetic thrust: $F = F_p + F_m$.

Finally, the electric force balances both the magnetic force and the pressure gradient and is essentially the only force balancing the pressure gradient in the parallel direction. The potential (figure 4.3d) features a maximum inside the plasma source on the axis, and then it slowly decreases as the electrons expand in the magnetic nozzle, giving rise to the ion acceleration. We observe a second increasing potential region in the top left corner as a peak of around 15V. The creation of this high potential region is probably to be attributed to the vicinity of the boundary conditions, which create a magnetically shielded region in this corner, and the quasi-neutrality of the model. Close to the thruster exit plane, the electrons are still strongly magnetized, thus it is difficult for them to access the top left corner region, limiting the plasma density. To keep quasi-neutrality, being the ions not constrained by magnetic field lines, a potential must rise to prevent them from reaching this region. Notwithstanding this, some experimental evidence exists that the electric potential may not decay monotonically in the transverse direction of a magnetic nozzle [119, 120], which could be explained by a non-zero ion thermal energy [121]. Further research will analyze this aspect of the simulation in detail.

4.3.2 Effect of the Q_a profile

The majority of the considerations discussed in Section 4.3.1 are still applicable for the power deposition profile B, with some differences.

The immediate effect of introducing a different Q_a profile is to produce a change in the electron temperature distribution, this is visible in figure 4.3h. For this case, the electron temperature spreads uniformly across the domain keeping a value between $3.4 - 5$ eV, and a low gradient pointing towards higher radii.

This fact radically changes the plasma density distribution and consequently the electron pressure gradient (refer to figures 4.3j and 4.3n), in particular, the plasma density appears to be more uniform in the plasma source and the peak density is

positioned at $R = 0$ mm. The electron pressure, in contrast with what was found for profile A, is now smoother and finds its maximum at the axis of symmetry. This creates a pressure gradient term $\partial p_e/\partial 1_\top$ that always points in the outward direction, thus also $j_{\theta e}$ does not change its sign (refer to figure 4.3m). On the contrary, three drag regions are present in the plasma plume. These again seem to be mainly due to the behavior of the pressure gradient in the corresponding regions, but it is not clear whether these are due to numerical noise or an actual phenomenon.

Finally, also the j_i current follows a different behavior (figure 4.3l) in contrast with the nominal case, with ion streamlines that feature a larger curvature in the outward direction. This, as visible in figure 4.3k, is probably due to the missing high radial component of the electric field in the plasma source whereas a stronger radial component exists close to the exit plane. Instead for both Q_a profiles, because of the low magnetic field divergence, the ion streamlines appear to be still closely following the magnetic field lines in the far plume.

This analysis suggests that the temperature gradient and distribution may have an important role in the plasma expansion along a magnetic nozzle. Further analysis in this aspect will be presented in a future work.

Lastly, in tab. 4.3.2 can be found as a summary of the thruster performances obtained for the two Q_a profiles.

	Q_a profile A	Q_a profile B
F	11.6 mN	9.5 mN
F_m	51.7%	46.6%
F_p	48.3%	53.4%
η_d	93.3%	87.4%
η_u	86.5%	80.5%
η_p	48.9%	43.4%
η_e	29.5%	22%
η_c	46.6%	50.6%
η_F	13.6%	9.1%

Where F_m and F_p are expressed as percentages of the total thrust F.

Concerning the efficiencies they are defined as follows. The divergence efficiency is the ratio of ion kinetic power in the z direction by the total ion kinetic power $\eta_d = P_{zi\infty}/P_{i\infty}$, the subscript ∞ refers to the free loss boundaries. $\eta_u = \dot{m}_{i\infty}/\dot{m}_p$ is the utilization efficiency. $\eta_p = I_\infty/I_{bound}$ is the production efficiency, defined as the ratio between the ion current to the free loss boundaries (I_∞) and the total ion current to all the boundaries (I_{bound}). $\eta_e = P_{p\infty}/P_a$ is the energy efficiency which is the ratio between the plume power at the free loss boundaries (thermal and kinetic power) divided by the deposited power. The conversion fraction is instead $\eta_c = P_{i\infty}/P_{p\infty}$, and finally, $\eta_F = F^2/(2\dot{m}_p P_a) \approx \eta_u \eta_e \eta_c \eta_d$ is the typical thrust efficiency. Note that

the definition of the partial efficiencies here presented may be slightly different from the ones used in the next Chapters about the experimental activities.

From table 4.3.2, it appears that while the percentage of magnetic thrust and pressure thrust over the total thrust, accounts for both cases about **50%**, the performance of the thruster obtained with profile A are better than the other case for each of the specified indicators but the conversion fraction.

The lower divergence efficiency of profile B can be attributed to the high radial electric field at the exit plane, which in turn is a consequence of the less localized power deposition at the axis. Whereas as appears from figure 4.3i, the lower T_e causes the neutrals to extend further and with higher density in the plume, resulting also in a lower η_u.

On the other side, because of the high electron temperature in the plume of profile A and since the electron thermal power represents the majority of the beam power (see figure 4.5b), the energy efficiency results to be higher for this case, with the drawback of having a lower conversion fraction.

Power Deposition Profile A   Power deposition profile B

(a)   (h)

(b)   (i)

(c)   (j)

(d)   (k)

(e)   (l)

(f)   (m)

(g)   (n)
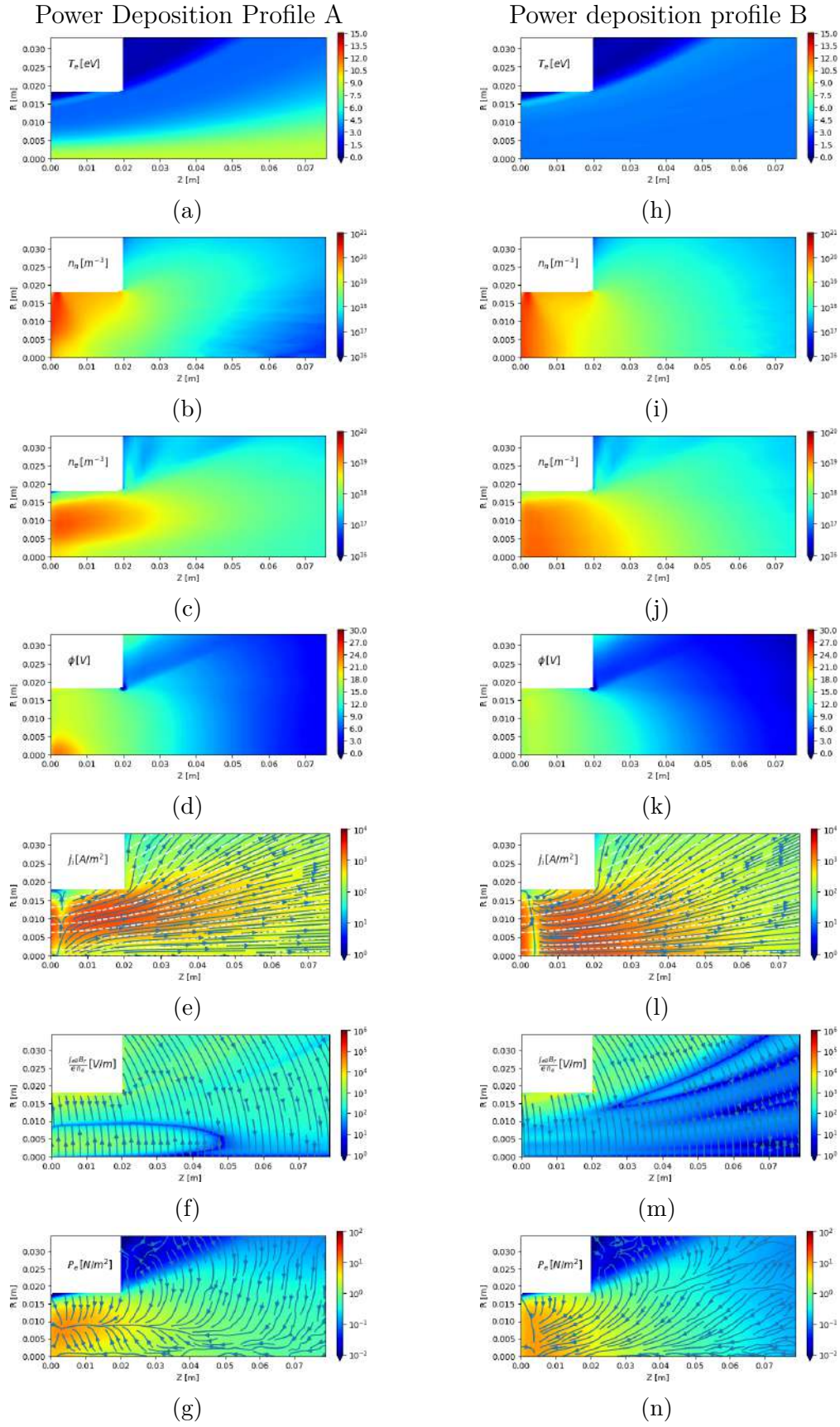
Figure 4.3: Comparison of the main transport parameters for the two power deposition profiles. Left: power deposition profile A. Right: power deposition profile B.
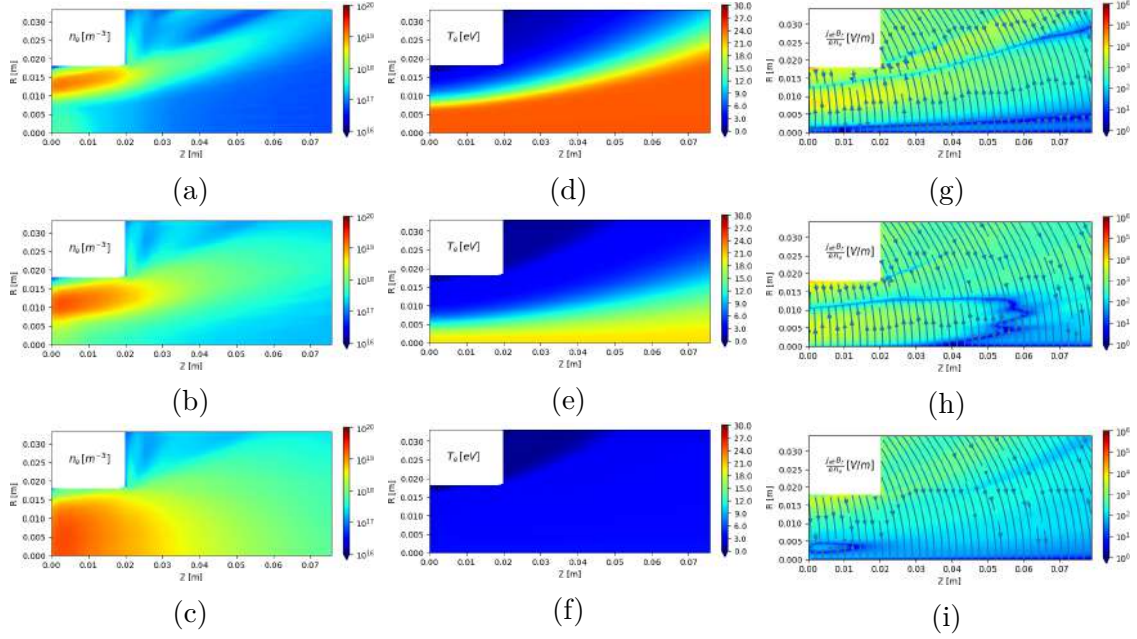
Figure 4.4: Plasma density n_e (a-b-c), electron temperature T_e (d-e-f) and magnetic force per electron (g-h-i) profiles, obtained at $P_a = 200$ W for mass flow rates of $\dot{m}_p = 1$ mg/s, $\dot{m}_p = 2$ mg/s and $\dot{m}_p = 3$ mg/s respectively.

4.3.3 Parametric analysis

The effects on the plasma transport due to the variations of the mass flow rate at a fixed coupled power (200 W) are now analyzed for the nominal power deposition profile A.

Figure 4.4-(a, c) shows the behavior of the plasma density when the propellant mass flow rate is varied between $\dot{m}_p = 1 - 3$ mg/s of Xenon. Similarly to what was seen in Section 4.3.1 the density and the electron temperature are strictly correlated. This is particularly visible in figure 4.4a and 4.4d where the high-density region is compressed towards large radii, implying an increase of electron temperature for smaller radii. For all the working points analyzed in this study, the electron temperature peak ranges between $4.5 - 25$ eV, resulting in line with what is found experimentally for other ECR thrusters in similar working points [19, 122].

Being the mass flow rate low and the injection radial, and given the large electron temperature, the majority of the neutrals are ionized before reaching the region close to the axis, for this reason, increasing $\dot{m}_p$ leads to a larger high-density region, for which the peak reaches the axis at $\dot{m}_p = 3$ mg/s as for the power deposition case B.

Interesting is the behavior of $j_{\theta e}$ in response to $\dot{m}_p$ changes, which as discussed in Section 4.3.2, is correlated with the density and temperature profiles. Referring to figure 4.4-(g, i), this becomes evident at low $\dot{m}_p$, the region contributing negatively to

the thrust expands into the plume because of the strong pressure gradient extending towards higher z. The opposite situation is found at $\dot{m}_p = 3$ mg/s, the negative thrust region almost disappears, thanks to the pressure forming a single axial peak with lower gradients, which in turn also leads to a lower $j_{\theta e}$ in the plume.

Although it is possible that in a self-consistent model, the microwave accessibility to the plasma (and thus the power deposition pattern) is altered by the change in mass flow rate, affecting globally the discharge characteristics, we see that very similar profiles to the ones found above can be obtained when the power is decreased from $P_a = 300 - 100$ W keeping a fixed mass flow rate of $\dot{m}_p = 2$ mg/s. These two control parameters play an approximately opposite role. In fact, the main parameter which determines the thruster performances is the power to mass flow rate ratio, which can be expressed as energy per injected particle:

$$E_p = \frac{P_a m_{Xe}}{\dot{m}_p e} \quad \text{[eV/particle]} \tag{4.5}$$

Where m_{Xe} is the Xenon molecular mass in kg and e is the electron charge. In figures 4.5a-(a, b, c, d) are shown the typical performance indicators plotted against the energy per particle E_p. It appears that, apart from outliers, the expected performances for a given E_p can be estimated directly from these plots without the need for new simulations.

Referring to figure 4.5a, the thrust efficiency η_F results to be mainly influenced by the effect of η_u, which decreases fast at low energy per particle, dropping from 0.9 to 0.6. This is an expected result since if more propellant is injected without increasing in turn the power, the lower is going to be the propellant utilization.

The divergence efficiency η_d, on the other hand, results to be very high in the whole range, staying between 80% and 90%, this is due to the characteristic shape of the ion streamlines seen in figure 4.3e, whereas the fact that it decreases at high energy per particle can be explained by the density profile seen in figure 4.4a, where the majority of the density and thus ion current is concentrated at high radii where the beam divergence is higher. Concerning the production efficiency η_p, it can vary between approximately 40% and 50%, its increase at low deposited power is due to the decreased ion current going to the walls as visible from figure 4.5b. As E_p is increased, more power is lost to the walls as the plasma moves to higher radii. Furthermore, it is found that the major cause of energy losses is represented by collisions and in particular excitation collisions. This happens especially at low levels of E_p where they can represent up to 60% of the input power.

Interestingly, the low conversion fraction η_c indicates that the expansion in the magnetic nozzle is far from over in the domain used in the present simulations. As the expansion continues farther downstream, it is expected that additional magnetic thrust, I_{sp}, and efficiency will be generated and a higher conversion fraction will be
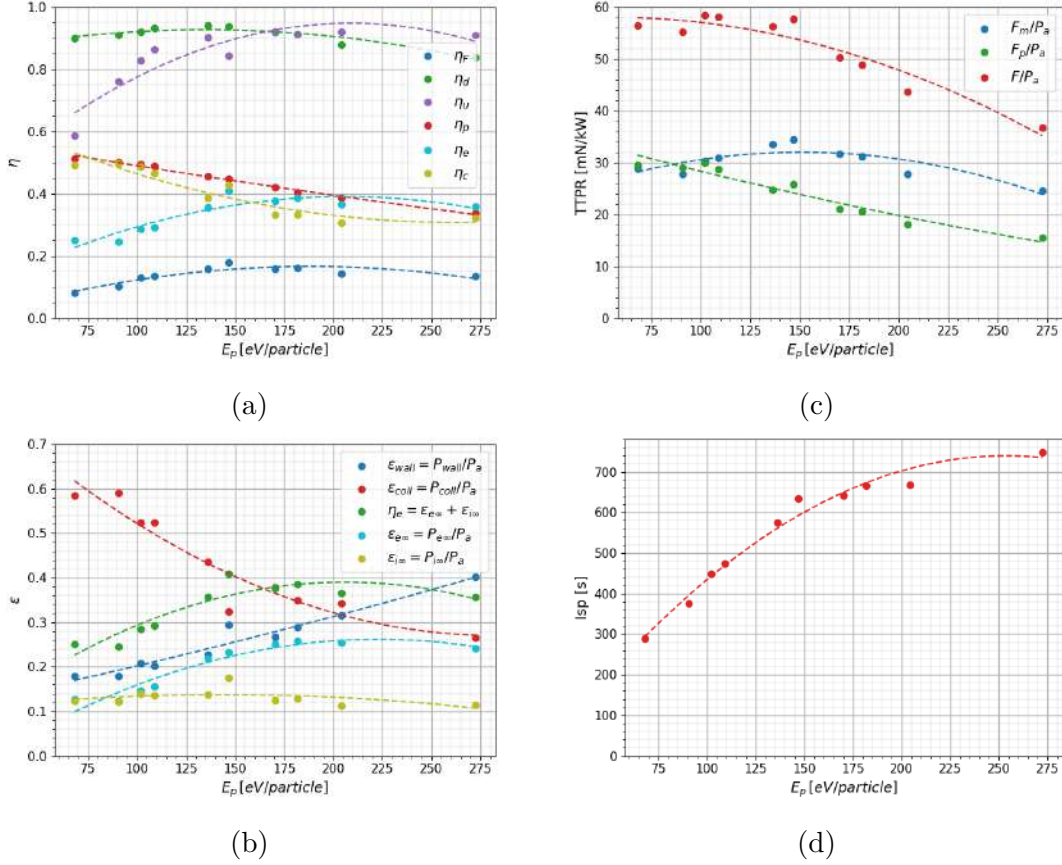
Figure 4.5: Primary performance indicators varying with the energy per particle E_p: Efficiencies (a), normalized losses and powers (b), Thrust to power ratios (TTPR) for magnetic and pressure thrust (c), Specific impulse (I_{sp}) (d).

reached. This seems to be more relevant the higher E_p, as shown in figure 4.6. This behavior is typical of magnetic nozzle thrusters, in fact as evidenced by experimental results, the ions are found to be still accelerating even at a distance of 200 mm from the thruster exit plane [123, 79]. as also found for the thruster object of this thesis (LIF measurements in Chapter 7).

Figure 4.5c shows the TTPR (Thrust To Power Ratio) with respect to the energy per particle. We see that at a fixed power, the total thrust decreases with the increase of energy per particle (decrease of mass flow rate). It appears also that the main contribution to the decrease is given by the faster decrease of pressure thrust. While the magnetic thrust initially increases with E_p in the range explored, the decrease of the magnetic thrust at higher E_p values could be explained by the larger negative thrust region seen in figure 4.4g. Furthermore, the percentage of magnetic thrust to the total power can change at different working points, varying from 67% to 48%, values that are in line with the 60% found by ONERA in the coaxial ECRT measurements [40].

Finally, from figures 4.5a-(a, c) different optimal operation points can be identi-

fied. If the maximum thrust efficiency is required, the energy per particle should be positioned between $E_p = 150 - 200$ eV/particle, where a $\eta_F \approx 17\%$ can be obtained. Although a clear maximum is not yet reached in the total thrust in figure 4.5c, it is expected that for a fixed P_a, a sufficiently large increase of $\dot{m}_p$ will eventually lead to a drop in T_e and a decrease in thrust. Thus if a higher thrust is requested, the mass flow rate should be increased up to reaching a $E_p = 75 - 125$ eV/particle. The opposite happens for the specific impulse where the optimum should be positioned in the vicinity of $E_p = 275$ eV/particle.
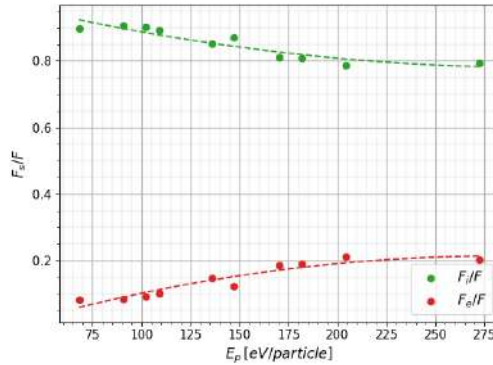
Figure 4.6: Electrons and ions contributions to thrust calculated at the free loss boundaries.

4.4   Summary

A Hybrid PIC-fluid model of the axisymmetric plasma discharge developed in an ECR circular waveguide thruster was used to simulate the novel ECRT developed in the frame of this thesis. This analysis identified the patterns of the main plasma transport quantities for two different power deposition profiles, and how these and the expected thruster performance change with the propellant mass flow rate and deposited power.

The results point out how the proposed power deposition maps strongly affect the electron temperature profile, leading to global changes in density, pressure, and potential distribution in the plasma source, consequently affecting the overall plasma discharge.

The electron temperature presents two different trends: a high peak on the axis of symmetry with a strong radial gradient or a peak in the proximity of the thruster walls with an almost homogeneous but lower temperature in the bulk plasma. The effects are visible in the main terms of the momentum equation namely the magnetic force and pressure gradient. The electron pressure can extend axially or radially, altering the magnitude and direction of $j_{\theta e}$. The magnetic force on the electrons varies accordingly and can present a region of negative contribution to thrust de-

pending on the pressure gradient direction relative to the magnetic field lines. The resulting potential alters the shape of the ion streamlines allowing them to cross the magnetic field lines from the top or bottom.

The parametric analysis has shown that the main driving parameter is the energy per particle. It was seen that, when this figure is increased, the negative electron magnetic thrust density region grows and that the plasma is pushed towards higher radii. Furthermore, the main expected trends in the thruster figures of merit have been presented. Especially at low energies per particle a large part of the injected power is lost in collisions (up to 60%), and the fraction lost decreases with E_p. The loss to the walls follows the opposite trend and increases for high E_p as the plasma is pushed towards the walls. The large thermal electron power found suggests the need to increase the simulation domain size because of incomplete ion acceleration in the far plume, especially at high energy per particle levels.

As a consequence of the limitations of the model used in this work, discrepancies with the experimental data are expected and observed in the following chapters. However, the work presented here represents a preliminary step in the understanding of the physics behind the ECR circular waveguide thruster and serves to point out some of the limitations of the current model. In particular, it was shown the need for a wave module capable of simulating the $m = \pm 1$ mode in a cylindrical plasma domain, so that self-consistent simulations are obtained. Furthermore, other aspects of the physics, believed to be important, will need to be included in the model, such as an anisotropic electron temperature and the effect of the diamagnetic field associated with the $j_{\theta e}$ currents. These, together with an improved modeling of the far field boundary conditions are believed to be fundamental for an analysis closer to reality and will be the subject of future works.

Chapter 5

Plume Characterization [2]

"History proves abundantly that pure science, undertaken without regard to applications to human needs, is usually ultimately of direct benefit to mankind."

- Irving Langmuir

The thruster prototype described in Chapter 3 is here characterized for the first time via plume measurements. The dependence of the plume's current profile on the set parameters and a description of the plume expansion are presented. These parameters are: input MW power, mass flow rate, electromagnet current, and propellant injection scheme. To assess the properties of the generated plasma, a Langmuir probe and a Faraday cup are used to characterize the plume. Finally, these measurements are used to attain a qualitative indirect estimation of the performance metrics.

The rest of the chapter is organized as follows: Section 5.1 presents the experimental setup; In Section 5.2, first a discussion on the microwave reflection coefficient and thruster wall potential is presented (Section 5.2.1), then the plume expansion is discussed in Section 5.2.2. Based on these results, in Section 5.2.3, an estimation of the thruster propulsive performances is carried out. Finally, the conclusions are gathered in Section 5.3.

---

[2]This chapter reproduces with adaptations the journal paper: M. R. Inchingolo, M. Merino and J. Navarro-Cavallé, "Plume Characterization of a Waveguide ECR Thruster", Journal of Applied Physics, 2023 [66].
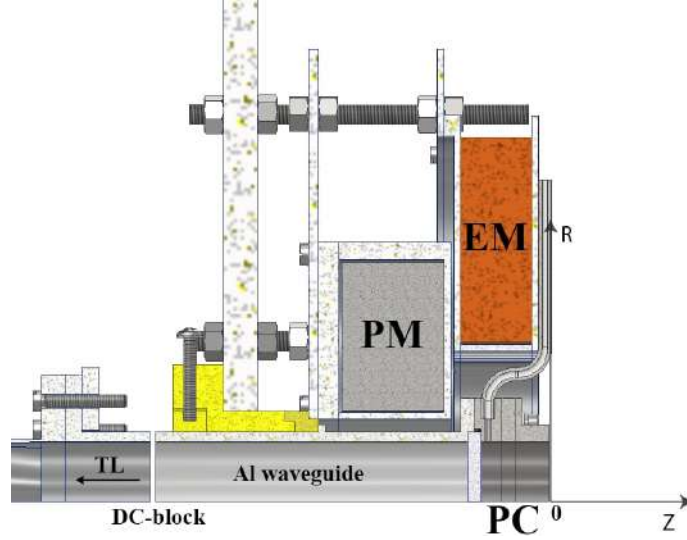
Figure 5.1: CAD section representation of the thruster assembly. The plasma discharge chamber (PC), the permanent magnet (PM) and the electromagnet (EM) are shown assembled on the mounting plate. The last segment (DC-block) of the transmission line (TL) is also shown.

5.1 Experimental Setup

The thruster design has been presented in Chapter 3, and the exit plane and centerline define the coordinate system as displayed in figure 5.1. In addition to the permanent magnet, the electromagnet is used. Its purpose is to displace the resonance position and alter the shape of the magnetic nozzle. The resonance can be displaced between $z = [-8.5, 1.5]$ mm when the electromagnet current I_c is increased from 0 to 50 Amps. $I_c = 40$ A corresponds to a resonance on the exit plane. The variation of resonance surface shape can be considered negligible for $I_c > 0$. For $I_c = 50$ A, the electromagnet provides a peak field along the thruster axis of 56 mT. For the experiments performed in this study the current was varied in the range $0 \le I_c \le 50$ A. Figure 5.2 shows the magnetic field streamlines for these two extreme situations.

The propellant (Xe) is fed into the thruster chamber through two independent orifices drilled on the injector v1 (refer to Section 3.2), "A" and "B" in figure 5.3. These holes are 1 mm in diameter. Axially, these are located 2 mm downstream from the thruster backplate ($z = -18$ mm). This design allows using the "A" only (Single injector – SI) or "A+B" (Double injector – DI) configurations as injection schemes. The mass flow rate is set and measured by a Bronkhorst EL-FLOW Select Xenon calibrated mass flow controller, with an accuracy of 0.1 sccm and 100 sccm full range.

The microwaves are fed through the TL described in Section 3.6, however at the time of this study the stub tuner is not present (#4 in figures 3.20 and 3.21). The directional coupler is used for forward and reflected power measurements (P_F and

86
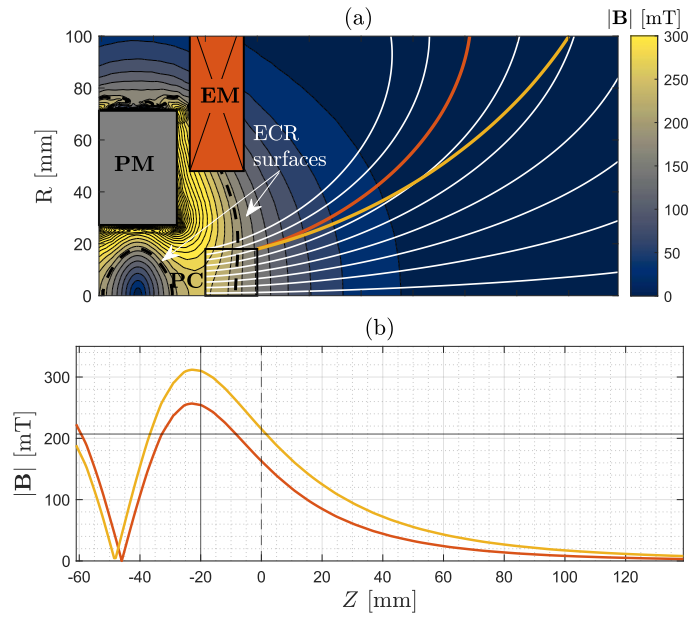
Figure 5.2: (a) 2D plot and streamlines (white) of the ECRT magnetic field in the nominal ($I_c = 0$ A case). The PC is shown as a black contoured box and the dashed black lines indicate the ECR magnetic field strength. Note that only one ECR surface is contained in the PC. The streamlines in red and orange are respectively the streamlines starting from the exit plane (PC side wall/corner) when the electromagnet current is: 0 A and 50 A. (b) Magnitude of the on-axis magnetic field for the two electromagnet current cases. The horizontal line represents the resonance field. The solid black vertical line is the backplate, and the dashed one, is the exit-plane.
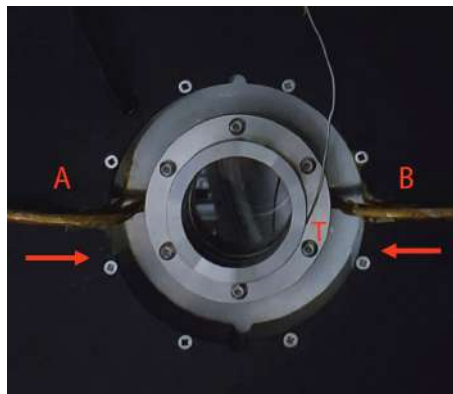
Figure 5.3: Injector position for the ECRT thruster breadboard. Single Injector mode employs: "A" only. Double Injector "A" and "B". "T" indicates the position of the discharge chamber wall thermocouple.

P_R respectively) using two independent power meters (Minicircuit ZX47-40LN).Once the output power P_{set} is set on the magnetron, the power delivered to the plasma (load) can be estimated as

$$P_T = P_F |S_{12}|^2 - \frac{P_R}{|S_{12}|^2}, \qquad (5.1)$$

in which S_{12} is the transmission coefficient of the TL and has been characterized using a Vector Network Analyser (VNA). For the TL here used, $|S_{12}|^2$ has been measured to be $|S_{12}|^2 = 0.859$. Note that the directional coupler discriminates between forward and reflected power with finite accuracy; in fact, a fraction of the forward power leaks into the reflected power port and vice-versa, as determined by its directivity parameter. The power meter thus sees a vector sum of the main and leaking power components. Hence, under high-level reflection, the power measurement accuracy is affected [54]. Due to this effect and to the insertion loss of the circulator (#2 referring to figures 3.20 and 3.21) in general P_F lies within 5% of P_{set}. The prototype characterization was performed across a range of $80 < P_{set} < 300$ W and mass flow rate of Xenon between $1 < \dot{m}_p < 40$ sccm.

For the reasons mentioned in Section 3.7, the vacuum chamber optical windows have been covered with metallic grids to prevent any stray radiation from leaking outside; a microwave leak detector calibrated for the working frequency was constantly used to monitor the radiation level.

In figure 5.4 a cut-view of the described assembly inside the vacuum chamber facility is presented. The vacuum chamber consists of a stainless-steel 304-316 cylinder 3.5 m long, with an inner diameter of 1.5 m. The chamber is equipped with the following pumps: a dry mechanical pump Leyvac LV80 with pumping speed of about 80 m^3/h, a pair of turbo-molecular pumps, Leybold MAGW2.200iP with 2000 l/s of pumping speed each, and three cryopanels, Leyvac 140 T-V. The total pumping speed is about 37,000 l/s for Xe, reaching an ultimate pressure of 10^{-7} mbar in dry conditions. This facility allows to keep an operational pressure between $2 \cdot 10^{-6}$ - $5 \cdot 10^{-5}$ mbar for a Xenon load of 1 to 40 sccm, being the pressure to gas load response approximately linear. The thruster axis is aligned with the vacuum chamber axis, and the thruster outlet section is about 2 m away from the chamber downstream wall, aiming to minimize the plume-chamber wall interaction.

Concerning the diagnostics setup, in this work, electrostatic probes are used: a Faraday cup (FC) to measure the ion current profile and provide information on the utilization efficiency and plume divergence, and a Langmuir Probe (LP) that provides properties such as the plasma density, potential, and electron temperature. Ref. [124] provides more information about the design of these two probes. The data analysis and procedures of Ref. [125] is used to retrieve the plasma properties from the scanned data, i.e. I–V characteristic curve of a LP. These two probes are mounted on a polar probe positioning system, shown in figure 5.4. This system is
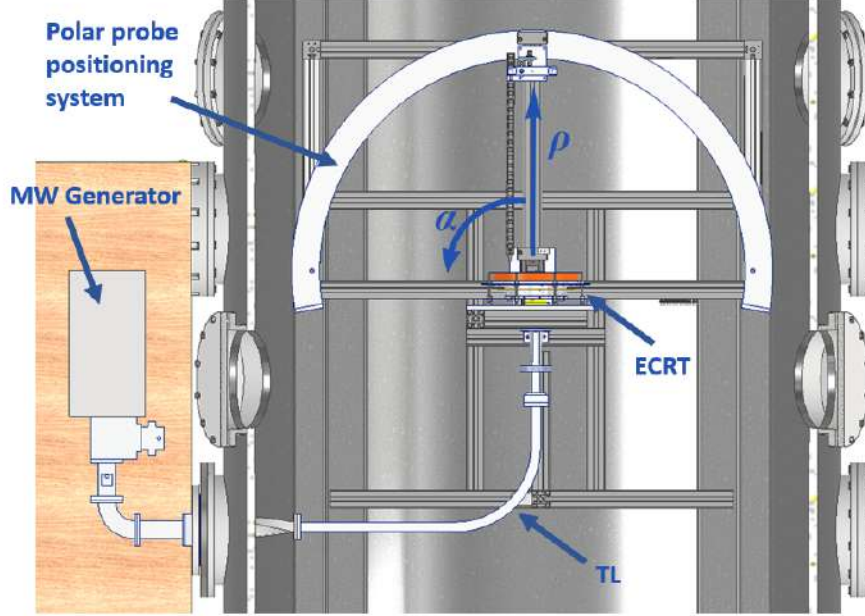
Figure 5.4: Cut-view of the experimental assembly within the vacuum chamber. Referring to figure 5.3, the injector hole A is positioned on the right of the ρ axis ($\alpha < 0$) and B on its left ($\alpha > 0$).

capable of moving probes on a plane along the radial ρ and polar α directions. The resolution of the system is about 0.3 mm and 1° for the radial and the polar direction respectively. The center of rotation of the probe positioning system is aligned with the center of the thruster exit plane. The LP was aligned with the thruster axis and used to scan the plume along the thruster axis line, in the range $50 < z < 400$ mm. The FC instead scanned the plume on an arch at constant $\rho = 400$ mm varying α within $-\pi/2 < \alpha < \pi/2$. The FC collector bias was kept constant along the sweep at -100 V.

Furthermore, the thruster wall temperature and PC wall floating potential were acquired during the overall test campaign. A K-type thermocouple was used for the temperature measurements, its position is shown in figure 5.3. In order to protect thermally sensible components such as the FFKM o-ring, the thruster wall temperature was not allowed to surpass $250°C$. On the other hand, the PC wall floating potential respect to the vacuum chamber ground, was monitored with a multimeter through an electrical wire connected to the outer part of the PC.

5.2   Results and discussion

The influence of four different parameters in the ECR response are investigated: the microwave power P_{set}, the mass flow rate $\dot{m}_p$, the injector type (SI, DI) and the electromagnet current, I_c. A comprehensive list of the tested configurations is available in table 5.1. Note that the electromagnet current scan has been performed

Inj.	$\dot{m}_p$	P_{set}	I_c	z_{probe}	Probe	Quantities
SI	1,4 sccm	300 W	0 A	150:400 mm	LP	n_i, T_e, ϕ
SI	1,2,4,8,20,40 sccm	80,175,300 W	0 A	400 mm	FC	J_i
DI	1,2,4,8 sccm	80,175 W	0 A	150:400 mm	LP	n_i, T_e, ϕ
DI	2,4,8 sccm	300 W	0 A	150:400 mm	LP	n_i, T_e, ϕ
DI	1,2,4,8,20 sccm	80,175,300 W	0 A	400 mm	FC	J_i
DI	40 sccm	80,300 W	0 A	400 mm	FC	J_i
DI	1,2,4 sccm	175 W	0-50 A	400 mm	FC	J_i

Table 5.1: Table summarising the tested cases and available data at different positions.

only for the DI configuration. Results are organised as follows. Firstly the microwave power data and thruster floating potential are shown in Section 5.2.1, these will serve as a reference for the rest of the discussion. Then, the plasma plume properties are discussed in Section 5.2.2. Finally, Section 5.2.3, provides an estimation of the propulsive capabilities of this prototype based on the results shown in the previous sections.

5.2.1 Microwave power coupling and thruster floating potential

The plasma generated inside the thruster discharge chamber acts as a termination load for the TL, as shown in figure 5.4. In general, the impedance of this load may differ from the TL characteristic impedance and vary with the operating point, resulting in a certain impedance mismatch, therefore some power is reflected back towards the generator.

A parameter quantifying the level of reflection is the load reflection coefficient:

$$\Gamma_L^2 = \frac{P_R}{P_F |S_{12}|^4}. \tag{5.2}$$

This quantity was tracked for all the operation conditions listed in Table 5.1. Analyzing the reflection coefficient enables the (partial) characterization of the plasma impedance. The results are shown in figure 5.5 (a-b). Globally, the measured Γ_L^2 ranges between $0.14 < \Gamma_L^2 < 0.54$. As for the mentioned directivity error in Section 5.1, the measured reflection levels can lead to an uncertainty in the thruster delivered power, P_T, ranging between 10% and 40%. Being the output microwave power set on the generator, P_{set}, independent from the level of reflection, for the sake of simplicity, the results in this chapter are presented in function of this variable.

According to figure 5.5 (a-b), the reflection coefficient peaks at low mass flow rates. At the highest power tested, 300 W, a minimum appears at intermediate $\dot{m}_p$. The trend appears to be consistent between the single and double injector configu-
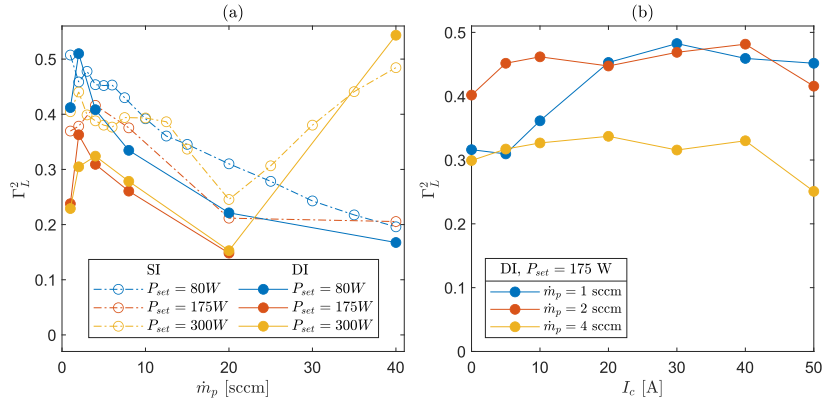
Figure 5.5: Ratio of reflected power for the tested working points and injector configurations; (a) as a function of $\dot{m}_p$ with $I_c = 0$ A, (b) varying I_c at $P_{set} = 175$ W for the DI configuration.
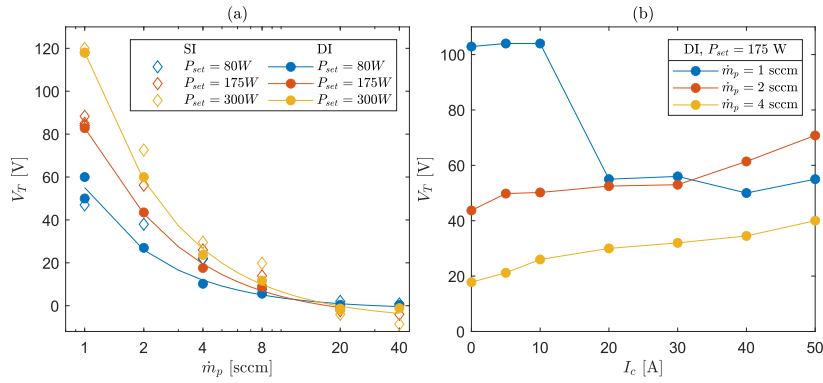
Figure 5.6: Thruster floating potential V_T for different operating conditions. (a) as a function of $\dot{m}_p$ with $I_c = 0$ A for three levels of power and the SI/DI configurations, (b) varying I_c at fixed $P_{set} = 175$ W for the DI configuration and three levels of mass flow rate.

rations, although in general, lower values of reflection coefficient are found for the double injector configurations. The high sensitivity to the mass flow rate shown by Γ_L^2 is most probably due to the effect that this has on the plasma density, the latter being one of the main parameters determining the propagation and absorption of MW. On the other hand, for a fixed set power $P_{set} = 175$ W, varying the electromagnet current has a small impact on the reflection coefficient in the explored parametric range, as shown in figure 5.5-b, except for the $\dot{m}_p = 1$ sccm case, in which a transition to a larger Γ_L^2 is found between $5 < I_c < 20$ A. Such a large reflection coefficient was not found in previous studies on waveguide ECRTs. This difference may be due to the absence of a Right Hand Polarizer upstream in the TL, and therefore to the reflection of the L wave, or as well to the discharge chamber design. Consequently, in the experiments analyzed in Chapter 6, a stub tuner is introduced in the TL to reduce the reflected power.

The thruster wall floating potential during operation, V_T, is shown in figures 5.6 (a-b). The value of this parameter depends on the plasma properties inside the PC and the sheath along its metallic walls, but also on the potential drop that develops along the plume and the sheath at the vacuum chamber walls. By ignoring the wall sheath potential drop, and assuming that the majority of the neutrals are ionised in the PC, V_T can be used as an approximate proxy for the kinetic energy of ions downstream. As for Γ_L^2, it also provides a reference for the thruster operating conditions.

Figure 5.6-a shows a decreasing trend of V_T with $\dot{m}_p$, and an increasing trend with P_{set}. At the largest mass flow rate tested, the measured floating potential approaches zero or slightly negative values. No substantial differences for V_T are noticed between the single and double injector configurations (figure 5.6-a). In MN thrusters, the ion energy downstream is expected to scale with the energy per particle, which goes roughly as $P_{set}/\dot{m}_p$. Indeed, a larger energy per particle is expected to increase the electron temperature T_e, the parameter with which the ion energy and V_T scale. Increasing the mass flow rate decreases the energy per particle, additionally, the electron temperature is further reduced by the increased collisionality, all these effects resulting in a lower V_T. For the same reason, a power increase at fixed $\dot{m}_p$ leads to larger V_T.

Referring to figure 5.6-b, an increase of V_T is observed with the electromagnet current I_c for $\dot{m}_p = 2$–4 sccm. A higher I_c generates a stronger (up to 20% increase at $I_c = 40$ A) and less divergent magnetic field within the PC; This increase in the field strength would reduce the plasma cross-field diffusion towards the lateral metallic walls of the PC, and as well, the reduced divergence would make less magnetic field lines to intersect them, "magnetic shielding". One of the consequences of this shielding is the reduction of plasma and energy losses to the walls, which translates into higher T_e at the plasma bulk, and consequently, a higher V_T. Another factor being affected by I_c is the ECR layer position, of which effects are less predictable.
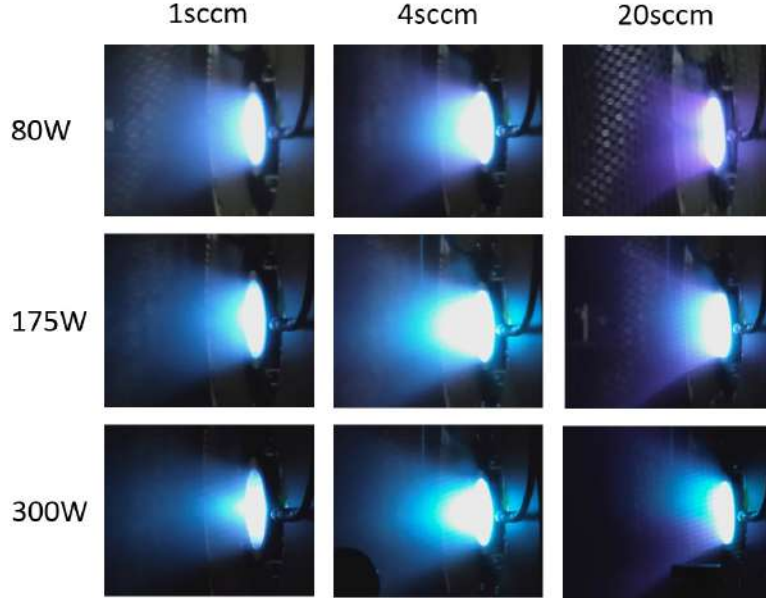
Figure 5.7: Pictures of the ECRT plume for the DI configuration at different working points. The electromagnet current is $I_c = 0$ A.

The direct impact is expected in the plasma-wave coupling, a phenomenon that requires a dedicated investigation [126, 62].

In the $\dot{m}_p = 1$ sccm case, an important drop in V_T is observed between $I_c = 10$ and 20 A. This V_T response at $\dot{m}_p = 1$ sccm, together with the behavior observed for Γ_L^2 in figure 5.5-b, suggests an abrupt change in the plasma-wave coupling mode and/or the overall operation of the device. Hence, the drop in V_T agrees with the strong increase of the reflection coefficient (thus lower power coupled to the plasma driving a lower T_e), despite the Γ_L^2 increase starts already for $I_c > 5$ A. The evidences provided for $\dot{m} = 2, 4$ sccm prove that the V_T can be nearly doubled by accurately choosing the magnetic field strength and shape.

5.2.2 Plasma plume expansion

Figure 5.7 shows photographs of the visible plume of the DI configuration for a set of working points. This set of images already provide interesting qualitative information on the plume properties. Variations in emitted visible light are noticeable. At low $\dot{m}_p$ the plume is bluish and bright; as the mass flow rate increases the plume becomes more violet/reddish. The plume reddening process starts from the magnetic field lines connected with the thruster lateral walls, and this region grows towards the axis as the mass flow rate is increased. Changes in the Xenon plume color are associated with different Xe excitation transitions. In particular, emission in the red (≈ 800 nm) and green-blue ($480 - 530$ nm) parts of the spectrum are more probable for neutral (Xe I) and ion excitation (Xe II) respectively [127, 128, 129]. A blue
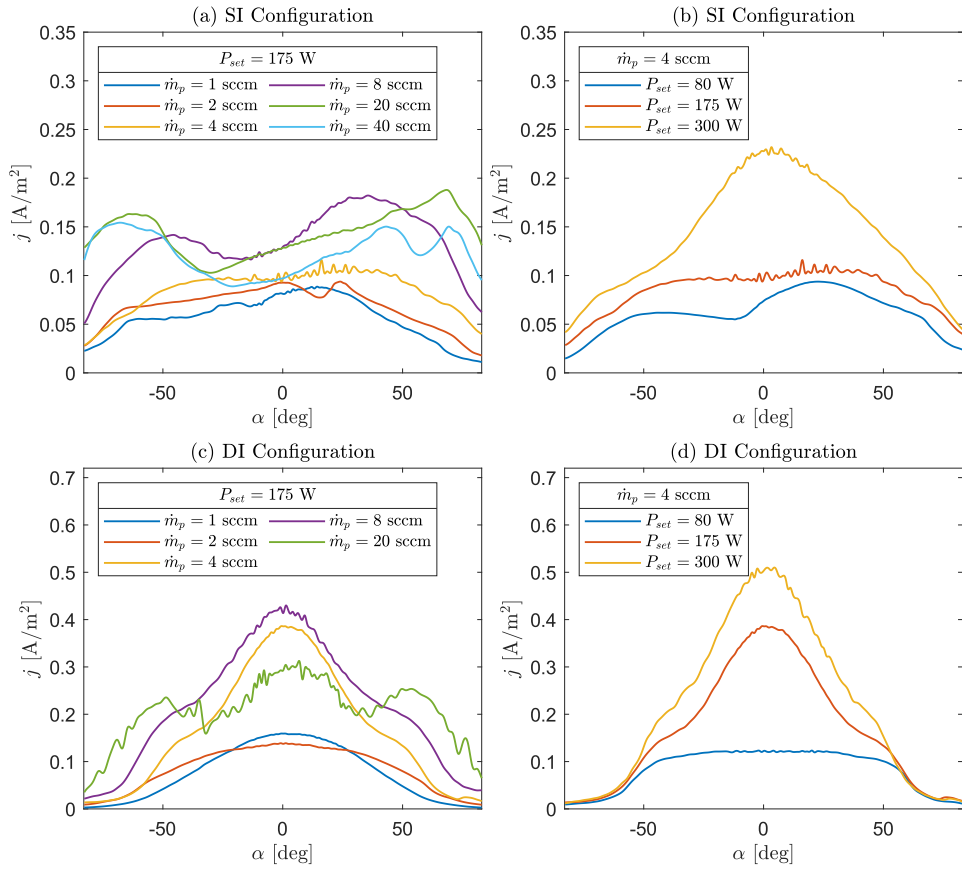
Figure 5.8: Faraday cup ion current measurements for the SI (plots a, b) and DI (c, d) injector configurations. Sweep of $\dot{m}_p$ (a, c), P_{set} sweep (b, d). The electromagnet current is $I_c = 0$ A for all the cases.
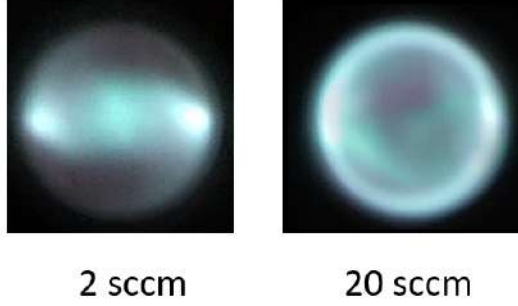
Figure 5.9: Front-view photographs of the ECRT discharge chamber while firing at P_{set} = 175W. The DI configuration is used.

plume is thus indicative of a relatively higher ionization level and hotter electrons. For the case $\dot{m}_p$ = 20 sccm and P_{set} = 300 W, the plume shows an asymmetric color pattern most probably due to a non-uniform neutral distribution within the PC. Concerning the shape, the plume edges (born at the lips of the PC) appear well-defined; different divergence angles are observable for the different working points. For low mass flow rates most of the light is coming from the central part of the beam, which widens as the mass flow rate is increased. Interestingly, the plume also appears to become hollow at the higher $\dot{m}_p$ tested. The latter can be also observed when looking at the thruster discharge chamber from the front, as shown in figure 5.9. The plasma appears to emit more light in proximity to the injectors at low mass flow rates and diffused all around the PC for 20 sccm. As we see next, these visually observed trends are confirmed by Faraday Cup ion current measurements.

Faraday Cup measurements

Figure 5.8 shows the measured ion current density j_i for the SI and DI configuration at different levels of P_{set} and $\dot{m}_p$. For the SI case (figures 5.8-a and 5.8-b) the plume presents a wide distribution of j_i and strong asymmetries for all the tested working points. This behavior is attributed to the non-uniformity of the neutral density inside the thruster chamber (caused by the asymmetric single injector), and to a consequently non-homogeneous power deposition at the ECR resonance layer.

As it can be seen in figure 5.8-a, increasing $\dot{m}_p$ at constant P_{set} results in a global increase of j_i. This trend holds except for the largest $\dot{m}_p$ values tested, which exhibit the aforementioned hollow plume.

Two trends can be observed when P_{set} is varied while keeping $\dot{m}_p$ constant (figure 5.8-b). Firstly, the current reaching the FC significantly increases with power, meaning that more plasma is produced for the same amount of propellant. Secondly, the plume shape is as well affected, a larger power concentrates the ion current in the central part of the plume. Indeed, the asymmetry at the higher P_{set} decreases, which suggests that plasma production within the PC is more uniform in this case.

For the DI case (figures 5.8-c and d), the profiles are visibly more symmetric and concentrate the ion current in the central part of the plume. The trends with $\dot{m}_p$ and P_{set} are otherwise the same as for the SI case: j_i increases with $\dot{m}_p$ and P_{set} in the range explored, except for the highest $\dot{m}_p$ value tested where the central peak is reduced.

Although the DI measurements reveal a more symmetric plume than in the SI configuration, relatively high current levels were still measured up to $\alpha = 50 - 60°$. On this regard, an important observation emerging from figure 5.8(c-d) is the development of lateral plume lobes for low $P_{set}/\dot{m}_p$ ratios. Visual inspection (figure 5.7 for 80W and 20sccm) suggest that the origin of these structures lies likely upstream in the PC. A possible interpretation is that more power is being coupled in proximity of the walls for low $P_{set}/\dot{m}_p$, thus leading to large plasma production in that region, increasing as well wall losses. Increasing $P_{set}/\dot{m}_p$ seems to concentrate the ion current in the central part of the plume.

In the following, we focus the discussion on the DI configuration only. Assuming plume axisymmetry, it is possible to estimate integrated plume properties such as the utilization efficiency η_u and the plume divergence angle α_D. As seen in figure 5.9, such an assumption may not be completely justifiable, since the emitted light from the front view appears to present two planes of symmetry in the PC, thus, axisymmetry would tend to overestimate the plume current. However, it is unknown how these structures propagate downstream and may be able to homogenize. Therefore, in the absence of FC plume measurements in the perpendicular plane, and to be able to further characterize the plume and obtain integrated properties, hereafter we will assume axisymmetry. In Chapter 6, the accuracy of this assumption is improved since plume measurements are taken with a diffused radial injection (injector v2, see Chapter 3).

The ion beam current, I_i, is given by

$$I_i = 2\pi\rho^2 \int_0^{\pi/2} j_i(\alpha)\sin(\alpha)\,d\alpha, \tag{5.3}$$

where j_i is the ion current density at each scanned angular position α. The utilization efficiency, assuming a singly-charged ion beam, is then defined as the (normalized) ratio between the ion beam current and the input mass flow rate,

$$\eta_u = \frac{\dot{m}_i}{\dot{m}_p} \simeq \frac{I_i m_{Xe}}{e\dot{m}_p}, \tag{5.4}$$

where $\dot{m}_i$ is the ion mass flow rate in the plume, e is the unit charge and m_{Xe} is the Xenon atomic mass. The divergence angle can be found considering the portion of
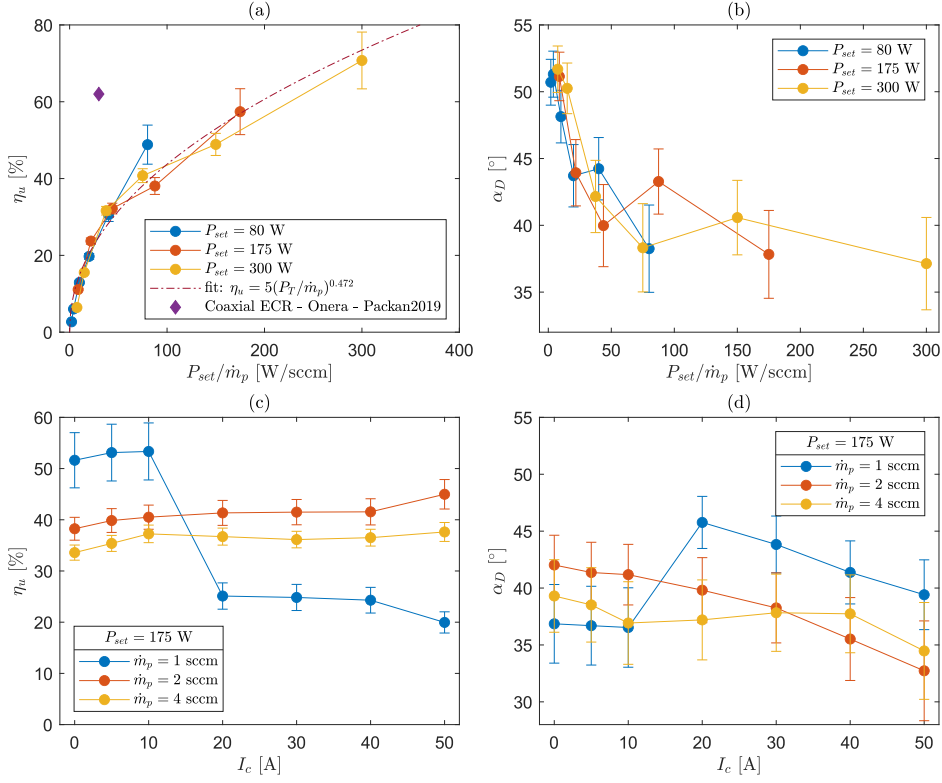
Figure 5.10: Utilization efficiency (a-c) and plume divergence angle (b-d) for the DI configuration. For (a) and (b) the electromagnet current is $I_c = 0$ A.

current directed in the axial direction,

$$\alpha_D = \cos^{-1}\left(\frac{I_{zi}}{I_i}\right), \tag{5.5}$$

where I_{zi} is computed assuming a conical expansion of the ions from the origin,

$$I_{zi} = 2\pi\rho^2 \int_0^{\pi/2} j_i(\alpha)\cos(\alpha)\sin(\alpha)\,\mathrm{d}\alpha, \tag{5.6}$$

Figure 5.10-a shows the computed utilization efficiency against the deposited power to mass flow rate ratio $P_{set}/\dot{m}_p$. At a constant P_{set}, as $\dot{m}_p$ increases, the provided energy per electron and consequently the ionization level are reduced. This makes η_u drop rapidly, in agreement with the expectations derived from the plume visuals in figure 5.7. A maximum of around $\eta_u = 70\%$ was achieved at $P_{set} = 300$ W and $\dot{m}_p = 1$ sccm. The utilization efficiency η_u is well described by a power law on $P_{set}/\dot{m}_p$; this is particularly true for the low power to mass flow rate range. At $P_{set} = 80$ W, for larger values of this ratio, the discrepancy from the fitted curve increases, showing that $P_{set}/\dot{m}_p$ is not the only driving quantity and other effects start to become predominant. Overall, the range $0-100$ W/sccm results in a low

utilization efficiency (well below 50%). Extrapolating this trend, larger values of $P_{set}/\dot{m}_p$ would be needed to obtain utilization efficiencies similar to those found for coaxial ECR thrusters [130]. The utilization efficiency depends on both the wall losses in the PC and neutral gas ionization. The measurements performed in this work are not sufficient for evaluating which effect is predominant, since a precise knowledge of the plasma conditions in the PC would be required. However, as we will see later in this section, the lower electron temperatures (see figure 5.12) for equivalent $P_{set}/\dot{m}_p$ respect to coaxial thrusters may be one of the main contributors.

It is worth noting that equation 5.4 neglects the presence of doubly-charged ions. This assumption is valid if the production of this ion species is much lower respect to the singly charged ones. In first approximation, the latter can be assessed by comparing the electron collision frequencies for the neutral ionization processes, as $\nu_{n\to i2}/\nu_{n\to i1} = R_{n\to i2}/R_{n\to i1}$, where R is the ionization reaction rate, n stands for neutrals and $i1, i2$ for singly and doubly charged Xe ions respectively. This ratio only depends on the electron temperature and ionization cross sections. Considering the case at $\dot{m}_p = 1$ sccm, and $T_e \approx 30$ eV upstream (value double than the one measured in the close plume, refer to figure 5.12), and using the Xenon ionization cross-sections from [131, 132, 133], this ratio is found to be $\nu_{n\to i2}/\nu_{n\to i1} = 5.4\%$. This number decreases with $\dot{m}_p$: for 2 sccm, the double ion production goes down to 3.5%. Note that two-step ionization ($i1 \to i2$) has not been taken into account for this estimation since it would require the knowledge of the relative densities of ions and neutrals in the PC. When using the measured ion current in the beam I_i, the presence of doubly-charged ions results in an overestimation of $\dot{m}_i$ and consequently of η_u. For the values provided above, η_u results to be overestimated of about 5.2% and 3.4% respectively [3]. However, the exact value of T_e in the PC is unknown, and the real fraction of doubly charged ions may be larger. ExB probe measurements should be carried out to experimentally verify this hypothesis.

Concerning figure 5.10-b, the divergence angle decreases with increasing $P_{set}/\dot{m}_p$. This result agrees with the comments made on figure 5.8, being this trend mainly driven by the development of the lateral plume lobes described above at low energies per particle. Other effects such as collisionality may also increase the divergence for large $\dot{m}_p$: the increased neutral density that results at high $\dot{m}_p$ increases the electron collisional rate ν_e in the near plume region, the Hall parameter ($\chi_H = eB/m_e\nu_e$) decreases and the magnetic nozzle becomes less effective in radially-confining the plasma. At the PC exit plane, χ_H is estimated to range between 10^3 and 10^1 as $\dot{m}_p$ is increased. The increased cross-field transport would increase α_D.

Figure 5.10-c shows a rather small increase of η_u with respect to I_c for $\dot{m}_p = 2-4$ sccm. Similar conclusions to the ones discussed for the increasing trend of V_T with I_c can be drawn as well for the slow increase seen for η_u. As expected, increasing I_c reduces the MN divergence (figure 5.10-d). As a side comment, we note that ion magnetization is not expected to play a relevant role in plume divergence. In fact,
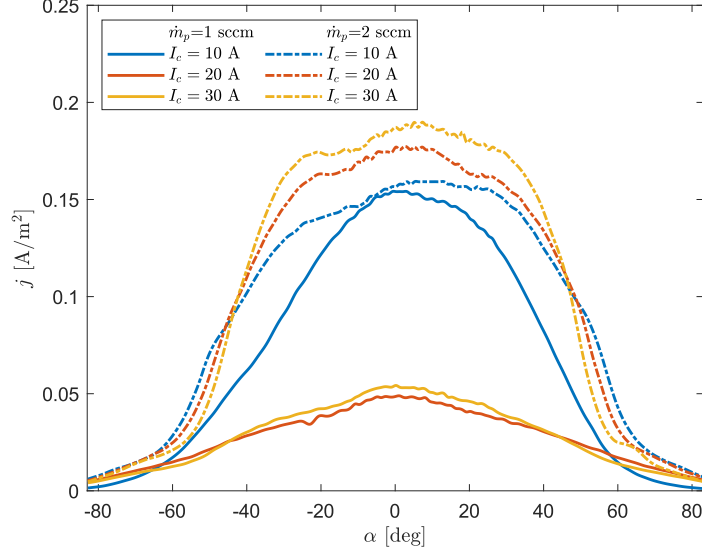
Figure 5.11: Faraday cup ion current measurements for $\dot{m}_p = 1-2$ sccm, $P_{set} = 175$ W and different I_c current levels. DI configuration.

referring to the dimensionless ion gyrofrequency, defined as $\hat{\Omega}_{i0} = eB_0R_t/(\sqrt{m_{Xe}T_e})$ [91, 75], values between $\hat{\Omega}_{i0} = 0.5-4$ are estimated for the full range of operating electron temperatures and coil currents. As discussed in [91], much larger values ($\hat{\Omega}_{i0}$ between $100-1000$) are needed to observe a noticeable plume divergence increase.

The decrease for η_u and the increase in α_D for the $\dot{m}_p = 1$ sccm case occurring at $I_c = 10-20$ A, is likely related to the change in operating point observed in Γ_L^2 and V_T (figures 5.5-b and 5.6-b). This transition is further investigated in figure 5.11, which shows the ion current density obtained for some representative tested cases when the current I_c is varied at constant set power. For $\dot{m}_p = 1$ sccm, the profiles clearly display a drop in ion current in the $I_c = 10-20$ A range. The pieces of evidence collected suggest a change of operating mode induced by the magnetic field variation, characterized by a lower power coupled (higher Γ_L^2), lower plasma density (lower utilization), and lower ion energy (reduced V_T), as well as a larger divergence. The origin of this mode change is still unknown and deserves further research. On the other hand, and for comparison, this transition does not occur in the $\dot{m}_p = 2$ sccm case, where the current concentrates towards the axis as expected from figure 5.10-d.

Langmuir Probe measurements

In a magnetic nozzle expanding into vacuum, the electron thermal energy is converted into ion kinetic energy as the ions are accelerated by the ambipolar electrostatic field, and most of this acceleration happens in the vicinity of the thruster exit [134, 76, 75]. Thus, in order to have a detailed description of the expansion, the
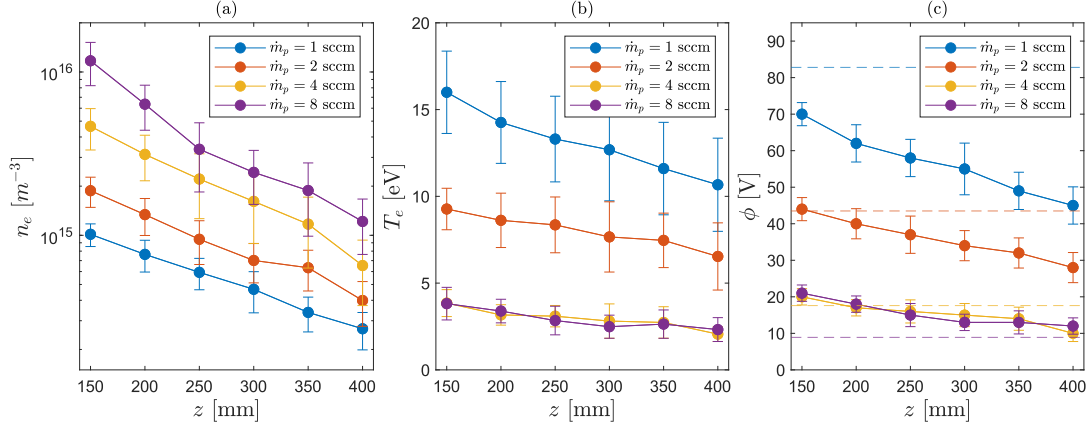
Figure 5.12: Electron density n, temperature T_e and plasma potential ϕ measured at different z along the plume. The dashed lines correspond to the thruster floating potentials. DI configuration, $P_{set} = 175$ W, $I_c = 0$ A.

LP measurements have to be conducted as close as possible to the source, from a minimum distance of 150 mm from the exit plane. Because of the intrusive nature of the LP, measurements at shorter distances were found to affect V_T and Γ_L^2. Furthermore, except for the measurements in Section 5.2.2, scans at closer positions presented artifacts in the I–V curve within the exponential electron current region, suggesting strong perturbations of the electron population. Refer to table 5.1 for the full list of positions and working points analyzed.

Being the trends for the other power levels comparable, $P_{set} = 175$ W is chosen as a representative case as shown in figure 5.12. Densities up to $n_e = 10^{16}$ m^{-3} were found at $z = 150$ mm, whereas approximately one order of magnitude lower values are found in the far plume. With these density ranges, the thin sheath cylindrical probe model for I-V curve analysis, is not applicable, and particularly at large negative biases, a large sheath with thickness in the mm range should exist for most of the cases. Downstream, this might result in a large error in ion saturation current and plasma density estimation. To mitigate these problems, plasma density is computed from the electron saturation current at the plasma potential, at which there is no sheath and the collection surface can be well approximated with the probe tip surface. However, this method has the disadvantage that, at the plasma potential, a considerable amount of electron current is being drawn, possibly affecting the electron population in the relevant magnetic tube.

Electron cooling takes place along the MN expansion [134, 121, 135]. T_e decreases roughly linearly with the distance from the thruster. However, a faster decrease in temperature is expected near to the exit plane [79]. A maximum temperature of about $T_e = 16$ eV was obtained at the working point $P_{set} = 175$ W and $\dot{m}_p = 1$ sccm at $z = 150$ mm. Interestingly, at similar positions in the plume and similar $P_{set}/\dot{m}_p$ values, up to 5 times higher T_e were reported in coaxial ECR thrusters [79].

The plasma potential (figure 5.12-c) follows a trend similar to T_e. The gradient of the plasma potential is commonly referred to as an ambipolar electric field and it is responsible for the ion acceleration in a magnetic nozzle [76]. The ions are found to be still accelerating at $z = 400$ mm, which is the maximum measurement distance achievable with the current positioning system setup.

Measurement of the Electron Energy Distribution Function

The second derivative of the electron current I_e, extracted from a Langmuir probe I-V curve, can be used to obtain a measurement of the Electron Energy Distribution Function (EEDF) with the so-called Druyvesteyn method [125, 136].

$$EEDF(\epsilon) = \frac{2}{e^2 A_p} \sqrt{2 m_e e \epsilon} \frac{\partial^2 I_e}{\partial \epsilon^2}, \qquad (5.7)$$

where $\epsilon = \phi - V_B$, being V_B the LP bias, and A_p is the probe collecting surface. One of the assumptions of this method is the plasma being isotropic, this is not the case for this study (and in general EP) since the plasma drifts downstream, however, the alignment described in Section 5.1 enables measurements of the non-drifting component of the EEDF. More caveats come from the presence of a magnetic field. Reliable measurements can be obtained if the Larmor radius, r_L, is significantly larger than the probe radius, for the measurements shown below, r_L is estimated to be larger than 1.5 mm. As equation 5.7 indicates, the calculation of the EEDF necessitates the estimation of the second-order derivative of the electron current, therefore this method is prone to generate noisy results or distorted curves due to excessive data averaging. For the case of this study, acceptable data quality is obtained only in close proximity to the exit plane, where the density is higher, and for DI configuration only. In addition to the ones shown in table 5.1, extra LP measurements are taken for the DI configuration at $z = 100$ mm for $\dot{m}_p = 1$ and 2 sccm.

Figure 5.13 shows the resulting EEDF for three cases. $\dot{m}_p = 2$ and 4 sccm show little deviation from Maxwellian distributions at temperatures respectively of about $T_e = 10$ and 4 eV. On the other hand, $\dot{m}_p = 1$ sccm presents a primary population at about $T_e = 26$ eV and a drifting population at larger energies, with mean energy at about 60 eV. Four measurements of the latter case have been taken, reproducing similar results. The fact that its presence is observed at $\dot{m}_p = 1$ sccm and $P_{set} = 175$ W only, suggests a relation with $P_{set}/\dot{m}_p$. The origin of this drifting population is currently unknown, speculatively, these may be produced by the resonance, and the low density ($\dot{m}_p = 1$ sccm) may be not sufficient for thermalization. More measurements are expected to be taken in the future to evaluate this or other hypotheses. Finally, high energy electrons for large $P_{set}/\dot{m}_p$ have also been observed using an RPA in Chapter 6, however at this stage it is not possible to infer if the two observed
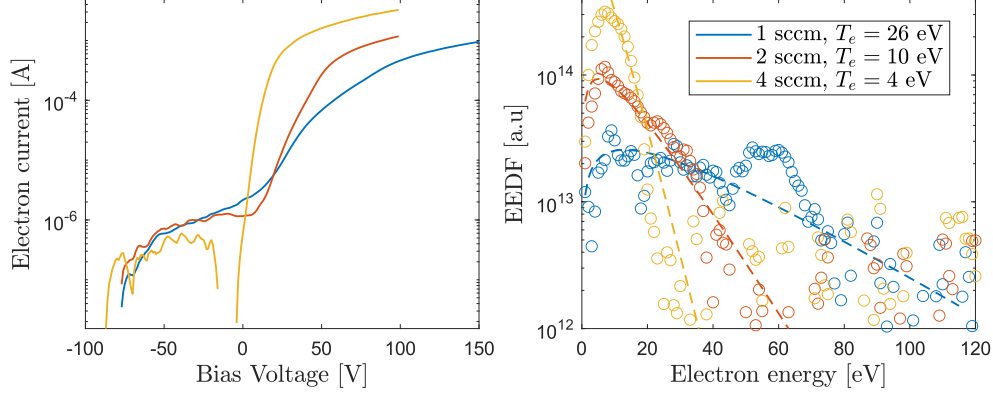
Figure 5.13: (a) Langmuir probe I-V curve. (b) Electron energy distribution function obtained with the Druyvestein method. The Langmuir probe measurements are taken at P_{set} = 175 W and $\dot{m}_p$ = 1, 2, 4 sccm (blue, red, and yellow respectively). The case at $\dot{m}_p$ = 4 sccm is taken at z = 150 mm while the other two cases at z = 100 mm.

phenomena are related.

Polytropic analysis

It is common to employ a polytropic electron model to discuss the cooling rate of electrons along the MN [121, 82, 135, 137, 84, 83, 85],

$$\frac{T_e}{n_e^{\gamma-1}} = \frac{T_{e0}}{n_{e0}^{\gamma-1}} = \text{Const.} \tag{5.8}$$

Such an empirical model offers a free parameter that can be fitted to experiments, and a simple way to take plume electron cooling effectively into account in fluid models. It should be noted though, that electron cooling in the near-collisionless plasma expansion is a non-local problem whose analysis necessarily requires a kinetic model. It has been recently shown [134, 138, 137] that electrons in the divergent MN subdivide into free, reflected, and trapped subpopulations, as determined by the competing effects of the confining axial electrostatic field and the expanding magnetic mirror force. The overall temperature of the electron species depends on the behavior and fraction of each of these subpopulations.

The fitted values of γ for each case are given in figure 5.14. For the case shown in 5.14, the found polytropic coefficient ranges between $1.23 < \gamma < 1.3$, hence lying in-between the isothermal and adiabatic scenario. In [79], Correyero et al. found values close to the ones here shown for the permanent magnet coaxial ECR thruster, however in the same study a different trend was found for the solenoid thruster showing a transition to an isothermal behavior further downstream. Similar results were also found by Kim et al. [139], however, for the measurements performed in
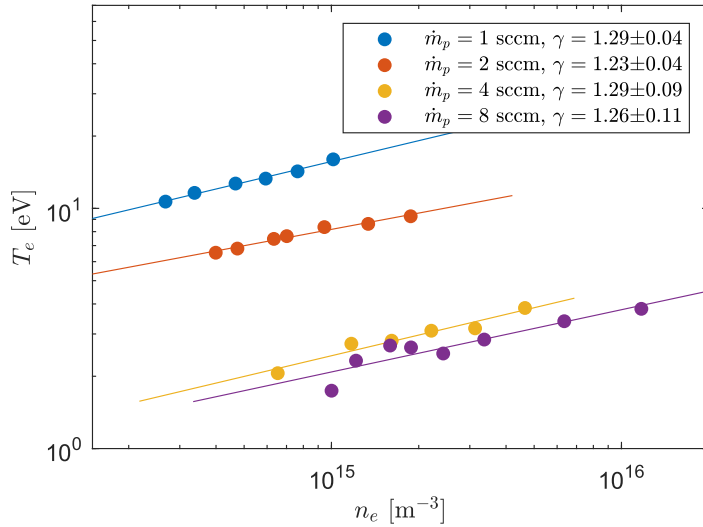
Figure 5.14: Example of polytropic coefficient γ fitting for the DI configuration, P_{set} = 175 W and I_c = 0 A.

this study this transition is not visible. A possible cause is the limited extension of the probed region along the expansion.

5.2.3 Estimation of propulsive performances

Finally, in this section the propulsive performance of the DI configuration is estimated using the available probe measurements. It is expected that inside the PC the plasma potential would rise above V_T proportionally to the electron temperature due to the presence of the wall sheath. Given the difficulty of measuring ϕ inside the source, the thruster floating potential is used here as a proxy of the ion potential drop at infinity and the energy that ions would have far downstream. Obviously, this neglects the potential drop that exists at the thruster and vacuum chamber walls in the corresponding plasma sheath. It also ignores the fact that not all ions see the full potential drop that develops between the PC and the vacuum chamber walls, as this depends on the location at which ions are generated (e.g., some ions could be produced already outside of the PC). Finally, it also ignores the effect of double ions and any ion energy lost in collisional events. With all these caveats, an estimation of the ion terminal speed can be obtained as

$$v_i = \sqrt{\frac{2eV_T}{m_{Xe}}}. \tag{5.9}$$

Ion energies similar to the thruster floating potential shown in this work were also found by Peterschmitt et al. [54] for the waveguide thruster in comparable conditions of input power and mass flow rate.
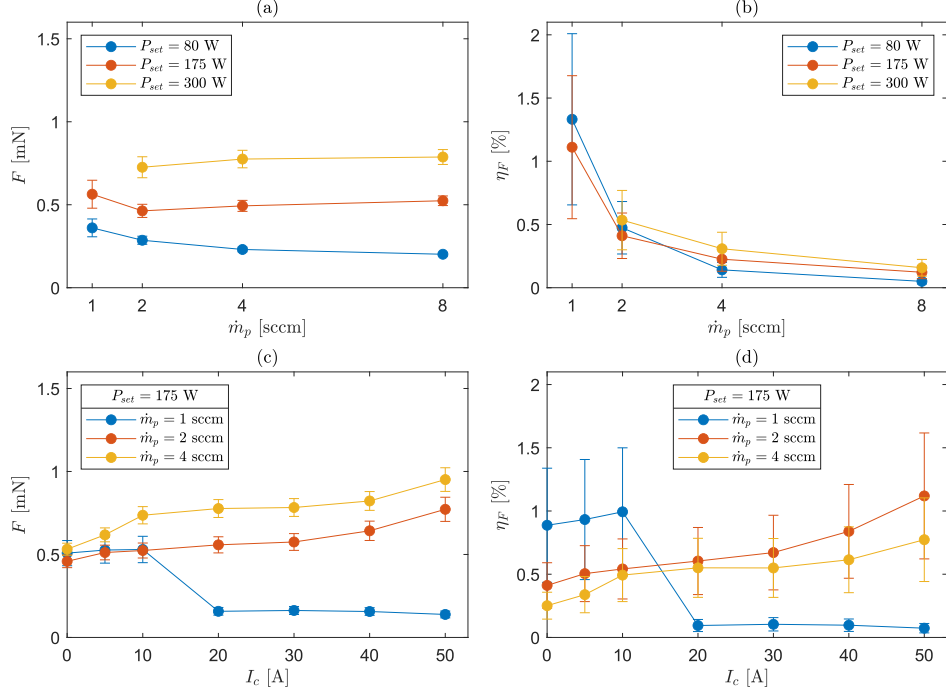
Figure 5.15: Thrust (a, c) and Thrust efficiency (b, d) estimations for the DI configuration. For (a) and (b) the electromagnet current is $I_c = 0$ A.

Assuming that ions are the sole species carrying momentum, the divergence angle and the utilization efficiencies found in Section 5.2.2 can be used to find a thrust estimate:

$$F \simeq \eta_u \dot{m}_p v_i cos\alpha_D. \tag{5.10}$$

This neglects the contribution of neutrals and electron pressure to thrust. The thrust efficiency η_F is then calculated as:

$$\eta_F = \frac{F^2}{2\dot{m}_p P_T} \simeq \frac{\dot{m}_p \eta_u^2 cos^2\alpha_D e\phi_{ep}}{m_{Xe} P_T}. \tag{5.11}$$

The computed values for these propulsive parameters are provided in figure 5.15.

The estimated thrust and thruster efficiency are below 1 mN and 1.5% respectively, values in line with those previously found by Sercel [41]. The thrust appears to stay rather constant with $\dot{m}_p$ for a fixed P_{set}, supposing a decrease in η_F. It has been seen in fact how reducing $P_{set}/\dot{m}_p$ lowers consistently the utilization efficiency and increases the divergence angle, both contributions appearing in equation 5.11. Hence, larger values of η_F are achieved at low mass flow rates.

Finally referring to figure 5.15 (c-d), increasing the electromagnet current leads to increased values of thrust and thrust efficiency, for $\dot{m}_p = 2$–4 sccm, $P_{set} = 175$ W. This trend is aligned with the increase of V_T, η_u, and decrease of α_D reported before.

The values found can provide a useful order of magnitude estimate of F and η_F. The error bars in figure 5.15 have been obtained by standard propagation of uncertainty, however, multiple factors might affect the accuracy of this estimation. Concerning the thrust F, the main source of error is believed to be the assumption on the potential drop seen by ions, underestimated by V_T. Furthermore, this neglect any thrust contribution by the residual electron pressure, which has been seen to be non-negligible in numerical studies [65, 56], Thrust estimation aside, one of the main contributions to the uncertainty of η_F is the power delivered to the thruster P_T, which differs from the power set P_{set}. Thrust balance and RPA (Retarding Potential Analyser) measurements must be carried out to obtain a better estimation of thrust and derived quantities, as well as a matching device should be used to reduce the power delivered uncertainty. All these improvements are implemented in Chapter 6.

Comparing these performance estimations with those reported for coaxial ECR thrusters for similar $P_{set}/\dot{m}_p$, we can attribute the lower performance mainly to a combination of the lower utilization and lower electron temperature. The internal structure of power absorption in the PC may play an important role in determining this temperature difference. As seen in the analysis, the large ion current densities found at large angles in some cases are indicative of large plasma densities in the proximity of the walls in the PC. This effect might increase the ion recombination at the walls, consequently, the electrons will lose further energy in re-ionizing the gas. The lower electron temperature promotes as well excitation, further increasing power losses.

5.2.4 Observation of metallic deposition

On a final remark, deposition of metallic material has been observed on the thruster backplate after about 6 h and 4 h of firing for the SI and DI configuration respectively. As shown in figure 5.16, the latter appears to be localized in proximity to the injection points, suggesting sputtering from the surrounding areas of the lateral walls. The absence of this deposition at the central part of the backplate may be justified by a "self-cleaning" process by ion-electron impact. The latter effect may be reduced for the backplate areas presenting magnetic field lines that intersect both the backplate and the lateral walls. The same effect has also been documented on coaxial ECRTs [140] and has been attributed to the electron population. Although significant changes in the performance have not been noticed during this campaign, after tens of hours of operations the accumulated conductive material is expected to affect MW propagation and MW-plasma coupling possibly deteriorating performance and limiting lifetime. It is speculated that this process could be reduced/avoided by an improved design of the magnetic field or with conically shaped PC lateral walls.
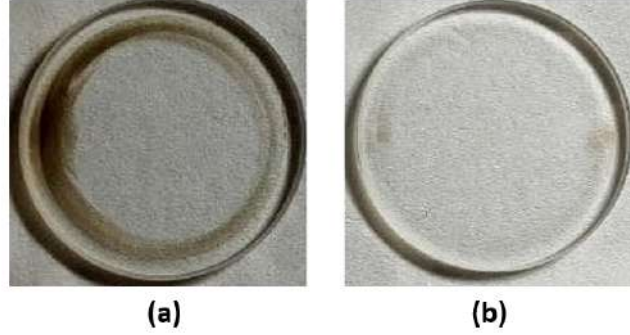
Figure 5.16: Metallic deposition on the quartz backplate for (a) SI configuration after about 6 hours of firing; (b) DI configuration 4 hours of firing.

5.3   Summary

The response of the thruster was explored by conducting plume measurements for different working conditions (mass flow rates and power), injector configurations, and magnetic fields (tuning the divergence of the MN and displacing the resonance surface location). Thruster temperatures, potentials, and transmission line reflections were also used to assess the operation of the device.

Concerning the microwave-plasma coupling, it has been shown that this varies considerably depending on the set parameters. The load reflection coefficient Γ_L^2 illustrates this clearly. The trends are consistent between the two injector strategies and Γ_L^2 can vary between $0.15 < \Gamma_L^2 < 0.5$ when the mass flow rate or power are varied. Because of the finite directivity of the directional coupler, the large value of Γ_L^2 encountered affects the coupled power measurements accuracy, this problem can be easily corrected with a matching device such as a waveguide stub tuner.

The propellant injector design has been shown to play an important role in determining the plume current profile. Although parallelisms can still be made between the plumes for the two injector types, a symmetric injection seems required to homogenise the neutral density distribution in the PC and obtain a symmetric plume.

The magnetic field strength and shape has as well a fundamental role, both from the point of view of the power coupling and plasma expansion in the magnetic nozzle. The tested I_c levels allowed for some cases to reduce the divergence by almost 10° and nearly double the thruster floating potential when the resonance is close to the exit plane. It was found as well that the magnetic field, can significantly alter the power coupling and thruster operation mode, suggesting that an accurate magnetic field sizing is essential.

Lastly, the LP and FC measurements allowed for characterizing the plume expansion, assessing partial efficiencies, and indirectly, the expected ion acceleration. The obtained quantities were used to obtain a rough estimation of the expected levels

for this device. Values below $\eta_F < 2\%$ have been obtained. It is believed that low electron temperatures and large wall losses could be the driving phenomena leading to the globally low propulsive performance. A refined estimation of the thruster performance and ion velocities is provided next in Chapter 6 and 7 with both additional indirect (RPA and LIF) plume measurements and direct thrust measurements.

Chapter 6

Direct and Indirect Thrust Measurements [3]

> *"Mankind will not forever remain on Earth but, in the pursuit of light and space, will first timidly emerge from the bounds of the atmosphere and then advance until he has conquered the whole of circumsolar space."*
>
> - Konstantin Tsiolkovsky

This chapter emerges as a follow-up study on Chapter 5. Direct thrust measurements are performed on the thruster prototype using a pendulum thrust balance with mechanically amplified displacement. Plasma plume diagnostics are also used to estimate the thruster partial efficiencies, to understand the main losses, and to perform a comparative analysis between directly and indirectly measured thrust.

The rest of the chapter is organized as follows. A short introduction to ECRT thrust measurements is presented in Section 6.1. In Section 6.2, the novelties introduced in the ECRT assembly, the thrust balance, the plasma probes, and their assembly in the vacuum chamber are presented; further details regarding the thrust balance calibration system and procedures are presented in Section 6.2.3. In Section 6.3, the thrust and plume measurements are shown and discussed. Finally, Section 6.4 summarizes the conclusions of this work.

---

[3]This chapter reproduces with adaptations the submitted journal paper: M. R. Inchingolo, M. Merino, M. Wijnen, and J. Navarro-Cavallé, "Thrust Measurements of a Waveguide Electron Cyclotron Resonance Thruster", Journal of Applied Physics, 2024 [67].

6.1   Introduction

As discussed in Chapter 1, thrust balance (TB) measurements have previously been performed on ECR thrusters. The first measurements were taken by Crimi and Miller in the '60s [36, 141, 33] who measured the magnetic thrust on the Mark VA-S thruster. Both noble gases (Ar, Kr, Xe) and mercury propellant were tested, however, the measurements for noble gases were undermined by entrainment and out-gassing. The thrust efficiency for the mercury propellant was found to be less than 10%.

In Ref. [45], Vialis *et al.* performed the first direct thrust measurements on a coaxial ECR thruster, measuring 1 mN of thrust with a thrust efficiency up to 11% (50W and 1 sccm of Xenon). In a more recent study, Peterschmitt *et al.* [54] performed the first comparison of thrust measurements between coaxial and waveguide-coupled ECR thrusters using Xenon as a propellant. The tested waveguide thruster was designed with the same dimensions and operated at the same working point as the coaxial version (diameter $D = 27.5$ mm, length $L = 20$ mm), 10–50 W of deposited power at 2.45 GHz for 1 sccm of Xenon propellant mass flow rate. To allow MW propagation in a waveguide of the same diameter as the coaxial thruster, a dielectric filling was used at the MW injection point. The different plasma-wave coupling resulted in thrust efficiencies of 5% and 1% respectively for the coaxial and waveguide thrusters. Additionally, a larger plume divergence and lower ion energy were found for the waveguide architecture.

In the previous chapter, electrostatic probe measurements and estimations suggested thrust levels and thrust efficiency below 1 mN and 2% respectively, input MW in the range of $80 - 300$ W at $1 - 4$ sccm of Xenon mass flow rate. Here, the first direct thrust measurements performed on this prototype are presented. These are also the first measurements of their kind for a Xenon-operated ECR waveguide thruster in this power range. These results are complemented by and compared against electrostatic probe measurements (Langmuir Probe, Faraday Cup, and Retarding Potential Analyzer) in the plume region, which allows for assessing and discussing partial efficiencies and thus the main loss mechanisms. This study also brings attention to the limits of typical indirect thrust measurements on similar devices and how they compare with direct ones.

6.2   Experimental setup

6.2.1   Thruster and power transmission line description

The same ECRT prototype described in chapters 3 and 5, has been used for this campaign. Previously, a two-hole injector was used, but this introduced visible

plasma azimuthal inhomogeneities in the plume. To reduce this effect, a multi-hole injector with 12 orifices of 1 mm in diameter is used in this experiment (Injector v2). These holes are uniformly distributed in a circular ring (i.e. lateral side of the PC, 2 mm downstream from the quartz window or backplate). Behind these orifices, two concentric annular cavities separated by a perforated wall, all made of stainless steel, help equalize the internal neutral gas pressure before being injected into the PC. The external cavity is connected to a threaded stainless steel tube that feeds the thruster with the propellant, Xenon.

The mounting on the thrust balance (TB) interface is shown in figure 6.1. To keep the thruster electrically floating and the magnetic field generator aligned to the discharge chamber, the same thruster mounting scheme of Chapter 5 was used. Therefore, the mounting plate, which keeps the overall alignment, is directly attached to the thrust balance as shown in figure 6.1. The PC exit plane and center-line define the coordinate system as displayed in figure 6.1. Although the electromagnet was kept mounted, this has not been used in this work, thus all the results shown in this chapter are obtained for the magnetic field generated by the PM alone.

In the previous chapter, it has been shown that the thruster can ignite with a mass flow rate up to $\dot{m}_p = 40$ sccm. However, the measurements reported here are only conducted at $\dot{m}_p = 2$, 4, and 8 sccm where better performance is expected.

Concerning the waveguide transmission line, since up to 50% reflected power was experienced in past experiments [66], a manual three-stub tuner has been added downstream of the directional coupler. Thanks to this component, the reflection coefficient (equation 5.2) is kept below 6% at the directional coupler for all thruster operating points. Consequently, the delivered power uncertainty is below 15%. An additional difference from the previous setup is an upgrade of the power meters connected to the directional coupler. Two Ladybug LB479A are used in this study.

6.2.2 Diagnostics

The vacuum chamber facility is the same as the one presented in Chapter 5. The thruster outlet section is about 2 m away from the chamber downstream wall and it is aligned with the chamber center line, aiming to minimize the plume-chamber wall interaction. As depicted in figure 6.1, the plasma discharge chamber and the magnetic field generator are directly attached to the TB interface. The TB used in this work has been presented extensively in reference [142], however, some additional upgrades have been introduced regarding the calibration system (see Section 6.2.3 for further details). The TB is based on the Variable Amplitude Hanging Pendulum with Extended Range (VAHPER) design by Polzin *et al.* [143]. The main peculiarity of this design is that it relies on a mechanical amplification of the displacement. For the case of the TB in this analysis, the angular displacement is amplified by a
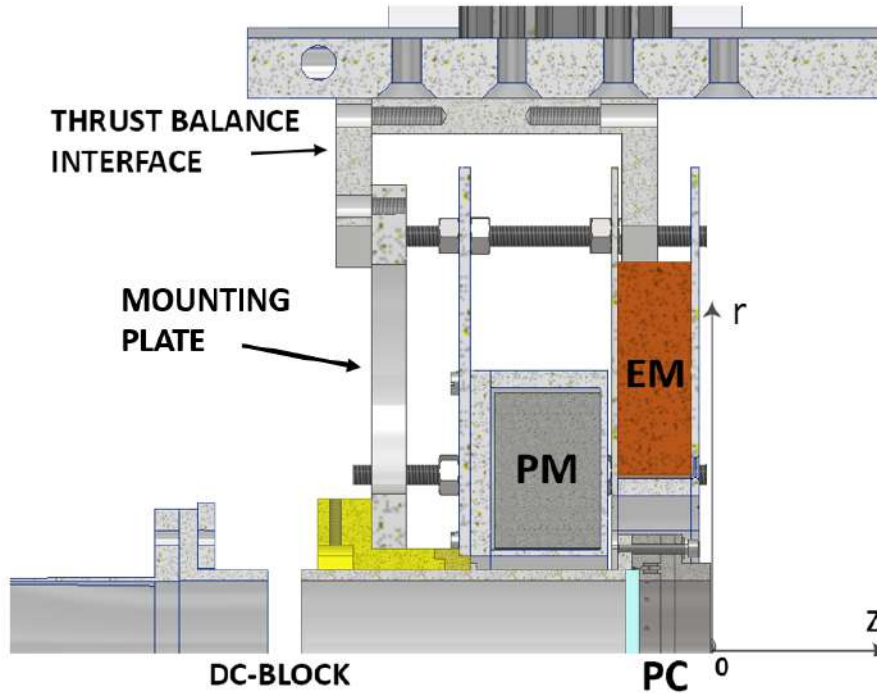
Figure 6.1: Cross section of the thruster assembly, PM stands for permanent magnet, EM for electromagnet and PC for plasma chamber. All the thruster elements (backplate holding the PC-waveguide, EM, and PM) are fixed mechanically to the thrust balance mechanical interface.

factor of 31 [142] at the sensor position. The displacement response of the TB is directly proportional to the thrust force, and the proportionality constant, which depends essentially on the mass distribution of the system (including the thruster) and stiffness of the hinges, is determined by means of calibration. In reference [142], a calibration system based on a voice coil was used. The voice coil applied a calibrated force to the vertical arm, causing a controlled displacement. In the case of permanent magnet thrusters, such as the one used in this work, the force applied by the voice coil may be affected by the interaction with the permanent magnet magnetic field, which is not negligible at the voice coil location. To avoid this problem, a new calibration system based on the use of pre-calibrated weights applied to an additional horizontal arm has been implemented. This calibration system, together with the TB measurement procedure is further discussed in section 6.2.3. On a side note, the DC-block axis and the thrust force vector are aligned, therefore an electric force, due to the thruster discharge chamber floating potential, V_T, between the two DC-block sides would be seen as a thrust. However, this force is estimated to be in the μN range in the experimental conditions here described and, therefore is considered negligible. This has been confirmed by actively biasing the thruster to up to 200 V (value higher than the V_T here measured), which did not result in any appreciable displacement on the thrust balance.

In addition to the TB, intrusive electrostatic probes were used: a Retarding

Potential Analyser (RPA), a Faraday Cup (FC), and a Langmuir Probe (LP). These were mounted on the polar probe positioning system located in front of the thruster as seen in Chapter 5.

The RPA (Impedance-Semion single button, four grids probe) was positioned at a distance of $\rho = 350$ mm from the thruster exit plane and used to assess the ion energy distribution function (IEDF), and ion mean energy, in the far plume. The FC measured the ion current profile and provided information on the utilization efficiency and plume divergence. The probe is equipped with an aperture diameter of $D_{FC} = 10$ mm. A bias of -120 V was typically used at the FC collector, a higher voltage resulted in the divergence of the collected ion current, being likely affected by either sheath expansion outside of the probe and/or secondary electron emission, increasing the effective aperture area ($A_{FC} = \pi D_{FC}^2/4$). The probe scanned the plume on a plane at constant $\rho = 350$ mm varying α within $-\pi/2 < \alpha < \pi/2$. Additionally, the Langmuir probe provided supplementary information on the local electron temperature, which was used to improve the understanding and discussion of the results. Ref. [124] provides more information about the design and operation of the Langmuir and FC probes used in this work. Propagation of uncertainty was used to assess the measurement error for the data presented in Section 6.3. Finally, the thruster discharge chamber floating potential V_T was acquired during the overall test campaign to assess the stability of the thruster's operating point while performing thrust balance and probe measurements.

6.2.3 Thrust Balance calibration system and thrust measurement procedure

This section describes the new calibration system employed for the thrust balance described in [142]. The use of calibrated masses for thrust balance calibration is an accurate, repeatable, and reliable means to obtain the displacement/force relation characteristic of the thrust balance assembly. Systems such as the ones described in [144, 145, 143] all rely on the use of calibrated masses (typically fishing weights) loaded on a wire. In those systems, their weights directly apply an equivalent thrust force on the pendulum by using a pulley; However, systems of that kind are subject to friction between the pulley and the wire, which must be taken into account for a precise measurement [144].

The system here described uses an additional calibration arm, perpendicular to the pendulum axis of length $L_{cal} = 170$ mm, the masses apply their weights on the arm, hence a torque is applied on the pendulum without the need for a pulley. A schematic representation of the new calibration system is presented in figure 6.2-a. The calibrated weights have a mass of $m_{cal} \approx 0.5$ gr. A precise measurement of their mass is obtained with a mass balance (Shimadzu AUW220D) with an accuracy in the mg range. These masses are loaded on a thin nylon wire ($\varnothing = 0.16$ mm) separated

by a distance of 25 mm, one end of the wire is attached to the calibration arm, while the other side is wrapped around a spool driven by a stepper motor. The reference for the spool angular position is provided by a limit switch which is pushed by a mechanical pin mounted on a second disk. The latter and the pulley are both 3D printed and equipped with gears. The gear ratio between them is 5, allowing up to five full rotations of the spool. A CAD representation of the assembly is provided in figure 6.2-b. As the spool is rotated, the masses are lowered and their weight is applied one by one on the calibration arm. This creates a torque on the TB that is recorded as displacement by the displacement sensor. The displacement provided is equivalent to the one given by a thrust force $F_{teq} = F_{cal}L_{cal}/L_t$, where L_t is the thrust vector distance from the vertical arm pivot point. The latter has been measured to be $L_t = 686.5$ mm. In order to keep the wire constantly under tension, at least one weight is always applied on both of its sides. In this work, between 3 and 5 weights are applied in total during the calibration procedure. A typical calibration output displacement is shown in figure 6.3. For this particular case, the calibration factor k_{cal} found for the balance is $k_{cal} = 66.88$ mN/mm with a relative uncertainty of 0.044%. Once k_{cal} is obtained, the thrust F_{TB} is simply obtained with

$$F_{TB} = \frac{L_{cal}}{L_t}k_{cal}y = \kappa_s y, \tag{6.1}$$

where y is the displacement due to the thrust force and κ_s is the equivalent stiffness of the balance.

Although the TB is equipped with a cooling system, thermal loads affect the position of the pendulum+thruster barycenter leading to TB displacement to drift with time. Thus, calibrations are performed before and in between thrust measurements to correct for this drift.

Thrust measurements are performed as follows: the desired $\dot{m}_p$ is set on the mass flow controller, the input power is set on the MW generator to obtain the thruster ignition, the thruster is ignited and left on for the time necessary to reach the steady state, condition monitored using V_T and Γ_L^2. Then the power and the mass flow are cut. The reference for the TB displacement is thus taken. An example of thrust measurement is shown in figure 6.4. A similar procedure is carried out for performing the neutral thrust measurements shown in figure 6.12-a, however for this case, no microwave power is provided as input.
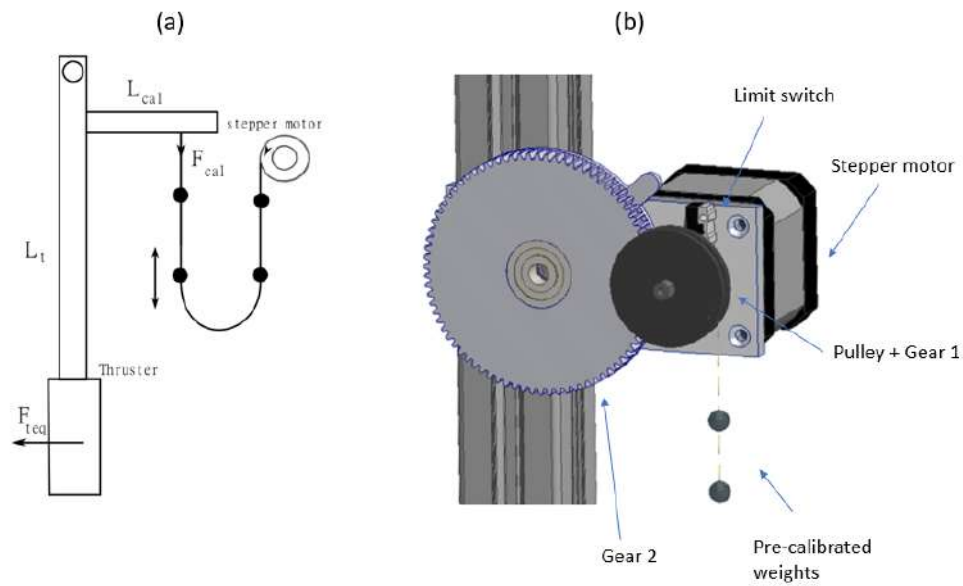
Figure 6.2: (a) Schematic representation of the weights calibration system. (b) CAD view of the weight calibration system.
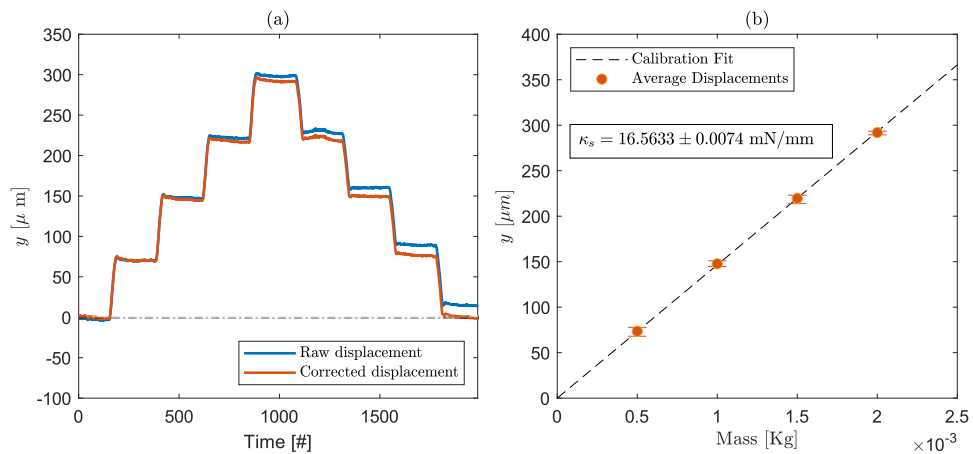
Figure 6.3: (a) Typical calibration output displacement. (b) Calibration curve resulting from the post-processing of the displacement in panel-a.
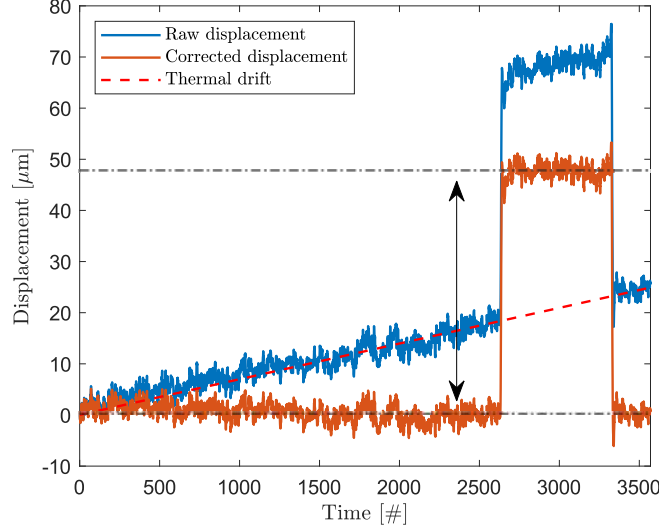
Figure 6.4: Example of thrust measurement. The water cooling system was on during this measurement.

6.3   Results

Results are organized as follows. First, the direct thrust measurements for a series of power and mass flow rates are presented and discussed in Section 6.3.1. In Section 6.3.2, the underlying physical mechanisms driving these performances are discussed with the help of plume measurements which are carried out with electrostatic probes (FC, RPA and LP). Additionally, the RPA measurements have shown the existence of high-energy electrons within the plume. These results and their consequences are discussed in Section 6.3.3. In Section 6.3.4, the overall data acquired through electrostatic measurements allow isolating the different contributions to efficiency, identifying those mechanisms that harm the overall thruster efficiency and providing an interpretation for the efficiency trends seen with direct thrust measurements. Lastly, Section 6.3.5 analyzes the primary sources of difference between the direct and indirect measurements conducted in this study.

6.3.1   Direct thrust measurements

Thrust measurements have been performed for three Xenon flow rates, $\dot{m}_p = 2$, 4 and 8 sccm, and power in the range $P_T = 60 - 350$ W. The TB described above has been used to evaluate the thrust produced by the ECRT, F_{TB}. Once thrust is measured, the specific impulse I_{sp} and thrust efficiency η_F can be computed as follows,

$$I_{sp} = \frac{F_{TB}}{\dot{m}_p g_0}; \qquad\qquad \eta_F = \frac{F_{TB}^2}{2\dot{m}_p P_T}. \qquad\qquad (6.2)$$

Results for F_{TB}, I_{sp} and η_F are shown in figure 6.5. The measured thrust levels fall in the range $F_{TB} = 1\text{--}3.5$ mN and scale almost linearly with power at a constant Xe flow rate. The maximum thrust, 3.5 mN, is reached at the working point of 8 sccm and 350 W. The thrust-to-power ratio, F_{TB}/P_T is also computed and lies between 5 and 20 mN/kW, decreasing with power for 2 and 8 sccm but staying rather constant for the case at 4 sccm. Repeated measurements under the same thruster operating condition typically yielded values within 5% of the reported ones.

The highest specific impulse, 800 s, was obtained at 2 sccm and 260 W. On the contrary, the lowest was reported for 8 sccm and 80 W, being only 200 s. Specific impulse I_{sp} scales well with $\sqrt{P_T/\dot{m}_p}$. The data points in the explored range can be fitted, with an average thrust efficiency of $\eta_F = 2.34\%$.
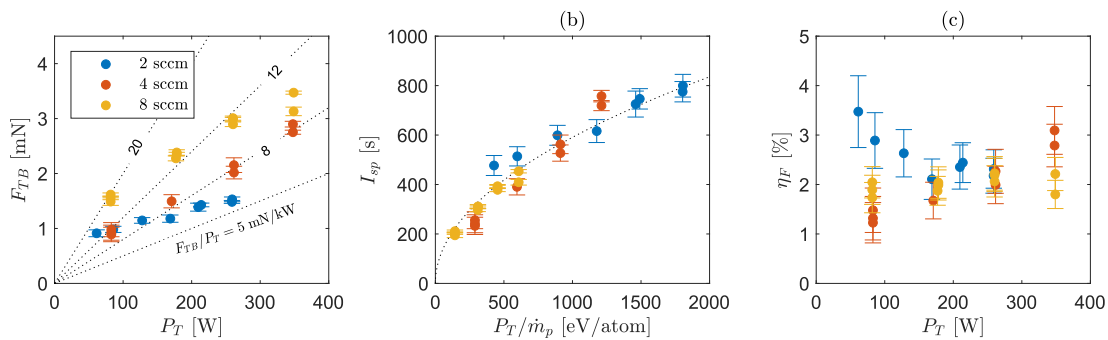
Figure 6.5: Direct thrust measurement results for a set of different $\dot{m}_p$ and power. (a) Measured thrust F_{TB}, the constant thrust-to-power ratio levels are shown as dotted lines. (b) Specific impulse I_{sp} as a function of $P_T/\dot{m}_p$. In the range studied, the latter scales well with $\sqrt{P_T/\dot{m}_p}$, the dotted curve represents the fitted I_{sp} at constant thrust efficiency $\eta_F = 2.34\%$. (c) Thrust efficiency η_F. Error bars have been obtained by the propagation of measurement uncertainties.

The thrust efficiency η_F ranges in 1–3.5% in the tested cases, being lower than the ones reported by Crimi with mercury propellant [33] at higher power levels ($\eta_F \approx 10\%$ at 800 W and 0.3 mg/s), but not far from those obtained by Peterschmitt ($\eta_F = 1\%$ at 25 W, 1 sccm of Xenon) [54].

No clear dependence on the mass flow rate and power was found for the thrust efficiency: η_F decreases with power for 2 sccm; it increases for 4 sccm; and remains fairly constant for 8 sccm.

6.3.2 Electrostatic probe measurements
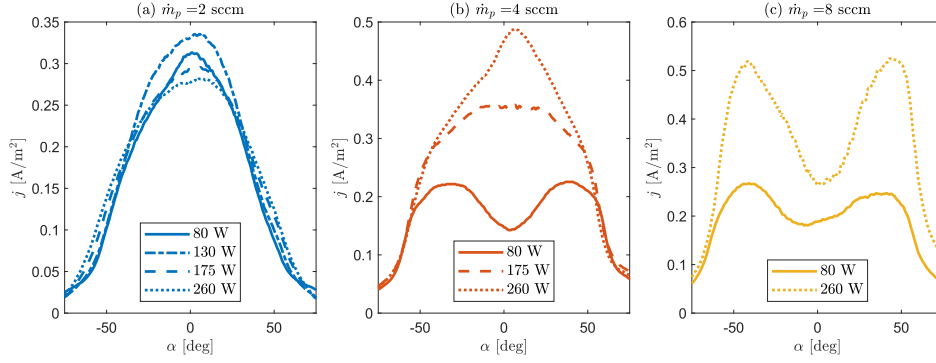
Figure 6.6: Faraday Cup ion current density profiles for $\dot{m}_p = 2$ sccm (a), $\dot{m}_p = 4$ sccm (b) and $\dot{m}_p = 8$ sccm (c), and various power levels. By considering the accuracy of current measurements and probe aperture diameter, the error on the measurement of j_i is estimated to be below 2%.
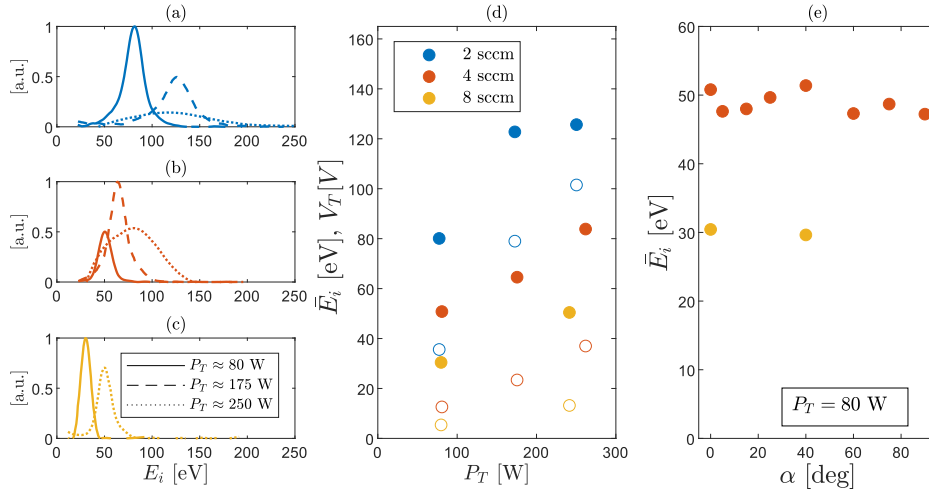
Figure 6.7: Retarding Potential Analyzer (RPA) measurements. (a-c) Ion energy distribution function (IEDF) for $\dot{m}_p = 2 - 4 - 8$ sccm (blue, red and yellow respectively). Solid, dashed, dotted lines indicate 80, 175 and 250 W respectively. (d) Mean ion energy $\bar{E}_i$ (filled dots) based on the IEDF results, and thruster floating potential V_T (empty dots). (a-d) measurements are taken on-axis at $\rho \equiv z = 350$ mm. Note that for the highest power case, the reflection coefficient was not constant, being $\Gamma_L^2 = 5$, 1 and 8% for 2, 4 and 8 sccm respectively. Thus the delivered power level resulted to be $P_T = 250$, 260 and 240 W. An average of 250 W is displayed in the legend. (e) Mean ion energy $\bar{E}_i$ at different azimuth angles (same $\rho = 350$ mm), only for 4 and 8 sccm (red and yellow) at 80 W. The uncertainty on $\bar{E}_i$ was estimated with uncertainty propagation to be <5% for the shown cases.

To understand the underlying physical mechanisms driving the observed performance, plume measurements were taken with electrostatic probes. The same mass

$$P_T = 80 \text{ W}$$

$\dot{m}_p = 2$ sccm $\dot{m}_p = 4$ sccm $\dot{m}_p = 8$ sccm
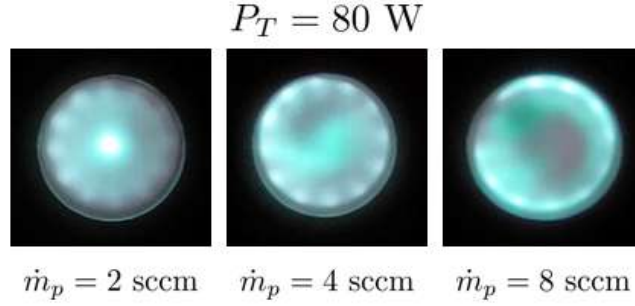
Figure 6.8: Front-view photographs of the ECRT discharge chamber while firing at $P_T = 80$ W. The Injector v2 is used.

flow rates as in Section 6.3.1 were tested (2, 4, and 8 sccm), for a subset of the power levels in figure 6.5. The FC ion current density as a function of the angular position, $j_i(\alpha)$, is shown in figure 6.6. j_i results from dividing the collected current by the aperture area of the probe, and is expressed as $j_i = I_{FC}/A_{FC}$. At 4 and 8 sccm, the increase of power leads to a larger amount of collected current at small angles, while at large azimuth angles, the power increase seems to play a little role in the collected current. At the lowest mass flow rate, 2 sccm, the effect of increasing power is unclear, a maximum on-axis current density is obtained for 130 W. In general, two qualitatively different ion current density profiles are observed, featuring a singly- or doubly-peaked plume ("hollow plume"). This structure, and also a triply-peaked plume, were observed in previous experiments (see Chapter 5)[66]. The transition from a double peak to a single peak profile depends on the power-to-mass flow rate ratio. The threshold for the transition to the single peak is found to be about $P_T/\dot{m}_p \gtrsim 500$ eV atom^{-1}. Thus, for the explored cases this transition is only observed at 4 sccm, while the 2 sccm and 8 sccm cases remain at the single/double peak profile respectively. This ion current profile structure might be linked to the propellant being injected in the radial direction (i.e. from the lateral walls of the PC). Additional measurements of the electron temperature, taken 130 mm downstream from the thruster outlet by means of the LP, confirm that the temperature on-axis of the ejected beam is lower (4 eV) than that off-axis (6 eV) at the same axial distance and $\alpha = 40$ deg. This suggests that, for low $P_T/\dot{m}_p$, there could be a tendency for power to be coupled more efficiently in the vicinity of the walls (i.e. gas injection location), potentially promoting ionization there, which, in turn, might lead to the formation of this hollow plume structure. To further investigate this hypothesis and obtain clues on MW power absorption, simulations employing similar approaches to those used in Ref. [56, 59] should be performed.

A confirmation of the considerations discussed above comes from figure 6.8 which shows front-view photographs of the discharge chamber during firing for $P_T = 80$ W. Increasing the mass flow rate moves the emitted visible light (produced by ionization/excitation processes) from the center towards the thruster walls. A similar

trend is also observed when the power is reduced at a fixed mass flow rate. This effect was already noticed in Chapter 5, demonstrating to be independent of the number of radial injector holes. Obviously, a large plasma production in proximity to the thruster walls is expected to lead to increased wall losses. On a side note, these pictures show as well the improvements in the azimuthal plasma homogeneity within the PC after the substitution of the propellant Injector v1 with Injector v2, being particularly effective at low mass flow rate.

The RPA is used to extract information on the ion velocity distribution function (IVDF) in the ρ direction, as a function of the ion kinetic energy K_i: $f(K_i)$ [146, 147]. Assuming the presence of singly charged ions only,

$$f(K_i) \propto \partial I_c / \partial V_{G2}, \tag{6.3}$$

$$K_i = \frac{1}{2} m_i v_i^2 = e(V_{G2} - \phi), \tag{6.4}$$

where I_c is the current collected by the RPA, V_{G2} is the ion energy scanning grid bias, v_i the local ion velocity and ϕ the plasma potential at the measurement location, m_i and e are the ion mass and the electron charge respectively. The resulting curve is the convolution of the actual IVDF with the probe apparatus transfer function. In the absence of information about the latter, in the rest of this study, the effects introduced by the probe apparatus are neglected and no corrections are applied to the IVDF. The ion mechanical energy, E_i, is defined as the sum of kinetic plus potential energy, $E_i = K_i + e\phi = eV_{G2}$. Thus, by assuming that along the expansion E_i is fully converted into kinetic energy and that the regime is collisionless, it is possible to obtain the ion energy distribution function (IEDF) for $\phi = 0$, i.e. at the vacuum chamber walls:

$$g(E_i) = \frac{1}{\sqrt{2m_i E_i}} f(E_i). \tag{6.5}$$

The obtained IEDFs are shown in figure 6.7 for the three mass flow rates and power levels. Looking at the shape of the IEDFs (panels a-c), the increase of power at constant mass flow induces a wider spread of the ion energies. Results in agreement with these were obtained through LIF measurements performed on this thruster in [68] where the spread in ion energies was referred to as axial kinetic temperature. In the present study, ion temperatures in the order of $4000 - 10000$ K were found for most of the cases. This is likely the effect of a widening of the ionization region over the acceleration region, i.e. ionization might happen at different potentials, and consequently, ions would reach different axial velocities at the measurement point, which is read as a spread of the IEDF. As a result, at high $P_t/\dot{m}_p$, some ions can reach $E_i > 200$ eV (2 sccm at 250 W). Panel 6.7-d shows the mean ion energy $\bar{E}_i = \langle E_i \rangle$ for the different working points. Overall, the trend is roughly linear with $P_T/\dot{m}_p$, which is coherent with the trend found for the specific impulse in figure 6.5-b with $\sqrt{P_T/\dot{m}_p}$. Similar trends were expected but not found by Sercel *et al.* in Ref. [19], likely due to larger variations of η_F in the range explored in that work. The
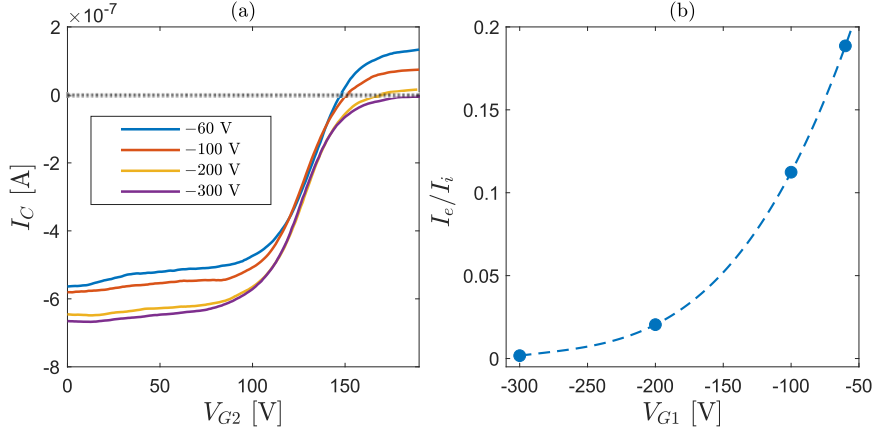
Figure 6.9: (a) RPA characteristic IV curves at four different biases of the primary electron repelling grid G1 (-60, -100, -200, -300 V). (b) Ratio of the electron to ion currents collected by the RPA. (a) and (b) have been obtained for one single operating point, $P_T = 175$ W, $\dot{m}_p = 2$ sccm. The RPA settings for the rest of the grids and collector are: G0 is floating and used as a reference potential, $V_{G2} = 0 - 190$ V, $V_{G3} = V_C - 10$ V and $V_C = V_{G1}$ V.

maximum here reported $\bar{E}_i$ is about 130 eV for 250 W and 2 sccm. This panel shows as well the floating potential with respect to the ground of the metallic walls of the thruster, denoted as V_T (empty circles). Because of the wall sheath and the spatial spread of the ionization region, V_T does not equal the mean ion energy. However, it exhibits the same trend as $\bar{E}_i$. Hence, in the absence of IEDF measurements, V_T could be used instead as a proxy to estimate mean ion energy. Panel 6.7-e shows that $\bar{E}_i$ barely depends on the azimuth angle, this observation will come in useful in Section 6.3.4.

Referring to equation 6.4, $v_{i\infty}$ is defined as the velocity of ions at the location where $\phi = 0$. The average ion velocity $u_{i\infty} = \langle v_{i\infty} \rangle$, ranges from 6.6 to 13.4 km/s, as obtained at the working points of 80 W, 8 sccm, and 250 W, 2 sccm, respectively. It is possible to define $\kappa_2 = \langle v_{i\infty}^2 \rangle / u_{i\infty}^2$ and $\kappa_3 = \langle v_{i\infty}^3 \rangle / u_{i\infty}^3$ being ratios of different moments of the velocity distribution function. These parameters provide information on the dispersion of the ion velocities, and for the data presented here, they result being $1 < \kappa_2 \leq 1.02$ and $1.02 \leq \kappa_3 \leq 1.08$. These will be used in Section 6.3.4.

6.3.3 Suprathermal electrons

Previous work on ECRTs [33, 54] has shown preliminary evidence of the existence of high-energy electrons in the plume. In both studies, electrostatic probes were used for the detection. Crimi *et al.* found such electrons in a waveguide ECRT (1-2 kW power range) by using an RPA, noting that biases up to -630 V on the primary electrons repelling grid were necessary to effectively repel all the electrons and only collect ions. On the other hand, Peterschmitt *et al.* [54] only found evidence of

energetic electrons in their coaxial ECRT prototype but not in the waveguide version. The experiments were done by using a Faraday cup to measure the current density at different collector biases, and a bias up to -300 V was found to be necessary to repel all the electrons.

Suprathermal electrons were also found for the thruster used in this study by using an RPA. As mentioned in Section 6.2, the RPA used is composed of four grids: the external grid (G0) which is exposed to the plume, the primary electron-repelling grid (G1), the ion energy scanning grid (G2) and the secondary electron repelling grid (G3). Downstream the grids lies the collector (C).

On-axis RPA scans at different G1 biases, V_{G1}, were taken for the case at $P_T = 175$ W and $\dot{m}_p = 2$ sccm. The I_C-V_{G2} curves resulting from the sweep of G2, are shown in figure 6.9-a. In the absence of electrons within the probe, negative collected currents ($I_C < 0$) are representative of ion currents and should tend to zero as V_{G2} is increased and all the ions are repelled. Interestingly, for $V_{G1} > -300$ V, and V_{G2} sufficiently large to repel all the ions, I_C is positive. This behavior is compatible with the collection of primary electrons with enough energy to overcome the repelling electric field established by G1, effectively behaving as an additional positive constant collected current along the IV curve. Other phenomena, such as secondary electron emission from the collector surface or ionization within the probe, are also known to be possible causes of deviations from the expected IV curve of an RPA. However, both effects would be observed as an additional negative current, thus they cannot explain the observed trend.

The performed test allows for estimating the amount of electron current reaching the collector depending on V_{G2}, under the assumption that primary electrons and single ions are the only species contributing to the current collection, and the grid transparency is the same for electrons and ions. The electron to ion collected current ratio, I_e/I_i is provided in panel 6.9-b, where I_e is obtained from the value of the I-V curve at sufficiently large V_{G2} ($\simeq 180$ V) and $I_i = I_C(V_{G2} = 0) - I_e$. The estimation of I_e/I_i has been done at four levels: V_{G1} = -300, -200, -100 and -60 V. In this range, I_i was found to be essentially independent on V_{G1} showing a variation of only 3.7%. Therefore, the current variation only comes from electron collection. These results suggest that electrons with an energy tail of up to 300 eV exist in the plume. At the same location and working point, an electron temperature of only $T_e = 11.5$ eV was measured with an LP. Hot electrons were not found at higher $\dot{m}_p$ and/or lower power levels, suggesting that their presence and energy depend on $P_T/\dot{m}_p$.

These conclusions might explain the absence of these electrons for the waveguide thruster of Ref. [54] since a maximum $P_T/\dot{m}_p$ of about 725 eV/atom was used in that study, about 40% lower than the one for the case shown in figure 6.9.

The existence of suprathermal electrons in ECR thrusters invalidates the common assumption of Maxwellian electron distribution, and further work must assess

their effects on expansion physics. Numerical studies [148, 149] have shown that, under certain circumstances, hot electrons could lead to the formation of a double layer across the plume expansion, perhaps similar to the one encountered by helicon plasma thruster experiments [150]. However, to the authors' knowledge, a double layer has not been observed yet in an ECRT and the origin and role of these energetic electrons on the plume expansion is not yet clear.

On the other hand, these measurements highlight the necessity for additional care when biasing electrostatic probes for magnetic nozzle ECR thrusters. This is particularly true for FCs since the collection of high-energy electrons would lead to an underestimation of the ion current density as seen by Petershmitt in [54]. With the assumption that electron-to-ion current ratios similar to those shown in figure 6.9-b, apply when using a Faraday Cup biased at -120 V (typical value used for the cases studied), the ion current collected could be underestimated by up to about 10%.

6.3.4 Assessment of partial efficiencies

Electrostatic probe measurements can be used to identify where performance losses occur by breaking down thrust efficiency into the product of several partial efficiencies, each associated with a different physical process in the operation of the device. In order to do this, certain hypotheses must be invoked. First, it is assumed that the collected ion current density consists of singly charged ions only. Second, the ion expansion is collisionless, axisymmetric, and conical from the location where the measurements are carried out ($\rho = 350$ mm) to infinity. Additionally, it is assumed that $\bar{E}_i(\alpha)$ does not vary much with the azimuthal angle, and therefore we take $\bar{E}_i(\alpha) = \bar{E}_i(0)$, which is partially supported by figure 6.7-e. To derive the partial efficiencies, we first introduce the integrals of different moments of the ion velocity distribution function.

The ion beam current I_i and its axial component I_{zi} are defined as:

$$I_i = 2\pi\rho^2 \int_0^{\pi/2} \bar{j}_i(\alpha)\sin(\alpha)\,\mathrm{d}\alpha, \tag{6.6}$$

$$I_{zi} = 2\pi\rho^2 \int_0^{\pi/2} \bar{j}_i(\alpha)\cos(\alpha)\sin(\alpha)\,\mathrm{d}\alpha, \tag{6.7}$$

being $\bar{j}_i(\alpha) = 0.5 \cdot (j_i(\alpha) + j_i(-\alpha))$ the symmetrically averaged ion current density profile obtained from the FC measurements presented in figure 6.6.

The ion momentum in the z direction $F_i(\rho)$ and beam power $P_i(\rho)$ through a

spherical surface of radius ρ around the source are

$$
\begin{aligned}
F_i(\rho) &= 2\pi\rho^2 \int_0^{\pi/2} \sin\alpha\, m_i \, d\alpha \int v_i v_{zi} f(v)\, d^3 v \\
&= 2\pi\rho^2 \int_0^{\pi/2} \sin\alpha \cos\alpha\, m_i n u_i^2 \kappa_2 \, d\alpha \\
&= \frac{m_i}{e} I_{zi} u_i \kappa_2,
\end{aligned}
\tag{6.8}
$$

$$
\begin{aligned}
P_i(\rho) &= 2\pi\rho^2 \int_0^{\pi/2} \sin\alpha \frac{1}{2} m_i \, d\alpha \int v_i^3 f(v)\, d^3 v \\
&= 2\pi\rho^2 \int_0^{\pi/2} \sin\alpha \frac{1}{2} m_i n u_i^3 \kappa_3 \, d\alpha \\
&= \frac{m_i}{2e} I_i u_i^2 \kappa_3 = \frac{I_i \bar{E}_i \kappa_3}{e\kappa_2},
\end{aligned}
\tag{6.9}
$$

where κ_2 and κ_3 are defined in Section 6.3.2. The dependence of F_i and P_i on the radial distance is due to the ions continuing their acceleration along the potential drop in the plume. At $\rho \to \infty$, $u_i \to u_{i\infty}$ as $\phi = 0$ and $\kappa_2(\rho), \kappa_3(\rho) \to \kappa_2, \kappa_3$ far downstream. Consequently, we can define $F_{i\infty}$ and $P_{i\infty}$.

Understanding that the largest thrust contribution in an efficient thruster is provided by the ion momentum, the thrust efficiency is approximated by:

$$
\eta_F \approx \frac{F_{i\infty}^2}{2\dot{m}_p P_T} = \eta_u \eta_d \eta_e \eta_s,
\tag{6.10}
$$

where:

$$
\eta_u = \frac{I_i m_i}{\dot{m}_p e},
\tag{6.11}
$$

$$
\eta_d = \left(\frac{I_{zi}}{I_i}\right)^2,
\tag{6.12}
$$

$$
\eta_e = \frac{P_{i\infty}}{P_T},
\tag{6.13}
$$

$$
\eta_s = \kappa_2^2/\kappa_3,
\tag{6.14}
$$

are the utilization, divergence, energy, and dispersion partial efficiencies, respectively.
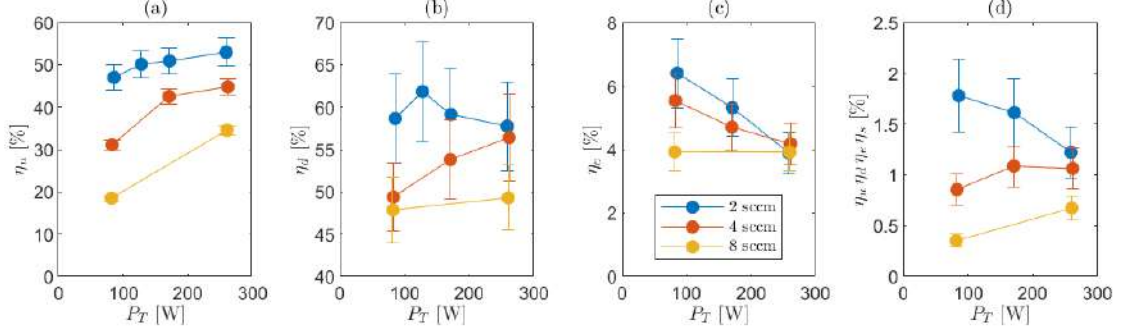
Figure 6.10: Partial efficiencies η_u, η_d, η_e as a function of P_T estimated from the electrostatic probe measurements, for $\dot{m}_p = 2 - 4 - 8$ sccm, blue, red and yellow respectively. (d) Shows the product $\eta_u \eta_d \eta_e \eta_s$ representing an indirectly estimated thrust efficiency, as opposed to the direct measurements shown in figure 6.5-c.

The dispersion efficiency, η_s, accounts for the spread in ion velocities in the radial direction ρ and has the smallest impact on the performance of the device. In fact, using the IEDFs available in figure 6.7, this quantity ranges between $0.97 \leq \eta_s < 1$.

The rest of the partial efficiencies computed according to equations 6.11-6.13 are shown in figure 6.10. Some general conclusions can be extracted. First, the utilization efficiency η_u increases roughly with $P_T/\dot{m}_p$ within the explored range. This is expected because, with more energy per electron available, ionization collisions become more likely to occur, improving the ionization rate. Nevertheless, η_u seems to saturate with power, to a value that decreases with the mass flow rate. At 2 sccm, the highest η_u obtained is around 53%. This means that even at this relatively high $P_T/\dot{m}_p$, the thruster is not able to produce a well-ionized beam.

Second, the divergence efficiency η_d (figure 6.10-b) depends directly on the ion current density profile which, as already discussed, can present one or two peaks. For the 2 sccm cases, which present a single peak profile, the increase of power barely modifies the current profile shape. Thus, the divergence efficiency is almost constant at about 60 %, however, a peak of η_d appears at 130 W. Looking at the corresponding ion current density profiles (figure 6.6-a) the ion current on axis increases going from $P_T = 80$ to 130 W, nevertheless it decreases when going to higher powers (as the current at large angles increases). A possible explanation for this trend might be associated with a larger amount of high-energy electrons collected by the FC when the power is raised, as it has been already discussed in Section 6.3.3. At 8 sccm, the plume profile shows two peaks in the range studied. Since more current is found on this annular structure ("hollow plume"), this results in a lower efficiency, roughly about 48%, but almost constant with P_T. For the intermediate case at 4 sccm, the transition from double to a single peak guides the increase of η_d with P_T.

Third, the energy conversion efficiency η_e (figure 6.10-c) stays below 7% for all the tested operating points. Note that, by defining η_e as equation 6.13, any power

deposited on the neutrals or the residual thermal energy on the electrons is neglected. This is clearly the lowest partial efficiency of those explored in this work and points to the large losses that exist in the discharge process as the main factor spoiling the performance. Inelastic collisional losses, the loss of neutrals, the particle and power fluxes to the PC surfaces, and the microwave power radiated away from the system, all can negatively affect η_e. In fact, these phenomena directly impact the mean ion energy $\bar{E}_i$ and ion current $\bar{I}_i$. The latter depends on the utilization efficiency, η_u, whereas $\bar{E}_i$ scales with the total potential drop in the plume, which is proportional to the electron temperature. Energy losses inside the PC, mainly inelastic collisions and plasma recombination at the thruster internal walls, lower T_e. Re-ionizing the propellant that recombines at the walls further lowers the electron temperature, increasing the losses.

At 2 sccm, η_e drops with power, indicating that the additional power does not translate into an efficient increase of the beam power. In fact, this extra power only induces a slight increase of the ion beam current i.e. higher η_u, and ion mean energy $\bar{E}_i$, but both magnitudes seem to be saturated with input power for this case. $I_i \cdot \bar{E}_i$ increases slower than P_T. This means that most of this extra power is diverted directly into power losses. The same reasoning applies for the 4 sccm case, but η_e decays at a lower rate with P_T, since the relative increase of $I_i \cdot \bar{E}_i$ is higher in the studied power range. At 8 sccm, η_e remains almost constant thanks to the noticeable increase of $I_i \cdot \bar{E}_i$, i.e. η_u almost doubles from 80 to 250 W, and $\bar{E}_i$ increases a factor of 1.7 approximately. Note that MW losses are likely not affecting η_e negatively, since as explained in Section 6.2, those are already taken into account in the estimation of P_T. Moreover, MW radiation from the thruster and power absorption at the quartz window are assumed to be negligible. As also observed in other devices [151] and in simulation results [152, 153], it is expected that the dominant loss mechanism are losses to the lateral and rear walls, together with excitation and (re-)ionization inelastic collisions. Indeed, the LIF measurements in Ref. [68], revealed a mean ion velocity of -500 m/s directed towards the backplate at $z = -10$ mm (middle of the discharge chamber) for the same thruster design as in this study.

An improved design of the magnetic field could help screen the lateral walls and reduce wall losses (magnetic shielding). However, the backplate, which is more difficult to shield, might still be subject to large plasma losses. Additionally, an improved design of the PC/injection may reduce the loss of neutrals and help increase η_u. Finally, to improve the divergence efficiency, a lower-diverging magnetic field outside of the thruster may be needed. However, as seen in figure 6.10-b for the 4 sccm case, a large contribution to the low η_d comes from the development of the hollow plume structure which is thought to depend on where the MW power is deposited and on the propellant injection.

As a result of the assumptions introduced in the estimation of the partial efficiencies, a discrepancy arises when comparing the thrust and thrust efficiency obtained
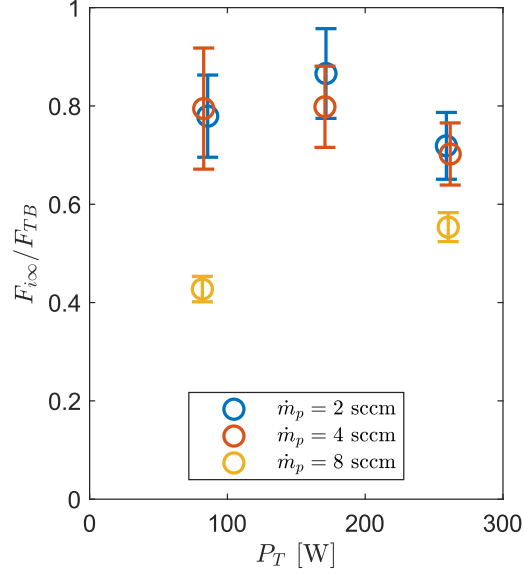
Figure 6.11: Ratio between the thrust estimated with electrostatic probes $F_{i\infty}$ (equation 6.8), and direct thrust measurements F_{TB}, for $\dot{m}_p = 2-4-8$ sccm respectively in blue, red and yellow.

with the TB with the one resulting from the indirect measurements (equation 6.10). Section 6.3.5 analyzes the main sources for this difference by comparing the direct and indirect thrust. Nevertheless, the product of the partial efficiencies presented here as in equation 6.10 can provide a qualitative interpretation for the different trends seen in η_F (refer to figure 6.5-c). This product is shown in figure 6.10-d. η_F for the 2 sccm case was shown to decrease with power, this trend is ascribed to the drop in η_e, since η_d and η_u stay rather constant. On the other hand, for the 4 sccm case, the transition from the hollow to single peak plume and the increasing utilization are enough to compensate for the slower decrease in energy efficiency, leading to a global increase of thrust efficiency with power. Lastly, at 8 sccm, the notable increase in η_u should logically result in a corresponding rise in η_F, given that η_d and η_e remain relatively constant. However, the absence of such a trend in figure 6.5-c may suggest a more pronounced discrepancy between direct and indirect measurements for this mass flow rate.

6.3.5 Direct vs Indirect thrust measurements

Table 6.1 and figure 6.11 compare the estimated ion thrust $F_{i\infty}$, evaluated as in equation 6.8, against the direct thrust measurements F_{TB}. The computed thrust is a fraction of the one measured by the TB, ranging between 43% and 86% of the latter. The thrust levels at 2 and 4 sccm show good agreement at lower power levels, but the agreement slightly reduces for the maximum power case (≈ 260 W). An opposite trend is observed for the working points at 8 sccm, however, $F_{i\infty}/F_{TB}$

m_p [sccm]	2			4			8	
P_T [W]	80	175	260	80	175	260	80	260
I_i [A]	0.067	0.073	0.076	0.090	0.122	0.128	0.106	0.198
I_{zi} [A]	0.052	0.056	0.058	0.063	0.089	0.096	0.073	0.138
η_u [%]	47.1	50.9	53.0	31.1	42.6	44.8	18.5	34.6
η_d [%]	58.7	59.1	57.7	49.4	53.8	56.4	47.8	49.3
η_e [%]	6.40	5.31	3.89	5.54	4.70	4.18	3.93	3.912
η_s [%]	99.2	99.2	97.4	99.4	99.1	99.3	99.1	99.1
$F_{i\infty}$ [mN]	0.76	1.03	1.08	0.74	1.19	1.46	0.66	1.62
$F_{e\infty}$ [mN]	<0.036	<0.049	–	<0.02	–	–	–	–
F_n [mN]	0.041	0.038	0.036	0.11	0.089	0.085	0.25	0.20
F_{TB} [mN]	0.98	1.19	1.51	0.93	1.49	2.08	1.55	2.96

Table 6.1: Table summarizing the data presented in Section 6.3.4 and Section 6.3.5. I_i and I_{zi} are the integral ion currents as defined in equations (6.6) and (6.7). η_u, η_d, η_e, η_s are the utilization, divergence, energy, and dispersion efficiencies as defined in equations (6.11)–(6.14). $F_{i\infty}$ and $F_{e\infty}$ are the ion and electron thrust contributions, following equations (6.8) and (6.16). F_n is the neutral thrust contribution from equation (6.17) for $T_n/T_n^0 = 3$. The direct thrust measurement F_{TB} is included in the next row for comparison.

is the lowest for this case, staying below 60%. In a similar way, in [45], Vialis *et al.* found that electrostatic probe measurements were underestimating direct thrust measurements of a coaxial ECRT by about 20% and partially attributed this effect to the intrusive nature of the FC. However, in the present study, no evident change in thruster performance was observed during FC operation.

The observed discrepancy between direct and indirect ion thrust estimation may stem from other contributions to thrust that have not been taken into account. The total thrust force, F, can be written as the sum of the axial momentum brought by all the species in the plasma plume:

$$F = F'_{i\infty} + F_{e\infty} + F_n; \qquad (6.15)$$

where $F'_{i\infty}$ is the ion thrust including the effects of multiply-charged ions and $F_{e\infty}$ and F_n are the thrust produced by electrons and neutrals respectively. These last two terms are generally neglected since their contribution is considered small with respect to the one of ions. However, for the case under study, this approximation may be unjustified.

Electrons have negligible inertia, hence, their main momentum contribution comes from their pressure $p_e = nT_e$. Assuming quasi-neutrality, a uniform electron temperature along the α direction, and $\kappa_2 = 1$, an approximation of F_e can be given

by the ratio of momentum fluxes of electrons and ions:

$$F_e \simeq F_i \frac{nT_e}{nm_i u_i^2} = \frac{F_i}{M_i^2}. \qquad (6.16)$$

where M_i is the ion Mach number. The latter can be evaluated by combining the results from LP and RPA measurements. However, we are interested in knowing $F_{e\infty}$ which requires the knowledge of $T_{e\infty}$. In the case of an experiment performed within a vacuum chamber, an expansion to infinity is not possible and a sheath will develop at the vacuum chamber walls where $\phi = 0$ V. Since, the electron temperature and density there are not zero, electrons may still provide a residual pressure. The electron temperature in the vicinity of the wall is not known, however, an upper bound to the momentum contribution of the electrons is provided by the T_e measurements at $\rho = 350$ mm, corresponding to the assumption of an isothermal expansion from there up to the walls. As an example, for the case at 2 sccm and $P_T \approx 175$ W, the electron temperature at $\rho = 350$ mm resulted to be $T_e = 11.5$ eV and the ion velocity $u_{i\infty} \approx 13$ km/s, leading to $F_{e\infty}/F_{i\infty} \approx 1/M_{i\infty}^2 = 4.6\%$. In reality, this value is expected to be lower both because of the electron cooling along the magnetic nozzle plume expansion and because of the breaking of quasi-neutrality within the sheath at the vacuum chamber walls, as the electron density is reduced with respect to the one of the ions.

Concerning the contribution of neutrals, F_n, we first introduce the cold gas thrust, F_n^0, defined as the force measured by the TB when only propellant but no MW power is injected (no plasma). F_n^0 is linear with the propellant flow rate as depicted in figure 6.12-a. After the thruster ignition, the flow of neutrals is reduced by ionization and can be approached as $\dot{m}_n = \dot{m}_p(1 - \eta_u)$. Conversely, their temperature $T_n^0 \to T_n$ increases thanks to the higher wall temperature, plasma-wall recombination generating energetic neutrals, and charge-exchange collisions [154, 78]. For any non-reacting neutral gas expanding into vacuum, $F_n \propto \dot{m}_n \sqrt{T_n}$, so

$$F_n \simeq F_n^0 (1 - \eta_u) \sqrt{\frac{T_n}{T_n^0}}, \qquad (6.17)$$

with F_n and T_n referring to plasma-on conditions. Obviously, the importance of the neutrals contribution to thrust increases with T_n and decreases with η_u. Using the η_u estimations from figure 6.10-a, the role of T_n is illustrated in Figure 6.12-b. The value of T_n is unknown and it is expected to vary with the thruster operating point, however, values between $800 - 900$ K are realistic in ECR sources and magnetic nozzles thrusters [78, 154, 155]. This points out that at 8 sccm (80 W), which is the case with the lowest utilization efficiency, neutral thrust could be worth up to 16% of the total thrust under the assumption of $T_n/T_n^0 = 3$, while this would be only 10% if neutral gas does not experience any heating after thruster ignition ($T_n = T_n^0$). On the other hand, for the case at $\dot{m}_p = 2$ sccm and 80 W, which presents a much higher
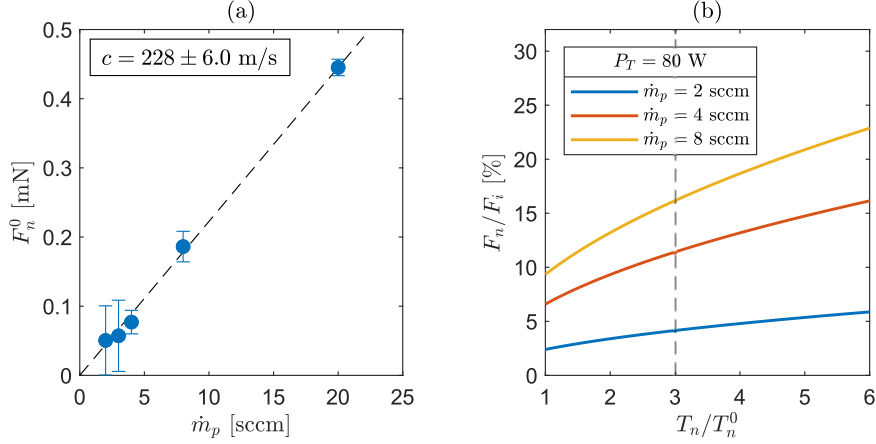
Figure 6.12: (a) Direct thrust measurements of cold Xenon propellant gas (temperature T_n^0) ejected from the thruster at different mass flow rates. (b) The expected contribution of the neutral thrust to the total thrust as a function of the temperature ratio T_n/T_n^0.

utilization, neutral thrust contribution would remain close to 4%. Thus, without invoking unrealistically high neutral heating, neutrals can only compensate partially for the discrepancy; furthermore, their contribution becomes relevant only for the low η_u cases.

In the previous sections, we have assumed the presence of singly charged ions only. However, multiple ionization might occur in the discharge chamber due to the relatively high electron temperature and plasma density available in this kind of device [13]. Referring to equation 6.7, the total axial current can be written as: $I_{zi} = I_{zi1} \sum_j R_j$, where j indicates the ion species and $R_j = I_{zij}/I_{zi1}$. An ExB probe would be necessary in order to experimentally measure the proportion and velocities of the different ion species. However, assuming these ions are subject to the same electric potential difference as singly-charged ones and that the velocity dispersion κ_2 does not vary for each species, a correction to the ion thrust can be written as:

$$F'_{i\infty} = F_{i\infty} \frac{\sum_j R_j / \sqrt{Z_j}}{\sum_j R_j} = F_{i\infty} \alpha_F \qquad (6.18)$$

where Z_j is the ion charge number. In [66], the double-to-single ion production ratio in the source was estimated using $\nu_{n\to i2}/\nu_{n\to i1}$, where ν is the electron collision frequency, n stands for neutrals and $i1$, $i2$ for singly and doubly charged Xe ions respectively. This value depends on T_e, which in turn is expected to increase with P_T and reduce with $\dot{m}_p$. Following the same procedure as in [66], we estimate $\nu_{n\to i2}/\nu_{n\to i1} \approx 5.5\%$ for 2 sccm and 260 W (case with the highest $P_T/\dot{m}_p$ in this study), where a $T_e = 15$ eV was measured at $z = 150$ mm, and a lower fraction for all other cases. Hence, considering the presence of doubly-charged ions only, the thrust $F_{i\infty}$ should be corrected with a factor of $\alpha_F \approx 0.97$. This correction

reduces the estimation of the measured indirect ion thrust, and therefore it cannot justify the thrust difference between direct and indirect measurements. Note that this correction due to double ions is not reflected in the data of table 6.1. On a side note, the possible presence of multiply charged ions would also affect the η_u estimation and thus F_n (refer to equation 6.17). Using the above-provided values, η_u might be overestimated by up to 5.2%, computed according to [3].

These estimations imply that other sources of disagreement may lie in the assumptions taken. One of these may be neglecting the effects of the high-energy electrons on the ion current density measurements with the FC, as discussed in Section 6.3.3. Indeed, a fraction of these electrons were found to have energies that exceeded the typical FC collector bias. If these electrons are not only present on the axis, then it would result in an underestimation of the utilization efficiency. This phenomenon may be responsible for the decrease of $F_{i\infty}/F_{TB}$ at 260 W for 2 and 4 sccm, but not for the 8 sccm case for which they were not observed. Hence, the reasons for the larger discrepancy at this mass flow rate are still unknown, and further investigation is warranted. It is reasonable to speculate that the thrust discrepancy may be partly due to an underestimation of the ion current density j_i measured by the FC. Charge exchange collisions in the far plume may cause such a phenomenon by producing both, fast neutrals and slow ions. The firsts are not detectable by an FC and little energy is lost in these collisions [61], whereas the probability of collection of a slow ion is reduced. This effect would result in an increased discrepancy between TB and indirect measurements, particularly for large mass flow rates due to the increased background pressure. A possible parallel effect contributing to the reduced measured current could be the effective FC aperture being smaller than the geometrical probe aperture (see Section 6.2): e.g. a $\approx$ 10% smaller effective FC aperture diameter relative to the geometrical one, D_{FC}, is enough to explain a 20% underestimation of I_i. This effect may be more pronounced for slower ions, such as those at 8 sccm, which could explain the larger discrepancy in that case.

6.4   Summary

Direct thrust and electrostatic probe measurements of a waveguide ECR thruster prototype have been presented and discussed. The prototype is able to produce up to 3.5 mN of thrust at 8 sccm and 350 W of input MW power (with $\eta_F = 2.1$ %). Thrust has been shown to present linear trends with power at fixed $\dot{m}_p$. At a lower mass flow rate, the thrust is reduced and the thrust efficiency is increased. A maximum thrust efficiency of $\eta_F = 3.5\%$ was measured for 2 sccm and 61 W (with $F_{TB} = 0.9$ mN), this value is in line with the low thrust efficiency measured in other similar devices. Electrostatic probe measurements allowed the identification of the loss mechanisms resulting in this low η_F. This was done by decomposing the latter into partial efficiencies.

The most constraining factor has been shown to be the energy efficiency, staying below 7% for all the cases studied, meaning that the greatest part of the input power is either lost to the walls or in inefficient plasma production, instead of axial beam power. The utilization efficiency η_u scales roughly with $P_T/\dot{m}_p$, and reaches a maximum of $\eta_u \approx 50\%$ being the second highest source of loss. This waveguide ECRT prototype also showed a high plume divergence. The divergence efficiency η_d is particularly low for the cases with low $P_T/\dot{m}_p$ since the plume becomes hollow at these operating points, a behavior which could be possibly linked to the neutral gas radial injection driving power absorption in proximity to the walls. Efforts to simulate the propagation and absorption of microwave power within the PC with numerical models are expected to further provide clues on these phenomena and will be the subject of future works. We suggest that an improved injector strategy, such as an axial injection, may help eliminate/reduce power coupling to higher radii, possibly also having repercussions on the utilization and divergence efficiency.

The RPA-IEDF measurements provided insights into additional phenomena: an increased dispersion of ion velocity with increasing power, suggesting an enlargement of the ionization region scaling with P_T and the presence of an energetic electron tail in the plume up to 300 eV. Further research is needed to understand the origins of these electrons and their effects on discharge physics since it could pave the way for enhanced performance in future thruster designs.

The plume measurements allowed for the indirect assessment of thrust. A discrepancy between the direct and indirect estimations was found. Estimates of thrust from other species suggest that hot neutrals could contribute significantly to the total thrust, but they are not enough to fully explain the data. The thrust contribution by multiply charged ions and electrons was also evaluated, however, their effect is considered marginal. Assuming that TB measurements are accurate within the provided accuracy range, it is suggested that FC ion current measurements could be a potential source of thrust discrepancy. The presence of energetic electrons, charge exchange collisions, and an overestimation of the Faraday Cup's effective aperture may contribute to an underestimation of the beam current. Future tests will aim to corroborate these hypotheses. The effect of charge exchange collisions on the thrust discrepancy may be investigated by varying the vacuum chamber pressure. On the other hand, iterations on probe geometries may help reduce the error on the FC effective collection area and enable the use of larger collector biases to repel energetic electrons.

Chapter 7

Laser Induced Fluorescence Measurements [4]

> *"It is difficult to say what is impossible, for the dream of yesterday is the hope of today and the reality of tomorrow."*
>
> - Robert H. Goddard

This section presents data that emerged from a joint collaboration between the CNRS-ICARE laboratory and the EP2 group. In this regard, the author has contributed by conceiving and designing the experiment, preparing the experimental setup, operating the ECR thruster, acquiring ECRT diagnostics telemetry data, and interpreting the results. The LIF setup, its preparation/operation, and the analysis of the lineshape were performed by A. Vinci [68] at the CNRS-ICARE laboratory. For this work, the author is the second author in the journal publication Ref. [68]. Results from this entry are reproduced with the consent of A. Vinci.

This chapter is organized as follows. The motivations of the study are outlined in Section 7.1, Section 7.2 presents the conditions of the experiment and the setup used. Section 7.3 presents the obtained lineshape data and velocity profiles. Finally Section 7.4 summarizes the work done and draws the conclusions.

---

[4]This chapter reproduces with adaptations the journal paper: A. E. Vinci, M. R. Inchingolo, S. Mazouffre, and J. Navarro-Cavallé, "Ion dynamics in the magnetic nozzle of a waveguide ECR thruster via laser-induced fluorescence spectroscopy", Journal of Physics D: Applied Physics, 2022 [68].

7.1   Motivation

The objective of this work is to provide insights into the ion dynamics within a magnetic nozzle and partially in the discharge chamber of a waveguide ECR thruster for different operational points. The impact of the magnetic nozzle divergence, the mass flow rate, and of the input power are here analyzed. Current knowledge of ion dynamics and plasma potential distribution within the discharge chamber of this device remains hampered by the constraints imposed by invasive diagnostic techniques. The sole existing data originates from non-self-consistent plasma simulations (Chapter 4). Moreover, despite the presence of magnetic nozzles in analogous devices, ion acceleration profiles along the nozzle have not been documented for waveguide thrusters, making it challenging to validate future MN models and plasma simulations that rely on this information.

In this context, the LIF technique is used to obtain, nearly un-intrusively, information on the mean ion velocity and the velocity spread of the singly charged ion population. An introduction to the LIF working principle is available in Appendix A.2.

7.2   Experimental setup

The following measurements have been taken in a separate instance from the results presented in chapters 5 and 6. However, the same thruster configuration (propellant injector v2, uniform radial propellant injector) and vacuum facility as described in Section 6.2 were used, additionally for these tests the electromagnet was also operated. The electromagnet used differs from the one discussed in chapters 3 and 5, since a wire with a smaller cross-section, but occupying approximately the same volume is used. Therefore the same magnetic field is obtained for smaller current levels I_c. The ratio between the number of turns (and thus current for equal B), for these two electromagnets is 3.36, so that, in this work, $I_c = 12$ A corresponds to a resonance positioned on the exit plane. The effects of the electromagnet on the magnetic field strength and divergence are shown in figures 7.1 and 7.2.

For this study, the forward power P_F, measured with a directional coupler, is used as a power reference to organize and display mean velocity results. The actual power coupled to the plasma, P_T, is lower than this value, owing to the losses in the TL and reflected power. P_T in general being about $15\% - 20\%$ lower than P_F. The power reflected, P_R, has been reduced to $< 5\%$ of P_F by using the directional coupler discussed in Chapter 3. Additionally, the thruster floating potential V_T is monitored throughout the overall campaign and used as a reference for evaluating thruster stability and repeatability across the performed tests.

Concerning the LIF experimental setup, the configuration resembles the one
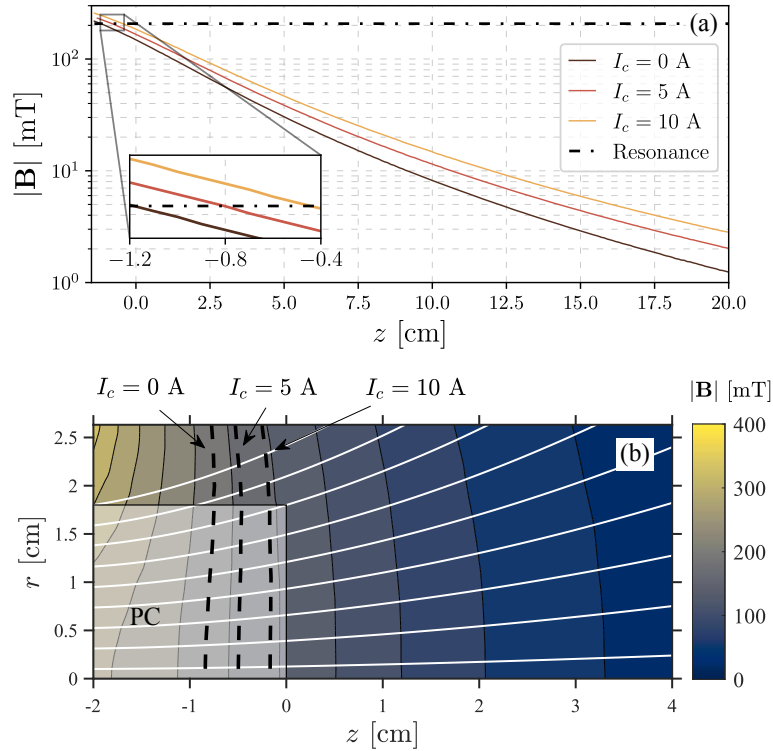
Figure 7.1: (a) Measured axial profiles of the ECRT magnetic field amplitude. The dash-dotted line indicates the resonance at 5.8 GHz. (b) Simulated 2-D maps of the MN highlighting with a dashed line the ECR surface as a function of I_c. The color map and the magnetic field streamlines (in white) refer to the $I_c = 0$. $z = 0$ refers to the exit plane of the PC.
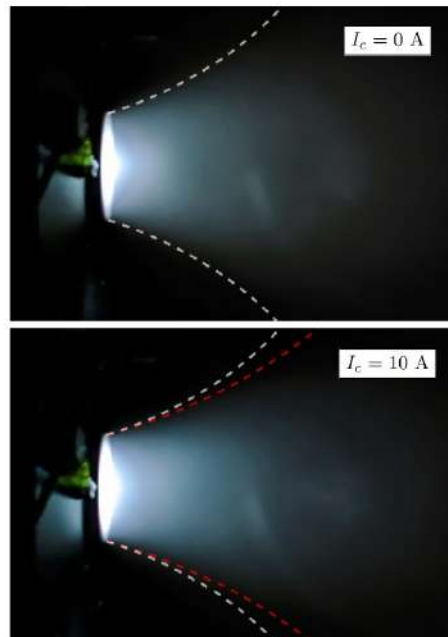
Figure 7.2: Photographs of the thruster in operation with two different magnetic nozzle shapes. The magnetic streamlines passing from the walls at the exit plane are shown with dashed lines, white for $I_c = 0$ A, red for $I_c = 10$ A.
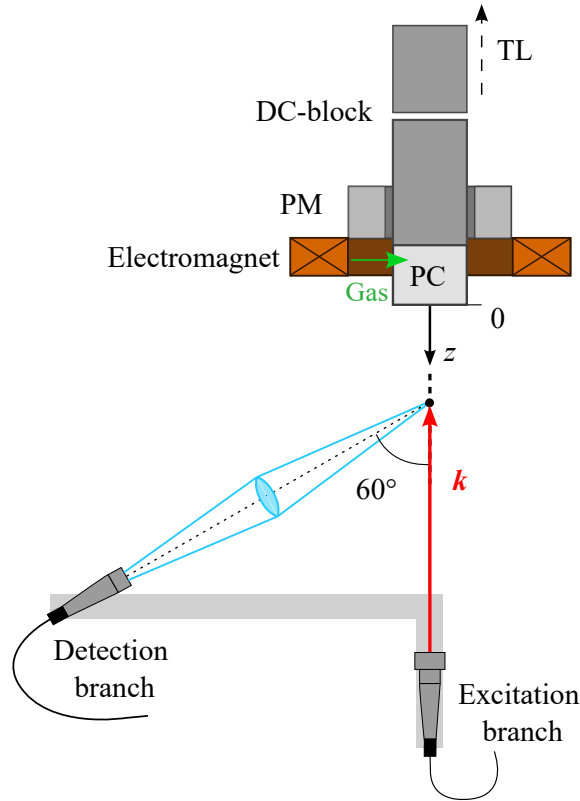
Figure 7.3: Schematic top view of the experimental setup. The thruster unit (top) and optical arrangement (bottom) are shown. Drawing not in scale.

employed in appendix A, however, some differences are present. The main ones account for the presence of a Fabry-Pérot interferometer for diagnosing laser mode-hop transitioning, and the use of a monochromator instead of a band-pass filter for filtering the fluorescence signal, the latter is amplified by a photomultiplier. These components are in the atmosphere segment. A thorough description of the optical bench used for this study is available at the following references [156, 157, 78, 68]. The probed species and energy levels transitions here used are the same as the ones available in the Appendix A in figure A.4.

A scheme of the vacuum segment is displayed in figure 7.3. The laser light emitted from the diode is coupled to an optical fiber, the latter ends in the vacuum chamber and is focused in a well-collimated beam (4 mm diameter) by a custom collimator constituting the excitation branch. The laser beam is aligned with the thruster axis along the overall experiment. The detection branch is composed of a bi-convex lens with a focal length of 6 cm, one focal point, intersecting the laser beam, determines the measurement location while the other couples the emitted light to an additional optical fiber which ends up at the monochromator on the optical bench. The detection branch is tilted at 60° relative to the thruster axis and excitation branch. The two branches are mounted on a rigid body, preventing any relative displacement, the latter is mounted on the same arm system described in Section 5.1.

The so-configured system allows measuring the Xe II (Xe ion) velocities along the thruster axis, v_z, in a range $-1 < z < 20$ cm, where $z = 0$ identifies the thruster exit plane. Farther than $z = 15$ cm the detection becomes limited by the low signal-to-noise ratio and the measurements are not possible for all the working points. Measurements in this on-axis range were taken for different ECRT operation regimes, obtaining three series of data which are here called: magnetic field, mass flow rate, and power series, for which the current I_c, the mass flow rate $\dot{m}_p$ and the forward power P_F are varied respectively. For the power series, the measurements are taken at a fixed position $z = 10$ cm. In this study, $P_F = 200$ W, $\dot{m}_p = 2$ sccm of Xenon, and $I_c = 0$ are considered the conditions for the reference case.

7.3 Results

7.3.1 Example lineshapes
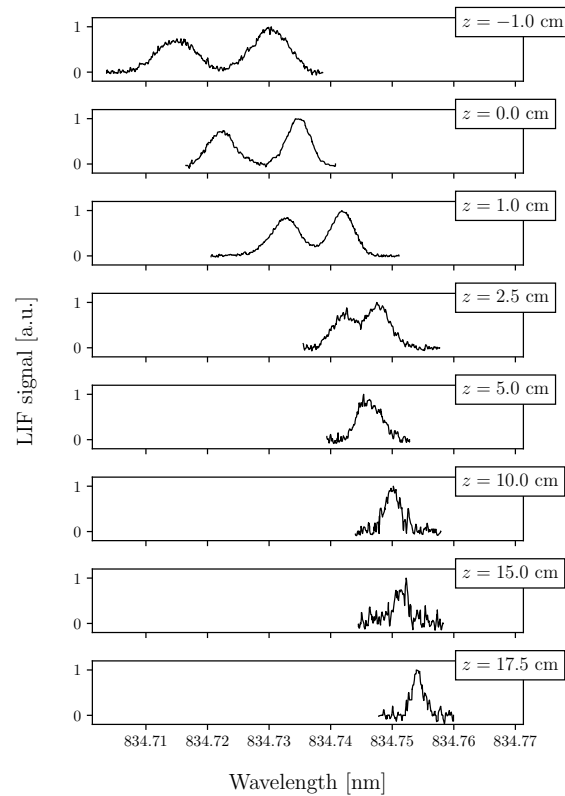
Figure 7.4: LIF spectra resolved along z. Wavelength values are expressed for air. Thruster operation parameters are: $P_F = 200$ W, $\dot{m}_p = 2$ sccm, $I_c = 0$ A.

Figure 7.4 shows a typical series of axial scans. In proximity to the exit plane ($z = 0$), the fluorescence profile is double-peaked. Farther downstream (e.g. at $z = 5$ cm in Figure 7.4), the two peaks merge in a single, broad profile, and eventually become a Gaussian-like spectrum for $z \geq 10$ cm. The intense magnetic field within the source

and the near-field plume significantly influences the splitting of atomic energy levels. In the presence of a relatively weak magnetic field, this phenomenon is known as the Zeeman effect, while in the case of a strong magnetic field, it is referred to as the Paschen-Back effect. The current experiment revealed a departure from a quasi-Gaussian profile at magnetic field strengths exceeding $B \approx 30$ mT. In previous LIF studies on ECR thrusters [79, 158], the observed experimental profiles did not exhibit such a pronounced deviation from a quasi-Gaussian shape, this difference has been attributed to the lower magnetic field strengths within the respective probed regions.

In the raw lineshapes, the most probable velocity of the species under investigation can be determined from the Doppler shift of the lineshape center. However, when the fluorescence light profile deviates from a quasi-Gaussian shape, it becomes challenging to accurately identify the shifted line center and consequently determine the most probable velocity. Thus, the retrieving of the most probable velocity requires modeling of the fluorescence profiles. The model used for the analysis of these data is detailed in [78] and in the reference therein included. The latter accounts for the discussed effect of the magnetic field on the lineshape, as well as for the emission lines of the seven most abundant isotopes of Xenon, determining the so-called isotopic shift (due to mass and volume differences of the atomic nuclei) and for the Hyperfine structure of isotopes with odd atomic number (^{129}Xe and ^{131}Xe). The ion temperature, T_i, quantifying the spread of velocities in the axial direction, is considered a free parameter in the model and is retrieved by fitting the experimental lineshapes with the modeled one. The ion temperature is assumed to be constant along the plume expansion. As an example of the fitting process, figure 7.5 shows the modeled lineshapes obtained for four different T_i, being $T_i = 5000$ K the one that better fits the measurements.

A kinetic temperature between 1400 and 6400 K is found to fit the data presented in this work. These are in the same order of magnitudes as the ones presented in Section 6.3.2.

It is noteworthy that the measured ion temperature in this study deviates significantly from the values reported in previous investigations of MN dynamics [78], where T_i values below 1000 K were observed. Considering the low plasma pressures expected for the plasma source here analyzed, such high temperatures cannot be explained by ion-electron collisions and consequent ion heating. Conversely, a large value of T_i in the axial direction, i.e. a dispersion in the axial velocity, suggests an extended ionization region overlapping with the acceleration region. This process then would lead to an anisotropy in the ion kinetic temperature between parallel and perpendicular directions. A similar phenomenon has been frequently observed in Hall thrusters, where the spread in axial velocity corresponds to the potential range across which ions are generated, reaching values up to a few tens of eV [156, 157, 159]. The ion kinetic temperatures here found do not reach these levels, a
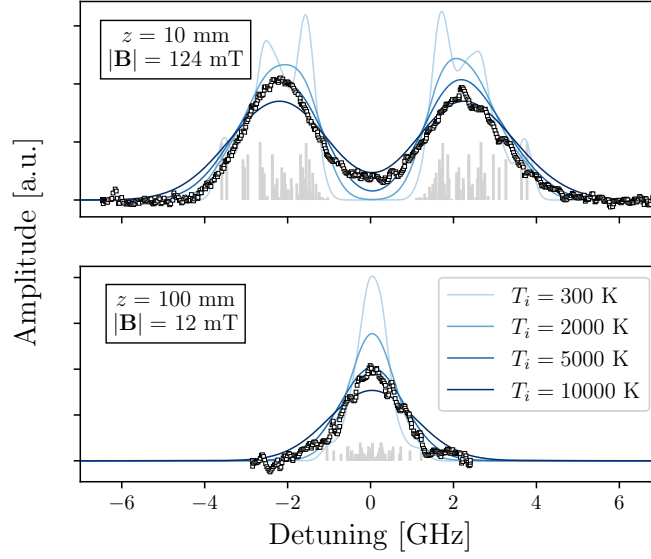
Figure 7.5: Comparison of experimental (squares) versus modeled (solid lines) line-shapes using arbitrary values for T_i. The experimental data points are Doppler-shifted to fit the model profiles. The bar plot images the allowed optical transitions. Thruster operation parameters are: $P_F = 200$ W, $\dot{m}_p = 2$ sccm, $I_c = 5$ A.

sign of the slower decay of the potential within the ionization region: the enhanced electron conductivity along the axial magnetic field lines prevents the development of large electric fields. Another possible cause that could originate apparent large ion kinetic temperatures, is unstable and/or oscillatory plasma behaviors during the lineshape acquisition. The thruster stability was constantly monitored through the microwave-reflected power and thruster floating potential, and the lineshapes were acquired only in steady-state operations, therefore low-frequency oscillations can be discarded as a possible cause.

7.3.2 Mean velocities

Results in terms of the most probable axial velocity of the ions are respectively reported in figures 7.6-7.7. The electromagnet current series, see figure 7.6, is recorded using constant values of $P_F = 200$ W and $\dot{m}_p = 2$ sccm, whereas the current driven in the external electromagnet is varied between $I_c = 0, 5, 10$ A. Increasing the electromagnet current has three main effects: (a) the magnetic field strength in the PC increases; (b) the ECR layer shifts downstream; (c) the expansion rate of the MN decreases or, in other terms, the nozzle becomes longer. It is observed that, at $z = -10$ mm, the ions are mostly directed towards the thruster backplate ($v_z \approx -500$ m s^{-1}), where they will recombine. This suggests that the peak in plasma potential within the PC is positioned between $-10 < z < 0$ mm. This result holds regardless of I_c. Although T_e measurements were not acquired during this campaign, referring to
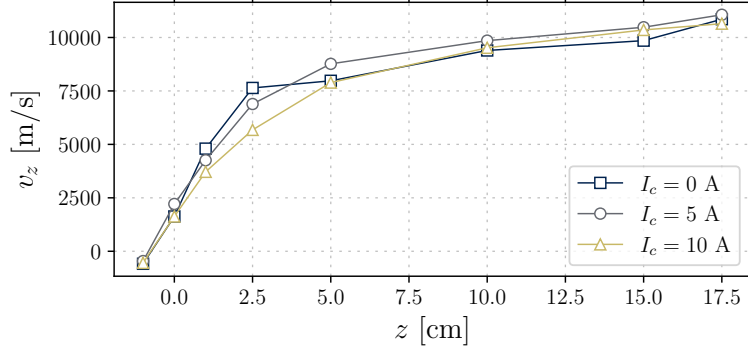
Figure 7.6: Most probable axial velocity profile of Xe II for different electromagnet currents. Constant thruster operation parameters are: $P_F = 200$ W, $\dot{m}_p = 2$ sccm.
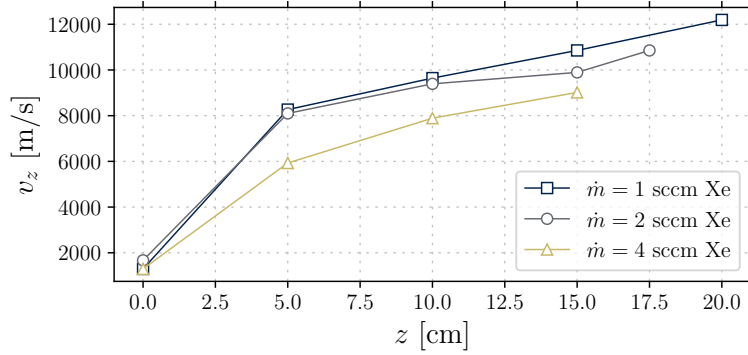
Figure 7.7: Most probable axial velocity profile of Xe II for different propellant mass flow rates. Constant thruster operation parameters are: $P_F = 200$ W, $I_c = 0$ A.

the previous chapters (Chapter 5 and 6), an electron temperature $T_e > 10$ eV should be expected at the thruster exit plane for this working point. The reported velocities at the exit plane $z = 0$, are measured to be in the range of $1600 - 2200$ m s^{-1}, hence the ions are found to reach supersonic velocities only a few centimeters downstream of the exit plane [80], being the exact position dependent on the magnetic nozzle divergence. Most of the momentum gain occurs within 5 cm downstream of the exit plane, yet at different rates depending on I_c. A higher I_c is associated with a lower acceleration, which is compatible with a lower axial variation rate of the magnetic field intensity. Farther downstream instead, any difference linked to the shape of the MN is smoothed out and every configuration leads to a nearly identical axial velocity profile. This suggests that varying I_c does not significantly affect the total plasma potential drop in this experiment. A rather constant V_T has been observed between the three working points ($\approx 70 - 80$ V), qualitatively confirming that the conditions in the source were similar. However, it is expected that a non-negligible difference among the various MN shapes might be preserved in terms of plume divergence, as it visually appears from figure 7.2 and as also discussed in Chapter 5, but for a different propellant injector.
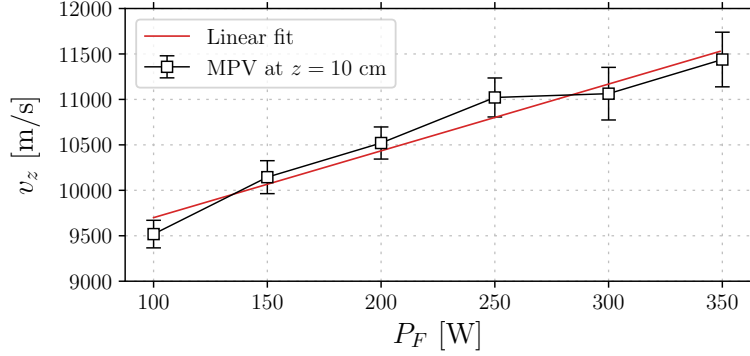
Figure 7.8: Most probable axial velocity of Xe II at $z = 10$ cm for different levels of input power. The error bar identifies the standard deviation given by T_i. Constant thruster operation parameters are: $\dot{m}_p = 2$ sccm, $I_c = 0$ A.

The mass flow rate series, refer to figure 7.7, is recorded using constant values of $P_F = 200$ W and $I_c = 0$ A. The farthest distance at which the ion velocity could be resolved is limited by the LIF signal-to-noise ratio. The latter deteriorates at larger mass flow rates due to larger collision rates giving a less populated group of ions in the metastable state. In accordance with previous observations reported in the literature in terms of specific impulse [67] and ion axial velocity [79, 78], ions gain a larger momentum as the pressure of neutrals drops. This phenomenon is attributed to two effects happening as the mass flow rate increases: a reduced amount of deposited energy per electron and a reduced mean free path for electron-neutral and ion-neutral collisions. The first effect leads to a reduced electron temperature, hence a smaller potential drop along the expansion. On the other hand, the electron-neutral collisions contribute to electron cooling inside the source therefore lowering the internal energy available for ion acceleration through the MN, whereas ion-neutral collisions represent a drag force component which further reduces the ion kinetic energy [80].

The input power series, whose results are reported in figure 7.8, is recorded at $z = 10$ cm at a constant value of $\dot{m}_p = 2$ sccm and $I_c = 0$ A. Within the explored range of P_F, the ion axial velocity along the MN axis shows an approximately linear growth with the microwave input power up to $P_F = 250$ W. As observed for the RPA measurements discussed in Section 6.3.2, saturation seems to occur for larger powers deviating from the linear trend as the thrust efficiency decays. The ion temperature has been found as well to be increasing with the input power, varying between 1400 K to 5500 K.

As opposed to the case shown in figure 7.7, increasing the power at constant $\dot{m}_p$ raises the available energy per electron, therefore T_e increases along with the plasma potential drop. It is noted that the value of v_z for $P_F = 200$ W measured in the power series differs by roughly 10% from the same point shown in figures 7.6 and 7.8. This discrepancy is attributed to a slightly different condition of the thruster operation since the two measurements are performed over different time frames. As a matter

of fact, the reading of the floating potential at the source walls differs by about 15 V from one day to the next. This qualitatively indicates that the conditions in the source were slightly different and most probably a lower plasma potential drop was achieved, giving rise to a difference in the measured ion velocity.

7.4 Summary

The dynamics of xenon ions have been spatially resolved by way of LIF spectroscopy along the axis of a circular waveguide electron cyclotron resonance thruster. In the near-field plume and inside the source chamber, inference of ion velocity and parallel ion temperature requires intensive lineshape modeling efforts. One must account for several broadening mechanisms, namely isotopic shift, hyperfine structure, and Paschen-Back/Zeeman effect. This is especially true for ECRTs operating at relatively high frequencies which implies the need for more intense magnetic fields to meet the resonance condition. Findings show that ions are considerably accelerated within a few centimeters downstream of the exit plane, although a non-negligible amount of kinetic energy is gained in the far-field region. When the divergence of the MN is reduced, the acceleration profile stretches out along the axis but altogether the ultimate on-axis ion velocity does not exhibit a visible dependence on the nozzle shape, in accordance with the simplest MN theories. As a general rule already observed elsewhere, a faster ion beam is attained at lower mass flow rates and higher levels of input power. Pertaining to the range explored in this experiment, it is observed that the ion velocity increases about linearly with input power. Overall, the largest ion velocity recorded here reads about 12000 m s^{-1} at $z = 20$ cm for 200 W of input power and 1 sccm of mass flow rate. Furthermore, negative ion velocities were found in the middle of the plasma chamber at $z = -10$ mm, indicating non-negligible ion flux lost at the thruster backplate, which emphasizes that this is an important loss term in the overall thruster efficiency. By modeling the fluorescence lineshape, it was possible to deduce the Doppler broadening width which reads about 1.5 GHz (full width at half maximum), yielding a parallel ion kinetic temperature in the order of a few thousands of K. This relatively high dispersion in ion axial velocity likely results from a broad ionization region which overlaps with the acceleration region. Measurements show no evidence of ion temperature evolution along the plume expansion axis, in agreement with collisionless MN theories. Further work must include measurements of complementary quantities of the expanding flow. Among others, it is of major relevance to investigate the neutrals' velocity, the neutrals' temperature, and the perpendicular ion temperature. The latter two are expected to be close to the chamber walls temperature, i.e. in the order of a few hundred K. Ultimately, iterations on the thruster design could target the propellant injector position to reduce the amount of back-streaming ions as well as altering the overlapping acceleration-ionization regions.

Chapter 8

Conclusions

> *"I used to think about how nice it would be to visit the planets. Of course, I didn't expect to see in my lifetime what has happened. I knew it would happen some day, but it came along faster than I at first thought."*
>
> - Clyde Tombaugh

This final Chapter summarizes the research conducted throughout this thesis and the conclusions that can be extracted. The summary is organized according to the thesis Chapter subdivision corresponding to the three test campaigns performed and the numerical simulation study. Future research line perspectives on waveguide ECR thrusters are finally discussed.

8.1   Main contributions

Prototype design

An ECRT prototype has been designed to be a versatile and compact experimental platform. This prototype represents the first ECRT designed and tested in Spain. An operating MW frequency of 5.8 GHz has been chosen to achieve a compact design (D_T = 36 mm) appropriate for the low target power ($<$ 400 W). The design of the discharge chamber allows for easy interchange of propellant injectors without the need for a complete redesign. Two propellant injectors were designed and extensively used during the performed campaigns. A radially magnetized ring magnet has been found to be the best solution for creating the magnetic nozzle and resonance field

B_{ECR} = 0.2 T. An additional electromagnet has been designed to add flexibility to the magnetic field topology allowing for the displacement of the resonance field and increase the length of the magnetic nozzle.

Plume Characterization

For the first time, the prototype's discharge has been investigated through plume measurements under diverse operating conditions, injector configurations, varying mass flow rates, power levels, and magnetic fields. The main results that emerged from this work are outlined below.

- For both the single and double injection configuration it has been shown that the thruster can ignite and operate in a wide range of working points. Although with deteriorated performance, operations are possible also largely outside of the design range (up to 40 sccm of Xenon).

- The microwave-plasma coupling has been monitored through the reflection coefficient, Γ_L. Reflections reached up to 50%, peaking at low and large mass flow rates. In the explored range the magnetic field (controlled by the electromagnet current) showed small effects on Γ_L, suggesting that the resonance position plays a minor role on this parameter. These effects have not been shown in previous research on waveguide ECRT, where a good power coupling in the order of 80 – 90% has been observed. A possible explanation for this phenomenon is a partial or complete reflection of the L mode. The use of a right-hand circular polarizer or a matching device could address the problem. The latter solution is used in the second test campaign.

- Faraday Cup measurements have allowed for assessing the plume profile for various conditions. As expected, a single radial injector produces strong asymmetries in the plume current, hence, although simple, it is not appropriate for propulsion purposes. On the other hand, a double radial injection scheme is sufficient to attain a symmetric plume on the scanned plane, although it does not guarantee axisymmetry. Large divergence angles, $35° < \alpha_D < 55°$ are observed, the latter is reduced with increasing energy per particle. At the largest mass flow rates the plume presents additional secondary peaks of current at large angles. These have never been observed before for a waveguide thruster since azimuthal measurements were not performed in the '60s and '90s. The utilization efficiency is also scaling with this quantity, achieving 70% only at the largest energy per particle (1 sccm, 300 W).

- The electron temperature has been assessed by use of a Langmuir probe. Relatively low values were found downstream $T_e < 16$ eV if compared to those found in coaxial ECRT. Electron cooling has been observed along the plume

axis showing values for the polytropic coefficient in the range of $1.23 < \gamma < 1.3$ as also found by other studies.

- The magnetic field has been found to be of great influence on the thruster floating potential and plume current. The expected impact on the divergence, predicted by basic magnetic nozzle theory, has been observed: a higher electro-magnet current (lower divergence of the field lines) has been found to reduce the divergence angle of the beam, up to $10°$ reduction has been obtained for $\dot{m}_p = 2$ sccm and $P = 175$ W. The thruster floating potential was also found to be affected, increasing about linearly with the electromagnet current. This can be associated with both an improved shielding of the PC metallic walls and a consequent increase of the electron temperature or an improved plasma/wave coupling due to the displacement of the resonance.

- A preliminary estimation of the thrust efficiency showed values below 2%. The latter has been obtained employing only the plume current measurements and the thruster wall floating potential as a proxy for the ion energy.

Indirect and Direct Thrust Measurements

Following the plume characterization results, the subsequent changes in the setup have been made: a stub tuner is introduced in the transmission line to reduce the reflected power, and thus improve the power coupled measurements; a uniform radial propellant injector is used to smooth azimuthal density gradients. The latter also brings the advantage of an improved accuracy of the axisymmetry assumption. Therefore this second campaign had the objective of completing the assessment of the partial efficiencies by incorporating ion energy and direct thrust measurements. Additionally, phenomena that have previously gone unnoticed have been observed and related measurements acquired. The key findings are as follows:

- Thrust balance measurements have provided a maximum thrust of 3.5 mN at 8 sccm and 350 W of input microwave power. The maximum thrust efficiency has been found for low powers and mass flow rates $\eta_F = 3.5\%$ (at 2 sccm and 61 W), in line with the preliminary estimations performed in the previous campaign.

- The analysis of the ion current within the plume, showed two possible plume profiles, presenting a single central peak or a hollow plume. A deviation from the single peak profile has been also observed for injector v1, however, for these tests this trend is more pronounced and occurs at higher power-to-mass flow rate ratios. The origin of this phenomenon is unclear, LP measurements performed for one of these cases showed T_e to increase off-axis suggesting that a larger fraction of power is coupled at higher radii, possibly in proximity to

the injectors. This hypothesis is supported by the front-view photos of the plasma chamber.

- The utilization efficiency has remained consistently below 50 % for $\dot{m}_p > 2$ sccm, being not affected by the change of the propellant injector.

- Similarly, low divergence efficiencies have generally been found, especially for these cases developing a hollow plume at values of $P_T/\dot{m}_p \leq 500$ eV atom $^{-1}$.

- The partial efficiency spoiling the most the total efficiency is found to be the energy efficiency, staying below 7% for all the cases studied. Hence the greatest part of the input power is either lost to the walls or in inefficient plasma production, but not in the formation of an energetic beam.

- Direct and indirect thrust measurements show an agreement between 43% and 86%. Neutrals contribution to thrust, which cannot be probed with electrostatic probes, can partially fill the disagreement. Preliminary findings suggest that the ion current may be slightly higher than previously thought, potentially representing an additional source of the thrust discrepancy.

- The RPA measurements have shown an increased dispersion of ion velocity with increasing power, suggesting a spatial expansion of the ionization region scaling with P_T.

- The presence of a population of energetic electrons with energies reaching up to 300 eV has been confirmed in the plume. This phenomenon has also been observed in coaxial ECRTs, but its origin and role in the expansion process remain unclear.

Laser Induced Fluorescence Measurements

In collaboration with the CNRS-ICARE laboratory, further measurements have been taken in the plume of the prototype featuring the injector v2. The laser-induced fluorescence spectroscopy technique has been used to probe Xenon ions nearly unintrusively, obtaining unprecedented data on the on-axis ion velocity profiles in the plume of a waveguide ECRT. The main results from the collaboration are summarized below.

- Most of the ion acceleration happens in the near plume region, in agreement with magnetic nozzle models. The sonic point is expected to be positioned only a few cm downstream of the exit plane.

- The electromagnet has been used to change the MN divergence. The MN divergence plays no role in the ultimate speed, but a longer nozzle (less divergent) reduces the velocity gradient (smaller $\partial v/\partial x$).

145

- Similarly to what has been observed with RPA measurements the ion velocity has been seen to scale with the energy per particle.

- Negative ion velocities have been measured on the plasma chamber axis at $z = -10$ mm. Meaning that the peak of the plasma potential is expected to be between $-10 < z < 0$ mm. This supports the expectations of large wall losses within the discharge chamber and the existence of a backflow.

- The ion axial kinetic temperature has been estimated in the order of a few thousand K. This result is in agreement with the RPA measurements and with the observations on the position of the peak in plasma potential.

Simulation of the ECRT discharge

A Hybrid PIC-fluid model developed at UC3M has been used to perform simulations of the plasma discharge and near-plume expansion of the ECRT prototype object of this thesis. In the absence of a dedicated wave model, the microwave power coupled to the plasma has been modeled for two imposed power absorption profiles, and the discharge physics studied for the two cases. To fit in the simulation requirements, a higher mass flow rate ($\dot{m}_p = 10 - 30$ sccm) than the design one has been used at a fixed power of 200 W. Nevertheless, several key features were observed:

- The two power deposition profiles have led to two distinct, electron temperature patterns, with positive or negative radial temperature gradients.

- As a result of the postulated power deposition profiles, where the density is increased the electron temperature is reduced.

- The effects of the electron temperature and density are reflected in the electron pressure which in turn drives the azimuthal electron current. Consequently, regions of magnetic drag produced by the electron theta currents can exist within the plume.

- A parametric analysis has been performed showing that performance levels scale with the energy per particle. It has been seen that, when this figure is increased, the negative electron magnetic thrust density region grows, and that the plasma is pushed further from the axis.

- Based on the data maps, performance metrics were assessed. The thrust efficiency has been calculated to be between $10\% - 20\%$. The utilization is between 60%–90%, and the energy efficiency is between 20%–40%. The divergence efficiency is around 90%.

The performed simulations did not completely agree with the later obtained experimental data for equivalent input conditions, both in terms of performance

metrics and plasma profiles. On a side note, while the simulations successfully produced a double-peaked hollow plume similar to the experimental findings, this hollow plume exhibits a large on-axis electron temperature, attributed to forcing the power absorption in a low-density region. However, experiments have observed the opposite effect, with the temperature peaking off-axis for these cases.

Additional work performed in the context of this thesis

Two additional side activities were performed in the context of this thesis.

- The design and testing of a Faraday cup for electrodeless plasma thrusters to evaluate the effects of several design parameters. The probe has been tested on a Helicon Plasma discharge. The effect of three set parameters has been analyzed: the collimator geometry, the collector length, and the collector material.

- A research stay at the Japanese Aerospace Exploration Agency aimed to study the near-cathode region of an ECR gridded ion thruster. The latter is believed to be the source of surface sputtering and cathode deterioration in the Hayabusa II mission. The Laser Induced Fluorescence technique has been used.

The main contributions and conclusions related to these activities are discussed in the respective appendices.

8.2 Future areas of research

This thesis has been motivated by the pursuit of attaining a purely electrodeless, and efficient, electric thruster. However, at the current stage of development, the waveguide ECR thruster here analyzed did not show compelling performance for propulsion applications. These findings are consistent with the results obtained by other research groups in past activities. Nevertheless, this thesis has contributed to a deeper understanding of the main loss sources, which is crucial for future thruster optimization. The developed prototype and the work carried out will pave the way for further studies and design improvements at the EP2 research group.

The measurements acquired in the plume alone, cannot provide a complete picture of the phenomena happening within the discharge chamber. The latter is a particularly difficult region to probe by experimental means without altering the discharge, therefore a similar knowledge would have to rely as well on modeling and numerical efforts.

There can be a number of factors contributing to the disagreement between the performed simulations and experimental data. First of all, there is a need to produce a self-consistent power deposition map, which was seen to have a large impact. Secondly, the boundary conditions imposed for these simulations were limited: a discharge chamber with fully dielectric walls was used, which differs from the condition of the experiment (dielectric backplate and metallic walls), the boundary conditions at infinity should also be improved with a more realistic zero-global current condition rather than a local one. Additional effects, which might play an important role in the discharge physics, will need to be included in the model; to name a few: the anisotropic electron temperature, electron cooling, and the effect of the diamagnetic field associated with the j_θ currents. Lastly, fine-tuning the free parameters in the simulations (related to the not-yet well-understood turbulent processes) might be necessary to fit the experimental data.

On the experimental side, the use of non-intrusive diagnostics should be prioritized to peek into the discharge chamber, as electrostatic probes would significantly perturb the discharge. A two-dimensional characterization of the inside region of the discharge chamber using LIF diagnostics could provide a map of the ion velocity vector and assess the flux at the walls. This information would be crucial for further verifying the theoretical models and validating simulation results. Analyzing the light emitted from this region through spectroscopy could also provide information on the ionization/excitation processes and devise strategies to reduce losses. More advanced tools such as Thompson scattering would allow probing the EEDF, which could be of paramount importance for characterizing the electron dynamics. Performing such an experiment would provide means to observe the high energy electron population that was found in this work (impractical with Langmuir probes), directly observe electron cooling along the magnetic nozzle expansion, or evaluate the effect of background pressure on the EEDF. All fundamental information to improve the existing models and knowledge. The study of plasma instabilities should also fall along future experimental efforts. These have never been characterized for a waveguide ECR thruster and may be a source of enhanced cross-field diffusion.

Last but not least, there is significant potential for further improvement in the thruster design. A better screening of the lateral walls should be prioritized. This can be achieved both by a less divergent magnetic field (also beneficial for the MN) or by using a geometry that follows the field lines (e.g. conical). Perhaps, reducing the length of the discharge chamber may result in a reduction of particle flux. In addition, research on alternative propellant injection strategies, magnetic field topologies, and materials for the discharge chamber has shown significant benefits in other thrusters, and it is expected that similar improvements can be achieved for this application.

Appendix A

Assessment of Xenon Ions Backflow by LIF Spectroscopy in the Plume of a Microwave Gridded Ion Thruster

"When I started on my research, I never expected I could invent the LED and laser diode."

- Shuji Nakamura

This chapter presents the work performed during a three-month research stay at the Institute of Space and Astronautical Science at the Japanese Aerospace Exploration Agency (ISAS-JAXA) centered on deepening knowledge and proficiency in the LIF technique. This work is part of the framework of the Hayabusa II mission, the asteroid Ryugu visiting spacecraft powered by Electron Cyclotron Resonance Gridded Ion Thrusters. This work has been performed under the supervision of professors Tsukizaki R. and Nishiyama K. (JAXA), and with the collaboration of the master's student Shirasawa R. of the University of Tokyo.

This chapter is organized as follows. Firstly, for an understanding of this work, Section A.1 introduces the problem and the working principle of the $\mu 10$ ion-thruster and hollow cathode of the Hayabusa II spacecraft explicating the purpose of this work. Secondly, the working principle of the Laser Induced Fluorescence (LIF) technique is introduced in Section A.2. The experimental setup is presented in Section A.3 and preliminary results are shown in Section A.4. Finally, in Section A.5 the work performed is summarized and conclusions are drawn.
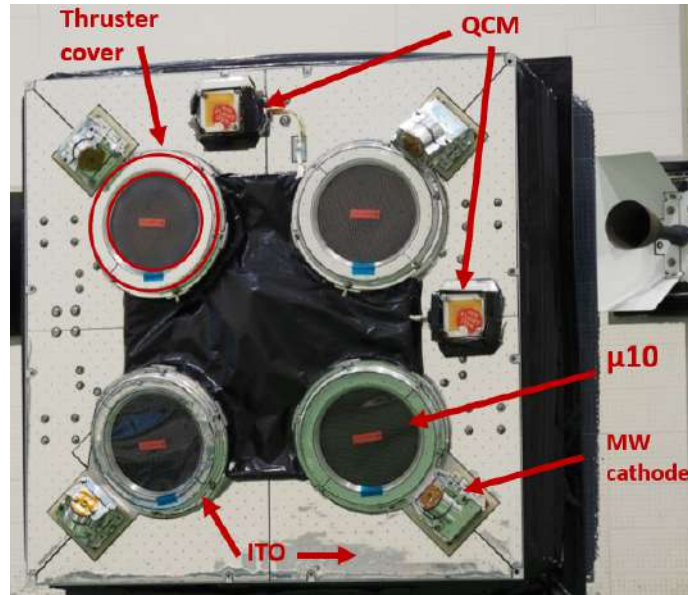
Figure A.1: Hayabusa II spacecraft thruster unit consisting of four μ10 thrusters equipped with one microwave cathode each. The two Quartz Crystal Microbalance (QCM), the ITO surfaces, and the thruster cover are also shown [162].

A.1 Background

The Japanese Aerospace and Exploration Agency (JAXA) with the Hayabusa I mission marked a fundamental step in space exploration by being the first spacecraft to ever return to Earth with a sample from an asteroid (asteroid Itokawa). Building on the successful sample collection of Hayabusa, the Hayabusa II mission was designed to collect samples from the Ryugu asteroid, broadening our understanding of asteroid composition and improving models of solar system formation. Both missions share the use of ion thrusters for spacecraft propulsion and interplanetary maneuvers.

The propulsion system of both missions consists of four ECR ion thrusters (μ10) mounted in a square pattern on gimbals for alignment with the spacecraft center of mass (refer to figure A.1). Both the Ion source and the neutralizer cathode use the ECR phenomenon for plasma generation. This allows for a substantially longer lifetime with respect to traditional systems using hollow cathodes or electron guns [3, 160]. On-ground testing with the ECR cathode working in diode mode has shown up to 70.000 h of operation without significant signs of performance reduction [161, 160]. On the other hand, the on-board neutralizers of Hayabusa I and II, have shown degradation after 7000-9000 h of operations.

The experimental campaign discussed in this chapter is part of the efforts towards the understanding of the reasons behind this discrepancy.

A.1.1 The μ10 ECR ion thruster

Figure A.2a shows a cross-section of the μ10 thruster and its electrical connections. The ion source is composed of a circular waveguide segment short-circuited on one hand and connected to the plasma discharge chamber (PC) on the other. The latter is terminated by carbon-carbon grids namely: screen, accel, and decel grids; responsible for plasma acceleration. Two series of ring magnets provide the magnetic field necessary for the ECR and PC plasma confinement, the PC is made of iron, hence realizing a magnetic circuit. Microwaves (MW) are injected into the waveguide through a cylindrical antenna placed at the back of the waveguide, they propagate towards the PC and are absorbed at the ECR interface. The setup used in Hayabusa II which is the same as the one used for the experiment discussed in this chapter, presents two Xenon-neutral propellant inlets, one at the back of the waveguide and one injecting directly in the PC between the two ring magnets. This injector design provided improved performance with respect to the Hayabusa I μ10 thruster which presented only the waveguide propellant injector [44].

The MW are produced by an oscillator resonating at 4.25 GHz, this low-power signal is delivered to an amplifier which will increase the power output. The MW are then delivered to the waveguide antenna through a coaxial cable. The entire thruster assembly is isolated from the ground thanks to the use of a DC block and a gas isolator, respectively for isolating the transmission line and the propellant line, since the discharge chamber is biased at large positive bias, the gas isolator also prevents discharges in the propellant tube.

(a)	(b)
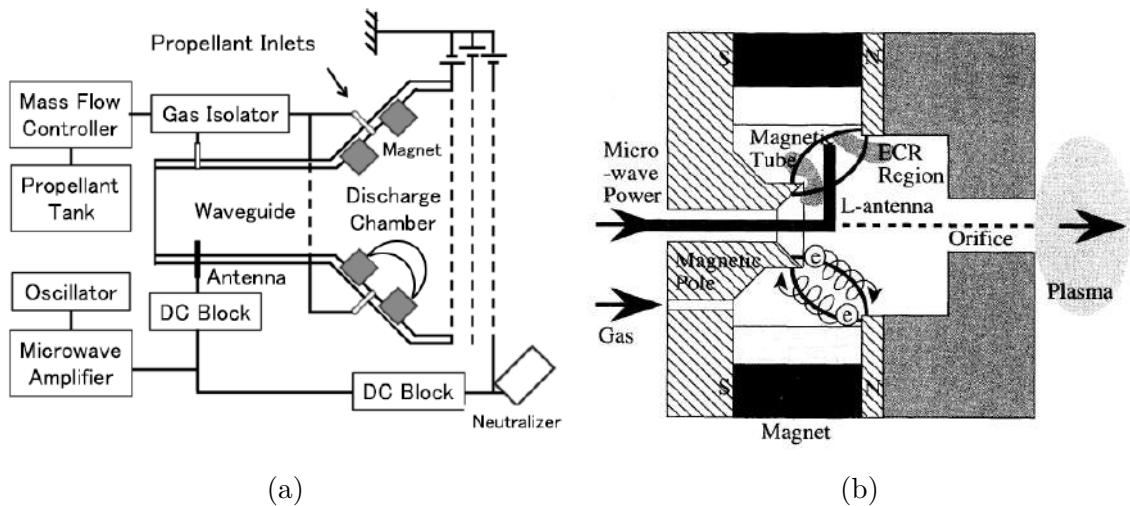
Figure A.2: (a) Cross-section scheme of the μ10 thruster Hayabusa II version. (b) Cross-section scheme of the ECR cathode. Source: (a) Tsukizaki *et al.* [163], (b) Kuninaka *et al.* [44], adapted with permission.

Equivalent MW transmission and propellant lines are also used by the cathode. Figure A.2b shows a cross-section of the cathode used during the experiments dis-

cussed here. The cathode acts as a small plasma source, the potential difference between the plasma plume and the cathode is responsible for extracting the electrons necessary for neutralization, on the other hand, the ions recombine on the neutralizer walls. Note that this kind of cathode is not provided with an emitter, plasma generation is achieved by using the ECR. The xenon-neutral gas is injected from the back of the cathode. The ECR region is defined by a ring magnet included in a magnetic circuit (figure A.2b), and the MW are delivered directly in this region by the use of an L-shaped antenna. The generated plasma is then expelled from an orifice.

Figure A.3 shows the electrical connections in a μ10 thruster when it is mounted in the vacuum chamber. In the experiments discussed in this chapter, the vacuum chamber is grounded, in space, the ground would be represented by the satellite common ground. As mentioned, on Hayabusa I and II, the propulsion unit consists of four thrusters, and up to three could be used at the same time. A typical problem arising when working with thruster clusters that use cathodes is the "cross-talk" phenomenon [161], in which a single cathode starts emitting the totality of the neutralization current, instead of splitting the current between the respective cathodes in the cluster. This in fact would reduce the lifetime. To prevent this phenomenon, the MW cathodes are biased negatively in current control mode at bias V_{cg}, so that the cathode current, I_c, can be chosen according to the beam current, I_b. In flight conditions, I_c is chosen to be $|I_c| = |I_b| + |I^+|$, I^+ being the excess current, typically $|I^+| = 3$ mA is used. Doing this allows for the reduction of the potential difference between the ion beam plasma potential, V_p, and the cathode, $V_{cc} = V_p + |V_{cg}|$ (V_{cc} is typically in the range of 50 V) [161]. This further improves the cathode lifetime reducing the energy of the ions impacting the cathode walls (for example those originated from CEX in the proximity of the cathode). The excess electron current is expected to be absorbed by the conductive ITO (Indium-Tin-Oxide) surfaces in proximity to the cathode as displayed in figures A.3 and A.1.

In normal operation conditions, the V_{cg} necessary to neutralize the plume is in the range of 30 V, this value increases over time as the cathode performance is decreased and the capability to extract current is reduced. Hayabusa II cathode power supplies can reach up to 50 V, this limit value has been currently reached for some of the cathodes in the thruster unit.

A.1.2 Problem Identification

Deposition on the surfaces surrounding the thruster was expected along the Hayabusa II mission as a consequence of material erosion from the thruster grids. To quantify the extent and impact of deposition, which could damage the solar panels or other exposed surfaces, the spacecraft thruster unit is equipped with QCM mass balances (figure A.1). Actual measurements during flight, evidenced instead erosion (mea-
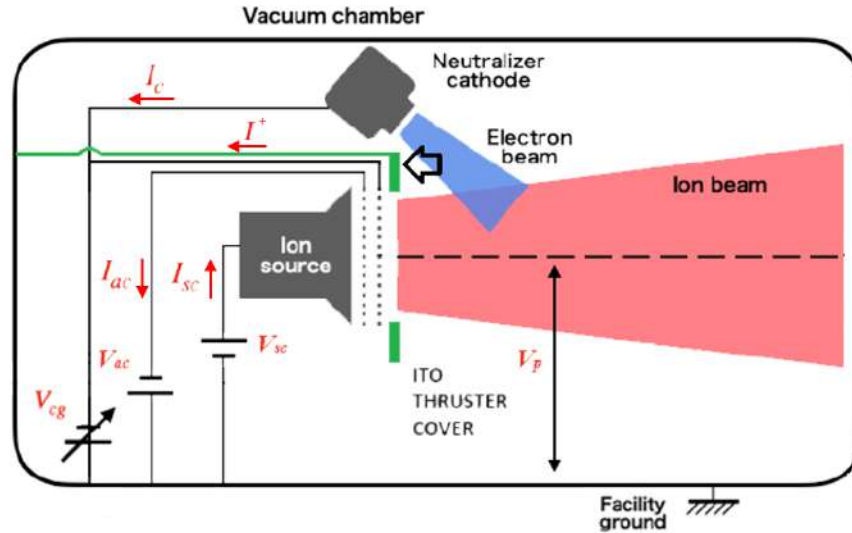
Figure A.3: Scheme of the electrical connections of the engineering model of the μ10 Hayabusa II ion thruster. Source: Nono *et al.* [161], adapted with permission.

sured negative mass), meaning that relatively high energy ions were back-streaming to the satellite eroding its surfaces.

Therefore, one emerging hypothesis behind the degradation of microwave cathode performance observed as an increase of $|V_{cg}|$ during spacecraft operations, is the deterioration of the ITO surfaces surrounding the thruster exit plane. These surfaces are made of a three-layer (conductor-insulator-conductor) composite material needed for thermal insulation and are thought to be the ones involved the most in the collection of the surplus current I^+ [161]. Imperfect utilization of the MW cathode and ion source allows neutral propellant to escape, fueling ionization events in the plume which may be the source of back-streaming ions. Deterioration of these surfaces by ion impact would expose the insulating layer, and the increase of resistivity would lead globally to an increase of $|V_{cg}|$.

Experiments aimed to provide more pieces of evidence in this regard were performed in [161], by Nono *et al.*. Where the role of current collection from these surfaces was analyzed by dividing them into segments that could be grounded or left floating. The floating condition served to simulate the scenario where insulating material from the ITO becomes exposed. The results showed that the surfaces in proximity to the cathode had the highest impact on the increase of $|V_{cg}|$ when they were floating. In [164], the same author, via Hybrid PIC-Fluid simulations of the plume of a μ10 thruster, has analyzed the potential for sputtering of the Charge-Exchange Ions (CEX) generated in the bulk plume, using the experimental data as a baseline. These ions were found to reach energies up to 30 eV when colliding with the surface surrounding the thruster, and they were impacting it with a large angle (velocity mainly radial).

Therefore, the current experimental efforts are directed towards providing evi-

dence that ions back-streaming toward the thruster cover surfaces have sufficient energy for sputtering the ITO surfaces, and expose the non-conductive layer. The LIF technique is optimal for this scope, being able to provide ion velocities with high resolution and minimum plasma disturbance. On the other hand, the low expected density for the back-streaming ions would make the fluorescing signal weak and the detection particularly challenging.

In this sense, the activities described in this chapter have the objective of preparing the LIF experimental setup, the $\mu 10$ engineering model thruster unit, the related interfaces, and performing preliminary LIF measurements to assess the feasibility of the study.

A.2 LIF Introduction

The Laser Induced Fluorescence technique is an optical diagnostic tool used to probe a gas. It offers a high spatial resolution (in the few millimeters range), in some applications temporal resolution, and very low intrusiveness if compared with electrostatic probes. LIF allows probing both a plasma and a neutral gas by analyzing the fluorescence light from the media, information like the Velocity Distribution function (VDF), the density and temperature of heavy species, and the magnetic and electric fields can be determined without introducing any solid object into the probed volume, resulting in a very powerful technique for numerous applications. Since the 90's [165] it has also been used in the electric propulsion field to determine plasma properties.
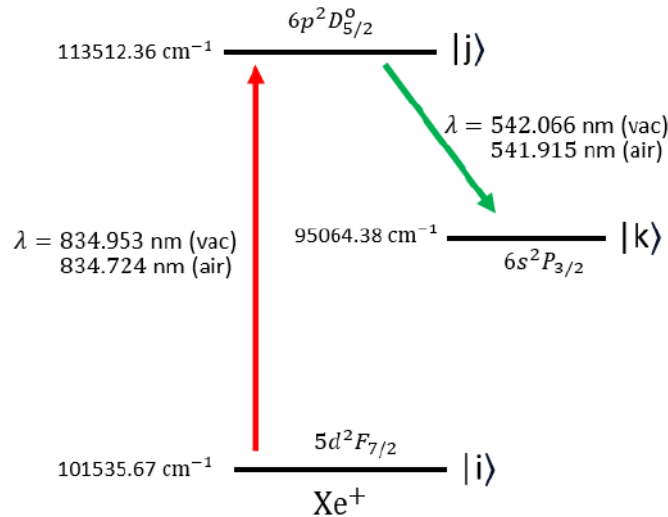
Figure A.4: Scheme of the LIF transition used in this work. Infrared laser photons increase the energy level of the Xe II (Xe $^+$) meta-stable quantum system $|i\rangle$ to $|j\rangle$. Green visible fluorescence light is emitted while transitioning from level $|j\rangle$ to $|k\rangle$.

The working principle of this technique is based on the possibility of pumping the transition of atoms or ions from one energy level state to a higher one by using light at a defined wavelength. Considering a two-level quantum system, as the one shown in figure A.4, the lower energy level, $|i\rangle$, can be pumped to the higher level, $|j\rangle$, via the absorption of a photon with energy equal to the difference of energy between the two states $\Delta E = E_j - E_i = h\nu_{ij}$. The higher level will then decay back to a lower energy level state $|k\rangle$ and in the process emit a "fluorescence" photon at a specific wavelength. The number of photons collected will be proportional to the number of atoms at the energy state $|i\rangle$ and, in low-intensity regimes, to the laser intensity, therefore by collecting this light it is possible to extract information on the probed population [166]. The excitation/de-excitation scheme used in the context of this thesis is shown in figure A.4, where a Xenon ion meta-stable population is probed.
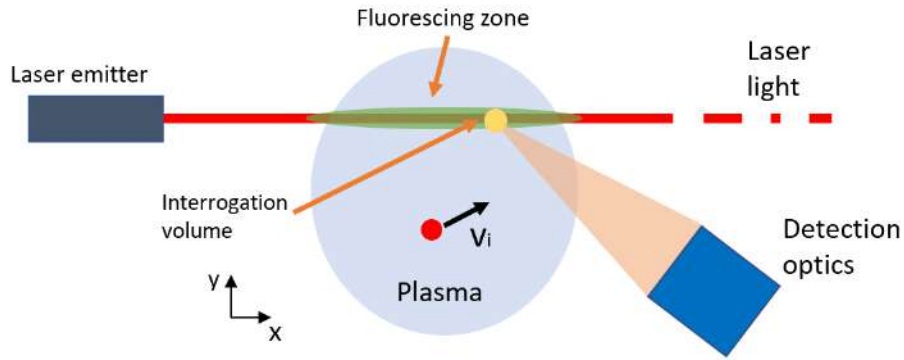
Figure A.5: Scheme of an LIF setup. The interrogation volume is determined by the intersection between the laser beam and the detection optics field of view. The probed velocity is in the laser beam direction, v_{ix}.

A laser source at the wavelength ν_{ij} is used to provide the excitation photons, constituting the excitation branch. On the other hand, a photomultiplier and a system of lenses are usually used to collect the emitted fluorescence light, these are referred to as the detection branch. Referring to figure A.5, the overlapping of the detection branch field of view and the laser beam constitutes the interrogation volume, in which the fluorescence light is observed and the gas properties are analyzed. This kind of setup can usually lead to spatial accuracy in the mm range.

In the reference frame of an atom moving at a certain velocity $\mathbf{v}$ with respect to an observer, the laser light at frequency ν will appear to be shifted to a frequency ν' as a consequence of the Doppler effect.

$$\nu' = \nu - \frac{\mathbf{k} \cdot \mathbf{v}}{2\pi}, \tag{A.1}$$

where $\mathbf{k}$ is the wave vector. For this reason, in the observer reference frame, a different frequency will be necessary to excite the transition of the moving atom.

Therefore, if ν_0 is the frequency exciting the transition of an atom at rest, the laser frequency, ν, exciting the transition of a moving atom will be:

$$\nu = \nu_0 + \frac{\mathbf{k} \cdot \mathbf{v}}{2\pi} \tag{A.2}$$

This is the basic principle, behind obtaining the VDF of an atomic population. The laser frequency is swept across a certain frequency span, and only the particles having velocity $\mathbf{v}$ so that equation A.2 is satisfied will absorb the photon and transition to the higher energy state, thus only these will fluoresce. Therefore, the fluorescence light is collected at each of these frequencies, the resulting curve is called a lineshape and in the simplest case, it can be used to directly recover the VDF using equation A.2. However, neglecting the effect due to the laser line frequency profile in continuous wave (CW), other effects usually exist altering the shape of the lineshape, these are called "broadening" mechanisms and may account for the existence of other transitions in proximity to the one of interest, these are due to the Hyperfine structure of atoms, the existence of isotopes within the probed gas (up to 9 isotopes naturally exist), the presence of external fields (Zeeman and Stark effects) or the use of excessive laser power resulting in a non-linear response to laser power (saturation broadening) [166, 167]. Therefore, the resulting lineshape will be a convolution of these effects and to retrieve the VDF a deconvolution method should be used [168, 169]. For simplicity, the results presented here do not involve a deconvolution process, an approach which is in general considered justifiable in the presence of low electric and magnetic fields and lasers used in CW regimes.

A.3 Experimental setup

A.3.1 μ10 thruster configuration and Vacuum chamber

The thruster and cathode units are mounted in a vacuum chamber equipped with a roughing pump, one turbo pump, and two cryo pumps. When operated, the background pressure reaches levels as low as 1e-7 mbar, while during thruster operations the pressure ranges between 5e-6 mbar and 2.7e-5 for a Xenon mass flow rate varying between 1 and 4 sccm.

In the context of this chapter, the engineering model of the Hayabusa II spacecraft thruster is used. As mentioned in Section A.1.1, this thruster is equipped with two propellant injectors, a waveguide injector, and a discharge chamber one. Following on a thruster characterization as shown in figure A.6-a, the total nominal input mass flow rate is set to 2.5 sccm of Xenon (a 2:1 ratio, discharge chamber: waveguide mass flow rate is used). The input microwave power to the source is $P_{T,MW} = 34$ W. The three grids are biased as follows: the screen grid is biased at the same potential of the PC, $V_{sc} = 1.52$ kV, the accel grid is biased at $V_{ac} = -0.37$

kV, the deceleration grid is biased at the same potential as the cathode. The biases here presented are all referred to the vacuum chamber ground. In this configuration, the beam current is about $I_b = 176$ mA as shown in figure A.6-a. In the context of these experiments, the ITO surfaces are not included in the experimental assembly, however, the conductive surfaces in proximity to the cathode are simulated by the aluminum thruster cover as displayed in figure A.10.

The MW cathode is positioned at 30° from the horizontal plane at a distance of 57 mm, and it is operated at 0.69 sccm and input MW power, $P_{C,MW} = 8$ W of MW power. The cathode is biased in current control mode to emit the current I_c as discussed in Section A.1.1, typically $V_{cg} \approx -37 \pm 5$ V, where the 5 V variation is a consequence of thermal transients.

(a)   (b)
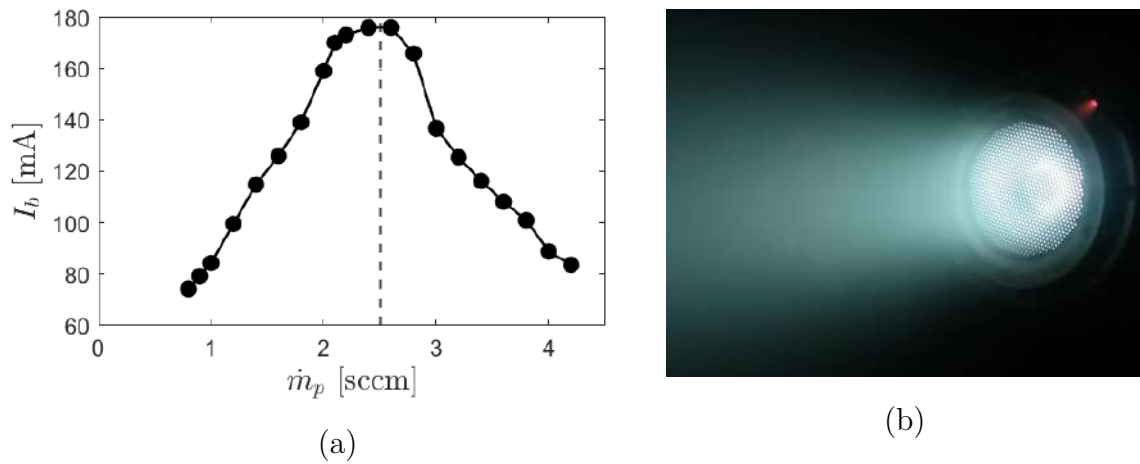
Figure A.6: (a) Variation of the discharge current, I_b, as a function of the total input mass flow rate for the Hayabusa II thruster engineering model. A 2:1 distribution of mass flow rate between the discharge chamber and waveguide is used. (b) Photograph of the μ10 ECR ion thruster during operations.

A.3.2 LIF setup

A LIF experimental setup is composed of an atmospheric side and a vacuum side. The atmospheric side accounts for the generation of the laser beam, laser properties measurements, and optical fiber coupling. In the vacuum side the laser beam is focused with collimation lenses and the fluorescence signal is captured with a photomultiplier. The interface between vacuum and air is realised with a custom-made vacuum chamber optical fiber feed-through. Figure A.7 shows a schematic view of the experimental setup. In the following, these two experimental segments will be described in detail.
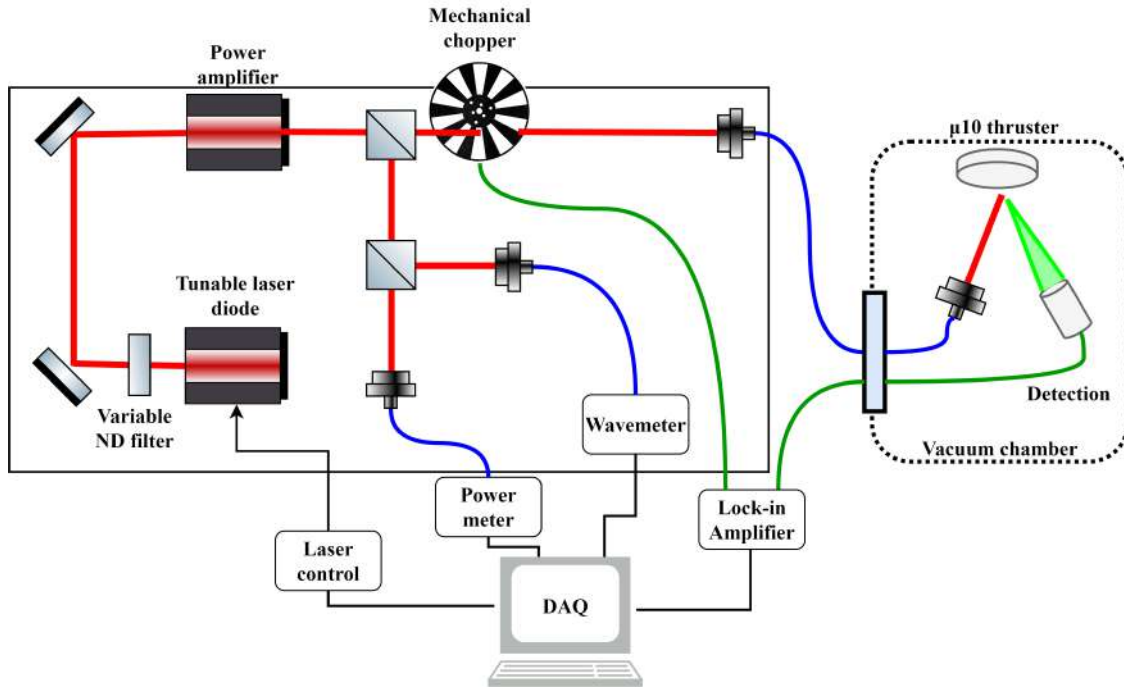
Figure A.7: Schematic view of the complete LIF experimental assembly. Red lines identify the laser beam. Green curves electrical connections, and blue ones multi-mode optical fibers.

Atmospheric side

Figure A.8 shows the experimental setup used during the experimental campaign. The primary laser beam is produced by a single-mode diode laser source (1), the diode is controlled by a Toptica Digilock 110, which is used to tune the laser frequency. Mod-hop-free operations are possible across a span of up to about 30 GHz. On average, the output power from this source is about 30 mW which does not provide enough power density for an LIF experiment, especially after being coupled to an optical fiber. Thus, a series of mirrors (2, 3) are used to align the laser beam to an optical power amplifier (Toptica BoosTA) (4). At the amplifier output, nearly 440 mW are available. Upstream the amplifier, a variable ND filter is positioned (11), this allows for fine-tuning and reducing the final power output, this is done to check for LIF signal saturation effects, which may perturb the recorded signal. The linear ND filter is mounted on a manual linear displacement stage. Downstream (4), a series of beam splitters (5, 7) withdraw power from the main beam and divert the resulting beams into two optical fiber couplers connected to multimode fibers: for wavelength measurements (9) and power measurements (10) respectively. Wavelength measurements are performed with a wave-meter ADVANTEST TQ825 while a Thorlabs S120C is used for power measurements. The output power from the laser diode shows a frequency dependence, thus the power measurements are used to normalize the fluorescence output. The main laser beam is modulated by a chopper (MC2000B) working at 6 KHz (6), essential for the fluorescence signal amplification

through the Lock-in amplifier technique. Finally, the light is efficiently coupled into a multimode fiber via an optical fiber coupling lens (PAL 20 NIR LC00), ultimately reaching the vacuum chamber.

During measurements, the Lock-in amplifier (AMETEK SR 7270 DSP) receives in input the continuous signal from the photo-multiplier and the reference square wave signal from the chopper. The output from the lock-in amplifier, together with the wavemeter and power meter is combined and recorded for post-processing with an OMNIACE III RA2300 data logger.
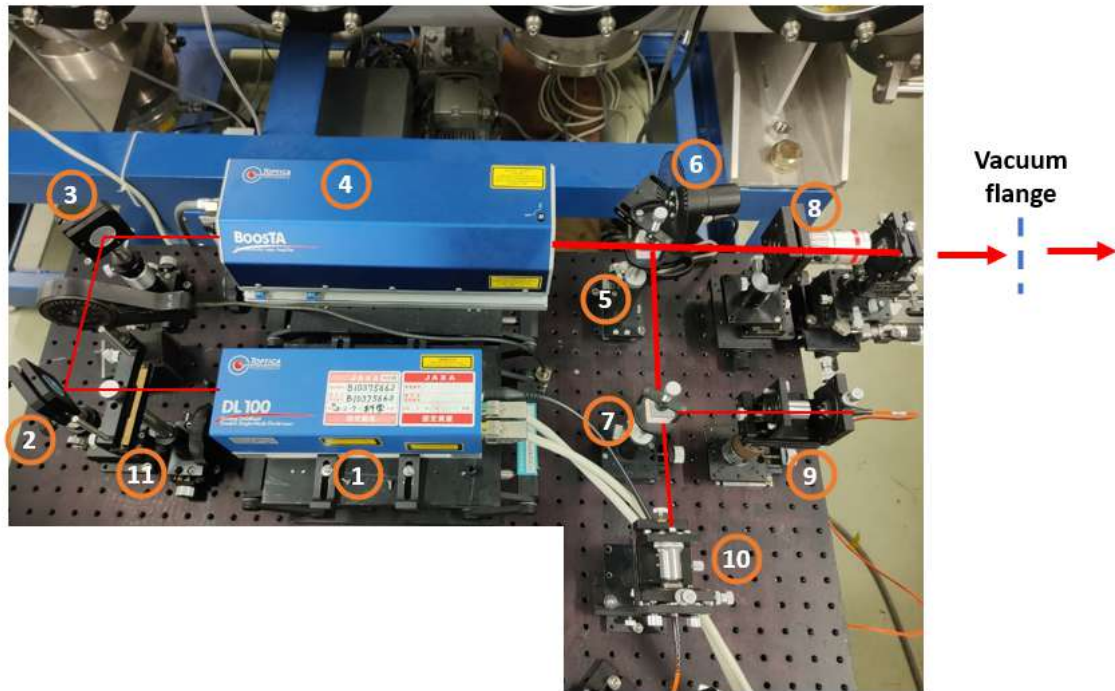
Figure A.8: Scheme of the atmospheric-side LIF setup. (1) Diode laser source, (2, 3) alignment mirrors, (4) laser amplifier, (5, 7) beam splitter, (6) chopper, (8, 9, 10) optical fiber couplers, (11) linear ND filter.

Vacuum side

The laser beam is introduced into the vacuum chamber through an optical fiber (Corning OM2 multimode fiber), and a collimator focuses the optical fiber output in a nearly parallel beam of about 4 mm in diameter. A power density of about 14 mW/mm^2 is obtained at the measurement point. The detection point can be anywhere along the laser beam path, its exact position is determined by the focusing point of the photomultiplier optical assembly as shown in figure A.9. The PMT detector is a Hamamatsu H11462, a mounting plate is used to allow the mounting of a band-pass filter, Thorlabs FL543.5, and focusing optics. The latter consists of two plano-convex lenses, the focal point is at 10 cm (Thorlabs LA1050-A).

Two versions of the vacuum segment have been tested. In the first setup, here

called configuration A, the velocity probed is mostly in the z direction, while the second, configuration B, allowed probing the radial velocity component. A schematic view of the two versions is shown in figure A.10-a and A.11. In version A, the laser beam is pointed toward the thruster cover with an angle of 14.5°, this angle is chosen to avoid positioning the optical fiber collimator assembly directly in front of the bulk plasma beam. This would cause aluminum sputtering and the deterioration of the surface of the lenses of the collimator and photomultiplier. In a second version, both the detection and laser optics are mounted on a 2-axis remotely controlled linear stage, which allows the movement of the assembly in 2D. For both configurations, the detection point is positioned at $r = 70$ mm.
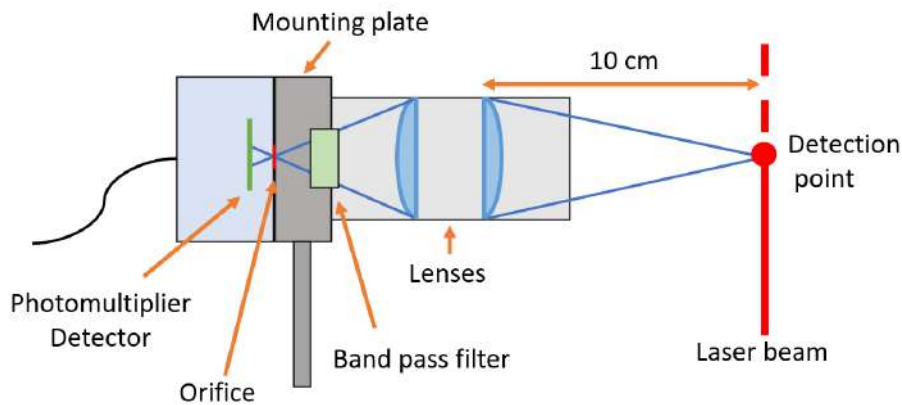
Figure A.9: Cut-view scheme of the photomultiplier optic assembly.

(a)

(b)
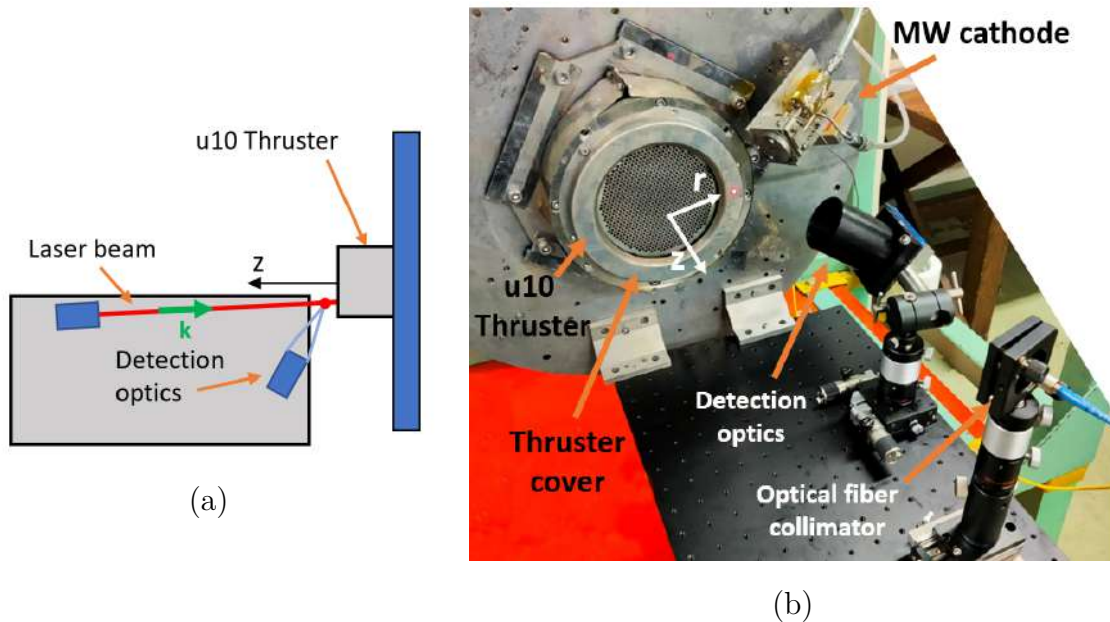
Figure A.10: (a) Schematic top view of the vacuum chamber configuration A. (b) Photograph of the vacuum chamber assembly for configuration A.

(a)

(b)
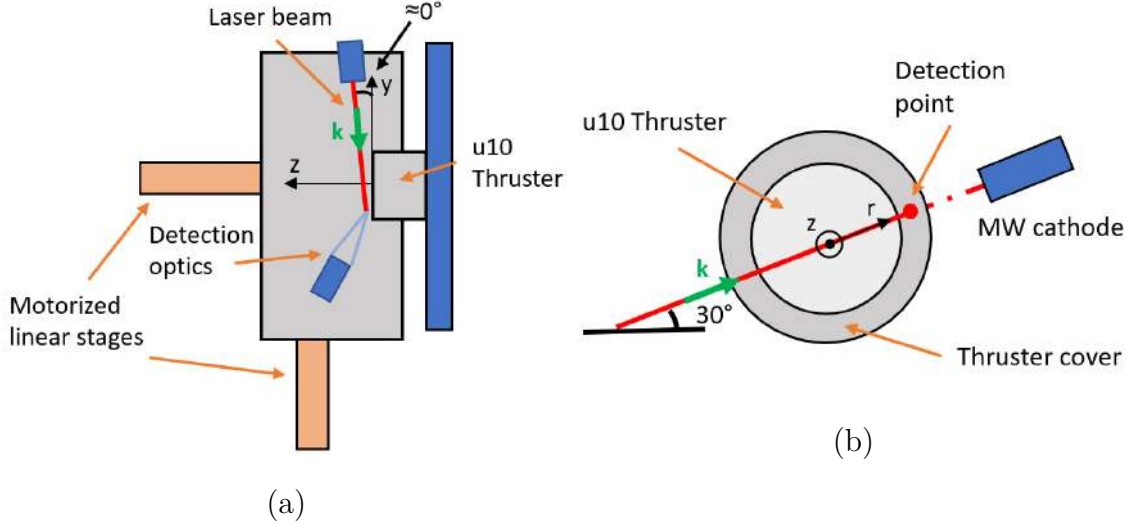
Figure A.11: Schematic top (a) and front (b) views for the configuration B.

A.4 Results and Discussion
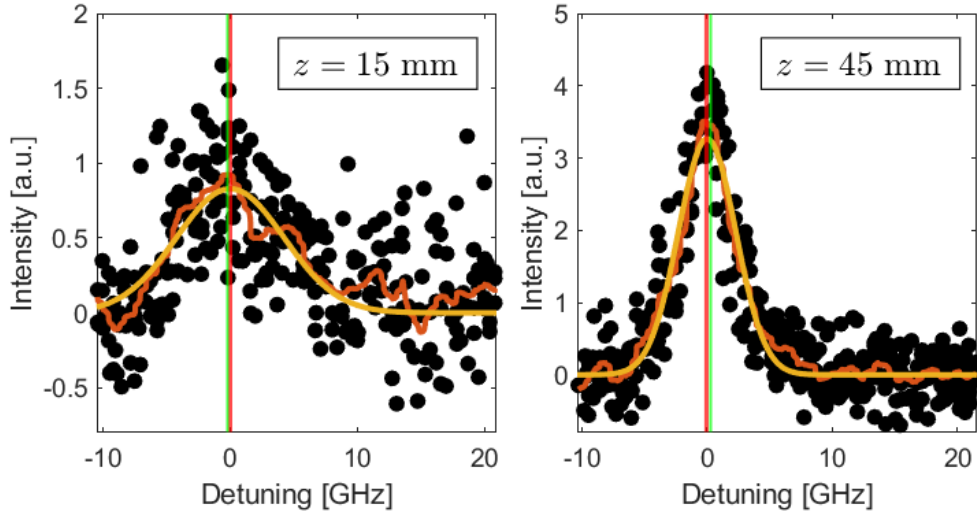
Figure A.12: Example LIF lineshape for configuration B obtained at $z = 15$ mm and $z = 45$ mm.

The two experimental setups described in Section A.3 are used to probe the IVDF in the two directions discussed. As mentioned, only fixed point measurements were performed for the A configuration since the motorized linear stages were not available at the time of the experiment. Referring to figure A.10, the detection point is positioned at $z = 15$ mm from the thruster cover and at $r = 70$ mm, where the thruster center-line and exit plane define the reference frame. While for configuration B measurements were taken for different positions along the z direction at $r = 70$ mm.
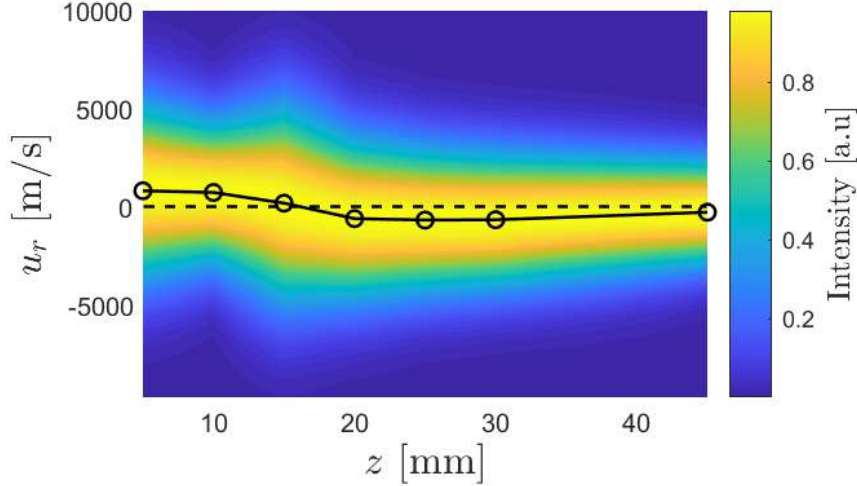
Figure A.13: LIF signal for configuration B measured along *z*. The solid lines and circular markers identify the most probable velocity at the measurement location. The zero velocity is highlighted with a dashed line.

An example of the measurements taken is shown in figure A.12 for $z = 15$ and $z = 45$ mm. Typical signal-to-noise ratios (S/N) for LIF measurements can reach up to 30, however, the S/N for the measurements here presented varies between about 2 and 4.4 depending on the measurement location. The main source of the poor signal quality is suspected to be the low density of the probed species, resulting in a low fluorescence signal level. However, some additional factors may contribute, such as the possible misalignment between the laser beam and the PMT or the orientation of the PMT itself, partially pointing the bulk plasma beam in its field of view. Additional noise is introduced by frequent discharges between the grids, appearing as steep peaks in the fluorescence measurements. The latter were filtered out while post-processing. The low S/N introduces a strong loss of information for the IVDF and a non-negligible uncertainty in the mean velocity determinations. For this reason, the mean velocities here presented are taken as the velocity at the Gaussian mean.

Only single-point measurements are taken for the A configuration. A set of five measurements is taken, showing a most probable velocity along the probing direction **k** (mainly axial velocity, refer to figure A.10-a), close to zero: $u_k \approx 35 \pm 265$ m/s. These results confirmed the existence and detectability of slow ions (with respect to the main ion beam accelerated by the gridded ion thruster), however, no additional measurements were taken at different positions using the A configuration.

As shown in figure A.13 in the radial direction (vacuum setup, configuration B), the lineshapes are found to be spread about the zero velocity center-line. The mean velocities found, depend on the probing position. Peak velocities up to $u_r \approx \pm 1000$ m/s were found in the scanned region. In proximity to the location of $z = 15$ mm, $r = 70$ mm (used for the A configuration) the radial speed changes sign meaning

that the slow ion population is on average directed inwards the plume for $z > 15$ mm. Previous measurements performed by Morishita *et al.*[48] have shown that, in the cathode vicinity, slow ions are attracted towards it so that a net electron current can be emitted to neutralize the ion thruster plume. This hints that a positive u_r is expected as the cathode is approached, explaining the decreasing trend seen in figure A.13 at $z = 45$ mm. Plasma plume potential measurements were taken in [161] and hybrid PIC-fluid simulations in [164], showing $V_p \approx 20$ V at $z = 150$ mm. Assuming a radially decaying potential profile [170, 171, 172, 164], larger mean velocities in the radial direction would be expected at the measurement location if the probed ions were originating from CEX collisions happening in the bulk plume ($u_r \approx 5000$ m/s). On the other hand, these velocities are only approached at the tail of the IVDF (figure A.13). The fact that the measured mean velocities are very close to zero in both directions supports the idea of these ions being produced in proximity to the measurement location, at the periphery of the plume, probably originating from charge exchange (CEX) collisions on neutral atoms from the MW cathode.

The acquired lineshapes offer potential insights into ion temperature T_i, suggesting values ranging from 5 to 14 eV, with a notable increase observed at lower z. Nevertheless, a comprehensive assessment necessitates a higher S/N and careful consideration of other broadening mechanisms other than Doppler broadening, as discussed in Section A.2.

Typically, sputtering is measured in terms of yield (atoms sputtered for impacting ions) and materials exhibit sputtering phenomena above a certain impacting ion energy threshold which is material dependent [173]. The exact threshold for the ITO material is unknown, however, tests were performed by Hu *et al.*[174, 175] for different ion energies (100 – 1000 eV with Xe gas), suggesting a threshold in proximity to 100 eV. The yield was found to peak for incidence angles of about 60°. Therefore for the case of the measurements here presented, neglecting the effect of the sheath at the cover surface, the reported mean velocities cannot explain sputtering phenomena. However, if the ion temperatures here estimated were to be confirmed, a fraction of the ions in the tail of the distribution may reach similar energies and cause sputtering over hours of thruster operations.

A.5   Summary

A degradation of the MW cathode performance was observed during the Hayabusa II mission after only 7.000 h of operation, in contrast with the 70.000 h of operation achieved during on-ground testing. One of the possible hypotheses for this performance loss has been attributed to a degradation of the ITO-covered surfaces surrounding the cathode by sputtering from charge-exchange ions. LIF was found to be an appropriate technique for studying the CEX ion population in a weakly

intrusive manner, motivating the work performed in this chapter.

The LIF setup has been assembled and tested, providing preliminary results. The tests performed have confirmed the detectability of slow ions and their velocity has been probed in two directions, radial and nearly axial. All the performed measurements showed the ion velocities being distributed around zero, with small variations of the most probable velocities not large enough to explain sputtering phenomena. Additionally, the data showed a rather large ion temperature in the order of some eV. If these results were to be confirmed a fraction of the ions in the tail of the distribution might have sufficient energy to cause sputtering (≈ 100 eV).

Although promising, these measurements showed a poor S/N ratio, which should be targeted in the next iterations. It is suggested that the latter could be improved with a better alignment of the laser beam/photomultiplier or by increasing the collection volume (accepting a loss in resolution), reflections of the laser light by the cathode surfaces should also be minimized. A better S/N ratio would allow showing deviations of the IVDF from Maxwellian distribution. To provide further information on the probed population, additional measurements should also target obtaining a 2D scan of the velocity vector in the area of interest. Finally, it would be ideal to evaluate the plasma potential in the proximity of the thruster cover to evaluate the potential drop in the sheath. This may be affected by the material properties, therefore the impact of the aluminum vs ITO should also be assessed. Electrostatic probes shall be used for this purpose, however, due to the low plasma density in this region these measurements may result in being highly intrusive.

Appendix B

Faraday Cup Design for Electrodeless Plasma Thrusters [5]

"Exploration is wired into our brains. If we can see the horizon, we want to know what's beyond."

\- Buzz Aldrin

Faraday cups (FCs) are widely employed in electric propulsion to measure ion currents. In the case of electrodeless plasma thrusters, the typically lower ion energies and larger electron temperatures make it necessary to adopt additional care when designing and testing FCs. In this work, the design of a FC is presented and the probe is used to scan the plume of a Helicon plasma thruster. A modular approach allows testing the effects of a set of design parameters on the collected ion current, namely two collimator types, the collector length, and collector material.

The rest of this chapter is organized as follows. In Section B.1 an introduction to the use of Faraday Cup for electric propulsion testing is made. The experimental setup employed for carrying out the experiment described in this study is outlined in Section B.2, following, the Faraday Cup probe design is described extensively in Section B.3.1. The plasma environment in which the FC probes are used is presented in Section B.4.1 and finally the effect of the design alternatives is analyzed in Section B.4. Lastly, Section B.5 wraps up the work done and outlines best practices for FC use, and provide recommendations for optimal probe design in electrodeless plasma thruster diagnostics.

---

[5]This chapter reproduces with adaptations the conference paper: M. R. Inchingolo and J. Navarro-Cavallé "Faraday Cup Design for Electrodeless Plasma Thrusters", 10th EUCASS Conference, Lausanne, Switzerland, 2023 [70].

B.1 Introduction

Electrodeless plasma thrusters have gained significant attention in the field of electric propulsion due to their potential for longer thruster lifetime [17, 16]. In order to understand the characteristics of these thrusters and optimize their performance, diagnostic tools such as Faraday probes (FP), Langmuir Probes (LP), Retarding Potential Analysers (RPA), etc. have been extensively used.

Faraday probes allow for the measurement of ion currents in the plasma ejected by the thruster, biasing an electrode to negative voltages to reflect electrons and capture ions. Simply planar FP probes [176] commonly present problems related to sheath expansion and Secondary Electron Emission (SEE), furthermore they do not discriminate the ion velocity direction capturing ions from the whole probe field of view. Depending on the plasma properties, these individual effects are known to artificially increase the collected ion current, reducing the accuracy of the ion current determination, and consequently also on the thruster performance estimation. To compensate for these effects, different designs have been proposed in the literature. For example, the Guarded Faraday Probes help reduce the effect related to sheath expansion [177, 178, 179]. Among the other probe designs, the Faraday Cup (FC) configuration has emerged as a widely used approach. This probe is provided with a collimator and a cup-shaped collector enclosed in the probe casing helping respectively reducing the probe field of view and enhancing the recollection of SEE. Additionally, the expansion of the sheath with the bias voltage is contained within the probe, thereby preventing an undesired rise in the collected ion current [176]. Because of these advantages and versatility FCs are extensively used as a diagnostic tool in a variety of fields: nuclear physics [180], plasma sources [181, 182], and electric plasma thrusters. All of these, present different characteristics in terms of ion energy, densities, electron temperature, etc., parameters that must be taken into account for an effective probe design. We can find in the literature a wide range of studies and design optimization on FCs [183, 180, 181], however, the majority of these are in the keV ion energy range, hence with very different requirements with respect to electrodeless plasma thrusters. A significant contribution to FCs for electric propulsion has been made by Brown D., Mazouffre S., and Hugonnaud V.[177, 178, 176, 183, 184]. In their respective studies, they proposed various probe types and prototypes for measuring the plume of different thrusters, exploring variations in collimator shape, aperture size, collector size, and material properties. However, no clear probe design has emerged yet for the plasma properties typical of an electrodeless plasma thruster. For magnetic nozzle thrusters, in particular, the ion energies are typically in the same order of magnitude as the plasma potential at the ion current measurement location, this fact is expected to play a role in the ion optics determined by the geometrical constraints in the probe. Additionally, several aspects have not been assessed yet extensively concerning the role of SEE

on the accuracy of the ion current measurements while working in these particular plasmas.

In this work, we aim to address the role of several design parameters: the collimator size and shape and the collector length and material. To perform these studies, a modular FC design is proposed. Additionally, a segmented collector is used to discriminate between the current collected at the lateral sides of the cup or at the back electrode. A Helicon thruster represents the source for the plasma under analysis, whose plasma properties are as well characterized by means of a LP and a RPA. Finally, this work provides some recommendations and guidelines or best practices for the use of FCs in the characterization of electrodeless plasma thrusters.

B.2   Experimental Setup

The plasma source used for the experiments of this work, is based on the thruster prototype described in Ref. [185]. The helicon plasma thruster is operated at 13.56 MHz. The radio-frequency (RF) power is generated with a power amplifier, SerenHR2100, and fed to the thruster thanks to a custom-made matching network by Sener Aerospacial S.A [186]. The thruster has been operated at a constant power of $P_F = 350$ W, being P_F the forward power set by the amplifier, however, about 10% of this power will be lost in the transmission line. Power is coupled to the plasma through a half-helical silver-coated antenna wrapped around a quartz tube with a diameter $D_T = 25$ mm and 150 mm long. The magnetic field required for helicon coupling and the magnetic nozzle is produced with a single coil operated at $I_c = 12$ A, producing a magnetic field peak of about 600 G at its center. The thruster is operated between 5 and 20 sccm of Xenon, the mass flow rate being controlled by a Bronkhorst EL-FLOW select Xenon calibrated mass flow controller, with a resolution of 0.1 sccm and 100 sccm full range. The tests have been conducted inside the main vacuum chamber of the UC3M laboratory. A description of the testing facility can be found in Chapter 5. The thruster axis is aligned with the vacuum chamber axis, and the thruster outlet section is about 2.5 m away from the chamber downstream wall to minimize plume-chamber wall interactions.

Concerning the diagnostics setup, in this work, only electrostatic probes are used. Initial experiments were performed to characterize the plasma source, thus in addition to the Faraday Cups (FC), object of this study and discussed in detail in Section B.3.1, two auxiliary probes are used for plasma characterization: a Retarding Potential Analyser (RPA, Impedance-Semion single button probe) and an RF compensated Langmuir Probe (LP). An additional description of the RF-compensated LP used in this work is available at Refs. [187, 124], for this test the Langmuir Probe tip electrode is 6 mm long, with a diameter of 0.256 mm. The data analysis and procedures of Ref. [125] are used to retrieve the plasma properties from

the scanned data, i.e. I–V characteristic curve of a LP.

These two probes are mounted on a polar probe positioning system. This system is capable of moving probes on a plane along the radial ρ and polar α directions (Figure B.1). The resolution of the system is about 0.3 mm and 1° for the radial and the polar directions respectively. The center of rotation of the probe positioning system is aligned with the center of the thruster exit plane. As discussed in Section B.4.1, these probes are used to retrieve the plasma properties at a distance from the thruster of $\rho = 395$ mm and $\alpha = 0 - 60°$ where the ion current measurements are performed with the FCs.
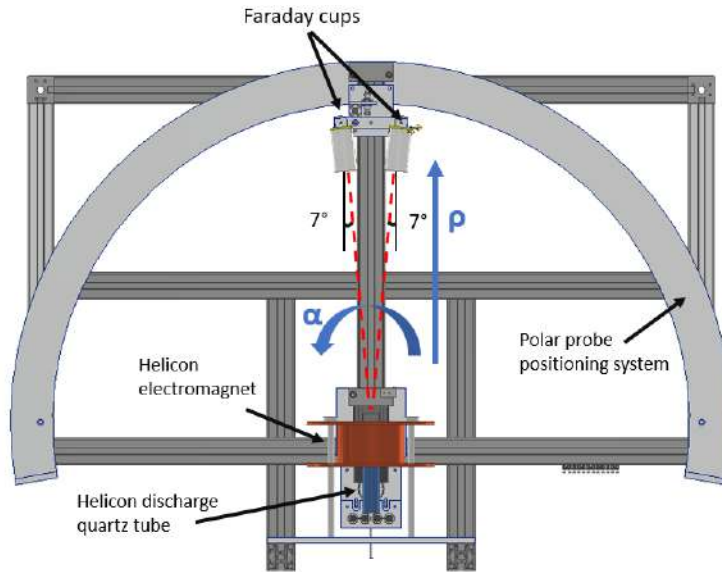
Figure B.1: Setup assembly.

Two probe bodies and their internal components were manufactured. Having two probes in the same setup reduces the need for multiple experiment mounting iterations and allows for scans to be performed under the same thruster and plasma conditions for a more significant probe comparison. The Faraday Cups (FC) analyzed in this work are mounted by pairs in the same arm holder discussed above, as shown in Figure B.1. The FCs are mounted symmetrically with respect to the radial direction at $\rho = 395$ mm, separated between each other by a distance of 96 mm and tilted by 7° so that the axis of the probes are pointing towards the thruster exit plane. However, due to this mounting strategy, only one probe is used at a time, so that the scan can happen for the same plume region.

B.3 Faraday Cup

B.3.1 Design

The modular FC design presented in this work allows varying easily the configuration of the internal components enabling the study of their importance on the collected current.

Figure B.2-a shows a CAD cross-section view of the probe design. From the left to the right, one can see the collimator and the collector. Particles enter the probe through the collimator orifice. Once inside, because of the large negative biasing (V_b) of the collector, a non-neutral Child-Langmuir sheath is formed. Consequently, the resulting electric field attracts the ions, their charge is collected at the collector electrodes once in contact, supposing as well the recombination as neutral gas. In this design, the collector consists of an aluminum tube here called "lateral collector" and an additional "U" shaped electrode positioned at the back of the tube and referred to as "back collector". The diameter of the lateral collectors used in this work is 15 mm. In this work, two lengths for the lateral collector are tested $L_c = 40$ and 20 mm. Additionally, two back collector materials are also tested namely Aluminum and Tungsten HA195. Both electrode types are biased simultaneously at the bias V_b. This segmented collector design allows separating the contribution to the total collected ion current I_T in the lateral collector current, I_L, and in the back collector one I_B, so that $I_T = I_B + I_L$. Hence, using this design it is possible to obtain data on the ion current distribution inside the cup, which can be a useful tool for result interpretation as done in Section B.4. The electrical connections to the FC collectors are realized with coaxial cables. The biasing voltage and the current measurement were obtained with a source-meter Keysight B2901A and a Keythley 6517B.

Conversely, in this study, two types of collimators are used, here defined as split (C1) and continuous (C2) collimators. A schematic view of C1 and C2 can

<center>(a)   (b)</center>
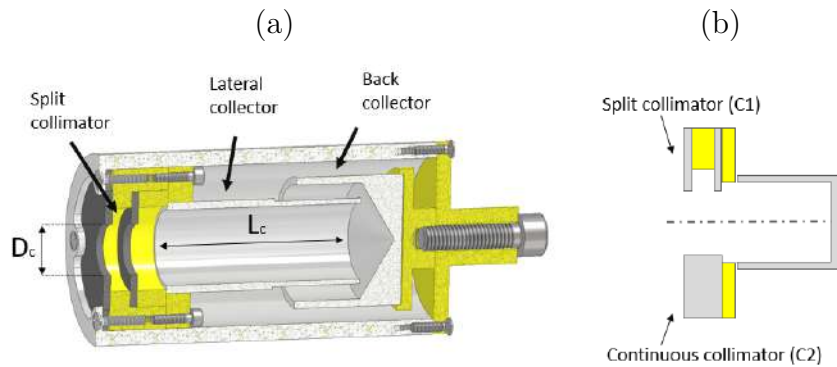
Figure B.2: (a) CAD cut-view representation of the Faraday Cup probe design equipped with collimator C1. (b) Schematic drawing (not in scale) of the two collimator types in this study. Dielectric insulators (Teflon, PLA) are shown in yellow.

be seen in Figure B.2-b. Both C1 and C2 share the same hole diameter of $D_c = 10$ mm, defining an aperture area of $A_c = \pi D_c^2/4 = 78.5$ mm^2. C1 is composed of two conductive graphite disks with a thickness of 1.5 mm separated by a distance of 4 mm (Figure B.2-a). C2 is a 10 mm long bored aluminum cylinder. Both of them are provided with an isolated electrical connection within the probe, making it possible to measure their floating potential and possibly apply an electrical bias.

The collimator defines the field of view (FoV) of the probe. The FoV can be described as the vertex of the cone in which an ion must be located to be collected by the probe. However, it is important to note that meeting this condition alone is not sufficient for collection. The orientation of the velocity vector of the ion also plays a significant role in determining whether it will be successfully collected by the probe. Ideally, a good Faraday Cup design would have the smallest field of view able to contain the thruster aperture, so that only the ions coming directly from the thruster and directed towards the FC would be collected.

The FoV of the probe equipped with C1 is 91.3° while for C2 it is 85°. Assuming ions travel only in straight lines, at each position in front of a Faraday Cup, only those within the allowed velocity vector range will be collected by the probe since they are in a collision course with the collector. The others will impact the collimator, casing, and dielectric components or not impact the FC at all. For each of these positions, one can define the maximum and minimum velocity vector angle (Θ_{max} and Θ_{min}) with respect to a reference (the probe axis for example) that would result in ion collection. Figure B.3-a shows the $\Delta\Theta = |\Theta_{max} - \Theta_{min}|$ that allows ions collection at each position in the field of view of an FC equipped with C1.An example scheme is shown in Figure B.3-b.

Figure B.3-a shows that $\Delta\Theta$ grows approaching the probe (lower X), meaning that the FC would be able to collect those ions from that position with a larger disparity on their velocity vector direction (larger $\Delta\Theta$). Being D_c comparable to

| (a) | (b) |
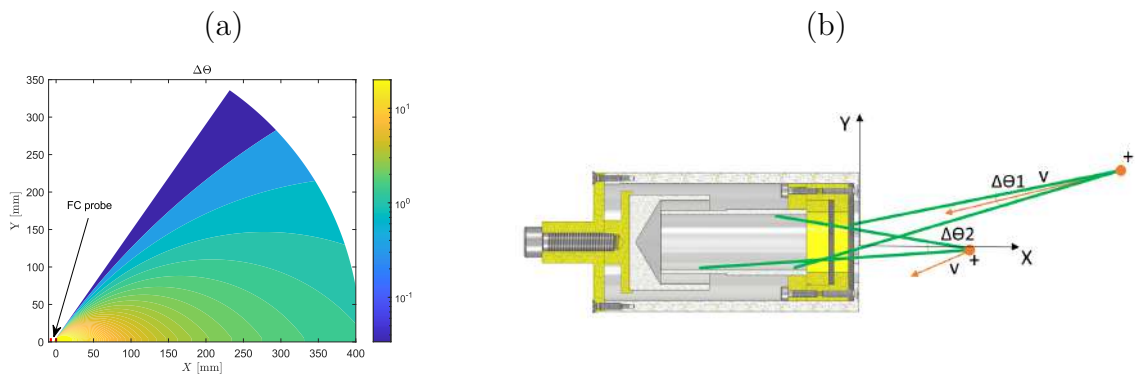
Figure B.3: (a) $\Delta\Theta$ in the FoV cone of a probe equipped with collimator C1. (b) Scheme showing two ions with allowed/not-allowed velocity vector for FC probe ion current collection. XY are the FC body axes.

ID	Collimator type	Collector length (L_c)	Back collector material
FC-A	Split (C1)	4 cm	Aluminium
FC-B	Continuous (C2)	4 cm	Aluminium
FC-C	Split (C1)	2 cm	Aluminium
FC-D	Split (C1)	2 cm	Tungsten

Table B.1: Table summarising the Faraday Cup design alternatives.

the thruster exit plane diameter D_T, placing the probe at closer distances would overestimate the ion current. This effect also becomes relevant in the presence of large amounts of CEX collisions with neutrals resulting in slow ions with a wider spread in velocity direction angle. [188, 189]. For this reason, the probes have been placed close to the farthest position allowed by the probe positioning system (395 mm from the thruster exit plane), as discussed in Section B.2.

Finally, in this study, different design alternatives are proposed for the internal elements, their differences are summarized in table B.1.

B.3.2 Operation and data post-processing

It is noteworthy to mention that, before the first use of the probe after assembling, an electrode cleaning procedure using electron bombardment has to be carried out. This allows for removing electrode surface impurities and obtaining reliable and consistent results: the probe is positioned in a region with higher density ($\rho = 100$ mm at 5 sccm), and both the lateral and back collector are biased to a high positive bias (typically $V_b = 200$ V). An example of the I-V characteristic curve collected before and after the cleaning procedure is shown in Figure B.4.
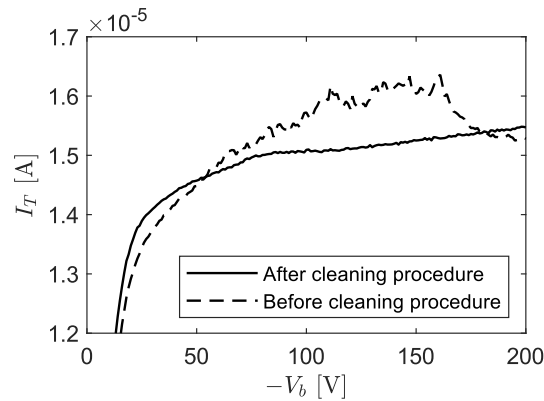
Figure B.4: I-V curve collected by the Faraday Cup before and after the cleaning procedure.

Two types of FC scans are performed in this study, I-V curves and plume scans. The I-V curves are obtained by keeping the probe at the measurement location and sweeping the bias of the collector from $V_b = 0$ to high negative bias to enter the ion

saturation region (typically $V_b = -130$ V or -200 V). The plume scans are performed at a fixed value of collector bias, $V_b = -100$ V since for this value the ion current is saturated for all the tested plasma conditions.

Assuming plume axisymmetry, and having measured the ion current density $j_i = I_T/A_{FC}$ at different angular positions α, it is possible to estimate integrated plume properties: the ion beam current, I_i, the utilization efficiency η_u and the plume divergence angle α_D. I_i is given by:

$$I_i = 2\pi\rho^2 \int_0^{\pi/2} j_i(\alpha)\sin(\alpha)\,d\alpha, \qquad (B.1)$$

Assuming a singly-charged ion beam, the utilization efficiency is then defined as the (normalized) ratio between the ion beam current and the input mass flow rate,

$$\eta_u = \frac{\dot{m}_i}{\dot{m}_p} \simeq \frac{I_i m_{Xe}}{e\dot{m}_p}, \qquad (B.2)$$

where $\dot{m}_i$ is the ion mass flow rate in the plume, e is the unit charge and m_{Xe} is the Xenon atomic mass. The divergence efficiency can be found considering the portion of current directed in the axial direction,

$$\eta_d = \left(\frac{I_{zi}}{I_i}\right)^2, \qquad (B.3)$$

with:

$$I_{zi} = 2\pi\rho^2 \int_0^{\pi/2} j_i(\alpha)\sin(\alpha)\cos(\alpha)\,d\alpha. \qquad (B.4)$$

B.4 Results

The influence of the design parameters on the ion current collection is here discussed. Firstly, in Section B.4.1 the plasma environment is assessed with the help of a LP and a RPA. In Section B.4.2, B.4.3, and B.4.4 the effect of the different tested collimators, collector length, and material are respectively analyzed.

B.4.1 Plasma Environment and test conditions

Knowing the plasma conditions at the Faraday Cup location can provide insights into the cup's performance and help the result interpretation. Furthermore, the data provided in this Section are essential for a correct design of a FC as discussed in Section B.3.1. As mentioned in Section B.2 a Retarding Potential Analyzer (RPA) and a Langmuir probe (LP) were used as auxiliary probes. The analysis of the I-V curve from a LP provided the ion density n_i, the electron temperature T_e, and the

plasma potential V_p. The RPA is used to determine the most probable total ion energy E_i (potential plus kinetic energy). The plasma properties were evaluated at the Faraday Cup probing position used for this experiment: $\rho = 395$ mm and $\alpha = 0 - 60°$.
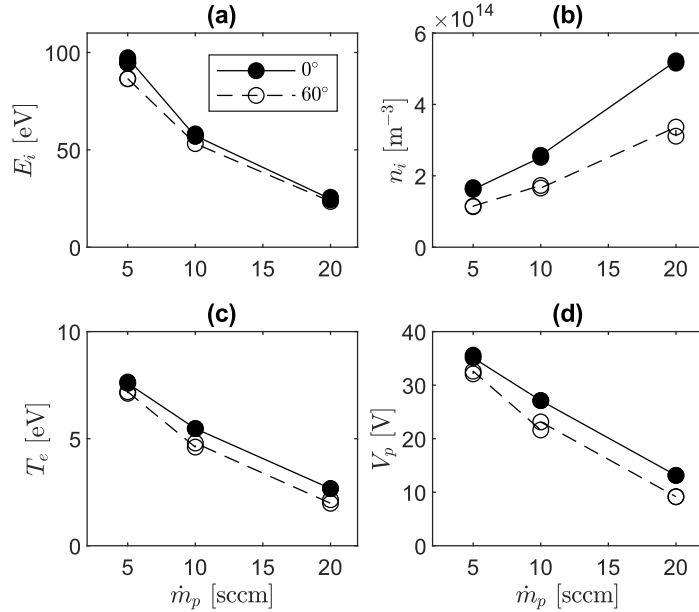
Figure B.5: Plasma environment at the FC probe distance. (a) Most probable ion energy E_i according to the IEDF measured by the RPA. (b,c,d) ion density, electron temperature, and plasma potential from the LP I-V characteristic curve.

As typically happens for Helicon plasma thrusters and, in general, magnetic nozzle thrusters [66], increasing the mass flow rate reduces the available energy per electron, and simultaneously increases the electron collision rate. This lowers the electron temperature (refer to Figure B.5-c), and consequently the potential drop available for the ions in the magnetic nozzle. Hence, E_i results are strongly dependent on the mass flow rate. Peak ion energies of about 100 eV were found on the axis (Figure B.5). However, E_i is found to be weakly dependent on the angular position. From the data available in Figure B.5, Debye lengths close to the one-millimeter range are expected to be found at these distances. Furthermore, the data provided can be used to obtain a useful order of magnitude for the ion current density j_i that the FC probes are expected to measure. j_i can be obtained as $j_i = n_i v_i e$, where v_i is the local ion velocity: $v_i = \sqrt{2(E_i - V_p)/m_{Xe}}$. Estimations of j_i provide values in the order of $0.15 - 0.35$ A/m^2, which as shown in the next section, is in line with the FC measurements.

B.4.2   Effect of the Collimator

Two different collimators have been tested: a split collimator (FC-A) and a continuous collimator (FC-B). Both designs share a similar geometrical view angle. The plume has been scanned at the probe nominal distance ($\rho = 395$ mm) with a fixed collector bias voltage of $V_b = -100$ V. The ion current density profiles obtained with the two collimator geometries are shown in Figure B.6 together with the computed propellant utilization efficiency. Firstly, the current density levels reached on the axis result being very close to the ones estimated just using the LP and RPA data. This is particularly true for the FC-A case. The plume presents a peak in the center for all the mass flow rates tested, however, local maxima are developed at around $\alpha = \pm 50°$ which tend to disappear as $\dot{m}_p$ is raised. This behavior is not yet completely understood, but it has been seen in other previous works [190]. One of the hypotheses is that a second less-magnetized beam forms in proximity to the discharge chamber walls, this might happen because of CEX collisions with the recombined ions at the walls.

The utilization and divergence efficiency have been estimated from these data, staying below 25% and 45% respectively. This result agrees with those presented in Section B.4.1, rising the mass flow rate reduces the electron temperature resulting in a lower ionizing capability. On the other hand, the disappearance of the lateral peaks makes the divergence efficiency improve with $\dot{m}_p$.
The two probes recover the same profile shape, but the measured current level is different. The split collimator (FC-A) shows about 45-50% more current with respect to the continuous collimator probe (FC-B). Since the shape is preserved, the differences in the divergence estimation are small.

To understand how the collimator design affects the current collection, I-V curve scans have been measured on the plume axis (Figure B.7). The segmented collector has been used as a diagnosing tool to investigate the source of this difference.
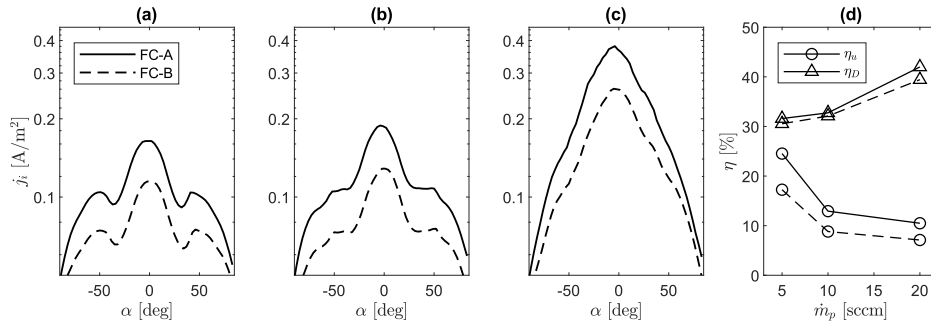
Figure B.6: Plume scans with FC-A and FC-B for three different mass flow rates, $\dot{m}_p = 5$ (a), 10 (b), and 20 (c) sccm. Panel (d) shows the propellant utilization efficiency η_u and the divergence efficiency η_d for the two probes at the different mass flow rates tested.
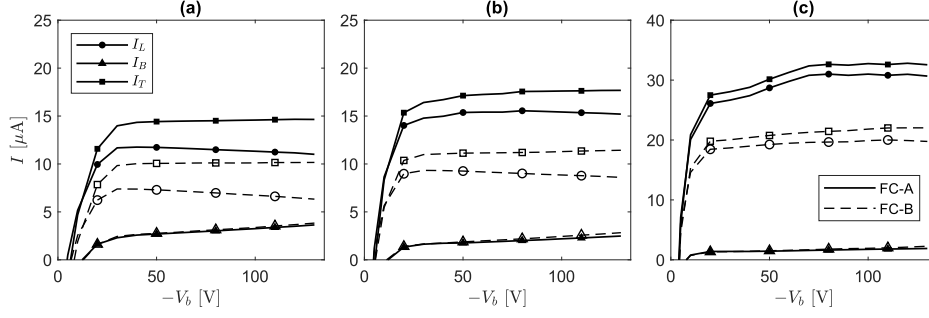
Figure B.7: I-V curves for the probe with split collimator FC-A (solid lines) and continuous collimator FC-B (dashed lines) for $\dot{m}_p$ = 5 (a), 10 (b) and 20 sccm (c). All the curves are taken on the thruster axis.
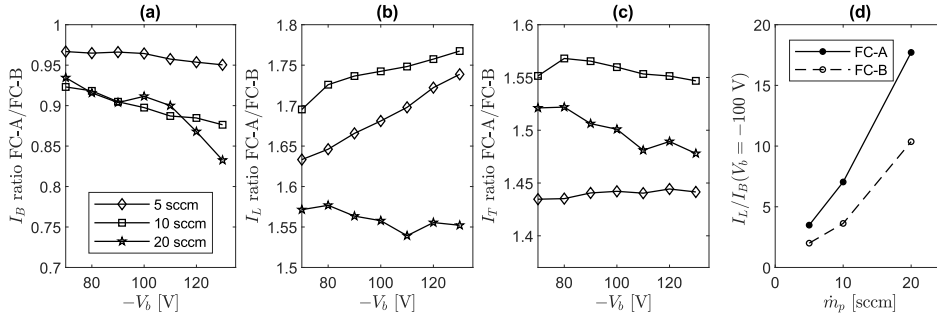
Figure B.8: Collected current ratios I_B (a), I_L (b), I_T(c) for $\dot{m}_p$ = 5, 10 and 20 sccm. (d) ratio between the lateral and back current collected for FC-A (solid) and FC-B (dashed).

Figure B.7 shows the I-V curves obtained for the back and lateral collector together with the total current as introduced in Section B.3.1. The previously observed discrepancy in the total current can also be seen in the I-V curves. For a useful comparison, the ion currents shown in Figure B.7, are displayed as ratios in Figure B.8. I_B is weakly dependent on which type of collimator is used. I_B for the probe FC-A is less than 5% lower than the one for the FC-B case, this value increases with the mass flow rate and can reach up to 15% for 20 sccm (Figure B.8-a). Thus, the greatest contribution to the total current discrepancy is brought by I_L, the probe using the split collimator collecting up to 75% more current (Figure B.8-b). This is also the source for the lower I_L/I_B ratio shown by the FC-B.

Finally, understanding how much current reaches the lateral collector with respect to the back one, can provide clues on the ion trajectory inside the probe. Referring to Figure B.8-d, the ratio of current I_L/I_B, increases with the mass flow rate, the value at 100 V was taken as reference. This effect must be related to the reduced ion energy with $\dot{m}_p$ as was shown in Figure B.5-a, the lower energy makes it easier for the sheath on the lateral collector to deflect ions towards itself rather than letting them proceed in a straight line towards the back collector.

To understand the origin of the reduced current collected by the lateral collector, a simplified 1D sheath model on the C2 continuous collimator has been employed. The electrons are assumed Maxwellian and the ions to enter the sheath with the Bohm velocity. Considering ion energy conservation, the model solves the Poisson equation in the sheath along a floating planar surface parallel to the Z direction (here representing the C2 collimator surface). The floating condition is achieved by setting the ion and electron flux at the surface to be equal. The floating surface extends from $Z = 0$ mm to $Z = 10$ mm. The domain extends several times the Debye length in the perpendicular direction Y. Note that, being 1D, the model assumes the plasma properties to be constant along the Z direction and neglects any boundary effect around the margins of the floating surface. The resulting perpendicular electric field within the sheath (E_Y) is used to propagate the trajectory of ions incoming at different distances Y from the surface, and initially traveling along the Z direction with a kinetic energy of $E_k = E_i - V_p$ at $Z = 0$.

Figure B.9 shows the resulting ion trajectories for the three tested plasma conditions at 5, 10, and 20 sccm. The electron temperature, ion energy and density required for the solution are those found experimentally and available in Figure B.5. The low ion kinetic energies involved if compared to the plasma potential, make it easy for the sheath to deflect ions in the direction perpendicular to the surface. The ions within a limit perpendicular distance from the surface Y_{lim} would end up colliding with the surface (collimator) and be neutralized. Y_{lim} thus depends on the combination of ion energy, and electric field E_Y. It is found that $Y_{lim} = 2.6$ mm, 3.45 mm, and 3.17 mm, for 5, 10, and 20 sccm respectively. Note that the ions at a sufficiently large distance from the surface will stay unaffected and continue traveling in the z direction as the perpendicular electric field decreases.

Although involving several important assumptions, this simple model is able to show that a significant part of the probe aperture area is lost because of the formation of a sheath on the surface of the collimator. This sheath is responsible
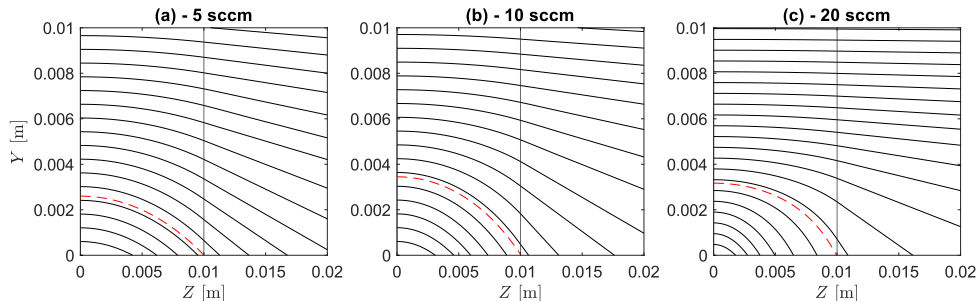
Figure B.9: Ion trajectory along a floating surface ($Y = 0$ m) for the plasma conditions (refer to Figure B.5) of $\dot{m}_p = 5$ sccm (a), $\dot{m}_p = 10$ sccm (b), $\dot{m}_p = 20$ sccm (c). The vertical line at $Z = 10$ mm, identifies the edge of the collimator. The trajectory in dashed red identifies the limit case for ion collection, Y_{lim}.

for the collection of part of the ions which are recombined at the collimator surface and are consequently not able to reach any collector.

The ions which are most affected are those traveling in proximity to the collimator surface and consequently are the ones that would have most probably been collected by the lateral collector. In this regard, the reduced I_L current collected by FC-B (refer to B.8-b), suggests that this effect is larger for the continuous collimator (C2). Neglecting 2D boundary effects between the disks composing C1, it is expected that this effect is substantially lower for this electrode since each disk is only 1.5 mm thick. On the other hand, both collimators are axially symmetric, which results in a null radial electric field at the axis. Thus, ions traveling in proximity to the axis will proceed unaffected by the sheath formation and collide with the back collector. This consideration is in agreement with the small difference between the current collected on the back collector by the two probes.

On a final note, the Y_{lim} found for the three mass flow rates shows that the ions are less affected by the sheath at 20 sccm with respect to the 10 sccm cases. As $\dot{m}_p$ increases the electron temperature decreases and the density increases, both effects reduce the Debye length $\lambda_D \propto \sqrt{\frac{T_e}{n_e}}$, hence tending to lower Y_{lim}. However, as seen in Figure B.5-a the ion energy is reduced with $\dot{m}_p$, making the ions easier to be deflected (tendency to enlarge Y_{lim}). Hence, the decreased Y_{lim} for 20 sccm if compared with the 10 sccm case, can be explained by the slower decrease in ion energy with $\dot{m}_p$ with respect to Debye length. This phenomenon increases the effective aperture area, possibly explaining the reduced disagreement between FC1 and FC2 observed at 20 sccm as seen in fig B.8-b and c.

B.4.3 Effect of the collector length

The length of the collector in a Faraday Cup is thought to be associated with the probe's capability of recollecting secondary electrons emitted by ions impacting the electrode surface [183]. Furthermore, as mentioned in Section B.3.1, the design of a FC should take into account the Child-Langmuir sheath expansion due to the applied voltage bias. Hence, in both cases, probes that are too short may affect the accuracy of the ion current measurement, either by losing the capability of recollecting SEE or by perturbing the external plasma respectively. The effect of the collector length has been tested by using the FC-A and C. Being FC-A equipped with a 4 cm long collector, and FC-C with a 2 cm collector. Both probes implement the split aluminum collector design.

Figures B.10-a and b, show the collected currents at 5 sccm for the two probes FC-A and FC-C as an illustrative case. Firstly, the two probes collect the same amount of total ion current I_T, both at $\alpha = 0°$ and $60°$. As visible in Figure B.10-c, this is true also for 10 and 20 sccm, being the disagreement in the same order of

the current variation due to the thruster repeatability ($\approx 5\%$). On the other hand, FC-A and FC-C show a clear difference in how I_T is distributed between the lateral and back collector. This is expected since the "field of view" of the back collector is larger for the 2 cm design, being closer to the collimator/probe aperture with respect to the 4 cm case. Moreover, while the total current is close to constant, the ratio of current I_L/I_B decreases for both probes with increasing $|V_b|$. This is more evident for probe FC-C where the ratio becomes lower than 1 for the 5 sccm case. A possible interpretation of this exchange of current between the lateral and the back collector might be linked to the shape of the iso-potential surfaces within the collector. As the applied negative bias potential increases, creating a thicker Child-Langmuir sheath, the iso-potential lines may become from concave (following the collector curvature) to flatter. The resulting electric field would affect the ion trajectory deviating the ions that were collected by the lateral collector at low $|V_b|$ towards the back collector.
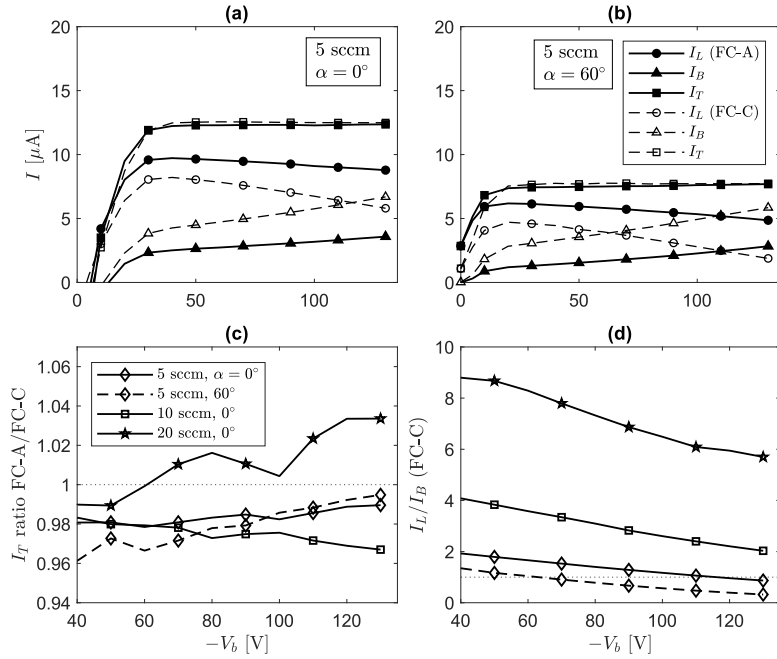
Figure B.10: (a-b) Ion currents collected at 5 sccm respectively for $\alpha = 0°$(a) and $\alpha = 60°$(b) for FC-A (solid line) and FC-C (dashed line). (c) Ratio of total current collected between the 4 and 2 cm probes. (d) Ratio of lateral to back collected current from the 2 cm probe (FC-C).

The case at 5 sccm, at $\alpha = 60°$ (Figure B.10-b) offers the possibility of having a similar ion energy to $\alpha = 0°$, but with lower density (refer to B.5-a and b). For this case, the effect is accentuated because of the increased characteristic sheath size within the probe. Hence, further decreasing the collector length, might be detrimental since the iso-potential lines could become convex and possibly affect the ion collection at low densities. However, conducting a non-quasi-neutral plasma

simulation, similar to those carried out for the RPA case by Cichocki et al.[147], would help verify these hypotheses by solving the potential distribution inside the probe under various measurement conditions.

B.4.4   Effect of the Collector material

Probe configurations FC-C and FC-D were used to test if the collector material has any influence on the ion current collection accuracy. For this purpose, the material of the back collector for FC-D has been chosen to be tungsten, which is expected to provide a lower SEE yield [191, 176]. Note that the collector length for this comparison has been chosen to be 20 mm since it shows a lower I_L/I_B, hence any effect inherent to the SEE from the back electrode would be accentuated and easier to be clearly identified.

Figure B.11 shows the relative difference between the total current collected by the two probes, with respect to the probe FC-C. Also for this scenario, small variations in I_T were observed, the current collected by FC-D is ± 1-4% lower than FC-C. However, this variation is small, being in the same order as the uncertainty on the repeatability of ion current measurements for successive firings of the Helicon thruster, concluding that if there is any SEE effect, this is small and can be disregarded. A similar result was also obtained by Engelman with a molybdenum collector [192].
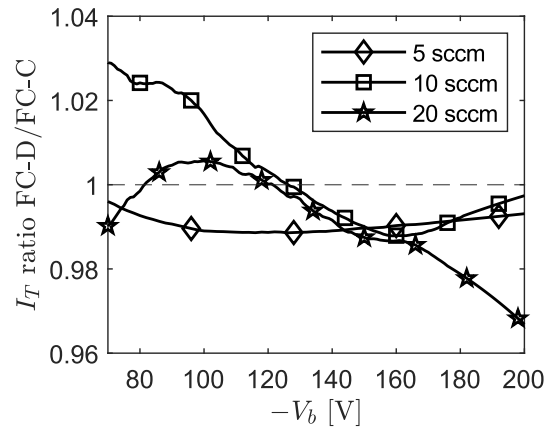
Figure B.11: Ratio between the total current I_T collected by FC-D (Back collector in Tungsten) and FC-C (Back collector in Aluminium).

Finally, the fact that the I_T current collection is insensitive to the probe length used in this study (20-40 mm long) and collector material (aluminum vs tungsten) points out that SEE generation or non-recollection of SEE could be a negligible effect in the range of ion energies used in this study.

B.5 Summary

A novel modular Faraday Cup prototype has been developed to identify the effects of several design parameters on the ion current measured. The impact of two types of collimator shapes (C1 and C2), collector length (4 and 2 cm long), and collector material (Aluminium and Tungsten) were analyzed. As a further diagnosing tool, the collector used is segmented into two parts (the lateral and back collector). This expedient made it possible to provide insights into the ion current distribution within the probes.

Auxiliary experimental data characterizing the plume of the thruster were obtained with a LP and an RPA. The resulting current density estimations obtained from the data they provided on the axis exhibit a promising agreement with those derived from FC-A. On the other hand, the probe equipped with the C2 collimator always showed about 50% less collected current with respect to the probe with C1. The measurements with the segmented collector allowed checking that the source of the current discrepancy is the lower amount of ions reaching the lateral collector. A simple 1D model of an electrostatic sheath has been proposed to explain the ion optics around the collimator region. It showed that the trajectory of the ions is curved towards the collimator by the electric field arising within the sheath. The ions are recombined at that wall, preventing them from being collected by the collector. This effect is expected to be stronger for C2 with respect to C1 because of its shape. Suggesting that thin collimators might be a better option. This phenomenon is expected to mainly affect the current collection on the lateral collector, in agreement with the experimental data.

Both the collector length and material were expected to influence secondary electron emission by ion impact. However, the proposed experiments have demonstrated that the variation in the total collected ion current among the tested probes is minimal. This suggests that, under the plasma conditions involved in this study, SEE emission and their recollection are not influenced by the probe's length or material. As a speculation, this lack of effect could be attributed to the low presence of secondary electrons under the tested conditions.

Furthermore, the study on the probe length has revealed that probes shorter than 2 cm could potentially disturb the upstream plasma in the low-density regions, thereby affecting the collection of ion current.

Although multiple parameters were investigated, it is not possible with the current experimental setup to evaluate the absolute accuracy of the probes on the ion current measured, since the total plume current is not known a priori: i.e. other design parameters might exist which could have a significant effect on the ion current collection, such as ion optics phenomena derived by border effects on the collimators or the diameter of the collector. Thus, to fully address the optimal probe design for

a FC for electrodeless plasma thrusters, 2D axisymmetric plasma simulation should be carried out to highlight any further phenomenon happening within the probe. Concurrently, an experimental calibration of the probes should be performed with a source providing a known current and with ions in comparable energy and density ranges as those in this study. This would ease probe design iterations and increase measurement accuracy.

Bibliography

[1] G.P. Sutton and O. Biblarz. *Rocket propulsion elements*. Wiley, 2010.

[2] HA Arbit, SD Clapp, and CK Nagai. *Lithium-fluorine-hydrogen propellant investigation Final report*. Tech. rep. 1970.

[3] D.M. Goebel and I. Katz. *Fundamentals of Electric Propulsion: Ion and Hall Thrusters*. Jet Propulsion Laboratory, Pasadena, CA, 2008.

[4] Euroconsult Rep. Brochure. *Satellites to be Built and Launched by 2030*. `https://digital-platform.euroconsult-ec.com/wp-content/uploads/2022/01/Extract_Sat_Built_2021.pdf`. Dec. 2021.

[5] R.G. Jahn. *Physics of Electric Propulsion*. Dover, 2006.

[6] D.M. Goebel, R.E. Wirz, and I. Katz. "Analytical ion thruster discharge performance model". In: *Journal of Propulsion and Power* 23.5 (2007), pp. 1055–1067.

[7] *Scheme of Hall Effect Thruster*. https://en.wikipedia.org/wiki/Hall-effect$_t$*hruster*. Accessed: 2023-12-14.

[8] *Scheme of Gridded Ion Thruster*. https://en.wikipedia.org/wiki/Gridded$_i$*on$_t$hruster*. Accessed: 2023-12-14.

[9] Archit Bapat, Pramod B Salunkhe, and Aakash V Patil. "Hall-effect thrusters for deep-space missions: A review". In: *IEEE Transactions on Plasma Science* 50.2 (2022), pp. 189–202.

[10] David R Jovel, Mitchell LR Walker, and Daniel Herman. "Review of High-Power Electrostatic and Electrothermal Electric Propulsion". In: *Journal of Propulsion and Power* 38.6 (2022), pp. 1051–1081.

[11] Stéphane Mazouffre. "Electric Propulsion for Satellites and Spacecraft: Established Technologies and Novel Approaches". In: *Plasma Sources Science and Technology* 25.3 (2016), p. 033002. DOI: `10.1088/0963-0252/25/3/033002`.

[12] F. Romano, Y.-A. Chan, G. Herdrich, C. Traub, and et al. "RF Helicon-based Inductive Plasma Thruster (IPT) Design for an Atmosphere-Breathing Electric Propulsion system (ABEP)". In: *Acta Astronautica* 176 (2020), pp. 476–483. DOI: `10.1016/j.actaastro.2020.07.008`.

[13] Anna J Sheppard and Justin M Little. "Performance Analysis of an Electron Cyclotron Resonance Thruster with Various Propellants". In: *Journal of Propulsion and Power* (2022), pp. 1–11. DOI: `10.2514/1.B38698`.

[14] K.A. Polzin. "Scaling and systems considerations in pulsed inductive plasma thrusters". In: *Plasma Science, IEEE Transactions on* 36.5 (2008), pp. 2189–2198.

[15] Jared P Squire et al. "VASIMR VX-200 Operation at 200 kW and Plume Measurements: Future Plans and an ISS EP Test Platform". In: *32nd International Electric Propulsion Conference*. 2011.

[16] Eduardo Ahedo. "Plasmas for space propulsion". In: *Plasma Physics and Controlled Fusion* 53.12 (2011), p. 124037. URL: `http://stacks.iop.org/0741-3335/53/i=12/a=124037`.

[17] SN Bathgate, MMM Bilek, and DR Mckenzie. "Electrodeless plasma thrusters for spacecraft: a review". In: *Plasma Science and Technology* 19.8 (2017), p. 083001.

[18] K. Takahashi. "Helicon–Type Radiofrequency Plasma Thrusters and Magnetic Plasma Nozzles". In: *Reviews of Modern Plasma Physics* 3 (2019), p. 3. DOI: `10.1007/s41614-019-0024-2`.

[19] J.C. Sercel. "An experimental and theoretical study of the ECR plasma engine". PhD thesis. California Institute of Technology, 1993.

[20] F Bourg, R Geller, B Jacquot, T Lamy, M Pontonnier, and JC Rocco. "Source d'ions multicharges MINIMAFIOS: Nouvelles caracteristiques". In: *Nuclear Instruments and Methods in Physics Research* 196.2-3 (1982), pp. 325–329.

[21] CM Lyneis et al. "Results with the superconducting electron cyclotron resonance ion source VENUS". In: *Review of scientific instruments* 75.5 (2004), pp. 1389–1393.

[22] R Geller. "ECRIS: The electron cyclotron resonance ion sources". In: *Annual Review of Nuclear and Particle Science* 40.1 (1990), pp. 15–44.

[23] S Bliani, R Geller, W Hess, B Jacquot, and C Jacquot. "A high intensity ECR stripped ion source". In: *IEEE Transactions on Nuclear Science* 19.2 (1972), pp. 200–203.

[24] D. B. Miller, E. F. Gibbons, and D. J. Ben Daniel. "Cyclotron resonance propulsion system". In: *AIAA Electric Propulsion Conference*. 1963, p. 33.

[25] R Bardet, T Consoli, and R Geller. "Experimental results on plasma acceleration by gradients of static magnetic and electromagnetic fields". In: *Nuclear Fusion* 4.1 (1964), p. 48.

[26] Térenzio Consoli and RB Hall. "Plasma acceleration by electromagnetic and magnetostatic field gradients". In: *Nuclear fusion* 3.4 (1963), p. 001.

[27] F Bourg, R Geller, and B Jacquot. "Source d'ions lourds multicharges caprice 10 GHz pour tous les elements metalliques et Gazeux". In: *Nuclear Instruments and Methods in Physics Research Section A: Accelerators, Spectrometers, Detectors and Associated Equipment* 254.1 (1987), pp. 13–21.

[28] B Jacquot, P Briand, F Bourg, and R Geller. "Source d'ions lourds caprice 10 GHz 2ωce". In: *Nuclear Instruments and Methods in Physics Research Section A: Accelerators, Spectrometers, Detectors and Associated Equipment* 269.1 (1988), pp. 1–6.

[29] CM Lyneis et al. "Results with the superconducting electron cyclotron resonance ion source VENUS". In: *Review of scientific instruments* 75.5 (2004), pp. 1389–1393.

[30] C Lyneis, D Leitner, M Leitner, C Taylor, and S Abbott. "The third generation superconducting 28 GHz electron cyclotron resonance ion source VENUS". In: *Review of Scientific Instruments* 81.2 (2010).

[31] P Suominen and F Wenander. "Electron cyclotron resonance ion sources with arc-shaped coils". In: *Review of Scientific Instruments* 79.2 (2008).

[32] Claude M Lyneis et al. "Fourth generation electron cyclotron resonance ion sources". In: *Review of scientific instruments* 79.2 (2008).

[33] G.F. Crimi, A.C. Eckert, and DB Miller. *Microwave Driven Magnetic Plasma Accelerator Studies (Cyclops).* Tech. rep. General Electric Company, Space Sciences Laboratory, Missile and Space Division, 1967.

[34] M. Nagatomo. "Plasma acceleration by high frequency electromagnetic wave in staticmagnetic field gradient". In: *6th Electric Propulsion and Plasmadynamics Conference.* American Institute of Aeronautics and Astronautics, Sept. 1967, p. 660. DOI: `10.2514/6.1967-660`. URL: `https://doi.org/10.2514/6.1967-660`.

[35] E.F. Gibbons, P. Gloersen, and D.B. Miller. *Cyclotron resonance propulsion system.* Tech. rep. General Electric Co. Missile and Space Vehicle Dept., Philadelphia, 1963.

[36] D. B. Miller and E. F. Gibbons. "Experiments with an electron cyclotron resonance plasma accelerator". In: *AIAA Journal* 2.1 (Jan. 1964), pp. 35–41. DOI: `10.2514/3.2210`. URL: `https://doi.org/10.2514/3.2210`.

[37] HG Kosmahl, DB Miller, and GW Bethke. "Plasma acceleration with microwaves near cyclotron resonance". In: *Journal of Applied Physics* 38.12 (1967), pp. 4576–4582.

[38] David B Miller and George W Bethke. "Cyclotron resonance thruster design techniques." In: *AIAA Journal* 4.5 (1966), pp. 835–840.

[39] K. Takahashi, T. Lafleur, C. Charles, P. Alexander, and R.W. Boswell. "Electron Diamagnetic Effect on Axial Force in an Expanding Plasma: Experiments and Theory". In: *Physical Review Letters* 107.23 (2011), p. 235001. DOI: `10.1103/PhysRevLett.107.235001`.

[40] T. Vialis, J. Jarrige, and D. Packan. "Separate measurements of magnetic and pressure thrust contributions in a magnetic nozzle electron cyclotron resonance plasma thruster". In: *Space Propulsion Conference*. 499. Seville, Spain, May 2018.

[41] J.C. Sercel. "Electron-cyclotron-resonance (ECR) plasma acceleration". In: *AIAA 19th Fluid Dynamics, Plasma Dynamics and Lasers Conference*. 1987.

[42] J.C. Sercel. "Simple model of plasma acceleration in a magnetic nozzle". In: *21st International Electric Propulsion Conference*. Vol. 1. 1990.

[43] DA Kaufman and DG Goodwin. "Plume characteristics of an ECR plasma thruster". In: *27th International Electric Propulsion Conference*. 1993.

[44] Hitoshi Kuninaka and Shin Satori. "Development and demonstration of a cathodeless electron cyclotron resonance ion thruster". In: *Journal of Propulsion and Power* 14.6 (1998), pp. 1022–1026.

[45] T. Vialis, J. Jarrige, A. Aanesland, and D. Packan. "Direct thrust measurement of an electron cyclotron resonance plasma thruster". In: *Journal of Propulsion and Power* 34.5 (2018), pp. 1323–1333.

[46] Kyoichiro Toki, Hitoshi Kuninaka, Kazutaka Nishiyama, Yukio Shimizu, and Ikkoh Funaki. "Technological Readiness of Microwave Ion Engine System for MUSES-C Mission". In: *27th International Electric Propulsion Conference, IEPC-01-174*. 2001.

[47] Wataru Ohmichi and Hitoshi Kuninaka. "Performance degradation of a spacecraft electron cyclotron resonance neutralizer and its mitigation". In: *Journal of Propulsion and Power* 30.5 (2014), pp. 1368–1372.

[48] Takato Morishita, Ryudo Tsukizaki, Kazutaka Nishiyama, and Hitoshi Kuninaka. "Plasma parameters measured inside and outside a microwave-discharge-based plasma cathode using laser-induced fluorescence spectroscopy". In: *Journal of Applied Physics* 131.1 (2022).

[49] Kazutaka Nishiyama, Satoshi Hosoda, Kazuma Ueno, Ryudo Tsukizaki, and Hitoshi Kuninaka. "Development and testing of the Hayabusa2 ion engine system". In: *Transactions of the Japan Society for Aeronautical and Space Sciences, Aerospace Technology Japan* 14.ists30 (2016), Pb_131–Pb_140.

[50] Gregory D Emsellem and Serge Larigaldie. "Development of the electrodeless plasma thruster at high power: investigations on the microwave-plasma coupling". In: *Proc. 30th Int. Electric Propulsion Conf.(Florence, Italy)*. 2007.

[51] J. Jarrige, P.Q. Elias, F. Cannat, and D. Packan. "Characterization of a coaxial ECR plasma thruster". In: *44th AIAA Plasmadynamics and Lasers Conference, San Diego*. 2013.

[52] Julien Jarrige, Paul-Quentin Elias, and Denis Packan. "Measurement of ion acceleration in the magnetic nozzle of an ECR plasma thruster". In: *Space Propulsion 2014*. 2014.

[53] F. Cannat, T. Lafleur, J. Jarrige, P. Chabert, P.Q. Elias, and D. Packan. "Optimization of a coaxial electron cyclotron resonance plasma thruster with an analytical model". In: *Physics of Plasmas* 22.5 (2015), p. 053503.

[54] Simon Peterschmitt and Denis Packan. "Impact of the Microwave Coupling Structure on an Electron-Cyclotron Resonance Thruster". In: *Journal of Propulsion and Power* 37.6 (2021), pp. 806–815.

[55] Victor Désangles et al. "ECRA Thruster Advances: 30W and 200W Prototypes Latest Performances". In: *Journal of Electric Propulsion* 2.1 (2023), p. 10. DOI: `10.1007/s44205-023-00046-x`.

[56] A. Sánchez-Villar, J. Zhou, M. Merino, and E. Ahedo. "Coupled plasma transport and electromagnetic wave simulation of an ECR thruster". In: *Plasma Sources Science and Technology* 30.4 (2021), p. 045005. DOI: `10.1088/1361-6595/abde20`.

[57] Á. Sánchez-Villar et al. "Comparison of a hybrid model and experimental measurements for a dielectric-coated coaxial ECR thruster". In: *Plasma Sources Science and Technology* 32.1 (2023), p. 014002. DOI: `10.1088/1361-6595/acb00c`.

[58] Jesús Perales-Díaz et al. "Hybrid plasma simulations of a magnetically shielded Hall thruster". In: *Journal of Applied Physics* 131.10 (2022), p. 103302. DOI: `10.1063/5.0065220`.

[59] Pedro Jiménez, Jiewei Zhou, JAUME Navarro-Cavallé, Pablo Fajardo, Mario Merino, and Eduardo Ahedo. "Analysis of a cusped helicon plasma thruster discharge". In: *Plasma Sources Science and Technology* 32.10 (2023), p. 105013. DOI: `10.1088/1361-6595/ad01da`. URL: `https://dx.doi.org/10.1088/1361-6595/ad01da`.

[60] Pedro Jiménez, Mario Merino, and Eduardo Ahedo. "Wave propagation and absorption in a Helicon plasma thruster source and its plume". In: *Plasma Sources Science and Technology* 31.4 (2022), p. 045009. DOI: `10.1088/1361-6595/ac5ecd`.

[61] B Wachs and B Jorns. "Background pressure effects on ion dynamics in a low-power magnetic nozzle thruster". In: *Plasma Sources Science and Technology* 29.4 (2020), p. 045002.

[62] Benjamin Wachs and Benjamin Jorns. "Optimization of an ECR Thruster using Two Frequency and Pulsed Waveforms". In: *AIAA Propulsion and Energy 2021 Forum*. 2021, p. 3382.

[63] Benjamin N Wachs and Benjamin A Jorns. "Sub-millinewton thrust stand and wireless power coupler for microwave-powered small satellite thrusters". In: *Review of Scientific Instruments* 93.8 (2022).

[64] Vlad-George Tirila, Alain Demairé, and Charles N Ryan. "Review of alternative propellants in Hall thrusters". In: *Acta Astronautica* (2023).

[65] Marco Riccardo Inchingolo, Mario Merino, and Jaume Navarro-Cavallé. "Hybrid PIC-Fluid Simulation of a Waveguide ECR Magnetic Nozzle Plasma Thruster". In: *Space Propulsion Conference 2021*. 00192. March 17-19: Association Aéronautique et Astronautique de France, 2021.

[66] M. R. Inchingolo, M. Merino, and J. Navarro-Cavallé. "Plume Characterization of a Waveguide ECR Thruster". In: *Journal of Applied Physics* 133.11 (2023), p. 113304. DOI: `10.1063/5.0138780`.

[67] Marco Inchingolo, Mario Merino, Mick Wijnen, and Jaume Navarro-Cavallé. "Thrust Measurements of a waveguide Electron Cyclotron Resonance Thruster". In: *Submitted to: Journal of Applied Physics* (2024).

[68] Alfio E Vinci, Marco R Inchingolo, Stéphane Mazouffre, and Jaume Navarro-Cavallé. "Ion dynamics in the magnetic nozzle of a waveguide ECR thruster via laser-induced fluorescence spectroscopy". In: *Journal of Physics D: Applied Physics* 56.2 (2022), p. 025204.

[69] R. Shirasawa, M. R. Inchingolo, T. Morishita, R. Tsukizaki, and K. Nishiyama. "Backflow Xenon Ions Measurement by Laser-induced Fluorescence Spectroscopy in the Plume of a Microwave Discharge Ion Thruster". In: *International Symposium On Space Technology and Science (ISTS), Kurume*. 2023.

[70] M. Inchingolo and J. Navarro-Cavallé. "Faraday Cup Design for Electrodeless Plasma Thrusters". In: *10th EUCASS Conference*. Lausanne, Switzerland, July 9–13, 2023.

[71] Thomas H Stix. *Waves in plasmas*. Springer Science & Business Media, 1992.

[72] J.A. Bittencourt. *Fundamentals of plasma physics*. Springer, Berlin, Germany, 2004.

[73] D. Cassady et al. "VASIMR performance results". In: *46th Joint Propulsion Conference*. 2010.

[74] F. Diaz and R. Chang. "The VASIMR rocket". In: *Scientific American* 283.5 (2000), pp. 90–97.

[75] Mario Merino and Eduardo Ahedo. "Magnetic Nozzles for Space Plasma Thrusters". In: *Encyclopedia of Plasma Technology*. Ed. by J. Leon Shohet. Vol. 2. Taylor and Francis, 2016, pp. 1329–1351.

[76] Eduardo Ahedo and Mario Merino. "Two-Dimensional Supersonic Plasma Acceleration in a Magnetic Nozzle". In: *Physics of Plasmas* 17.7 (2010), p. 073501. DOI: `10.1063/1.3442736`.

[77] E. B. Hooper. "Plasma detachment from a magnetic nozzle". In: *Journal of Propulsion and Power* 9.5 (1993), pp. 757–763. DOI: `10.2514/3.23686`.

[78] Alfio E Vinci, Stéphane Mazouffre, Víctor Gómez, Pablo Fajardo, and Jaume Navarro-Cavallé. "Laser-induced fluorescence spectroscopy on xenon atoms and ions in the magnetic nozzle of a helicon plasma thruster". In: *Plasma Sources Science and Technology* 31.9 (2022), p. 095007.

[79] S Correyero, J Jarrige, D Packan, and E Ahedo. "Plasma beam characterization along the magnetic nozzle of an ECR thruster". In: *Plasma Sources Science and Technology* 28.9 (2019), p. 095004. DOI: `10.1088/1361-6595/ab38e1`.

[80] TA Collard and BA Jorns. "Magnetic nozzle efficiency in a low power inductive plasma source". In: *Plasma Sources Science and Technology* 28.10 (2019), p. 105019.

[81] Kazunori Takahashi, Trevor Lafleur, Christine Charles, Peter Alexander, and Rod W Boswell. "Axial force imparted by a current-free magnetically expanding plasma". In: *Physics of Plasmas* 19.8 (2012), p. 083509.

[82] JM Little and EY Choueiri. "Electron Cooling in a Magnetically Expanding Plasma". In: *Physical Review Letters* 117.22 (2016), p. 225003.

[83] Kazunori Takahashi, Christine Charles, Rod W Boswell, and Akira Ando. "Thermodynamic analogy for electrons interacting with a magnetic nozzle". In: *Physical review letters* 125.16 (2020), p. 165001.

[84] A. Vinci, Q. Delavière-Delion, and S. Mazouffre. "Electron thermodynamics along magnetic nozzle lines in a helicon plasma". In: *Journal of Electric Propulsion* 1.4 (2022).

[85] June Young Kim, Kyoung-Jae Chung, Kazunori Takahashi, Mario Merino, and Eduardo Ahedo. "Kinetic Electron Cooling in Magnetic Nozzles: Experiments and Modeling". In: *arXiv preprint arXiv:2212.07161* (2022).

[86] Jaume Navarro-Cavallé, S. Correyero, and E. Ahedo. "Collisionless electron cooling on magnetized plasma expansions: advances on modelling". In: 34th *International Electric Propulsion Conference*. paper 2015-117. Kobe, Japan, July 6-10: Electric Rocket Propulsion Society, 2015.

[87] Manuel Martínez-Sánchez, Jaume Navarro-Cavallé, and Eduardo Ahedo. "Electron Cooling and Finite Potential Drop in a Magnetized Plasma Expansion". In: *Physics of Plasmas* 22.5 (2015), p. 053501. DOI: `10.1063/1.4919627`.

[88] W. Cox, C. Charles, R.W. Boswell, and R. Hawkins. "Spatial retarding field energy analyzer measurements downstream of a helicon double layer plasma". In: *Applied Physics Letters* 93.7 (2008), p. 071505.

[89] K. Terasaka, S. Yoshimura, K. Ogiwara, M. Aramaki, and M.Y. Tanaka. "Experimental studies on ion acceleration and stream line detachment in a diverging magnetic field". In: *Physics of Plasmas* 17.7 (2010), p. 072106.

[90] K. Takahashi, Y. Itoh, and T. Fujiwara. "Operation of a permanent-magnets-expanding plasma source connected to a large-volume diffusion chamber". In: *Journal of Physics D: Applied Physics* 44.1 (2011), p. 015204.

[91] Mario Merino and Eduardo Ahedo. "Plasma detachment in a propulsive magnetic nozzle via ion demagnetization". In: *Plasma Sources Science and Technology* 23.3 (2014), p. 032001. DOI: 10.1088/0963-0252/23/3/032001.

[92] David M Pozar. *Microwave engineering*. John wiley & sons, 2011.

[93] F AST. "The annual compendium of commercial space transportation: 2018 [J]". In: *Federal Aviation Administration* (2018).

[94] *Satellite Database*. https://www.ucsusa.org/resources/satellite-database. Accessed: 2023-11-01.

[95] Richard R Hofer and Thomas M Randolph. "Mass and cost model for selecting thruster size in electric propulsion systems". In: *Journal of Propulsion and Power* 29.1 (2013), pp. 166–177.

[96] Elaine M Petro and Raymond J Sedwick. "Survey of moderate-power electric propulsion systems". In: *Journal of Spacecraft and Rockets* 54.3 (2017), pp. 529–541.

[97] J.C. Sercel. "Electron-cyclotron-resonance (ECR) plasma thruster research". In: *24th Joint Propulsion Conference*. 1988, p. 2916.

[98] F. Cannat, J. Jarrige, T. Lafleur, P.Q. Elias, and D. Packan. "Experimental geometry investigation of a coaxial ECR plasma thruster". In: *Proc. of the 34th Int. Electric Propulsion Conf.(Kobe-Hyogo, Japan)*. 2015, pp. 2015–242.

[99] Eduardo Ahedo and Mario Merino. "On plasma detachment in propulsive magnetic nozzles". In: *Physics of Plasmas* 18.5 (2011), p. 053504. DOI: 10.1063/1.3589268.

[100] ET Thostenson and T-W Chou. "Microwave processing: fundamentals and applications". In: *Composites Part A: Applied Science and Manufacturing* 30.9 (1999), pp. 1055–1071.

[101] M Möller and H Linn. "New microwave frequency 5.8 GHz for industrial applications". In: *Key Engineering Materials* 264 (2004), pp. 735–738.

[102] Nathan Marcuvitz. *Waveguide handbook*. 21. Iet, 1951.

[103] Roger B Marks and Dylan F Williams. "A general waveguide circuit theory". In: *Journal of research of the National Institute of Standards and Technology* 97.5 (1992), p. 533.

[104] Geoff H Bryant. *Principles of microwave measurements*. Vol. 5. IET, 1993.

[105] E.B. Hooper. "Plasma flow resulting from electron cyclotron resonance heating on a magnetic hill". In: *Physics of Plasmas* 2 (1995), p. 4563.

[106] T. Lafleur. "Helicon plasma thruster discharge model". In: *Physics of Plasmas* 21.4 (2014), p. 043507.

[107] Alvaro Sánchez-Villar, Jiewei Zhou, Mario Merino, and Eduardo Ahedo. "PIC/fluid/wave Simulations of the Plasma Discharge in an ECR Plasma Thruster". In: 36th *International Electric Propulsion Conference*. IEPC-2019-633. Vienna, Austria: Electric Rocket Propulsion Society, 2019.

[108] D. Packan et al. "The MINOTOR H2020 project for ECR thruster development". In: 35th *International Electric Propulsion Conference*. IEPC-2017-547. Electric Rocket Propulsion Society, 2017.

[109] Adrián Domínguez-Vázquez. "Axisymmetric simulation codes for Hall effect thrusters and plasma plumes". PhD thesis. Universidad Carlos III de Madrid, Leganés, Spain, 2019.

[110] Daniel Pérez-Grande. "Fluid modeling and simulation of the electron population in Hall effect thrusters with complex magnetic topologies". PhD thesis. Universidad Carlos III de Madrid, Leganés, Spain, 2018.

[111] Adrián Domínguez-Vázquez, Jiewei Zhou, Pablo Fajardo, and Eduardo Ahedo. "Analysis of the plasma discharge in a Hall thruster via a hybrid 2D code". In: 36th *International Electric Propulsion Conference*. IEPC-2019-579. Vienna, Austria: Electric Rocket Propulsion Society, 2019.

[112] Filippo Cichocki, Adrián Domínguez-Vázquez, Mario Merino, and Eduardo Ahedo. "Hybrid 3D model for the interaction of plasma thruster plumes with nearby objects". In: *Plasma Sources Science and Technology* 26.12 (2017), p. 125008. DOI: `10.1088/1361-6595/aa986e`.

[113] Filippo Cichocki, Mario Merino, Eduardo Ahedo, Juan Manuel Catalán, and Adrián Domínguez-Vázquez. "Application of EP2PLUS 3D code to plasma thruster plumes and discharges". In: *EPIC workshop*. London, UK, 2018.

[114] Daniel Pérez-Grande, O. González-Martínez, Pablo Fajardo, and Eduardo Ahedo. "Analysis of the numerical diffusion in anisotropic mediums: benchmarks for magnetic field aligned meshes in space propulsion simulations". In: *Applied Sciences* 6.11 (2016), p. 354.

[115] D. Pérez-Grande, J. Zhou, A. Domínguez-Vázquez, P. Fajardo, and E. Ahedo. "Development updates for a two-dimensional axisymmetric hybrid code for plasma thruster discharges". In: 35th *International Electric Propulsion Conference*. IEPC-2017-201. Atlanta, GA: Electric Rocket Propulsion Society, 2017.

[116] E. Ahedo and V. Pablo. "Combined effects of electron partial thermalization and secondary emission in Hall thruster discharges". In: *Physics of Plasmas* 14 (2007), p. 083501.

[117] E. Ahedo, J.M. Gallardo, and M. Martínez-Sánchez. "Effects of the radial-plasma wall interaction on the axial Hall thruster discharge". In: *Physics of Plasmas* 10.8 (2003), pp. 3397–3409.

[118] Jiewei Zhou, Daniel Pérez-Grande, Pablo Fajardo, and Eduardo Ahedo. "Numerical treatment of a magnetized electron fluid within an electromagnetic plasma thruster code". In: *Plasma Sources Science and Technology* 28.11 (2019), p. 115004.

[119] C. Charles. "High density conics in a magnetically expanding helicon plasma". In: *Applied Physics Letters* 96.5 (2010), pp. 051502–051502.

[120] Justin M Little and Edgar Y Choueiri. "Electron Demagnetization in a Magnetically Expanding Plasma". In: *Physical review letters* 123.14 (2019), p. 145001.

[121] Mario Merino and Eduardo Ahedo. "Influence of Electron and Ion Thermodynamics on the Magnetic Nozzle Plasma Expansion". In: *IEEE Transactions on Plasma Science* 43.1 (Jan. 2015), pp. 244–251. DOI: `10.1109/TPS.2014.2316020`.

[122] T. Lafleur, F. Cannat, J. Jarrige, P.Q. Elias, and D. Packan. "Electron dynamics and ion acceleration in expanding-plasma thrusters". In: *Plasma Sources Science and Technology* 24.6 (2015), p. 065013.

[123] J. Jarrige, S. Correyero Plaza, P.Q. Elias, and D. Packan. "Investigation on the ion velocity distribution in the magnetic nozzle of an ECR plasma thruster using LIF measurements". In: 35th *International Electric Propulsion Conference*. IEPC-2017-382. Atlanta, GA: Electric Rocket Propulsion Society, Fairview Park, OH, 2017.

[124] Mick Wijnen. "Diagnostic Methods for the Characterization of a Helicon Plasma Thruster". PhD thesis. Universidad Carlos III de Madrid, Leganés, Spain, 2022.

[125] Robert B. Lobbia and Brian E. Beal. "Recommended Practice for Use of Langmuir Probes in Electric Propulsion Testing". In: *Journal of Propulsion and Power* 33.3 (2017), pp. 566–581. DOI: `10.2514/1.B35531`.

[126] Théo Vialis. "Développement d'un propulseur plasma à résonance cyclotron électronique pour les satellites". PhD thesis. SORBONNE UNIVERSITE, 2018.

[127] Yu Daren, Ding Jiapeng, and Dai Jingmin. "Spectrum diagnosis for fuchsia plume of Hall effect thruster with xenon as propellant". In: *Plasma Science and Technology* 8.6 (2006), p. 685.

[128] Daisuke Kusamoto and K Komurasaki. "Optical diagnosis of plasma in a channel of Hall thrusters". In: *International Electric Propulsion Conference.* 1997, pp. 405–410.

[129] Xi-Ming Zhu et al. "A xenon collisional-radiative model applicable to electric propulsion devices: II. Kinetics of the 6s, 6p, and 5d states of atoms and ions in Hall thrusters". In: *Plasma Sources Science and Technology* 28.10 (2019), p. 105005.

[130] Danis Packan et al. "H2020 MINOTOR: Magnetic nozzle electron cyclotron resonance thruster". In: 36th *International Electric Propulsion Conference.* IEPC-2019-875. Vienna, Austria: Electric Rocket Propulsion Society, 2019.

[131] *BIAGI Database.* `https://nl.lxcat.net`. Accessed: 2022-12-06.

[132] *NIFS Database.* `https://dbshino.nifs.ac.jp`.

[133] Horatiu C Dragnea, Alejandro Lopez Ortega, Hani Kamhawi, and Iain D Boyd. "Simulation of a Hall effect thruster using krypton propellant". In: *Journal of Propulsion and Power* (2020).

[134] M. Martínez-Sánchez, J. Navarro-Cavallé, and E. Ahedo. "Electron cooling and finite potential drop in a magnetized plasma expansion". In: *Physics of Plasmas* 22.5 (2015), p. 053501.

[135] Eduardo Ahedo, Sara Correyero, Jaume Navarro, and Mario Merino. "Macroscopic and parametric study of a kinetic plasma expansion in a paraxial magnetic nozzle". In: *Plasma Sources Science and Technology* 29.4 (2020), p. 045017. DOI: `10.1088/1361-6595/ab7855`.

[136] M.A. Lieberman and A.J. Lichtenberg. *Principles of plasma discharges and materials processing.* John Wiley and Sons, Hoboken, NJ, 2005.

[137] Mario Merino, Judit Nuez, and Eduardo Ahedo. "Fluid-kinetic model of a propulsive magnetic nozzle". In: *Plasma Sources Science and Technology* 30.11 (2021), p. 115006. DOI: `10.1088/1361-6595/ac2a0b`.

[138] Gonzalo Sánchez-Arriaga, Jiewei Zhou, E Ahedo, Manuel Martínez-Sánchez, and Jesús José Ramos. "Kinetic features and non-stationary electron trapping in paraxial magnetic nozzles". In: *Plasma Sources Science and Technology* 27.3 (2018), p. 035002.

[139] June Young Kim, KS Chung, Seongcheol Kim, Jong Hyeon Ryu, Kyoung-Jae Chung, and YS Hwang. "Thermodynamics of a magnetically expanding plasma with isothermally behaving confined electrons". In: *New Journal of Physics* 20.6 (2018), p. 063033.

[140] Simon Peterschmitt and Denis Packan. "Comparison of Waveguide Coupled and Coaxial Coupled ECRA Magnetic Nozzle Thruster using a Thrust Balance". In: *Proc. of the 36th Int. Electric Propulsion Conf.(Vienna, Austria)*. 2019, pp. 2019–188.

[141] D.B. Miller, E.F. Gibbons, and P. Gloersen. "Cyclotron resonance propulsion system". In: *Electric Propulsion Conference*. 1962, p. 2.

[142] M. Wijnen, J. Navarro-Cavallé, and P. Fajardo. "Mechanically Amplified Milli-Newton Thrust Balance for Direct Thrust Measurements of Electric Thrusters for Space Propulsion". In: *IEEE Transactions on Instrumentation and Measurement* 70 (2021), p. 3505318. DOI: 10.1109/TIM.2020.3037305.

[143] Kurt A Polzin, Thomas E Markusic, Boris J Stanojev, Amado DeHoyos, and Benjamin Spaun. "Thrust Stand for Electric Propulsion Performance Evaluation". In: *Review of Scientific Instruments* 77.10 (2006), p. 105108. DOI: 10.1063/1.2357315.

[144] Brett Robert Tartler. "Construction and performance of an inverted pendulum thrust balance". PhD thesis. Massachusetts Institute of Technology, 2010.

[145] Andreas Neumann, Jens Simon, and Jens Schmidt. "Thrust measurement and thrust balance development at DLR's electric propulsion test facility". In: *EPJ Techniques and Instrumentation* 8.1 (2021), p. 17.

[146] Ian H Hutchinson. "Principles of plasma diagnostics". In: *Plasma Physics and Controlled Fusion* 44.12 (2002), p. 2603.

[147] Filippo Cichocki, Jaume Navarro-Cavallé, Alberto Modesti, and Gonzalo Ramírez Vázquez. "Magnetic Nozzle and RPA Simulations vs. Experiments for a Helicon Plasma Thruster Plume". In: *Frontiers in Physics* 10 (2022). DOI: 10.3389/fphy.2022.876684.

[148] Eduardo Ahedo and Manuel Martínez Sánchez. "Theory of a Stationary Current-Free Double Layer in a Collisionless Plasma". In: *Physical Review Letters* 103.13 (2009), pp. 1–4. DOI: 10.1103/PhysRevLett.103.135002. URL: http://link.aps.org/doi/10.1103/PhysRevLett.103.135002.

[149] Mario Merino and Eduardo Ahedo. "Two-dimensional quasi-double-layers in two-electron-temperature, current-free plasmas". In: *Physics of Plasmas* 20.2 (2013), p. 023502. DOI: 10.1063/1.4789900.

[150] C. Charles and R. Boswell. "Current-free double-layer formation in a high-density helicon discharge". In: *Applied Physics Letters* 82.9 (2003), pp. 1356–1358.

[151] DF Berisford, Roger D Bengtson, and Laxminarayan L Raja. "Power balance and wall erosion measurements in a helicon plasma". In: *Physics of Plasmas* 17.3 (2010), p. 033503.

[152] J. Zhou, A. Domínguez-Vázquez, P. Fajardo, and E. Ahedo. "Magnetized fluid electron model within a two-dimensional hybrid simulation code for electrodeless plasma thrusters". In: *Plasma Sources Science and Technology* 31.4 (2022), p. 045021.

[153] Pedro Jiménez, Luis Chacón, and Mario Merino. "An implicit, conservative electrostatic particle-in-cell algorithm for paraxial magnetic nozzles". In: *Submitted to: Journal of Computational Physics* (2023). arXiv: 2305.07146.

[154] J Hopwood and J Asmussen. "Neutral gas temperatures in a multipolar electron cyclotron resonance plasma". In: *Applied physics letters* 58.22 (1991), pp. 2473–2475.

[155] Toshiki Nakano, Nader Sadeghi, and Richard A Gottscho. "Ion and neutral temperatures in electron cyclotron resonance plasma reactors". In: *Applied physics letters* 58.5 (1991), pp. 458–460.

[156] S Mazouffre, V Kulaev, and J Pérez Luna. "Ion diagnostics of a discharge in crossed electric and magnetic fields for electric propulsion". In: *Plasma Sources Science and Technology* 18.3 (July 2009), p. 034022. DOI: 10.1088/0963-0252/18/3/034022. URL: https://doi.org/10.1088/0963-0252/18/3/034022.

[157] Stéphane Mazouffre. "Laser-induced fluorescence diagnostics of the cross-field discharge of Hall thrusters". In: *Plasma Sources Science and Technology* 22.1 (Nov. 2012), p. 013001. DOI: 10.1088/0963-0252/22/1/013001. URL: https://doi.org/10.1088/0963-0252/22/1/013001.

[158] Benjamin Wachs and Benjamin Jorns. "Background pressure effects on ion dynamics in a low-power magnetic nozzle thruster". In: *Plasma Sources Science and Technology* 29.4 (2020), p. 045002.

[159] J.J. Szabo. "Fully kinetic numerical modeling of a plama thruster". PhD thesis. Massachusetts Institute of Technology, 2001.

[160] Kazutaka Nishiyama, Satoshi Hosoda, Ryudo Tsukizaki, and Hitoshi Kuninaka. "In-flight operation of the Hayabusa2 ion engine system on its way to rendezvous with asteroid 162173 Ryugu". In: *Acta Astronautica* 166 (2020), pp. 69–77.

[161] Ayumu Nono, Takato Morishita, Satoshi Hosoda, Ryudo Tsukizaki, and Kazu-
      taka Nishiyama. "Effect of spacecraft surface conductivity on voltage of
      microwave neutralizer in gridded ion thrusters". In: *Acta Astronautica* 212
      (2023), pp. 130–138.

[162] *Nikkei Technology Online.* https://xtech.nikkei.com/dm/article/
      COLUMN/20141028/385367/.

[163] Ryudo Tsukizaki, Toshiyuki Ise, Hiroyuki Koizumi, Hiroyoshi Togo, Kazutaka
      Nishiyama, and Hitoshi Kuninaka. "Thrust enhancement of a microwave ion
      thruster". In: *Journal of Propulsion and Power* 30.5 (2014), pp. 1383–1389.

[164] Ayumu Nono et al. "Numerical investigation of ion back flow of a microwave
      discharge ion thruster". In: *International Symposium on Space Technology
      and Science, Kurume, Japan.* Mar. 2023.

[165] W RUYTEN and D Keefer. "Characterization of electric thruster plumes
      using multiplexed laserinduced fluorescence measurements". In: *23rd Plas-
      madynamics and Lasers Conference.* 1992, p. 2965.

[166] Stéphane Mazouffre. "Laser-induced fluorescence spectroscopy applied to elec-
      tric thrusters". In: *Von Karman Institute for Fluid Dynamics, STO-AVT-VKI
      Lecture series 263* (2016), p–10.

[167] Alfio E Vinci and Stéphane Mazouffre. "Enhanced electron heating in the
      magnetic nozzle of a radio-frequency plasma via electron cyclotron reso-
      nance". In: *Europhysics Letters* 141.4 (2023), p. 44002.

[168] Wensheng Huang. "Study of Hall thruster discharge channel wall erosion via
      optical diagnostics". PhD thesis. University of Michigan, 2011.

[169] S Mazouffre, G Bourgeois, Laurent Garrigues, and E Pawelec. "A comprehen-
      sive study on the atom flow in the cross-field discharge of a Hall thruster".
      In: *Journal of Physics D: Applied Physics* 44.10 (2011), p. 105203.

[170] R.I.S. Roy, D.E. Hastings, and N.A. Gastonis. "Ion-thruster plume model-
      ing for backflow contamination". In: *Journal of Spacecraft and Rockets* 33.4
      (1996), pp. 525–534.

[171] PCT De Boer. "Electric probe measurements in the plume of an ion thruster".
      In: *Journal of propulsion and power* 12.1 (1996), pp. 95–104.

[172] Jesús Perales-Díaz, Filippo Cichocki, Mario Merino, and Eduardo Ahedo.
      "Formation and neutralization of electric charge and current of an ion thruster
      plume". In: *Plasma Sources Science and Technology* 30.10 (2021), p. 105023.
      DOI: 10.1088/1361-6595/ac2a19.

[173] Y. Yamamura and H. Tawara. "Energy Dependence of Ion-Induced Sputter-
      ing Yields From Monatomic Solids at Normal Incidence". In: *Atomic Data
      and Nuclear Data Tables* 62 (1996), pp. 149–253.

[174] Sidney Hu, A Joshi, Vadim Khayms, Brian Emgushov, Lance Werthman, and Vincent Smentkowski. "Hall thruster plume effects and sputtering of spacecraft surfaces". In: *37th Joint Propulsion Conference and Exhibit*. 2001, p. 3356.

[175] John Fife, D Vangilder, D Kirtley, and M Gibbons. "Initial use of a 3-d plasma simulation system for predicting surface sputtering and contamination by hall thrusters". In: *33rd Plasmadynamics and Lasers Conference*. 2002, p. 2125.

[176] S Mazouffre, G Largeau, L Garrigues, C Boniface, and K Dannenmayer. "Evaluation of various probe designs for measuring the ion current density in a Hall thruster plume". In: *35th International Electric Propulsion Conference*. IEPC-2017-336. 2017.

[177] Daniel L Brown and Alec D Gallimore. "Evaluation of ion collection area in Faraday probes". In: *Review of Scientific Instruments* 81.6 (2010).

[178] Daniel L Brown, Mitchell LR Walker, James Szabo, Wensheng Huang, and John E Foster. "Recommended Practice for Use of Faraday Probes in Electric Propulsion Testing". In: *Journal of Propulsion and Power* 33.3 (2016), pp. 582–613. DOI: 10.2514/1.B35696.

[179] M.L.R. Walker, R.R. Hofer, and A.D. Gallimore. "Ion collection in Hall thruster plumes". In: *Journal of Propulsion and Power* 22.1 (2006), p. 205.

[180] E Cantero et al. *Performance Tests of a short Faraday Cup designed for HIE-ISOLDE*. Tech. rep. 2013.

[181] Smruti Ranjan Mohanty, Heman Bhuyan, Nirod Kumar Neog, Rabindra Kumar Rout, and Eiki Hotta. "Development of multi Faraday cup assembly for ion beam measurements from a low energy plasma focus device". In: *Japanese journal of applied physics* 44.7R (2005), p. 5199.

[182] J Prokpek et al. "Development and first experimental tests of Faraday cup array". In: *Review of Scientific Instruments* 85.1 (2014).

[183] Valentin Hugonnaud, Stéphane Mazouffre, and David Krejci. "Faraday cup sizing for electric propulsion ion beam study: Case of a field-emission-electric propulsion thruster". In: *Review of Scientific Instruments* 92.8 (2021).

[184] Hugonnaud Valentin and Mazouffre Stéphane. "Optimization of a Faraday cup collimator for electric propulsion device beam study: Case of a Hall thruster". In: *Applied Sciences* 11.5 (2021), p. 2419.

[185] J Navarro-Cavallé, M Wijnen, P Fajardo, and E Ahedo. "Experimental Characterization of a 1 kW Helicon Plasma Thruster". In: *Vacuum* 149 (2018), pp. 69–73. DOI: 10.1016/j.vacuum.2017.11.036.

[186] V. Gómez et al. "RF Power-Plasma Coupling Experimental Results in a Helicon Plasma Thruster Prototype". In: 36th *International Electric Propulsion Conference*. IEPC-2019-365. Vienna, Austria: Electric Rocket Propulsion Society, 2019.

[187] AE Vinci, Stéphane Mazouffre, Marco R Inchingolo, Víctor Gómez, Pablo Fajardo, and Jaume Navarro-Cavallé. "Probing xenon atoms and ions velocity in the magnetic nozzle of a helicon plasma thruster". In: *37th International Electric Propulsion Conference*. 2022.

[188] Kristi de Grys, Dennis Tilley, and Randy Aadland. "BPT Hall thruster plume characteristics". In: *35th Joint Propulsion Conference and Exhibit*. 1999, p. 2283.

[189] Richard R Hofer, Mitchell LR Walker, and Alec D Gallimore. "A Comparison of nude and collimated Faraday Probes for Use with Hall Thrusters". In: *27th International Electric Propulsion Conference*. Electric Rocket Propulsion Soc. Fairview Park, OH. 2001, pp. 01–020.

[190] Jaume Navarro-Cavallé et al. "Development and Characterization of the Helicon Plasma Thruster Prototype HPT05M". In: 36th *International Electric Propulsion Conference*. IEPC-2019-596. Vienna, Austria: Electric Rocket Propulsion Society, 2019.

[191] Homer D Hagstrum. "Auger ejection of electrons from tungsten by noble gas ions". In: *Physical Review* 96.2 (1954), p. 325.

[192] S.F. Engelman and J.M. Fife. *Hemispherical Measurements of the SPT-140 Plume*. Tech. rep. 2002.